Forschungsbericht 2026-02

Aerodynamic Interaction of Multiple Bodies in Hypersonic Flow

Patrick Seltner

Deutsches Zentrum für Luft- und Raumfahrt
Institut für Aerodynamik und Strömungstechnik
Abteilung Über- und Hyperschalltechnologien
Köln

DLR Deutsches Zentrum
für Luft- und Raumfahrt

Forschungsbericht 2026-02

Aerodynamic Interaction of Multiple Bodies in Hypersonic Flow

Patrick Seltner

Deutsches Zentrum für Luft- und Raumfahrt
Institut für Aerodynamik und Strömungstechnik
Abteilung Über- und Hyperschalltechnologien
Köln

145	Seiten
75	Bilder
13	Tabellen
123	Literaturstellen

Deutsches Zentrum
für Luft- und Raumfahrt

Herausgeber:

Deutsches Zentrum
für Luft- und Raumfahrt e. V.
Wissenschaftliche Information
Linder Höhe
D-51147 Köln

ISSN 1434-8454
ISRN DLR-FB-2026-02
Erscheinungsjahr 2026
DOI: 10.57676/9890-qp63

Wiedereintrittstrajektorie, Aerodynamische Wechselwirkung, Weltraumschrott, Asteroid, Gasdynamik, Hyperschallwindkanal, Shock-Wave Surfing, Freiflugtechnik, Stereo-Tracking

Patrick SELTNER
DLR, Institut für Aerodynamik und Strömungstechnik, Köln

Aerodynamische Wechselwirkung mehrerer Körper in Hyperschallströmungen

RWTH Aachen Universität

Asteroiden und Weltraummüll stellen eine erhebliche Bedrohung dar, die für den Schutz der Bevölkerung und für die sichere und nachhaltige Nutzung des Weltraums immer relevanter wird. Aerodynamische Effekte, die während des Eintritts dieser Objekte aus dem Weltraum in die Atmosphäre auftreten, sind entscheidend für die zuverlässige Vorhersage der Flugbahnen und der Aufprallfläche der überlebenden Fragmente. Die vorliegende Arbeit wirft einen neuen Blick darauf, wie das aerodynamische Verhalten von einzelnen und mehreren stumpfen Körpern mit Hyperschallgeschwindigkeit ihre Bewegung beeinflusst. Der Einfluss von Form und Orientierung des Körpers auf seine Aerodynamik und Stabilität steht im Mittelpunkt dieser Veröffentlichung. Im Hyperschallwindkanal H2K des Deutschen Zentrums für Luft- und Raumfahrt (DLR) in Köln wurden Freiflugexperimente mit Einzel- und Tandem-Körperanordnungen aus Kugeln, Würfeln und Zylindern durchgeführt. Dabei erfasste das Hochgeschwindigkeits-Stereotracking die Bewegungen des Modells während des Freiflugs und die Hochgeschwindigkeits-Schlieren-Videografie lieferte die Visualisierung der Strömungstopologie. Die Ableitungen der Bewegungsdaten und aerodynamische Koeffizienten wurden in einem umfangreichen Datenauswertung ermittelt. Die beobachteten Effekte für mehrere interagierender Körper umfassen verschiedene Arten von Stoß-Stoß-Interaktionen und Nachlauf-Stoß-Interaktionen.

Re-entry Trajectory, Aerodynamic Interaction, Space Debris, Asteroid, Gasdynamics, Hypersonic Wind Tunnel, Shock-Wave Surfing, Free-Flight Technique, Stereo Tracking
(Published in English)

Patrick SELTNER
German Aerospace Center (DLR), Institute of Aerodynamics and Flow Technologies, Cologne

Aerodynamic Interaction of Multiple Bodies in Hypersonic Flow

RWTH Aachen University

Asteroids and space debris pose a significant threat, which is becoming more relevant for the protection of the population and for the safe and sustainable use of space. Aerodynamic phenomena that occur during the atmospheric entry of these objects from outer space are crucial for the reliable prediction of the flight trajectories and the impact footprint of surviving fragments. This work takes a new look at how the aerodynamic behavior of single and multiple blunt bodies traveling at hypersonic speed affect their motion. The influence of the body shape and orientation on its aerodynamics and stability is the focus of this publication. Free-flight experiments have been carried out in the hypersonic wind tunnel H2K at the German Aerospace Center (DLR) in Cologne with single and tandem body arrangements of spheres, cubes and cylinders. High-speed stereo-tracking captured the model motions during free-flight, and high-speed schlieren videography provided documentation of the flow topology. Motion derivatives and aerodynamic coefficients have been determined in an extensive post-processing. The observed phenomena for multiple objects include different types of shock-shock interactions and wake-shock interactions. In this research, the results show that the geometry of the body has an immense influence on the aerodynamic loads and thus on the motion behavior.

Aerodynamic Interaction of Multiple Bodies in Hypersonic Flow

Aerodynamische Wechselwirkung mehrerer Körper in Hyperschallströmungen

Von der Fakultät für Maschinenwesen
der Rheinisch-Westfälischen Technischen Hochschule Aachen
zur Erlangung des akademischen Grades eines Doktors der Ingenieurwissenschaften
genehmigte Dissertation

vorgelegt von

Patrick Matthias Seltner

Berichter: Univ.-Prof. Dr.-Ing. Karl Alexander Heufer
Hon.-Prof. Dr.-Ing. Ali Gülhan

Tag der mündlichen Prüfung: 30.10.2025

Acknowledgement

An dieser Stelle möchte ich mich bei allen Menschen bedanken, die mich bei der Erstellung dieser Arbeit unterstützt und ermutigt haben. Ohne euch wäre diese nicht möglich gewesen!

Zunächst möchte ich mich bei Prof. Dr. Alexander Heufer und Prof. Dr. Ali Gülhan bedanken für die wissenschaftliche Betreuung dieser Dissertation. Darüberhinaus danke ich Prof. Dr. Ali Gülhan herzlich für die gewährte Freiheit und die stetige Unterstützung, die mich immer wieder darin bestärkt hat, am Ball zu bleiben. Ebensfalls bedanke ich mich bei Sebastian Willems für die direkte Betreuung beim DLR mit seiner fachlichen Expertise und Geduld in Diskussionen sowie seiner kritischen Durchsicht meiner wissenschaftlichen Texte.

Mein Dank gilt meinen Kolleginnen und Kollegen für das angenehme und kollegiale Arbeitsklima sowie die stets vorhandene Hilfsbereitschaft. Besonderen Dank richte ich an Ansgar Marwege, Daniel Kirchheck und Dirk Allofs für die Ermutigung und den produktiven Austausch während unserer Doktoranten-Treffen, um den roten Faden der Arbeit nicht zu verlieren. Für die sorgfältige Durchsicht und die wertvollen Hinweise zur Verfeinerung des Manuskripts danke ich Pawel Goldyn und Ciro Salvi. Ich schätze sehr die vielen bereichernden Diskussionen und Anregungen von Dennis Daub, Dominik Neeb und Thomas Gawehn während der Auswertung und Interpretation der Messdaten. Für die zuverlässige Vorbereitung und Durchführung der Experimente im H2K danke ich Michael Kosbow und Marco Schmors, die meine Extrawünsche immer bestmöglich berücksichtigt haben.

I also gratefully acknowledge the help provided by Eric Stern and the ATAP team, who gave me much valuable advice in the early stages of this work. Great thanks also go to Ludovic Taguema, who made an important contribution to this work through his master's thesis.

Schließlich und vor allem möchte ich meiner Familie und meinen Freunden danken. Meinen Eltern und meiner Schwester danke ich für die kontinuierliche Unterstützung während meines gesamten Studiums. Nicht zuletzt danke ich Dir, Laura, für die unermüdliche Geduld, die emotionale Stütze und die treue Begleitung während dieser langen Reise. Dir und Fritz danke ich für die schönen Momente abseits der Arbeit, die nicht nur die Balance, sondern auch die nötige Motivation gegeben haben. Diese Arbeit widme ich euch.

Köln, im Dezember 2025 Patrick Seltner

Abstract

Asteroids and space debris pose a significant threat, which is becoming more relevant for the protection of the population and for the safe and sustainable use of space. Aerodynamic phenomena that occur during the atmospheric entry of these objects from outer space are crucial for the reliable prediction of the flight trajectories and the impact footprint of surviving fragments. This work takes a new look at how the aerodynamic behavior of single and multiple blunt bodies traveling at hypersonic speed affect their motion. The influence of the body shape and orientation on its aerodynamics and stability is the focus of this publication. Free-flight experiments have been carried out in the hypersonic wind tunnel H2K at the German Aerospace Center (DLR) in Cologne with single and tandem body arrangements of spheres, cubes and cylinders. High-speed stereo-tracking captured the model motions during free-flight, and high-speed schlieren videography provided documentation of the flow topology. Motion derivatives and aerodynamic coefficients have been determined in an extensive post-processing. The observed phenomena for multiple objects include different types of shock-shock interactions and wake-shock interactions. In this research, the results show that the geometry of the body has an immense influence on the aerodynamic loads and thus on the motion behavior. The final lateral velocity of trailing cubes is found to be many times greater than that of spheres regarding shock-wave surfing. This study has identified that the trailing drag coefficient of two axially aligned objects varies strongly with their relative streamwise distance. Several datasets from these experiments have already been successfully used for comparison with numerical simulations.

Zusammenfassung

Asteroiden und Weltraummüll stellen eine erhebliche Bedrohung dar, die für den Schutz der Bevölkerung und für die sichere und nachhaltige Nutzung des Weltraums immer relevanter wird. Aerodynamische Effekte, die während des Eintritts dieser Objekte aus dem Weltraum in die Atmosphäre auftreten, sind entscheidend für die zuverlässige Vorhersage der Flugbahnen und der Aufprallfläche der überlebenden Fragmente. Die vorliegende Arbeit wirft einen neuen Blick darauf, wie das aerodynamische Verhalten von einzelnen und mehreren stumpfen Körpern mit Hyperschallgeschwindigkeit ihre Bewegung beeinflusst. Der Einfluss von Form und Orientierung des Körpers auf seine Aerodynamik und Stabilität steht im Mittelpunkt dieser Veröffentlichung. Im Hyperschallwindkanal H2K des Deutschen Zentrums für Luft- und Raumfahrt (DLR) in Köln wurden Freiflugexperimente mit Einzel- und Tandem-Körperanordnungen aus Kugeln, Würfeln und Zylindern durchgeführt. Dabei erfasste das Hochgeschwindigkeits-Stereotracking die Bewegungen des Modells während des Freiflugs und die Hochgeschwindigkeits-Schlieren-Videografie lieferte die Visualisierung der Strömungstopologie. Die Ableitungen der Bewegungsdaten und aerodynamische Koeffizienten wurden in einem umfangreichen Datenauswertung ermittelt. Die beobachteten Effekte für mehrere interagierender Körper umfassen verschiedene Arten von Stoß-Stoß-Interaktionen und Nachlauf-Stoß-Interaktionen. Die Ergebnisse dieser Untersuchung zeigen, dass die Geometrie des Körpers einen immensen Einfluss auf die aerodynamischen Lasten und damit auf das Bewegungsverhalten hat. Es wurde festgestellt, dass die finale Quergeschwindigkeit beim Shock-Wave-Surfing von Würfeln um ein Vielfaches höher ist als die von Kugeln. Diese Studie hat gezeigt, dass der Luftwiderstandsbeiwert von zwei axial-ausgerichteten Objekten stark mit ihrem relativen Abstand in Strömungsrichtung variiert. Mehrere Datensätze aus diesen Experimenten wurden bereits erfolgreich zum Vergleich mit numerischen Simulationen verwendet.

Contents

List of Figures

List of Tables

Nomenclature

Abbreviations

2DoF	Two-Degrees-of-Freedom
3DoF	Three-Degrees-of-Freedom
6DoF	Six-Degrees-of-Freedom
ARC	Ames Research Center
AoA	Angle of Attack
BS	Bow Shock
C-C	Cube-Cube
CFD	Computational Fluid Dynamics
CMOS	Complementary Metal-Oxide-Semiconductor
CoG	Center of Gravity
CoP	Center of Pressure
D4D	Design for Demise
DES	Detached Eddy Simulation
DIC	Digital Image Correlation
DLR	German Aerospace Center
DRAMA	Debris Risk Assessment and Mitigation Analysis
EF	Expansion Fan
ESA	European Space Agency
FoR	Frame of Reference
GCS	Global Coordinate System
GOM	Gesellschaft für Optische Messtechnik
H2K	Hypersonic Wind Tunnel Cologne
HRSST	Helmholtz Research School on Security Technologies
ISS	International Space Station
IS	Impingement Shock
LCS	Local Coordinate System
LED	Light-Emitting Diode
LEO	Low Earth Orbit
MCMC	Markov Chain Monte Carlo
MRC	Moment Reference Center
NASA	National Aeronautics and Space Administration
NEO	Near-Earth Object
NUTS	No-U-Turn Sampler
ODE	Ordinary Differential Equation
ORSAT	Object Reentry Survival Analysis Tool
PEEK	Polyether Ether Ketone

RMSD	Root-Mean-Square Deviation
S-C	Sphere-Cube
S-S	Sphere-Sphere
SD	Standard Deviation
SJ	Supersonic Jet
SL	Shear Layer
SSD	Shock Stand-off Distance
SSI	Shock-Shock Interaction
SWBLI	Shock-Wave/Boundary-Layer Interaction
SWS	Shock-Wave Surfing
TNT	Trinitrotoluene
TS	Transmitted Shock
WSI	Wake-Shock Interaction
WT	Wind Tunnel

Latin Symbols

A	surface area
a	acceleration
C	Passey's constant
C_{A}	axial force coefficient
C_{D}	aerodynamic drag force coefficient
C_{F}	force coefficient
C_{L}	aerodynamic lift force coefficient
C_{l}	rolling moment coefficient
C_{M}	moment coefficient
C_{M}	aerodynamic pitching moment coefficient
C_{m}	pitching moment coefficient
C_{N}	normal force coefficient
C_{n}	yawing moment coefficient
c_{p}	Newtonian pressure coefficient
C_{Y}	side force coefficient
d	diameter
E	kinetic energy
F	force
f	shape factor
F_{D}	drag force
g	gravitational acceleration
I	principal moment of inertia about axis
I_{yy}	principal moment of inertia along y-axis
L	rolling moment
l	length
M	moment

$\mathcal{M}$	molar mass
M	pitching moment
m	mass
Ma	Mach number
N	yawing moment
$\vec{n}$	unit normal vector
n	refraction index
N_0	Avogadro number
P	polarizability
p	pressure
q	dynamic pressure
R	Gelman-Rubin statistic
r	radius
Re	Reynolds number
Re_u	unit Reynolds number
S	area
T	temperature
t	time
v	velocity
X	axial force
x	x-coordinate
Y	side force
y	y-coordinate
Z	normal force
z	z-coordinate

Greek Symbols

α	angular acceleration
β	shock angle
$\varDelta$	difference
δ	shock stand-off distance
η	shock distance
ϑ	pitch angle
θ	polar angle
κ	ratio of specific heats
λ	eigenvalue
ν	local deflection angle
ρ	density
σ	standard deviation
φ	roll angle
ϕ	azimuthal angle
ψ	yaw angle

Subscripts & Superscripts

0	reservoir/initial condition
1	primary body
2	secondary body
B	balance reference frame
i	index
m	material condition
max	maximum value
pro	projected condition
r	ram condition
ref	reference value
S	shock condition
T	final lateral value
t	theoretical value
$\widehat{\square}$	normalized value
∞	free-stream condition

1 Introduction

1.1 Scope of Current Study

Aerodynamic behaviors of single and multiple blunt bodies traveling at hypersonic speed play a major role in several important situations of atmospheric entry. Applications can be found for both the human-generated and natural world. On the one hand, re-entry of single or multiple vehicle like operating, decommissioned or mission-related space objects can be attributed to human-generated situations including stage separation of launch vehicles, descending of spacecrafts and deorbiting of space debris, just to name a few. On the other hand, such examples as binary asteroids entering the planetary atmosphere and fragmented asteroids after atmospheric breakup occur in the natural world. Both kinds of situations differ generally from each other in re-entry conditions, body structure and shape.

In general, the atmospheric entry is the motion of an object from outer space through the atmosphere of a planet or a moon, whereby the entering bodies experience an aerothermodynamic deceleration process transforming kinetic and potential energy finally into thermal energy in a short time. In the following, the term 're-entry' is used for both the reentry of terrestrial objects and the entry of celestial objects. As the objects in question are not designed to survive re-entry, they partially demise and breakup as shown in figure 1.1. This sketch illustrates the different phases of a generic object from outer space re-entering an atmosphere. The space object enters the atmosphere with a certain flight path and velocity undergoing a ballistic re-entry trajectory. As it flies deeper into the atmosphere, aerodynamic drag and heating reaches a significant level due to the interaction of the moving object with the fluid. Ablation effects and mechanical stresses on the object rises, leading to initial breakup. Several fragments develop, which determine again individual trajectories. Further breakups appear that increase the number of objects and individual trajectories. Aerodynamic interactions between these objects appear like Shock-Shock Interaction (SSI) and Wake-Shock Interaction (WSI) influencing their flight trajectories, attitudes and velocities. In the case of SSI, the bow shocks of two bodies interact aerodynamically causing locally higher surface pressures. This can lead to separations of bodies with large lateral velocities. WSI phenomenon is the aerodynamic interaction of the wake of a leading object with the bow-shock of a trailing object that effects a reduction of inflow velocity and thus a drafting of the downstream body. Moreover, the separation of the fragments is also driven by its rotational motion causing lift forces. During the descent, some of the fragments fully demise, whereas some objects survive and impact the ground surface. The area of impacting bodies is called impact footprint. If the fragments reach the surface with hypersonic speeds, crater fields will be formed [51].

Flight trajectory and velocity of re-entering objects as well as the resulting impact footprint are strongly effected by the aerodynamic behavior of single bodies as well as the aerodynamic interaction of multiple bodies. Especially, WSI is of fundamental importance for our understanding

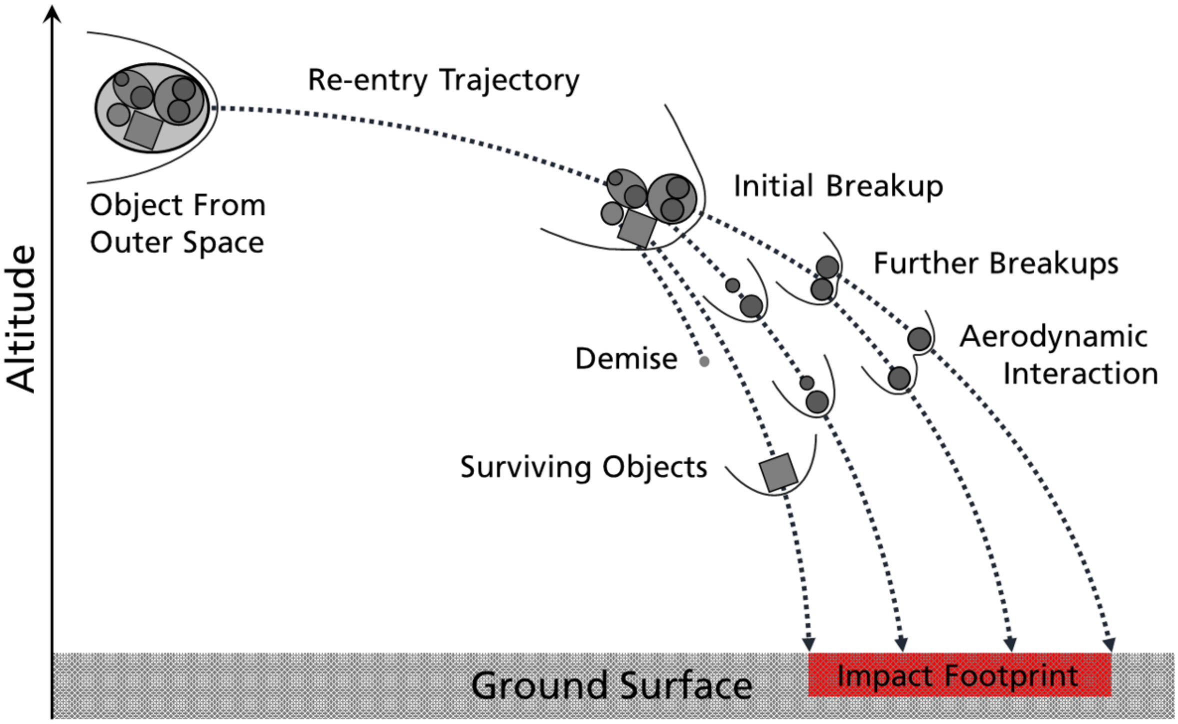

Figure 1.1: Schematic re-entry trajectory of a generic object from outer space

of the impact footprints with respect to the crater depth due to the higher kinetic energy of drafting fragments. However, these effects occurring during atmospheric entry are so complex that state-of-the-art aerodynamic models and engineering tools are still not accurate enough to model them satisfactorily. The relevance of the topic is discussed in detail in section 1.2. Therefore, the aim of the research at hand is to analyze comprehensively the aerodynamics of single bodies and multiple interacting bodies in hypersonic continuum flow fields. These studies were carried out by means of Wind Tunnel (WT) experiments on representative blunt bodies in the Hypersonic Wind Tunnel Cologne (H2K) at the German Aerospace Center (DLR) in Cologne. This kind of geometry was chosen because fragments after breakup are rather blunt than streamlined [87], whereby compressibility effects dominate the aerodynamics in contrast to viscous effects [48]. In this study, objects entering the atmosphere are regarded as spheres, cubes, cylinders and combinations of them. While spheres were mostly used in the past for modeling asteroids as described section 1.4, cubes and cylinders are particularly relevant due to the increasing number of satellites orbiting the Earth. In various test series with one or two bodies, free-flight tests were performed at Mach 7 by using a non-intrusive stereo-tracking measurement technique and high-speed schlieren videography. This setup allows to develop a better understanding of the motion behavior and the flow topology of rotating bodies both in aerodynamic independence and in aerodynamic interaction such as SSI or WSI. The focus here is on the impact of body shape and inclination, whereby spheres, cubes and cylinders were investigated in single-body experiments and configurations with two spheres, a sphere followed by a cube and two cubes were studied in multi-body experiments. In addition, the question of how the body shape and inclination affect the separation behavior may address the gap between the observed strewn fields with their corresponding maximal lateral separation velocities as in [87] and previous scientific investigations.

Since the present work concentrates on the aerodynamic behavior, high-temperature effects were neglected. This is reasonable as the impact of high-temperature effects on the surface pressure distribution and in consequence the aerodynamic forces are generally limited as shown in the experimental comparative study by Tanno *et al.* [109]. In particular, this insensitivity was demonstrated by Vincenti and Kruger [115] for dissociation as well as by Artemieva and Shuvalov [7] for ablation and radiation. A fixed free-stream Mach number in low hypersonic flow regime was chosen for all of the present experiments, whereby its aerodynamic behavior can be transferred to the results of typical re-entry events with higher flight velocities under the consideration of the Mach number independence principle [42, 80].

1.2 Relevance of the Topic

Aerodynamics of single or multiple bodies in high-speed flows is highly relevant for civil security in the fields of atmospheric entry of space debris, asteroids and launch vehicle components. Determining their flight trajectories, velocities and sizes helps to predict the impact footprint of objects entering from outer space, and potentially affect it in the case of controlled objects, with the purpose to protect people and property from harm. The impact footprint in turn strongly depends on the aerodynamic behavior [87].

A number of roughly 12 000 intact space objects in Earth's orbits is the result of more than 60 years of human space flight and exploitation [111]. Only half of those spacecrafts are still operating [27], whereas the decommissioned spacecrafts pose a risk of on-orbit collisions and breakups strongly increasing the number of space debris objects [30]. As the first of all, Kessler and Cour-Palais [52] postulated a chain reaction due to disintegrating objects in 1978 that could lead to the exponential growth in the amount of artificial objects in space associated with a hazard for future spaceflight. Especially in Low Earth Orbit (LEO), the growth of space debris significantly increases the likelihood of further collisions. Thus, there is a need to limit and reduce the amount of inactive objects. Naturally, the orbits of space objects gradually decay in LEO due to the continuous exposure to atmospheric drag. Most of these decommissioned spacecrafts are not or just partially able to perform active maneuvers after their end-of-life engendering an uncontrolled atmospheric entry subsequent to the natural orbital decay. As a consequence, it is not possible to actively affect their flight trajectories and hence the impact footprint of not fully demised re-entry bodies. This impact footprint can be hundreds of kilometers long and tens of kilometers wide provoking an unacceptable on-ground risk for population with regard to the increasing number of space debris [54]. In contrast, an active debris removal by means of orbital and aerial maneuvers enables a controlled re-entry into atmosphere. As a result, the impact footprint and time window can be affected in such a way that the surviving objects impact an uninhabited area (ideally ocean) and thus sustain the casualty probability below an acceptable risk.

Several different re-entry analysis tools were developed by a large number of space agencies and research institutes with the aim to predict the re-entry trajectories including disintegration processes and to assess the on-ground casualty risk [69]. By use of these prediction tools, governmental institutions and private satellite operators are able to take appropriate measures in advance of re-entry events in order to protect the population. Moreover, re-entry analysis tools should also be applied for the design of next-generation satellites with the purpose to guarantee a safe and complete demise of the objects during the re-entry in Earth's atmosphere. However, the occurring effects during atmospheric entry are so complex that state-of-the-art engineering tools are still not accurate enough to satisfactorily model them. A good example of their weaknesses could be observed prior to the uncontrolled re-entry of the Chinese space station Tiangong 1 in 2018. Due to the uncertainty in the forecast of the physical properties of Earth's atmosphere, it was not possible to predict the time and location of the ground impact with any degree of accuracy. Four weeks before the atmospheric entry, the prediction of the European Space Agency (ESA) varies by several days regarding the time window and between 43° North and 43° South latitudes regarding the impact area [29]. Besides the limitation to forecast the properties of the upper atmosphere, complex aerodynamic effects like the interaction of multiple bodies and the rotation of a single body are mostly neglected for available re-entry analysis tools.

In 2013, the unforeseen Chelyabinsk bolide event gained attention in the public and scientific community. A relatively small asteroid with a diameter between $17\,\mathrm{m}$ to $20\,\mathrm{m}$ entered the Earth's atmosphere over Russia having an estimated energy equivalent to approximately 500 kilotons of TNT [13]. During the re-entry, an airburst provoked a blast wave over densely populated area causing damages on infrastructure and injuries of more than thousand persons [93]. This impact event demonstrated the underrated risk of small asteroids with diameters of tens of meters to do serious harm considering that these small objects are often unknown in contrast to the kilometer-sized Near-Earth Objects (NEO) monitored by space organizations. In addition, such impactors with equal or higher energy than the asteroid over Chelyabinsk will statically enter Earth's atmosphere every 20 years [15] showing the relevance of the topic. More research on meteor physics including the problem of asteroid fragmentation and separation is necessary in consequence.

1.3 Review of Single-Body Aerodynamics

In the 20th century, comprehensive research on aerodynamic forces of simple blunt geometries in super- and hypersonic flow fields were carried out to primarily gain knowledge about the aerodynamic behavior of missiles and projectiles. Commonly, flow experiments like wind tunnel or ballistic range tests were performed with spherical [9, 19, 20, 43, 47, 48, 62, 70, 104], cubical [35, 41, 48] and cylindrical [37, 48, 73, 89, 92, 114] shapes. These studies are solely focused on symmetric flow configurations.

Much of this previous work has been conducted to determine the factors influencing the aerodynamic drag force F_D. There are dimensionless quantities such as the drag coefficient C_D, which are more suitable to describe the aerodynamic behavior in general. This parameter is normalized by using the free-stream dynamic pressure q_∞ and the reference area S_{ref} based on the length l or the diameter d. It is defined as follows:

$$C_\mathrm{D} = \frac{F_\mathrm{D}}{q_\infty S_{ref}} \tag{1.1}$$

Spherical bodies are adequately studied test objects, which are relevant for modeling the re-entry trajectories of asteroids or propellant tanks. In several studies, the effect of Reynolds number [9, 19, 43, 70], Mach number [9, 19, 20, 43, 47, 48, 70, 104], Knudsen number [43, 70], ballistic coefficient [47, 104] and roughness [19, 62] on spherical drag were explored. All of them point out an independence of the Mach number on the drag coefficient under hypersonic conditions with an approximate value of $C_\mathrm{D} = 0.92$ [48].

During the first half of the last century, many studies were conducted on rotationally symmetric shapes in high-speed flows, which are common for many human-generated space objects such as rocket bodies, propellant tanks, satellite payloads, modules of space stations. In doing so, cylindrical objects with different blunt (e.g. flat) and streamlined ends (e.g. conical, spheroidal and ogival) were investigated over a wide range of Mach numbers [37, 48, 92, 114]. Vennard [114] and Rouse [92] called attention that drag coefficient significantly depends on Mach number at transonic and supersonic speeds as well as it is affected by the forebody shape in axial flows. Moreover, they suggested to decrease drag by streamlining the body. The extent of drag reduction here hinges on the nose-to-length ratio of cylinder's blunted face, which was found by Hoerner [48] with the help of his extensive collection of experimental data. Gowen and Perkins [37] have shown in their analysis by circumferential surface pressure measurements that the Reynolds number in supersonic flow regime reveals no appreciable effect on surface pressure and drag coefficient for cylinders in cross flows and a Reynolds number range from 10^5 to 10^6. Wind tunnels tests with oblique cylinders at Mach number 6.86 and Angle of Attack (AoA) between $15°$ and $90°$ were carried out by Penland [89] implying a dependency of the lift and drag coefficient on the AoA. Furthermore, they identified an almost constant value of the drag coefficient for Mach numbers higher than four for cylinders in cross flow with an approximate value of $C_\mathrm{D} = 1.24$ (based on $S_{ref} = ld$). Unlike Penland, Hoerner's value tends to a constant level of $C_\mathrm{D} = 1.21$ for hypersonic inflows based on the same experimental dataset in combination with additional datasets at similar test conditions. For a cylinder in axial flow, he stated a rough convergent value of $C_\mathrm{D} = 1.65$ (based on $S_{ref} = \pi d^2/4$), while the base drag of both configurations tends towards zero at hypersonic speeds. Furthermore, Hoerner mentioned that the cylinder length has no noticeable effect on drag coefficient under supersonic axial-stream as tested in the aspect ratio (l/d) range from 2 to 5. In [73], Maslach and Schaaf investigated the drag of cylinders in the transition from continuum to free molecular flow under supersonic conditions, which suggests a continuous increase between the two flow regimes.

Less investigations have been carried out on cubes, which are of some interest in the context of space debris behavior (e.g. cubesats) during re-entry into Earth's atmosphere. Hansche and Rinehart [41] have shown the dependence of the Mach number on the aerodynamic drag coefficient for rotating cubes free-flying in sub-, trans- and supersonic flows. A rough convergent value of $C_\mathrm{D} = 1.66$ for higher Mach numbers ($Ma_\infty > 4.0$) is given by Hoerner [48].

Flow fields of simple blunt geometries are complex. Figure 1.2 represents an exemplary sketch of a single sphere in hypersonic flow based on schlieren images of [112], which is a well-studied research object. The main flow features, as described in [5], are shown in the figure and are

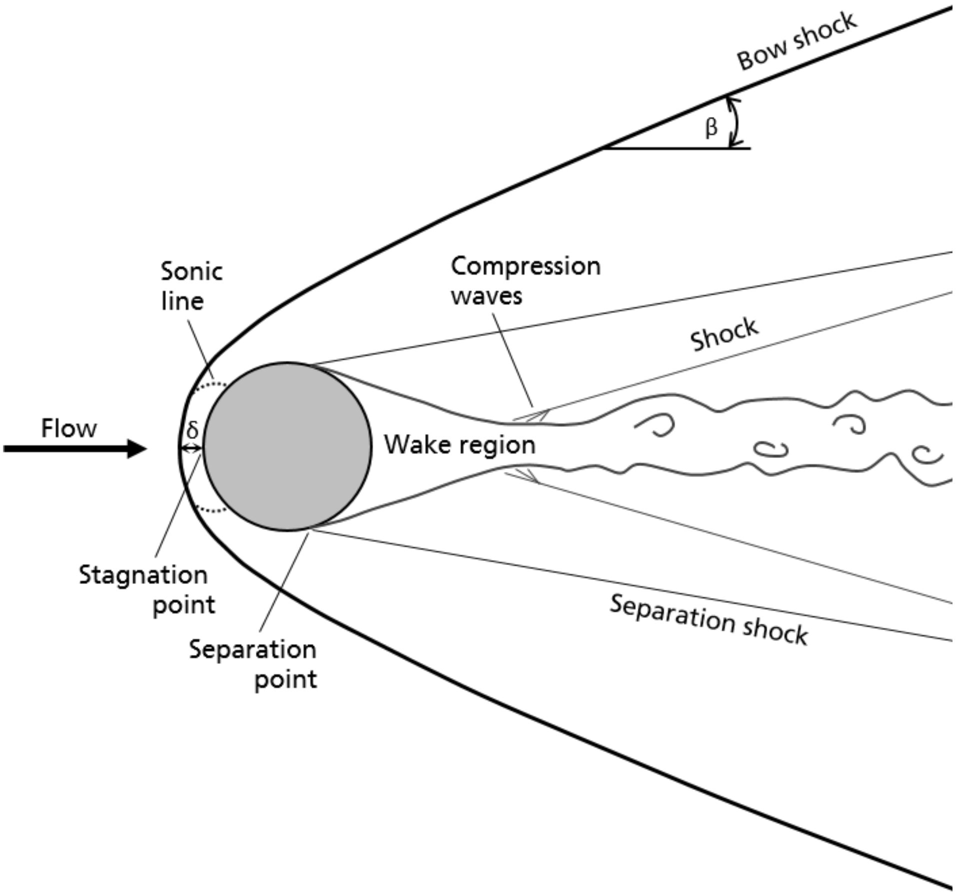

Figure 1.2: Schematic flow topology of a single sphere in hypersonic flow field

common for blunt body shapes. The flow in the sketch is going from left to right. In front of the sphere, the flow is compressed by a detached bow shock that has a normal shape upstream the sphere's stagnation point and gradually becomes more oblique further downstream. The local angle between tangent of bow shock and inflow direction is called shock angle β. The flow is slowed down to subsonic speeds by the normal shock. It is then accelerated along the surface of the sphere and reaches Mach 1 at the sonic line. The distance from stagnation point to normal part of bow shock is known as the Shock Stand-off Distance (SSD) δ. Around the sphere, the flow is deflected outwards during acceleration until it reaches a certain point at which the boundary layer separates from the surface and a separation shock develops. A wake region occurs downstream the separation point, which is subsonic in near-wake and supersonic in far-wake. At its shear layer, compression waves arise, which build an oblique shock at their intersection.

As summarized in table 1.1, the presented review reveals that most researchers have tended to focus only on drag of generic bodies in symmetric flow configurations. Moreover, their experimental setups often exhibit weaknesses due to flow interferences by sting supports [48, 89, 104] and WT walls [37, 48, 73], negligence of flow phenomena by use of 2D measurements [37, 89] or lack of measurement resolution [9, 19, 20, 41, 47]. The present work purposes to address this gap by offering results of high-fidelity experimental data of various inclined

Table 1.1: Summary of results from literature review

Geometry	Configuration	Result	Reference area	Source
Sphere	Variable AoA	$C_\mathrm{D} = 0.92$	$\pi d^2/4$	[48]
Cube	Uncontrolled rotation	$C_\mathrm{D} = 1.66$	l^2	[41]
Cylinder	Side-on	$C_\mathrm{D} = 1.24$	ld	[89]
Cylinder	Side-on	$C_\mathrm{D} = 1.21$	ld	[48]
Cylinder	End-on	$C_\mathrm{D} = 1.65$	$\pi d^2/4$	[48]
Cylinder*	Variable AoA	$C_\mathrm{D} = C_\mathrm{D}\,(90°)\sin^3(\vartheta)$ $C_\mathrm{L} = C_\mathrm{L}\,(90°)\sin^2(\vartheta)\cos(\vartheta)$	ld	[89]

* oblique cylinder

generic bodies in hypersonic flow fields, whereby the aerodynamic drag force, lift force and pitching moment are determined by the use of a non-intrusive measurement technique.

1.4 Review of Multi-Body Aerodynamics

In last decades, a significant amount of research has been performed on aerodynamic interactions between separating bodies in high-speed flows largely related to the atmospheric breakup of asteroids. Results from detailed analytical [44, 58, 59, 72, 84, 87], numerical [6, 7, 10, 16, 58–61, 64, 66, 67, 71, 103, 108, 118, 120–122] and experimental [16–18, 26, 55, 58–60, 64, 65, 84–86, 95, 108, 117, 118, 122, 123] studies are available in the literature. Most of the publications deal with two-body scenarios in supersonic or hypersonic flows.

The first systematic analysis considering interaction phenomenon was made by Passey and Melosh [87], who examined various terrestrial crater fields of past impact events and derived the well-known scaling law of the final lateral velocity v_T between the leading and trailing body of radii $r_1 \geq r_2$ based on their constant C with values in the range of 0.02 to 1.52. This equation is defined as:

$$v_T = \sqrt{\frac{3}{2} C \frac{r_1}{r_2} \frac{\rho_\infty}{\rho_m}} v_\infty \tag{1.2}$$

where the subscripts ∞ and m denote the free-stream conditions of the flow and the material conditions of the object, respectively. They identified that gravity, rotation and SSI of the flow around the fragments are the major effects on dispersion, while their work was limited merely to lateral separation. However, Schultz and Sugita [95] have shown in ballistic range tests that small fragments of a debris cloud collimate rather than disperse, whereby they move along the bow shock followed by an entrainment in the shock-bounded region of the main body. In contrast, Laurence and Deiterding [58] found that these fragments travel along the bow shock of another upstream object due to SSI, which became known as Shock-Wave Surfing (SWS). Such surfing behavior has been observed in several studies [6, 7, 61, 65, 66, 84, 86, 123].

There is a vast amount of literature [6, 7, 26, 120–123] on equal-sized generic blunt bodies in SSI and partly in WSI situations. In the experiments about projectiles in tandem configurations, Erengil *et al.* [26] stated that the drag of the trailing body in a near-wake is less than that of the leading one, which decreases drastically if both bodies are axially aligned with the inflow. The reason of this drag reduction was found in the surface pressure distribution of the secondary body, whereby the pressure in the stagnation point is approximately $5\,\%$ of the single-body value. Furthermore, a significant local pressure peak was measured slightly downstream of the stagnation point resulting from the high momentum of the wake's shear layer. Artemieva and Shuvalov [6] carried out numerical simulations concerning the motion of two objects with a mainly cylindrical shape in various relative configurations, and revealed a strong dependency on the aerodynamic forces. For side-by-side arrangements, high repulsive forces were noted that rapidly decrease with increasing lateral distance tending to zero. Moreover, an escape of an object from the near-wake of another was described in their analysis with tandem cylinders of unequal size in axial flow. In a further study, Artemieva and Shuvalov [7] investigated the aerodynamic interaction of up to 27 identical objects, which extends the validity of the collimation effect to a large number of fragments. Aeroballistic experiments on tandem cubes were conducted by Zhukov *et al.* [122, 123] demonstrating that both axially aligned bodies experience no change in flight attitude when the trailing body is located in the far-wake of the other ($\frac{\Delta x}{l} \approx 20$).

Many efforts have been made to study the SSI between two unequally sized spheres of different diameter ratios in proximal configurations [10, 58–61]. Laurence *et al.* [59] have shown a strong impact of the size ratio on the lift coefficient of a trailing body being placed downstream of a larger one. Unsteady separation behavior of freely moving spheres was subsequently analyzed in [58, 61]. These studies provided the evidence that the qualitative separation behavior and the final lateral velocity of secondary smaller spheres varies widely with both the diameter ratio and the initial alignment angle of the two spheres. As a result, a critical diameter ratio for a given initial alignment angle and vice versa a critical initial angle for a given diameter ratio were determined at which the transition from entrainment to expulsion of the trailing object occurs. Secondary bodies that are axially aligned in vertical direction to the primary ones are entrained within the region enclosed by the primary bow shock for low diameter ratios $\frac{d_2}{d_1} \leq 0.5$, whereas they are expelled from the region for high values $\frac{d_2}{d_1} \geq 0.625$ [61]. Moreover, the critical values represent the limiting cases that enables SWS having a final lateral velocity close to maximum.

Due to the focus on spherical bodies of previous publications, subsequent researches [66, 71, 85] have studied other blunt geometries to enable rotational effects on the aerodynamics of two interacting objects to be investigated. For a cube lying initially next to a sphere, a similar separation behavior as in Laurence and Deiterding [58] and the occurrence of SWS phenomenon on the cube were both observed by Li *et al.* [66]. It was found that the duration of SWS is extended by the rotation, which lead to a higher final lateral velocity. In addition, an initial lateral distance of $\frac{\Delta z}{d} > 1.2$ was determined for which this effect disappears. By performing 2D Euler simulations, Lukashenko and Maksimov [71] investigated side-by-side configurations of differently shaped objects applying circles, squares and rectangles. They were the first to report that the shape of the object heavily affects the separation behavior and therefore the lift force and lateral velocity, whereas the geometry of the neighboring body has no significant influence on the lateral motion. Moreover, Lukashenko and Maksimov [71] confirmed the findings of Li *et al.* [66] on extended shock-wave surfing due to the rotation effect and mentioned an increase of the lift force and final lateral velocity through higher aspect ratio of the geometry. Recently, Park *et al.* [85] experimentally studied side-by-side configurations of different pairings of spheres, cubes and cylinders, whereby they found that the lateral separation is the result of both the shock-shock interaction and the lift force due to inclination. The authors also pointed out that the final lateral velocities of cylinders and cubes are nearly twice as large as of spheres. In more recent works dealing with spheres on a wedge in inviscid [103] and viscous flows [16], it was shown that higher Mach numbers increase the likelihood of SWS. The authors of both studies [16, 103] additionally identified a highly repulsive force due to shock reflection in proximity to the wall declining considerably with increasing distance.

In comparison with research discussed so far, current activities are focused on the aerodynamic interaction of multiple bodies with more than two objects [86, 117, 118], the rarefaction effect on SSI [17, 18] and multi-body aerodynamics of specific problems [55, 64]. Free-fight tests with up to six initially contiguous spheres were conducted by Park and Park [86], implying a decrease of the critical diameter ratio and an increase of final lateral velocity for SWS as soon as the number of objects increases. In their setup with four identical spheres initially placed in proximal tetrahedron arrangements, Whalen *et al.* [118] have shown that the bodies undergo a radial spreading rather than a circular motion, with the final lateral velocity depending on the original polar position. Furthermore, they point out a stable region at the rear for two-body configurations in which the trailing sphere is resistant to separation and remains in contact with the leading body. By means of tandem-sphere configurations in a low-density facility, Cardona *et al.* [17] highlight that the shape of the interacting bow shocks in rarefied flows differs from the one in continuum flows provoking higher drag coefficients for the different types of SSI. In the publication of Leiser *et al.* [64], it was established that the flight-scaled aerodynamic loads due to SSI on a generic model of the International Space Station (ISS) with three cylinders in L-shape are lower than the yield strength of the connection structures. The experimental study by Kovács *et al.* [55] has also shown the characteristic lateral separation behavior in terms of a free-flying annular ring impinged by a detached shock from a stationary cylinder. Moreover, Patel and Navarro-Martinez [88] discovered in their numerical analysis that a cylinder directly behind another experiences a reduction in heat transfer and surface pressure on the forebody, provoking a change in the peak heat transfer of up to $-90\,\%$ and a change in stagnation pressure of up to $-40\,\%$ related to an isolated body.

Based on the findings of the presented literature, it can be concluded that the important factors influencing separation behavior are the size ratio and the relative positing. Depending on the relative configuration of two objects, the inflow condition of the trailing body varies, whereby wake and bow shock of the leading object have contrary effects on the resulting forces and accelerations of the downstream object. In general, WSI decreases the aerodynamic forces, while SSI increases it. Four idealized types of motion behavior were identified from previous work [57, 72] as drafting, entrainment, expulsion and shock-wave surfing being illustrated in figure 1.3 for two spheres. Initial velocities of the secondary body relatively to the primary are neglected here. The relative accelerations $\varDelta a$ of the secondary body referred to the primary one are presented in the schematic, which are divided into an axial ($\varDelta a_x$) and a lateral component

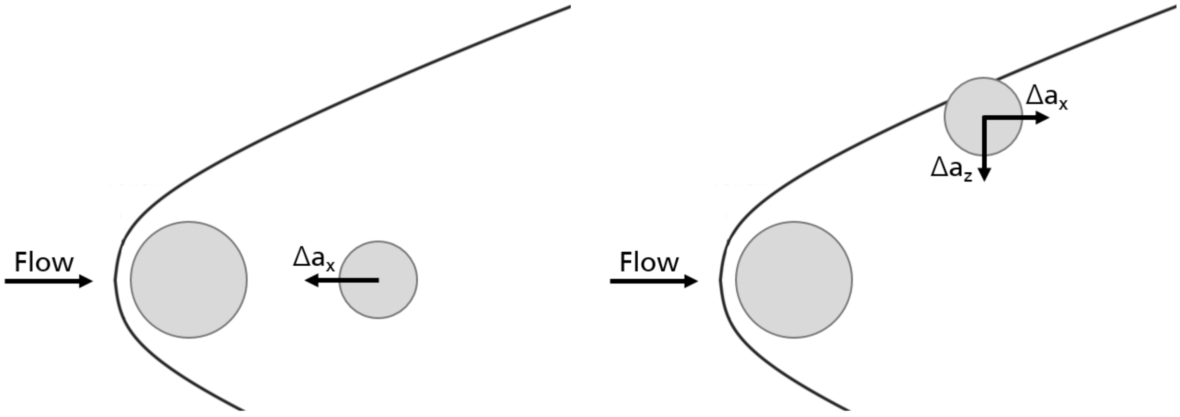

(a) Drafting **(b)** Entrainment

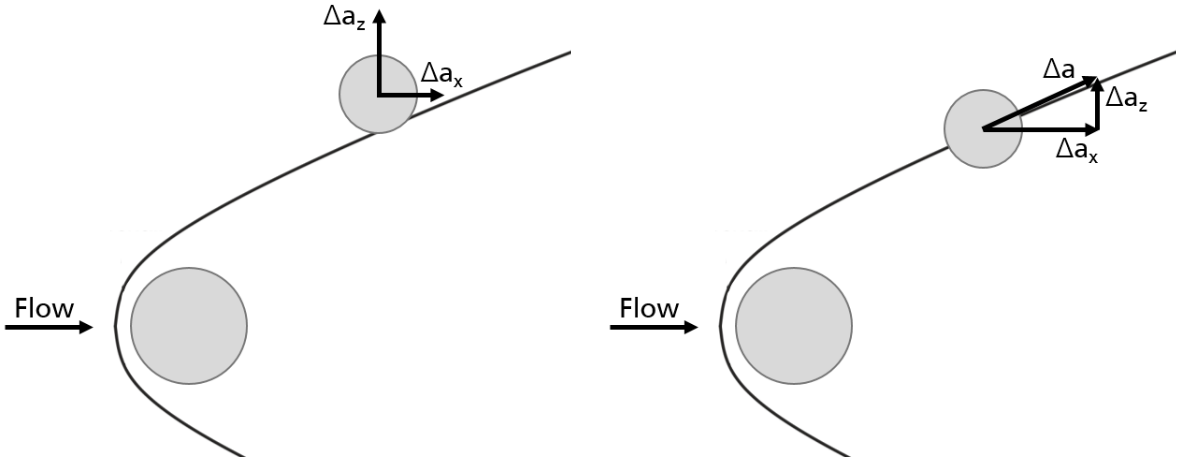

(c) Expulsion **(d)** Shock-Wave Surfing

Figure 1.3: Schematic of motion behavior types along with relative aerodynamic accelerations

(Δa_z). If the trailing body is positioned immediately behind the leading body in the wake region, the acceleration will be smaller than that of the upstream object due to the reduction in static and dynamic pressure (see figure 1.3a). This leads to a negative Δa_x in such a way that the trailing body moves towards the leading one. As the lateral distance of the bodies becomes larger, the trailing object escapes the impact of the wake region and nears the primary bow shock's area of influence, which causes the increase of the axial drag force and the development of a lateral lift force due to the higher pressures of the SSI phenomenon. Edney [23] was the first to classify the interaction of two shock waves in terms of their flow topology as shown in figure 1.4, characterizing the strongly position-dependent pressure and heat flux distribution on the surface of the trailing blunt body. From this it can be concluded that the position of the shock impingement on the surface of the secondary body determines whether the motion behavior is attractive or repulsive. If the upper side is impinged by the shock wave, the sphere will experience an attractive force and hence an entrainment (see figure 1.3b); whereas the sphere will experience a repulsive force and hence an expulsion (see figure 1.3c), if the bottom side is impinged by the shock wave. Moreover, there is a critical position in between, where SWS is possible causing a great axial and lateral separation over long distance (see figure 1.3d).

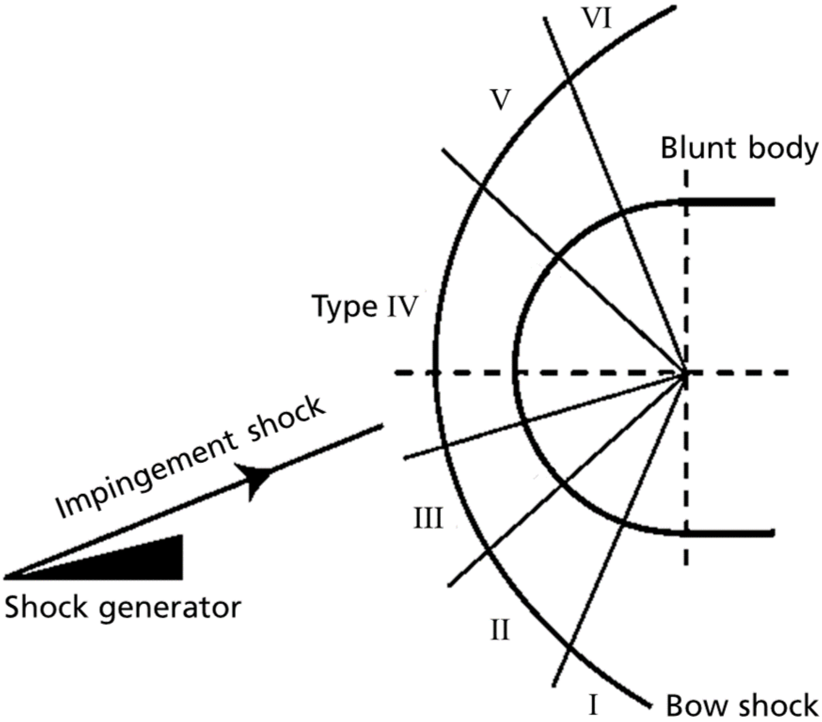

Figure 1.4: Schematic of Edney's types of shock-shock interaction [81]

This is achieved by a parallelism of the secondary sphere's relative acceleration vector and primary bow shock's tangent [57], which can be written as:

$$\frac{\Delta a_z}{\Delta a_x} = \tan(\beta) \ \wedge \ \Delta a_x > 0 \tag{1.3}$$

$$\frac{\partial \left(\Delta a_z / \Delta a_x \right)}{\partial z} < 0 \tag{1.4}$$

This criterion also leads to the argumentation that SWS occurs for blunt rather than streamlined bodies, because $\Delta a_z/\Delta a_x$ of these lifting bodies is usually higher than the slope of the tangent. However, the parallelism condition is not sufficient for SWS over a long distance. For this purpose, the stability condition has to be fulfilled, whereby a change in the lateral position has to result in a contrary change in the relative acceleration ratio [72]. This can be formulated as:

In real multi-body scenario, it is often a combination of these motion behaviors, that can also lead to oscillating flight trajectory of the trailing fragment [58, 71, 91]. After a period of fragment interaction, the secondary object ends in a certain flow region in which it stays for the rest of the flight. These final zones were noted in a recent study [91], where three major and two minor zones were identified, which differ from each other in the state of the flow. Near-wake, far-wake and free-stream region can be assigned to the major zones, whereas in front of the primary fragment and the shock region are part of the minor ones. It is more likely to reach a major than a minor final zone, because the former is a steady-state flow regime in contrast to the transitional characteristic of the latter.

Based on the review presented above, it is apparent that aerodynamic interactions, especially SSI phenomena, of multiple bodies in supersonic and hypersonic flow are well documented by a large number of analytical and numerical work. However, the amount of reliable experimental investigations is rare, particularly with regard to non-spherical test objects. Furthermore, less studies were conducted concerning the effect of WSI. The purpose of this study is to develop an understanding of the motion behavior and the flow topology during SSI and WSI, focusing on the impact of body shape and inclination with respect to tandem arrangements of spheres and cubes in hypersonic flow fields.

1.5 Remarks on Current Study

The present script describes the experimental setups and the results of several test series, which were performed in the course of my doctoral studies. After introducing the subject of the work in the present chapter, the applied models and methods of the experimental tests are outlined in chapter 2. It provides all important information on the test facility, the WT models, their instrumentation and the experimental setup. The next chapter looks at the post-processing of the measurement data as well as the associated uncertainty analysis. Chapter 4 is dedicated to the investigation of single-body aerodynamics that contains the aerodynamic coefficients of different blunt generic bodies as a function of the AoA. Subsequently, the aerodynamic interactions of two blunt bodies in various relative configurations are studied in chapter 5. Finally, detailed conclusions are drawn in the chapter 6.

This dissertation is embedded in the DLR's cross-sectoral area Security Research, as the subproject entitled Civil Security. The overall program objective is the research and development in the fields of space, aeronautics, energy and transport that have relevance for defense and security in the face of European and international cooperation activities. On this account, an international collaboration was initiated with NASA's Ames Research Center (ARC) as research partner being responsible for the numerical investigation. This work has been performed within the framework of the program Helmholtz Research School on Security Technologies (HRSST) and benefited from a funding by the DLR program directorate Defence & Security.

Parts of this study were already published in journals or in collections:

- Seltner, P. M., S. Willems, and A. Gülhan, "Aerodynamic coefficients of free-flying cubes in hypersonic flowfield", *Journal of Spacecraft and Rockets*, vol. 56, no. 6, pp. 1725–1734, 2019. DOI: `10.2514/1.a34345`

- Register, P. J., M. J. Aftosmis, E. C. Stern, J. M. Brock, P. M. Seltner, S. Willems, A. Gülhan, and D. L. Mathias, "Interactions between asteroid fragments during atmospheric entry", *Icarus*, vol. 337, no. 113468, 2020. DOI: `10.1016/j.icarus.2019.113468`

- Seltner, P. M., S. Willems, and A. Gülhan, "Mehrkörperaerodynamik während der Fragmentation beim atmosphärischen Wiedereintritt", in *Sicherheitslagen und Sicherheitstechnologien - Beiträge der ersten Sommerakademie der zivilen Sicherheitsforschung 2018*, Zivile Sicherheit, Ellebrecht, S., N. Eschenbruch, and P. Zoche, Eds., 1. ed, vol. 19, Muenster: LIT Verlag, 2020, pp. 157–182, ISBN: 978-3643145475
- Seltner, P. M., S. Willems, A. Gülhan, E. C. Stern, J. M. Brock, and M. J. Aftosmis, "Aerodynamics of inclined cylindrical bodies free-flying in a hypersonic flowfield", *Experiments in Fluids*, vol. 62, no. 9, 2021. DOI: `10.1007/s00348-021-03269-6`
- Seltner, P. M., S. Willems, and A. Gülhan, "Aerodynamic interactions of blunt bodies free-flying in hypersonic flow", *Experiments in Fluids*, vol. 65, no. 80, 2024. DOI: `10.1007/s00348-024-03818-9`

The following papers and posters were presented on conferences containing partial outcomes of the present work:

- Venkatapathy, E., A. Gülhan, M. J. Aftosmis, J. M. Brock, D. Mathias, D. Neeb, D. Rodriguez, P. M. Seltner, E. C. Stern, and S. Willems, "In pursuit of improving airbust and ground damage predictions: Recent advanced in multi-body aerodynamic testing and computational tools validation", Poster presented at *Fifth Planetary Defense Conference (PDC)*, Tokio: International Academy of Astronautics (IAA), 2017
- Seltner, P. M., S. Willems, and A. Gülhan, "Experiments on the aerodynamic interaction of multiple free-flying objects", Poster presented at *61st Course of Hypersonic Meteoroid Entry Physics (HyMEP)*, Erice, 2017
- Seltner, P. M., S. Willems, and A. Gülhan, "Experimental determination of aerodynamic coefficients of simple-shaped bodies free-flying in hypersonic flow", in *First International Conference on High-Speed Vehicle Science Technology (HiSST)*, Moscow: Council of European Aerospace Societies (CEAS), 2018

2 Experimental Models & Methods

This chapter introduces models and methods applied within the experimental study. It addresses the involved test facility, its flow characterization as well as the wind tunnel models including instrumentation. Furthermore, the experimental setups of different test series, which were conducted during the present work, are described including an improved free-flight technique.

2.1 Hypersonic Wind Tunnel Cologne

2.1.1 Overview & Operating Principle

All experiments were carried out in the Hypersonic Wind Tunnel Cologne (H2K) located at the Supersonic and Hypersonic Technologies Department of the DLR. This facility is an intermittently working blowdown wind tunnel with a free-jet test section. Exchangeable axisymmetric contoured Laval nozzles are applied for fixed design Mach numbers facilitating an axially symmetric homogenous flow. Eight resistance heaters are employed to adjust the reservoir temperature and hence to prevent condensation of the dry air during expansion in the nozzle. The desired Reynolds number can be adjusted by varying the reservoir pressure p_0 and the reservoir temperature T_0. The major facility attributes of H2K are summarized in table 2.1.

A schematic of the H2K facility is shown in figure 2.1, which is used in the following to describe the operation principle. The flow is going from left to right. High-pressurized dried air from pressure vessels is heated in the electric heaters. In advance of the actual WT run, this heated air stream is exhausted into the atmosphere during the adjustment of mass flow and electric power. As soon as the desired reservoir temperature and pressure are reached, the 3/2-way

Table 2.1: Facility attributes of H2K

Parameter	Feasible values
Mach number	4.8, 5.3, 6.0, 7.0, 8.7, 11.2
Unit Reynolds number	$2.0 – 20 \cdot 10^6 \, \frac{1}{\mathrm{m}}$ *
Nozzle exit diameter	600 mm (360 mm at Mach 4.8)
Reservoir pressure	2.5 – 55 bar
Reservoir temperature	max. 1000 K
Mass flow	max. 20 kg/s
Electric power	max. 5 MW
Typical run time	30 s

* depending on Mach number

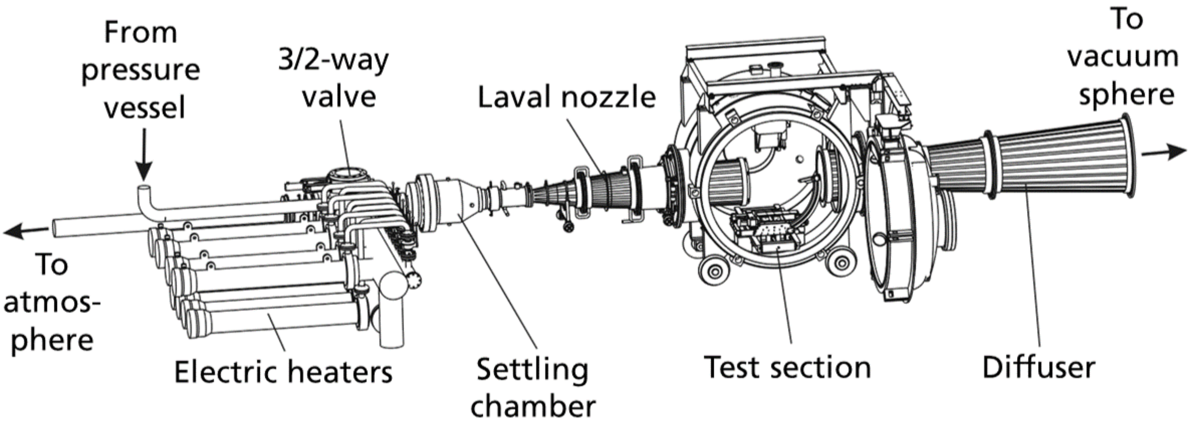

Figure 2.1: Schematic setup of the H2K wind tunnel

valve is triggered to release the air through several turbulence grids of different widths and a honeycomb in the settling chamber, that smooth out the turbulence and parallelize the flow. Subsequently, the air is accelerated through the Laval nozzle to hypersonic flow velocities and is released into the test section as a free jet. Finally, the airflow exits through the diffuser into the vacuum sphere, which is required to reach the necessary pressure ratio. Further details on the test facility can be found in [76].

The nominal test conditions of the conducted experiments in the present work are given in table 2.2, whereby the free-stream conditions were determined based on the reservoir conditions by using the steady isentropic one-dimensional relations and the ideal gas law. The viscosity of air, needed for the calculation of the Reynolds number, is calculated by the use of Sutherland's formula as in [46] with a linear interpolation for the low-temperature regime. The free-stream Mach number is based on a nozzle calibration and varies slightly with the Reynolds number as described below. Please note that the reservoir pressure for the tests with cylinders differs slightly from the other values (see table 2.2). The reason for this is a new sensor that has used an incorrect calibration during the setting of flow conditions, but this was corrected during post-processing.

2.1.2 Flow Characterization

The Mach-7 nozzle was employed for the present aerodynamic testings, which passes a flow with turbulent boundary layer into the vacuum of the test section. A free jet with an axially

Table 2.2: Nominal test conditions

Ma_∞ $[-]$	p_0 [kPa]	T_0 [K]	p_∞ [kPa]	T_∞ [K]	ρ_∞ $\left[\frac{\mathrm{kg}}{\mathrm{m}^3}\right]$	v_∞ $\left[\frac{\mathrm{m}}{\mathrm{s}}\right]$	q_∞ [kPa]	$Re_{\mathrm{u}\infty}$ $\left[\frac{10^6}{\mathrm{m}}\right]$
7.001	520	600	0.126	56	0.00787	1046	4.307	2.1
6.998	480*	600	0.116	56	0.00728	1046	3.981	2.0

* test series with cylindrical bodies was performed at a different flow condition

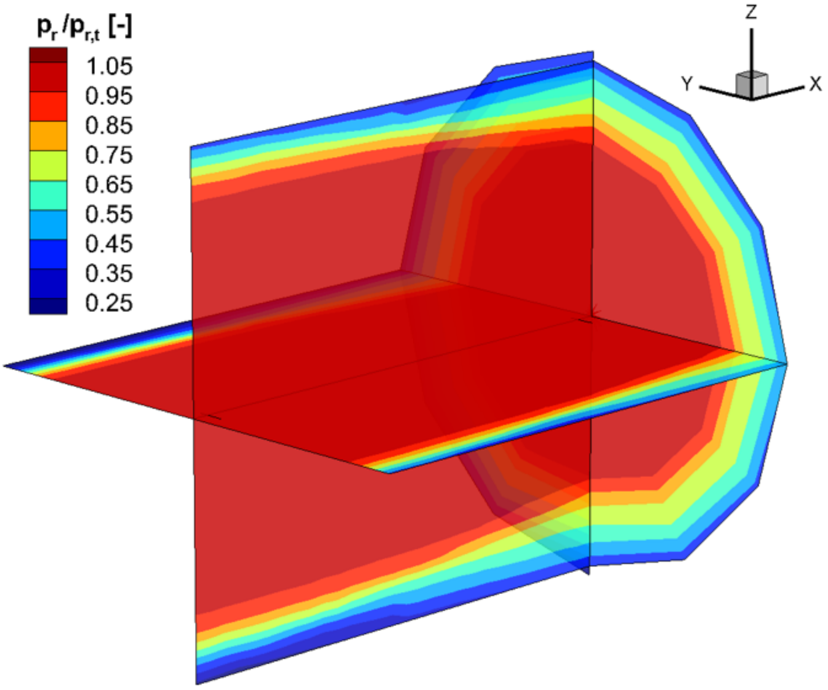

Figure 2.2: Ratio of locally measured ram pressure to theoretical ram pressure of the free jet for the Mach-7 nozzle at flow conditions of $p_0 = 2350\,\mathrm{kPa}$, $T_0 = 662\,\mathrm{K}$, $Re_{\mathrm{u}\infty} = 8.3 \cdot 10^6\,\frac{1}{\mathrm{m}}$; flow direction is the positive x-direction; core flow is defined by the red area ($0.95 < p_r/p_{r,t} < 1.05$)

symmetric homogenous flow and a shear layer between core flow and ambient vacuum develops. Figure 2.2 presents its flow characteristics from experimental measurement for the applied nozzle as the ratio of locally measured and theoretical ram pressure with a unit Reynolds number of $Re_{\mathrm{u}\infty} = 8.3 \cdot 10^6\,\frac{1}{\mathrm{m}}$ showing slices of the horizontal, vertical and axial plane. By using the isentropic relation of adiabatic stagnation pressure behind a normal shock based on the reservoir pressure, the theoretical ram pressure $p_{r,t}$ is calculated with equation (2.1).

$$p_{r,t} = p_0 \left[1 + \frac{2\kappa}{\kappa+1}(Ma_\infty^2 - 1)\right]^{-\frac{1}{\kappa-1}} \left[1 - \frac{2}{\kappa+1}(1 - \frac{1}{Ma_\infty^2})\right]^{-\frac{\kappa}{\kappa-1}} \tag{2.1}$$

For this flow characterization, a measuring rake was in use, which was equipped with 29 Pitot probes in a plane, as described in [76]. This rake was rotated each 30° from 0° to 180° and displaced each $20\,\mathrm{mm}$ along the flow direction from nozzle exit with $x = 0\,\mathrm{mm}$ to $580\,\mathrm{mm}$. Thus, each axial plane is resolved by 203 measurement points.

The usable homogeneous core flow is defined for the present work by a maximum local ram pressure deviation of $5\,\%$ in relation to the theoretical ram pressure (figure 2.2). As a result, the cross-sectional area of the core flow slightly decreases in the direction of flow because of the growing shear layer and has an average diameter of roughly $420\,\mathrm{mm}$. This cross-sectional area is dependent on the Reynolds number, as well. A decreasing Reynolds number results in a thicker boundary layer at the nozzle exit as well as a thicker shear layer of the free jet, whereby the Mach-number-defining ratio of nozzle exit to narrowest cross-section decreases in the same way as the Mach number decreases [76]. Thus, the design Mach number of the nozzle has to be corrected by the Reynolds number. This was considered for the free-stream Mach number in table 2.2. Furthermore, it should be noted that these calibration data ($Re_{u\infty} = 8.3 \cdot 10^6\,\frac{1}{\mathrm{m}}$) do not perfectly represent the ram pressure field of the present measurements ($Re_{u\infty} = 2.0 \cdot 10^6\,\frac{1}{\mathrm{m}}$) due to different shear layer thicknesses. However, these data are still used for the present definition of the core flow, because the impact on the shear layer is low.

2.2 Wind Tunnel Models

As objects of research, three blunt geometries were employed with spherical, cubical and right circular cylindrical models. For the test series with the stereo tracking method, the nominal dimensions are $50\,\mathrm{mm}$ in diameter (for spheres and cylinders), $100\,\mathrm{mm}$ in axial length (for cylinders) and $50\,\mathrm{mm}$ in edge length (for cubes), while the cube's edge length is $41\,\mathrm{mm}$ for tests with two bodies. It is intended that the sphere and the cube have the same mass and material density for the multi-body experiments, which allows a direct comparison of the accelerations. All models were crafted from magnetic steel alloys, with several test articles of each shape manufactured for this work. The mass was measured with a precision scale and the moment of inertia was computed based on the actual mass and dimensions. An overview of the typical model properties is given in table 2.3.

For the application of the present marker-based stereo tracking technique, a random arrangement of circular point markers on the test article's surface is necessary as a pattern for an unique identification of the surface points over time. Due to the high frame rates and the associated short exposure time, a high contrast between the point markers and its background is required to enable a clear point detection on the image pairs. For this reason, the surfaces of the test articles were varnished matt-white with matt-black circular point markers on it, which is shown in figure 2.3. This coating is brushed by hand with an average thickness of $0.06\,\mathrm{mm}$. Its manufacturing accuracy has a relative Standard Deviation (SD) of $10\,\%$, which is based on several measurements at different positions after and before the coating.

In addition, completely different spherical bodies were applied for just one test series with WT balance instrumentation. Unlike the varnished test objects, these models without varnish are smooth and have an arithmetic average roughness of up to $0.1\,\mathrm{\mu m}$. A distinction is made between a geometry without and with drilling. The former presents an ordinary spheres for use

Table 2.3: Typical properties of varnished models

Geometry	d [mm]	l [mm]	m [kg]	I_{yy} [$10^{-3}\,\mathrm{kg\,m^2}$]	ρ_m [$\mathrm{kg\,dm^{-3}}$]	Material number
Sphere*†	50	N/A	0.502	0.126	7.7	1.4125
Cube*	N/A	50	0.981	0.402	7.85	1.0037
Cube†	N/A	41	0.502	0.140	7.7	1.4112
Cylinder*	50	100	1.540	1.527	7.85	1.0037

* used for single-body experiments
† used for multi-body experiments

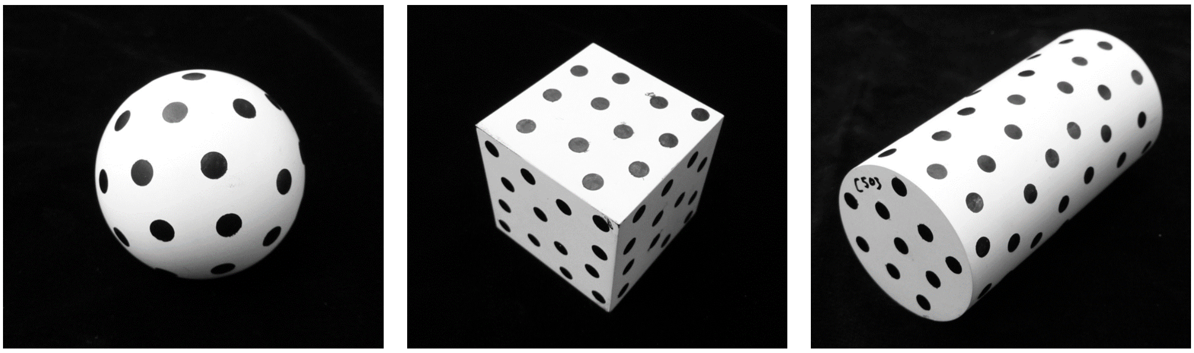

(a) Sphere **(b)** Cube **(c)** Cylinder

Figure 2.3: Applied WT models covered with circular point markers

(a) Sphere without drilling **(b)** Sphere with drilling

Figure 2.4: Applied smooth WT models using the example of 70-mm-sized spheres

as a free-falling model (see figure 2.4a), while the latter is a sphere with a center blind hole on the rear for use as a sting-mounted test object (see figure 2.4b). The blind hole here serves as an interface between model and WT balance via an adapter. Together with four smaller inclined locking holes with screws around the main hole, it is ensured that a very good alignment of the balance and the sphere's center is guaranteed as well as no displacements arise during the WT tests. These two types of models were available in three sizes with nominal diameters of $50\,\mathrm{mm}$, $70\,\mathrm{mm}$ and $100\,\mathrm{mm}$, whereby all of them were manufactured from different types of stainless steel except for the largest sphere with drilling. In a preliminary test with a steel model, a strong oscillation of the sphere with balance support was observed due to the high model mass. Thus, the mass was decreased by the use of Polyether Ether Ketone (PEEK) as applicable material, which minimizes the effect of bending and oscillation of the balance support system during the tests. All typical parameters of the used smooth test models are summarized in table 2.4. Further information can be found in the Master's thesis of Taguema [107].

Table 2.4: Typical properties of smooth models

Geometry	Drilling	$d\,[\mathrm{mm}]$	$m\,[\mathrm{kg}]$	$I_{\mathrm{yy}}\,[10^{-3}\,\mathrm{kg\,m^2}]$	Material
Sphere	No	50	0.502	0.125	1.4125
Sphere	Yes	50	0.440	0.113	1.4307
Sphere	No	70	1.352	0.677	1.4034
Sphere	Yes	70	1.384	0.696	1.4034
Sphere	No	100	4.173	4.173	1.4404
Sphere	Yes	100	0.675	0.670	TECAPEEK

2.3 Free-Flight Technique

An advanced free-flight technique was applied in the test section of the H2K enabling single and multiple synchronized releases of models with subsequent entirely free movement of them in the flow. By the use of this technique, aerodynamic interferences due to a sting support or a balance are prevented. An experimental setup using the free-flight technique is shown in figure 2.5, where the initial positions of sphere-cube pairs on the model dropping system are shown in the upper right corner of figure 2.5b. In general, the initial positioning below refers to the setting at the start of the experiment. Initially, the measurement chamber is under vacuum and the test articles are held by an electromagnet located at the ceiling of the chamber. The initial pitch angle ϑ_0 here is defined by the model alignment on the holder. In order to facilitate a precise model alignment and angle adjustment, an adjustable angle mounting plate or a fixed mounting support is used to cover a broad range of pitch angles. After initiating the flow, the free jet needs up to $3\,\mathrm{s}$ to reach the desired flow conditions. Upon this state is achieved, the test models are released from the holders and fall through the measurement chamber at conditions close to vacuum. When passing the top jet shear layer, the increasing stagnation pressure (shown in figure 2.2) causes an inhomogeneous pressure distribution on the model surfaces leading to positive lift forces as well as a rotation of the bodies, especially the cube. Subsequently, the effective test time begins as soon as the trailing object (or the single body) is completely within the homogenous core flow and ends as soon as one of the test articles reaches the edge of the core flow. At the end, the models cross the lower part of the shear layer before they are caught at the bottom of the test section. The entire fall duration is approximately $0.4\,\mathrm{s}$ for the applied setups, whereby the effective test time is about $0.1\,\mathrm{s}$ and represents the time window for post-processing the measurement data.

During the present work, the free-flight technique was improved by enabling several model drops per run for configurations with single or multiple bodies, which benefits a reduction of operation costs and time, allowing more tests per day. For this purpose, a mechanical dropping mechanism with an open guide pipe and a contoured wheel designed for sphere shapes were developed, which also enables the use of test articles with non-magnetic materials. In hold condition, the spheres are placed one after another in the guide pipe being aligned with the gravitational vector, whereby the bottommost object is located in a contoured slot of the wheel at the end of the pipe. As soon as the dropping system is triggered by an external signal, a stepping motor rotates the wheel via a shaft and the sphere is released through the opening of

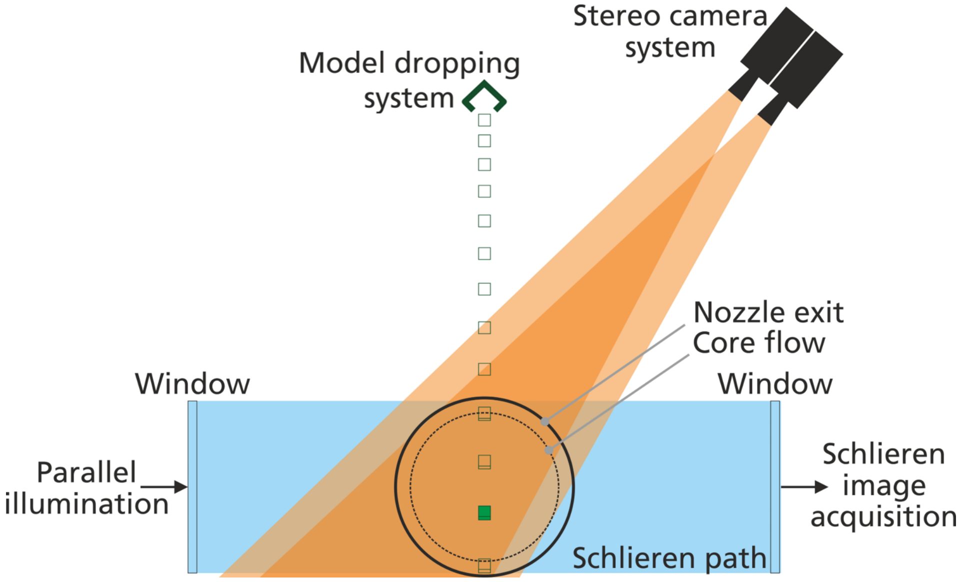

(a) Schematic layout

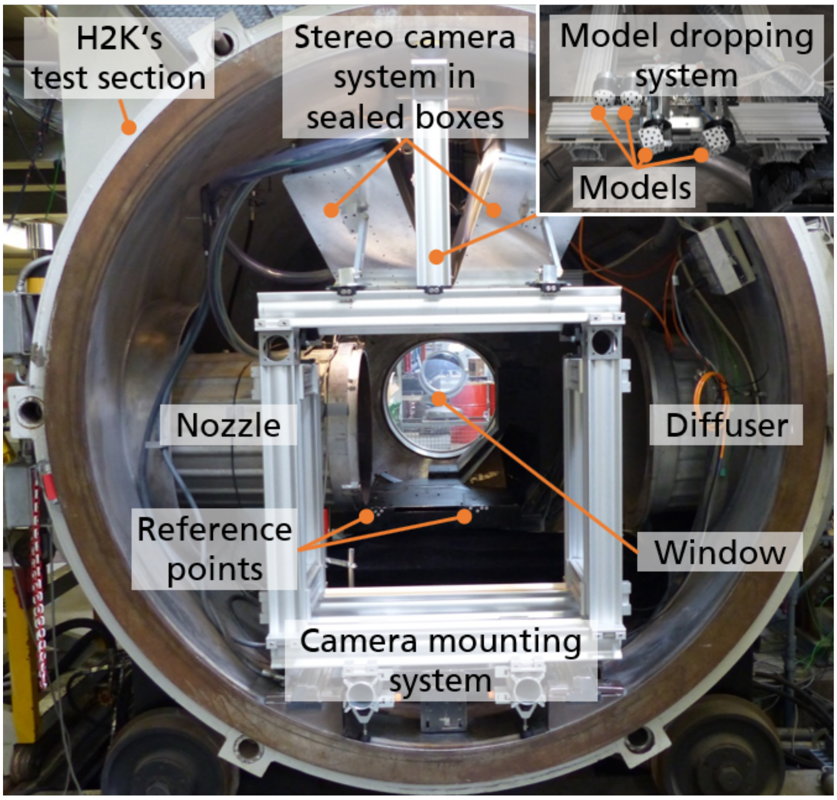

(b) Image of H2K's test section

Figure 2.5: Experimental setup of full-free-flight approach in H2K's test section including stereo tracking technique and schlieren system

the guide pipe. At the same time, the next sphere in the pipe moves into the next slot of the wheel and the procedure repeats. In doing so, two or three model drops per run of the WT were realized, whereby a time delay between the releases ensures a steady state of the flow for each free flight.

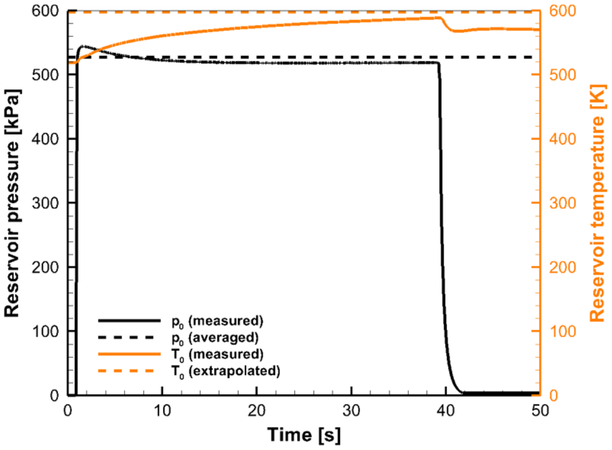

Figure 2.6: Exemplary evolution of reservoir pressure and temperature during WT run

2.4 Instrumentation

The instrumentation used in various combinations for the different test series are described below.

2.4.1 Facility Instrumentation

During each test, the facility operating conditions like p_0 and T_0 were measured in the settling chamber of H2K with a sampling rate of $50\,\mathrm{Hz}$. The reservoir pressure was measured with a GE Druck PDCR 921 absolute pressure transducer, which has a total full-scale accuracy of $\pm 4.2\,\mathrm{kPa}$. For free-flight tests with cylinders and multiple bodies, a more precise pressure sensor of the UNIK 5000 series from the same manufacturer was employed with a total accuracy of $\pm 2.8\,\mathrm{kPa}$ for reservoir pressures between 250 and $5500\,\mathrm{kPa}$. For the measurement of the reservoir temperature, a thermocouple type K class 1 from MTB Sensor-Technik was applied having a total accuracy of $\pm 1.5\,\mathrm{K}$.

An example of reservoir pressure and temperature traces is shown in figure 2.6 having an increased test time of $40\,\mathrm{s}$ to enable a more precise determination of T_0. The flow is released through the test section roughly $1\,\mathrm{s}$ after start of recording. Meanwhile, the reservoir pressure directly jumps up to the desired value after a short start-up period, whereas the measurement signal of the reservoir temperature slightly increases without attaining the nominal value. Due to the response time of the thermocouple, the test time is too short for the sensor to reach equilibrium at the current test conditions. An extrapolation of T_0 was hence carried out to determine the actual reservoir temperature by fitting an exponential function to the temperature gradients in time. The reason for choosing this sensor is that thermocouples with lower mass are too fragile for use in H2K and would break quickly. As a result, this systematic error has to be considered for the uncertainty of T_0 affecting an increase of $\pm 4.0\,\mathrm{K}$.

2.4.2 Schlieren Videography

High-speed schlieren videography was used to characterize the flow field around the test articles over time. The schlieren technique takes advantage of the variations in refractive index effected by density gradients in the flow by use of collimated light beams. Rays experience angular deflections when they traverse through a fluid region characterized by inhomogeneous density distributions leading to a spatial variation in the intensity of light. A knife edge is applied to block deflected light rays that increases the contrast of this intensity distribution. For further information on the flow visualization by schlieren technique, please refer to [102, 110] for the functional principle or to [21] for the actual implementation in H2K.

The H2K is equipped with a stationary schlieren system being located outside of the test section, whereby the 3D flow features are visualized in a 2D image by means of this line-of-sight method. A single-path Z-type schlieren setup with light source, two spherical mirrors, knife-edge and high-speed camera was used, that is suited to capture sharp images. Parallel light beams cross the test section through two windows (see figure 2.5a). As a light source, a $1000\,\mathrm{W}$ xenon arc lamp was used. For the acquisition of image sequences, a Photron FASTCAM APX-RS model 250K high-speed camera with a monochrome CMOS sensor was used that provides frame rates up to $3\,\mathrm{kHz}$ at full $1024 \times 1024\,\mathrm{pixel}$ resolution. This maximum frame rate at full frame was used in this study that allows high-speed recording of the model motion and flow structures as the bow shock. The exposure time was set to $2\,\mu\mathrm{s}$, except for the single-cylinder and multi-body tests with values of $4\,\mu\mathrm{s}$. For the test series with semi-free-flight setup (see section 2.5.3), a Photron FASTCAM SA-X2 model 480K high-speed camera was applied capturing with $12.5\,\mathrm{kHz}$ at full $1024 \times 1024\,\mathrm{pixel}$ resolution and an exposure time of $2.5\,\mu\mathrm{s}$.

2.4.3 Stereophotogrammetry

A high-speed stereo tracking system based on the detection of marker points on the model surface was applied to reconstruct the three-dimensional flight trajectory and attitude of the freely flying models. Stereo tracking as a particular technique of stereophotogrammetry represents a robust non-intrusive measurement technique based on two or more photographic images to determine the static and dynamic motion characteristics of objects in all six degrees of freedom. In the present setup, two synchronously recording cameras in stereoscopic arrangement were placed inside the test section above one schlieren window having a view on the measurement volume at an angle of roughly 60° against the horizontal plane in order to avoid obstructing the schlieren path (see figure 2.5). There are two main reasons for integrating the cameras into the test section, namely to minimize optical effects due to density changes caused by the ambient air and to enable an optimal perspective. This setup ensures the observation of a measurement volume in the order of $600 \times 600 \times 600\,\mathrm{mm}$. Both cameras were from the same series, namely Photron FASTCAM SA-X2 model 1080K, in order to have the same image sensor. Each camera was equipped with a Titanar B24 measuring lens that has a focal length of $24\,\mathrm{mm}$. These two cameras were enveloped in sealed boxes and supplied with external cooling air to prevent overheating due to the surrounding vacuum during the operation of WT. Moreover, a stiff mounting of the stereo camera system was guaranteed so that it is resistant to vibration leading to decalibration.

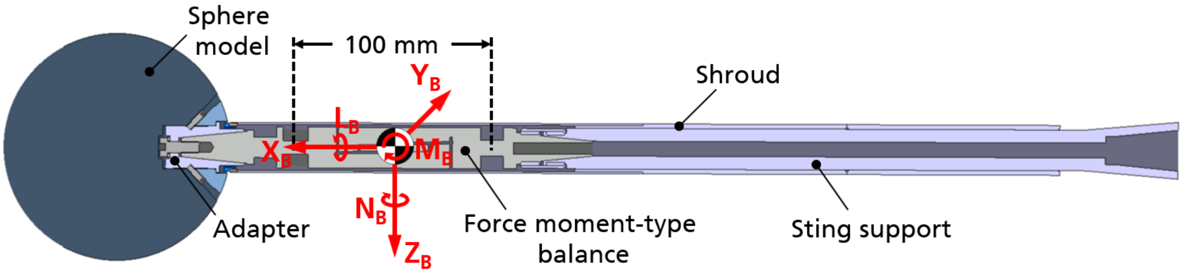

Figure 2.7: Setup of strain-gauge balance DLR 8201 with definition of balance reference frame

For both cameras, a frame rate of 12 kHz at 1024×1024 pixel resolution was set. This high frame rate at full resolution was used because of the short free-flight time in a split second with the purpose of acquiring sufficient data points for high-quality results after post-processing. Due to a short exposure and a small aperture, a light source with high intensity is essential to acquire high-contrast images. Therefore, four 86 W plus four 38 W high-power LED with a color temperature of 5000 K were mounted onto an aluminum ring, which functions as capacitive cooler. Another reason for the use of this light source is the cold-white property ensuring a high yield of FASTCAM series blue-sensitive CMOS sensors. Each camera was equipped with one of these LED aluminum rings that were concentrically mounted on the optical window of the camera box benefiting an optimal illumination.

In advance of each test series or after setup modifications, a default calibration with a fixed procedure was carried out as outlined in section 3.2.1.

2.4.4 Force Moment-Type Balance Instrumentation

Just for the experimental setup with a free-falling and a fixed sphere, the trailing model was equipped with a six-component strain gauge balance, namely DLR 8201 (see figure 2.7), allowing a Six-Degrees-of-Freedom (6DoF) force and moment measurement. This balance type is an in-house design by DLR that has multiple strain gauges applied at well-defined positions to determine all three forces and all three moment components. The DLR 8201 balance features design loads of $X_{Bmax} = 50\,\mathrm{N}$ (axial), $Y_{Bmax} = 90\,\mathrm{N}$ (side) and $Z_{Bmax} = 150\,\mathrm{N}$ (normal) for the force components as well as of $L_{Bmax} = 3.2\,\mathrm{N\,m}$ (roll), $M_{Bmax} = 8.6\,\mathrm{N\,m}$ (pitch) and $N_{Bmax} = 4.3\,\mathrm{N\,m}$ (yaw) for the moment components. It has a diameter of 18 mm and a distance between both instrumented sections of 100 mm. This balance was selected as the best compromise between the model-to-sting-diameter ratio and the feasible axial load being close to the expected values. From a previous study by Taguema [107], it was shown that the sting effects are negligible for the present setup, whereby the drag for a configuration with a balance is 0.1 % less than without mounting supports. For the data acquisition, a sampling rate of 5 kHz was used.

A static calibration of the wind tunnel balance is a standard procedure in DLR that was performed before the test series as described in section 3.3.1.

2.5 Experimental Setup

Two primary setups were employed in the WT for the present study, which have sometimes slightly different modification from run to run. First, a full-free-flight approach was used with one or two blunt bodies to determine the aerodynamic behavior without aerodynamic interference due to supports. Second, a semi-free-flight approach was applied with a free-falling and a sting-mounted sphere to determine directly measured reference force data over a wide range of lateral distances as well as to capture the flow topology at a desired comparable relative position. For both setups, a free-flight technique is involved as described in section 2.3. The definition of the coordinate systems as well as the nomenclature for aerodynamic coefficients is outlined in the following.

2.5.1 Frame of Reference

Figure 2.8 depicts the Frame of Reference (FoR), where x, y and z are the Cartesian coordinates as well as g is the gravitational acceleration. The aerodynamic coefficients of lift force C_{L}, drag force C_{D} and pitching moment C_{M} are specified in the spatially fixed FoR of the Global Coordinate System (GCS). For test cases with two bodies, the subscripts 1 and 2 represent the primary (or leading) and secondary (or trailing) object. The origin of the right-handed GCS (red axes) is spatially fixed in the center of the nozzle's exit plane. It has the positive x-axis pointing downstream, the y-axis in the transverse direction and the positive z-axis pointing vertically up. Body-fixed Local Coordinate Systems (LCS) (blue axes) are defined in the Centers of Gravity (CoG) of the test articles so that the x-axis of the sphere is parallel to the global x-axis at $t = 0\,\mathrm{s}$, while the x-axis of the cube and cylinder is normal to one of their bases. It is expected that the model motions for the present experimental setup occur in an xz-plane. Hence, the main influence factor in the experiments with multiple bodies is the relative distance between primary and secondary body in x- and z-direction (shown in figure 2.8), namely streamwise ($\varDelta x$) and vertical ($\varDelta z$) separation distance. Another investigated parameter for cubes and cylinders is the pitch angle ϑ as shown in figure 2.8, which designates the angular displacement between the global and local x-axis of the respective body. Here, $\vartheta = 0°$ means that a base surface is orthogonal to the flow. The positive direction of rotation is clockwise by viewing along the y-axis.

In the present study, several designations of configurations with respect to the body orientation are used as described in the following. In figure 2.8, a cube is shown in an edge-exposed orientation, whereby the line from one cube's edge center to its CoG is parallel to the global x-axis. A further orientation of the cube is plane-exposed, which is defined by a parallelism of global x-axis and one surface normal. For the cylindrical bodies, one configuration is called base-exposed, when the base area is orthogonally exposed to the flow. Furthermore, a side-exposed configuration means that the symmetry axis of the cylindrical body is orthogonal to the flow direction.

In addition, the shock radius r_S is shown in figure 2.8. This parameter represents the radius of the primary bow shock at the position of the secondary object being calculated with the modified equation for the shock shape by Billig [12] proposed by Prévereaud [90].

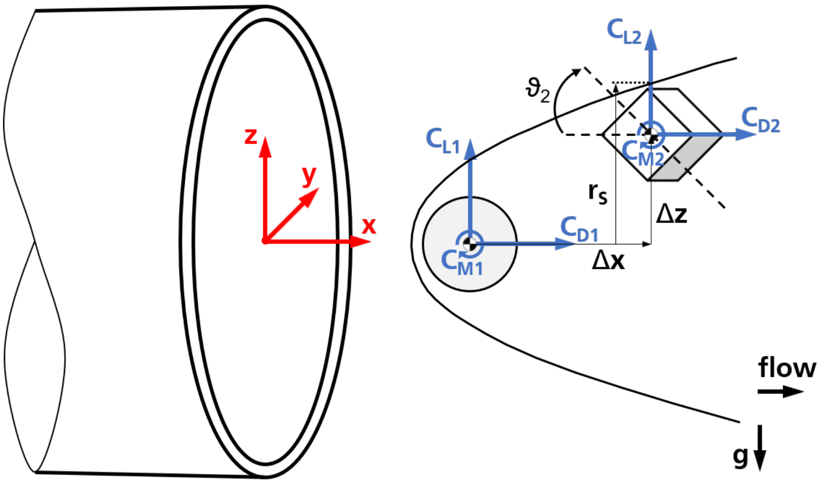

Figure 2.8: Nomenclature and definition of global coordinate system with respect to nozzle exit

2.5.2 Full-Free-Flight Setup

Figure 2.5 shows the experimental setup of fully free-flying test objects by the use of the free-flight technique with mechanical and electromagnetic dropping mechanism as described in section 2.3. In addition, measurement techniques such as schlieren videography were employed to document the flow topology as well as stereophotogrammetry to indirectly measure the forces and moments. The full-free-flight setup was applied for most of the present test series like WT experiments with single spheres, cubes and cylinders on the one hand, or with pairs of spheres and cubes on the other hand. For the single-body experiments, only the electromagnetic dropping mechanism was utilized, whereby the use of two or three electromagnets enable several drops per run. Thereby, the dropping mechanism was positioned in such a way that model's CoG is located at $z = 550\,\mathrm{mm}$ in the initial position, which is a good trade-off between the required distance to free jet's shear layer to prevent a premature detachment of the test object and the possible drop height to increase the effective test time. In axial direction, the first model was located at $x = 110\,\mathrm{mm}$ with further objects at $x = 260\,\mathrm{mm}$ and $410\,\mathrm{mm}$. For the multi-body experiments, only electromagnets were used for leading and trailing bodies in the test series with pairs of spheres and cubes, whereas both mechanical and the electromagnetic dropping mechanism were employed for tests with two or three synchronized drops of sphere pairs, so that the former was used for the leading sphere and the latter for the trailing sphere. In doing so, the leading bodies were placed at $x = 120\,\mathrm{mm}$ and $180\,\mathrm{mm}$ with the same position in z-direction as the first model of the single-body configurations for the setup with only electromagnets, while the trailing bodies were positioned at $x = 240\,\mathrm{mm}$ and $360\,\mathrm{mm}$. Regarding the trailing object, a variation of z_2 was conducted with initial downward displacements up to $125\,\mathrm{mm}$ based on the basic level of $z = 550\,\mathrm{mm}$.

2.5.3 Semi-Free-Flight Setup

The semi-free-flight setup is depicted in figure 2.9 by the use of the free-flight technique for the non-stationary leading sphere and a sting support for the stationary trailing one as shown in figure 2.7. In addition, the fixed object was instrumented with a wind tunnel balance for force and moment measurement as well as schlieren videography was applied for flow visualization. The dropping mechanism here consists of an electromagnet with the same positioning as the first object of the full-free-flight approach, whereby just single drops were realized with this setup. However, the mechanical dropping mechanism was used for the sphere with a diameter of $100\,\mathrm{mm}$, because the holding force of the electromagnet is too weak. The stationary sphere was placed in the light beam of the schlieren system and was aligned with the nozzle's centerline. To enable a defined relative position, the model was adjustable in axial direction by means of a movable model support system, which was connected to the internal balance of the test article via a sting. In doing so, the balance was mounted inside the rear of the sphere model by the use of an adapter, but it was not entirely integrated due to its length. Because of exposed parts, the balance is covered by a shroud with a diameter of $22\,\mathrm{mm}$ in order to protect it from the flow as well as to prevent measurement signals due to direct flow exposure. During the installation of the model and its support system, the axial component of the balance was aligned with the flow direction (x-axis of GCS) as well as the lateral and normal components were adjusted to the y- and z-axis. Afterwards, the accuracy of the adjustment, measurement chain and post-processing procedure has been verified by means of different weights placed on a defined position. If the recorded results fit within a given uncertainty, the setup is ready to use.

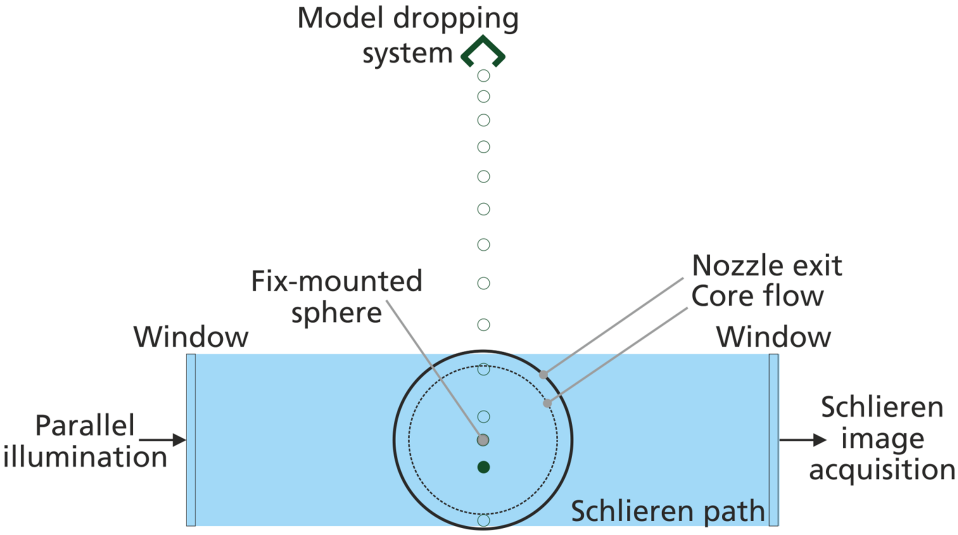

(**a**) Schematic layout

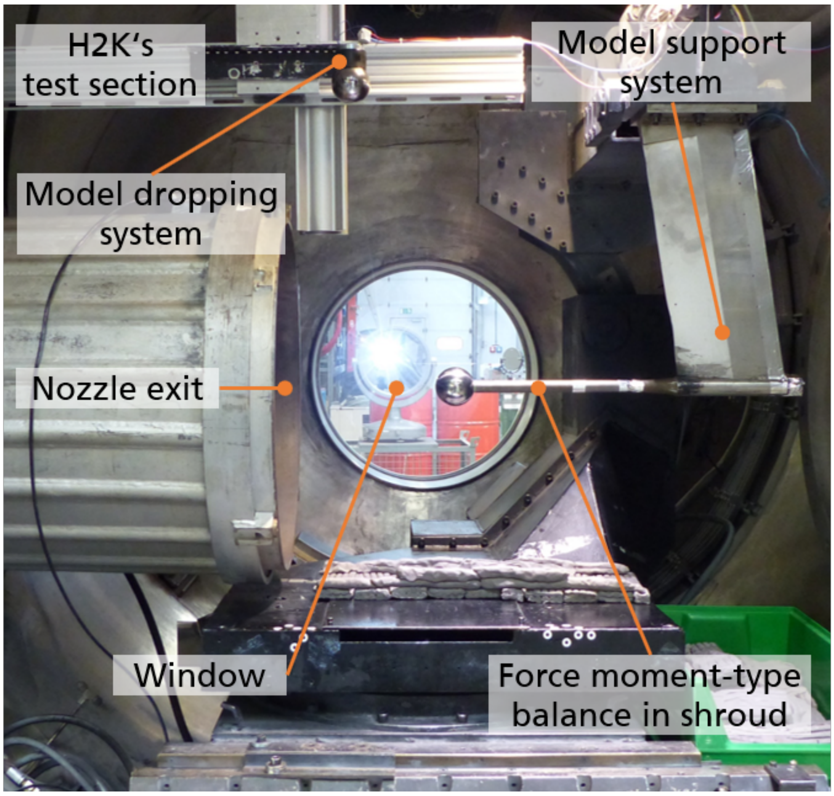

(**b**) Image of H2K's test section

Figure 2.9: Experimental setup of semi-free-flight approach in H2K's test section including force moment-type balance instrumentation and schlieren system

3 Data Processing

In this chapter, the post-processing with uncertainty analysis of the measurement results is described in detail. On the one hand, the workflow of the motion data from the stereophotogrammetry approach is outlined in section 3.2, while on the other hand the workflow of the force and moment data from the balance analysis approach is shown in section 3.3. In addition, section 3.5 presents the modified Newtonian flow theory, which analytically determines the aerodynamic coefficients for the single blunt bodies.

3.1 General Definitions

As a result of the post-processing, the aerodynamic coefficients are determined, which are the primary quantities of interest in this work. Common definitions of the force and moment coefficients are used as given in equations (3.1) and (3.2), whereby they can be determined by the translational acceleration a and the angular acceleration α, on the one hand, or by forces F and moments M, on the other hand.

$$C_{\mathrm{F}i} = \frac{F_i}{\frac{\kappa}{2} p_\infty Ma_\infty^2 S_{ref}} \quad \wedge \quad F_i = m a_i \tag{3.1}$$

$$C_{\mathrm{M}i} = \frac{M_i}{\frac{\kappa}{2} p_\infty Ma_\infty^2 l_{ref} S_{ref}} \quad \wedge \quad M_i = I_i \alpha_i \tag{3.2}$$

The free-stream static pressure p_∞ is not directly measured in the present study, but it is determined by the use of the isentropic relation [31] based on the measured reservoir pressure p_0, the free-stream Mach number Ma_∞ and the ratio of specific heats κ for diatomic gases as defined in equation (3.3).

$$p_\infty = \frac{p_0}{\left(1 + \frac{\kappa-1}{2} Ma_\infty^2\right)^{\frac{\kappa}{\kappa-1}}} \tag{3.3}$$

The reference area S_{ref} is defined as the base area according to equation (3.4), which depends on the applied geometry.

$$S_{ref} = \begin{cases} \frac{\pi}{4} d^2; & \text{for sphere \& cylinder} \\ l^2; & \text{for cube} \end{cases} \tag{3.4}$$

As the reference length l_{ref}, the diameter d is employed for spherical and cylindrical bodies, while the edge length l is applied for the cube shape.

3.2 Post-Processing System of Stereophotogrammetry Data

A complex post-processing system was developed for the present work to determine high-quality aerodynamic coefficients based on the image pairs recorded by the stereo tracking system (as outlined in section 2.4.3). Figure 3.1 illustrates its process description consisting of four main parts, whereby the Digital Image Correlation (section 3.2.2) including the Calibration (section 3.2.1) and the Six-DoF Motion Tracking (section 3.2.3) provide the models' 6DoF motion data consisting of CoG positions and orientation angles. On this basis, the aerodynamic force and moment coefficients are determined by means of the Coefficient Determination (section 3.2.4) and optimized by means of the Optimization of Parametric Model (section 3.2.5). For the first two parts, the commercially available software ARAMIS Professional 2017 was used, which is developed and distributed by Gesellschaft für Optische Messtechnik (GOM). Furthermore, two in-house tools were implemented in LabVIEW and Python for the last two parts.

3.2.1 Calibration

As shown in figure 3.1, a standardized calibration procedure was performed before each test series under ambient condition to gain information about the intrinsic and extrinsic camera parameters, which ensures a highly accurate measurement. In doing so, an image series of a differently positioned calibration object with a known pattern of reference points is recorded [32, 36]. On the one hand, the intrinsic camera parameters are determined, which are dependent of the used camera type. These include the focal length of the camera lens as well as the pixel size, the resolution, the principle point coordinates and the tilt of the image sensor, which leads to the mathematical modeling of the distortions and other aberrations due to the lenses as well as the glasses of the camera boxes. On the other hand, the extrinsic camera parameters like the position and orientation in 3D space are calculated for each camera of the stereoscopic configuration. An original GCS is set in the calibration process, as well. The highly accurate GOM-specific calibration object CC20 with 24 uncoded and 20 coded reference points was applied for the present study, which have calibrated lengths of $493.680\,\mathrm{mm}$ and $494.156\,\mathrm{mm}$. As a result, the calibration deviation is $2\,\mu\mathrm{m}$ for all conducted tests except for the test series with cylindrical bodies that have a value of $7\,\mu\mathrm{m}$. These deviations are significantly lower than

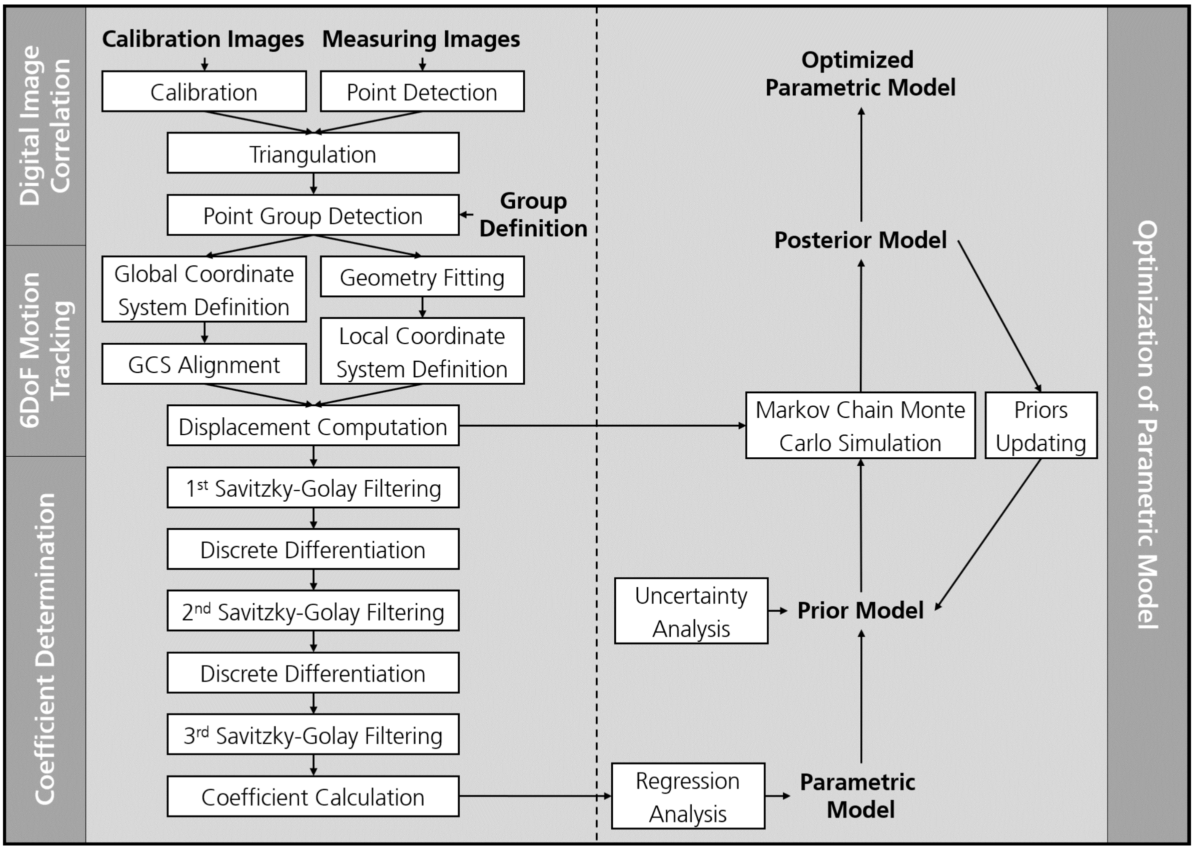

Figure 3.1: Schematic description of post-processing by use of the stereophotogrammetry data

the spatial resolution of the cameras, as the data processing uses a sub-pixel detection approach as described in section 3.2.2.

3.2.2 Digital Image Correlation

In general, Digital Image Correlation (DIC) is a photograph-based method using cross-correlations for non-intrusive deformation and motion analysis providing data about displacement and strain [75]. Refer to figure 3.1 for a detailed illustration of this part. In the present work, a point-based DIC technique is applied that provides three-dimensional time-resolved quantities as coordinates and displacements of a point or a group of points in a measurement volume by the principle of triangulation. This allows the CoG position in 3D space and the body orientation of the model motion to be reconstructed on the basis of the recorded sequence of synchronized image pairs from the stereo tracking cameras along with the calibration parameter. Its functional principle is described below based on [36, 106].

First, the point markers on the gray-value measurement images have to be detected. Elliptical contours are fitted on the circular point geometries to consider their angle of inclination relative to the image plane as well as the curvature of the models, using the contrast value as a transition from white to black for the fitting. For the detection of such elliptical contours, the local image details are binarized, whereby the image pixels are converted in black or white depending on a defined threshold. Contiguously closed black areas across the entire image are detected as possible candidates. In the next step, a shape factor eliminates all non-elliptical candidates. Furthermore, a preset point diameter selects candidates with the correct size. The centers of the ellipses are the measurement points. These centers serve as the initial value for an iterative fitting, whereby strong gray value gradients running from the center along different directions determine contour points for the ellipse fitting. Thus, a very precise center detection in subpixel resolution is enabled, which is also ensured by accuracy parameters such as the maximum deviation of the real gray value transition and the aforementioned point diameter.

Second, the three-dimensional coordinates of point markers are reconstructed by means of triangulation between corresponding images from two views of the same point. This requires the calibration parameters such as the positioning of the cameras in relation to each other and the mathematical model for optical aberration. Together with the two 2D coordinates in the images of an observed point, its 3D coordinate in space can be calculated.

Third, the detected point markers have to be unambiguously identified over time to determine their displacement. Point groups are defined by merging points of the same solid object, whereby an irregular arrangement of point markers is mandatory. In doing so, unique triangles of measurement points with unique combinations of point-to-point distances are available, which are used to identify them at different times with the help of point neighborhoods. A preset identification threshold parameter defines therefore the maximum deviation distance to ensure an unambiguous assignment.

3.2.3 Six-Degrees-of-Freedom Motion Tracking

For the present analysis, the point groups are employed to determine the three positions in streamwise (x), spanwise (y) and vertical (z) direction as well as the orientations roll (φ), pitch (ϑ) and yaw angle (ψ) of the test objects with respect to the well-defined GCS (as described in section 2.5.1). To see how this part fits into the overall workflow, consult figure 3.1.

First of all, a stationary reference point group with at least three elements is used to define a spatially fixed GCS. For accurate measurement data, the coordinate axes have to be set in such a way that the x-axis is aligned with the inflow and the z-axis is parallel to gravity. On that account, an additional free-fall (without flow) plus a free-flight (with flow) test with a single sphere were performed and post-processed. For the correct alignment of the z-axis, the trajectory of the free-falling sphere is used to determine the direction of gravity. The computed free-flying trajectory and the z-axis define a plane, whose normal is the y-axis of the GCS. As a result, the z-axis is unambiguously determined. Subsequently, the corresponding three-dimensional bodies are fitted on the tracked point groups of the respective test article by the method of least squares. Body-fixed LCSs are defined in the CoG of the objects with a FoR as specified in section 2.5.1. Taken both types of coordinate systems together, the three-dimensional angular and translational displacements of each free-flying object can be computed over time with regard to the absolute GCS.

3.2.4 Coefficient Determination

With the time-resolved displacement data, the motion derivatives of the test models are determined after a number of sequential processing steps, which are listed in figure 3.1. First, the signals are smoothed by filtering and differentiated by discrete differentiation to obtain the translational and angular velocities. The same procedure is carried out for the accelerations. Afterwards, the second-derivative signals are smoothed again. These several signal-processing steps were necessary because the measurement data show slight noise, mainly due to optical and vibrational effects, as described later in section 3.4. In addition, the signal-to-noise ratio is unfavorable for the motion derivatives due to the short time steps. As a consequence, the acceleration calculation is very sensitive to noise in the position and orientation data as the double differentiation leads to a quadratic noise growth.

A conventional Savitzky-Golay filter is applied for the present study, which fits piece-by-piece polynomial functions to the noisy signal by the method of least squares [79, 94]. In particular, the Savitzky-Golay filter ensures a digital smoothing that removes higher frequency components and treats the remaining frequency spectrum equally to prevent the distortion of the signal tendency [79]. In the present setting, this filter was set to a first-order polynomial with subsets between 141 and 201 adjacent data points depending on the noise characteristic.

The discrete differentiation of the motion data is performed by a central finite difference quotient as in [25]. In comparison to forward or backward methods, central difference offers second-order accuracy and also prevents time shifts in the derived signals.

Unlike the procedure described in the previous paragraphs, the motion data of WSI configurations exhibit a singularity in the measured signals due to a short impulse when the objects collide. This would result in strong distortions of the motion derivatives in the neighborhood of the singular point. For this reason, the moment in time of the collision is determined, and the datasets before and after it are post-processed separately for each component of motion. The singular point is calculated by finding the discontinuity in the second derivative of streamwise position data. Since the points at the start and the end of the series can be just insufficiently calculated with the conventional Savitzky-Golay filter due to artificial extensions, the noise reduction is weaker for data points close to the moment of collision. Hence, the last points before the impact as well as the first points after it are filtered by polynomial fittings with specified constraints in contrast to the other part of the dataset being smooth by the Savitzky-Golay filter. In the course of this, a third-order polynomial is fitted to the edges of measurement data, which fulfills a set of constraints concerning the same value in position, velocity and acceleration at the intersection of Savitzky-Golay-filtered and polynomial-fitted motion data as well as the same accelerations of the two datasets at the point shortly before and after the collision event. Following this, both parts of the data are merged before differentiation using the common procedure with central finite difference quotients. After each differentiation, the polynomial order of fitting is reduced by one. The Savitzky-Golay filter has the same settings as in the test cases without singularity, except that a polynomial order of 2 is assumed for the first filtering of the position signals.

For the determination of the aerodynamic coefficients, the test time was chosen so that the flow conditions are steady-state and the single or trailing model is completely within the core flow (as described in section 2.3) to minimize acceleration uncertainties due to deviations of the stagnation pressure. The force and moment coefficients are calculated by using equation (3.1) and equation (3.2), where the reference area is defined by equation (3.4). To determine the lift coefficients, the vertical (z) force component is separated from gravity by assuming the local gravitational acceleration of $g = 9.811\,27\,\frac{\mathrm{m}}{\mathrm{s}^2}$ according to Achner [1] on the basis of a measurement on site.

3.2.5 Optimization of Parametric Model

Part of the aim of this dissertation is to derive relationships from the measurement data that are modeled by mathematical functions through a combination of model structure, model parameters and physical variables. Therefore, a non-linear regression analysis is performed for the single-body configurations by means of trigonometric functions to estimate relations between aerodynamic coefficients and pitch angle. The experimental data are fitted by a method of successive approximation to determine the model parameters. This evaluation step is part of the Optimization of Parametric Model in figure 3.1.

An optimization algorithm can be used to increase the accuracy of the parametric model, with the model parameters from the regression analysis serving as initial conditions. The determination of aerodynamic forces and moments based on the motion of rigid bodies is an inverse problem [68], since the aerodynamic loads are not measured directly but derived from the observed flight trajectories and attitudes. These results from tracking show significant uncertainties, which have a disproportionately large influence on the aerodynamic coefficients by solving the inverse problem. A better approach is therefore to solve the forward problem by means of mathematical optimization to minimize the difference between model-predicted outputs and measurements. The relationship between aerodynamic loads and motion behavior can be described by a system of Ordinary Differential Equations (ODEs). In doing so, the equations of motion are solved to determine the time series of positions and orientation angles using the parametric model of the aerodynamic coefficients. These calculated motion data are compared with the measurements in order to evaluate the deviation. Based on this, the model parameters of the aerodynamic coefficients are calibrated.

For solving continuous non-linear optimization problems, Markov Chain Monte Carlo (MCMC) methods are the appropriate approach due to the complex mathematical model of the present physical system with a high-dimensional parameter space of uncertain model parameters. MCMC is a class of sampling algorithms that enable the numerical approximation of the Bayes' theorem. Compared to iterative methods like the Gauss-Newton algorithm, which are known for their high computational efficiency and robustness, the MCMC approach offers the advantage of enabling uncertainty estimation by use of distributed parameters [78]. On the one hand, these parameters include the known probability distributions of the error-prone physical quantities like test conditions and model properties, as well as on the other hand, the unknown distributions of the model parameters for the aerodynamic coefficients with an initial estimate from the regression analysis. Both together are part of the prior model, which serves as input for the MCMC simulations. The first step is to draw a sample from these probability distributions, which is then used to compute the motion data based on the mathematical model. In the next step, the outcome is compared with the observed flight trajectory and attitude from the 6DoF motion tracking to evaluate whether the sample is accepted for the posterior distribution. This

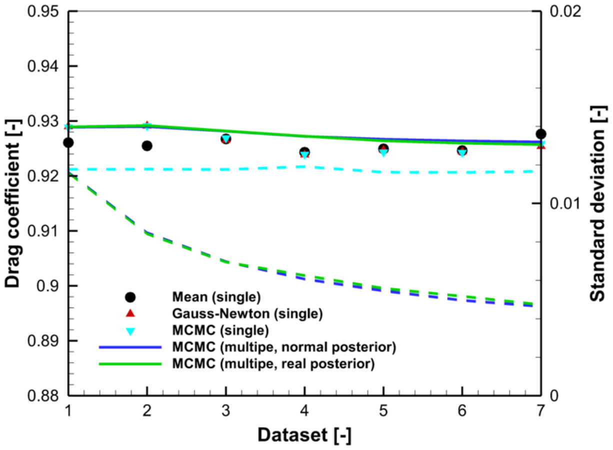

Figure 3.2: Comparison of results from MCMC simulations for a single sphere concerning drag coefficients (solid lines and circle symbols) and their standard deviations (dashed lines)

is true if the computed motion data is within the measurement uncertainty of the observed data. If the sample is accepted, it serves as origin for the next sample, which makes the sequence of samples a Markov chain. For this purpose, the No-U-Turn Sampler (NUTS) algorithm is used, which works with a gradient-based sampling of continuous variables to enable fast convergence to the target distribution at a high sampling speed as described by Hoffman and Gelman [49]. The sampling algorithm generates new samples until the configured number of accepted samples is reached. To guarantee the validity of the outcome, the processing described above is carried out in parallel with several Markov chains. In doing so, the convergence of the posterior distributions between the chains is checked with the diagnostic of the Gelman-Rubin statistic R [34], where $R \approx 1$ indicates a likely converging target distribution of the chains. In the present MCMC simulations, 4 Markov chains with a target of 2000 accepted samples were defined, ensuring a Gelman-Rubin statistic of less than 1.05.

In order to increase the accuracy of the parametric model and thus the aerodynamic coefficients, a multiple-sample approach is used here to reduce the random errors on the overall measurement uncertainty. Priors updating is applied therefore, whereby the posterior distributions of the initially unknown parameters from a MCMC simulation are used to adjust their prior distributions. A further simulation is performed with the updated prior model, which is compared with another dataset of observed motion data for acceptance testing. After several repetitions of this processing, an optimized parametric model with estimated overall uncertainty is obtained.

An example of the results from MCMC simulations is shown in figure 3.2 for a test case with a single sphere, whereby the drag coefficient (solid lines and circle symbols) and its Standard Deviation (SD) (dashed lines) are presented. This line chart displays the experimental results of several datasets from different wind tunnel tests, each consisting of a large number of data values. The datasets are post-processed separately in the single-sample approach and iteratively for the multiple-sample approach as outlined in the previous paragraph. For the single-sample approach, the drag coefficient of MCMC simulations (cyan circle symbols) is compared with the outcome of the Gauss-Newton algorithm (red circle symbols) and the mean of an entire dataset (black circle symbols). It can be seen that both optimization algorithms show a very good agreement, while the mean value deviates from it in some cases. For the multiple-sample approach, the drag coefficient seems to converge towards the value of $C_{\mathrm{D}} = 0.926$. The variance of the drag coefficient is greater in the approach with single samples than with multiple samples. Concerning the calculated standard deviations from MCMC simulations, the SD is almost constant at around 0.012 for the separate processing, while it is more than halve with 0.005 after the iterative processing with seven datasets. This result demonstrates the great advantage of the multiple-sampling approach. Furthermore, figure 3.2 depicts the outcomes for which the real posterior distributions (green lines) from MCMC simulations and the idealized normal distributions (cyan lines) are used for the prior updating. It is apparent that the resulting drag coefficient and its standard deviation show no significant differences. Hence, the assumption of idealized distributions is well suited, which increases the stability of the simulations.

In the present study, the post-processing with MCMC simulations is carried out just for the single-sphere configurations. This test case represents a simple application as it can be treated as a system of two uncoupled equations of motion that can be solved analytically. It was shown that this approach works and can improve the quality of the aerodynamic coefficients determined on the basis of measured motion data. In addition, the procedure for MCMC simulations was verified for this type of motion and can be adapted for the other configurations. For more complex configurations with non-spherical or multiple objects, the system of equations consists of several coupled non-linear ODEs due to the dependence between the positions and orientations of the objects on the one hand and their aerodynamic coefficients on the other. However, the complex evaluation procedure is beyond the experimental focus of this study, which is why the motion data of non-spherical single-body and all multi-body tests were post-processed without mathematical optimization but with uncertainty analysis and regression analysis for the single-body configurations.

The following lessons learned from the MCMC simulations can be used to solve the ODE system of more complex configurations. First, the ODEs cannot be solved analytically, which necessitates a numerical approach. The solution has a very high sensitivity to the time step, especially the further away the data point is from the initial position. With the available experimental data, the definition of the time step based on the sampling rate leads to high deviations of the time series' last data points beyond the measurement uncertainties, which means that a convergence of the Markov chains is not achieved. One possible approach to avoid this problem is to use a lower constant or a residual-based adaptive time step in combination with an interpolation for the comparison with the measurement data. Second, due to the complex model with high dimensionality, a fine-tuned setting of the MCMC simulations such as the selection of sampling algorithm, the frequency of tuning, the number of accepted samples and the initial conditions of the unknown model parameters is necessary to achieve convergence of the results. This is very time-consuming, which is why simplified test cases can sometimes be used for the adjustment of settings to reduce the time required. Third, MCMC simulations involve a high computational effort, whereby it takes several days to weeks for a single dataset to be processed. However, Markov chains offer the advantage that multiprocessing enables the independent performance of several Markov chains with one chain per core.

3.3 Post-Processing System of Force Moment-Type Balance Data

The force and moment measurement with in-house-developed WT balances is a well-established and commonly used measurement technique at DLR, which is why the calibration and the subsequent post-processing of data follow a standard procedure. For this reason, the following is a brief description of the calibration (section 3.3.1) as well as the determination of aerodynamic loads (section 3.3.2).

3.3.1 Calibration

At a dedicated test stand, the calibration of the six-component balance DLR 8201 was conducted by means of highly accurate reference weights with different masses. In doing so, the same setup of balance and sting as in the WT tests was applied that enables the correction of the sting bending with regard to the model's angle of incidence within an uncertainty of $\pm 0.1°$. As a result of the calibration, all components have shown regular behavior as well as acceptable errors. Table 3.1 presents the results of the balance calibration as maximum error including non-linear interference between the components. This study focuses on the axial (X_B), normal (Z_B) and pitching (M_B) components with relative maximum errors of less than or nearly equal to $0.1\,\%$ referring to the design loads.

3.3.2 Balance Analysis

During the wind tunnel testing, the measurement values of the balance and the facility instrumentation are acquired simultaneously, which are stored together in one data file. These data were post-processed together with the calibration information by an in-house tool for balance analysis, whereby the voltage signals of the six strain gauges are converted into aerodynamic loads in the end. To begin this process, the load data experience an offset correction by the use of outputs without aerodynamic loads that are recorded in a reference measurement prior to the flow experiment. Afterwards, all quantities are sampled to a common frequency based on the probe of the reservoir pressure, which is computed by means of linear interpolations.

Table 3.1: Maximum error from balance calibration of DLR 8201

	Design load	Maximum error
X_B [N]	50	±0.0570
Y_B [N]	90	±0.0258
Z_B [N]	150	±0.0303
L_B [N m]	3.2	±0.1275
M_B [N m]	8.6	±0.0019
N_B [N m]	4.3	±0.0110

Since the internal balance is not mounted in such a way that its center is identical to the CoG of the model, the signals of gravity-loaded strain gauges are corrected from the mass impact depending on the adjusted AoA. In the next step, the tool computes the aerodynamic loads from the voltage signals by a data reduction matrix considering the non-linear interference behavior of the sensors. Once the loads are extracted, the force coefficients (C_{A}, C_{Y} and C_{N}) as well as the moment coefficients (C_{l}, C_{m} and C_{n}) are determined by the use of equations (3.1) and (3.2). To obtain the aerodynamic coefficients in the defined FoR as in section 2.5.1, the moment coefficients of pitching and yawing are converted into values referred to the CoG, because the center of model's base plane is predefined as Moment Reference Center (MRC), as well as the directions of the force components in x and z are reversed. The conversion formula of the relevant aerodynamic drag force, lift force and pitching moment coefficient are given in equations (3.5) to (3.7) under the assumption of a zero angle of incidence, which is reasonable as the measurements were performed for a sphere that is in the same plane as the trailing body and the free-stream vector.

$$C_{\mathrm{D}} = -C_{\mathrm{A}} \tag{3.5}$$

$$C_{\mathrm{L}} = -C_{\mathrm{N}} \tag{3.6}$$

$$C_{\mathrm{M}} = C_{\mathrm{m}} - \frac{x_{ref}}{l_{ref}} C_{\mathrm{N}} \tag{3.7}$$

Finally, a digital low-pass filter with a cut-off frequency of $100\,\mathrm{Hz}$ is applied to the load data. For the following representation of the results, the time frame has its origin at the moment when the drag coefficient is at its lowest, which occurs as soon as the centers of both spheres are aligned.

3.4 Uncertainty Analysis

Like all measurements, the data from the experiments are also subject to errors. The following analysis deals with the estimation of the measurement chain uncertainties and their influence on the aerodynamic coefficients. This section begins by examining different occurring sources of uncertainty during the tests and ends by determining the resulting overall uncertainties of the stereophotogrammetry and the force moment-type balance.

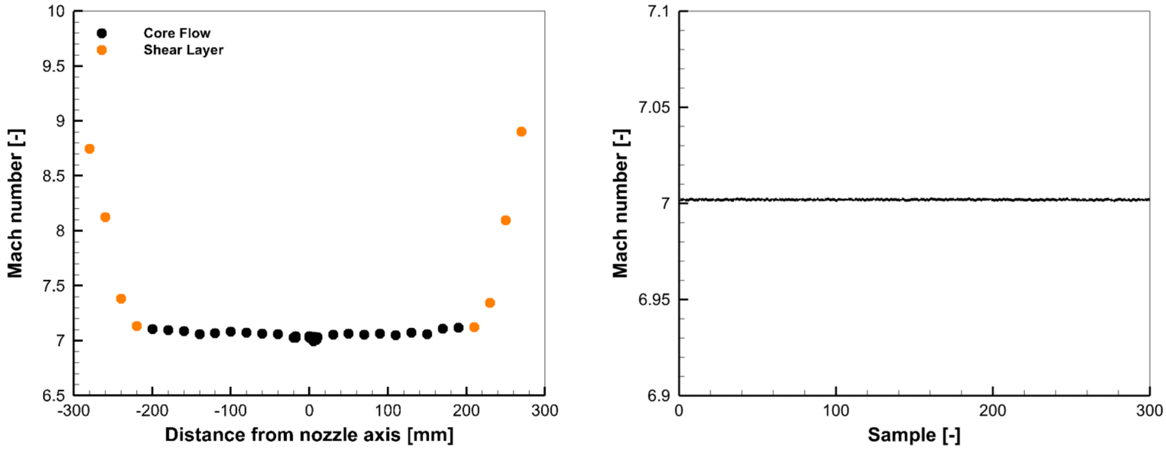

(a) Spatial distribution

(b) Temporal distribution

Figure 3.3: Free-stream Mach number distribution of Mach-7 nozzle along vertical direction at $x = 240\,\mathrm{mm}$ and $y = 0\,\mathrm{mm}$, as well as over time on nozzle axis at $x = 225\,\mathrm{mm}$, $y = 0\,\mathrm{mm}$ and $z = 0\,\mathrm{mm}$

3.4.1 Sources of Uncertainty

There are some sources of uncertainty associated with the WT experiments, which are explained in the following.

Flow Quality

The flow of the low-enthalpy facility H2K is steady for several seconds after a short period of flow establishment (see figure 2.6), whereby the steady-flow period is the relevant test time. Nevertheless, there are slight variations of the flow velocity in space and time. Based on the data of the flow characterization as described in section 2.1.2, the Mach number distribution is determined by use of the isentropic relation as in equation (2.1). Figure 3.3a presents the free-stream Mach number along the vertical direction in the vicinity of the first model trajectory. The measurement values in the shear layer show a large scatter here, while the free-stream Mach numbers in the core flow exhibit minor deviations indicating a good flow quality. On the basis of all data from the core flow, a standard deviation of 0.0242 is calculated. Because the spatial resolution of the flow characterization is smaller than the model size, 3×3 data points are used to determine the mean free-stream Mach number of the flow condition, whereby the standard deviation of the mean is 0.0081.

In order to determine the temporal deviations, the Pitot pressure on the nozzle axis was recorded in additional measurements via a pressure transducer of the Kulite® XCQ-080 series with a range of $35\,\mathrm{kPa}$ and a total accuracy of $\pm 0.1\,\%$ relative to the full-scale value. The sampling rate was $3\,\mathrm{kHz}$. The pressure signal is used to determine the total pressure in front of a normal shock using equation (2.1) and thus the unit Reynolds number in order to estimate the influence of the boundary layer in the WT nozzle on the Mach number. Figure 3.3b shows a trace of the derived free-stream Mach number on the centerline of the core flow. It is apparent that fluctuations with a standard deviation of 0.0003 appear in the course of Mach number, which also applies to the entire centerline at different axial positions. In comparison, the spatial deviation is significantly greater than the temporal deviation, so that this source of uncertainty can be neglected. In contrast to the actual free-stream Mach number of 7.000 based on the actual Reynolds number, the mean value in figure 3.3b differs by approximately 0.002 from it. This discrepancy can be explained by the thermal sensitivity of the Pitot probe provoking a zero shift in pressure signal and hence the calculated Mach number, because the stagnation temperature is significantly higher than the maximal operating temperature of 120 °C. However, this error in measurement is neglected for the determination of uncertainties, because in this case only the variance is of interest.

Structural Vibration

Great vibrations due to the flow occurs during the operation of the H2K, which are expected to be transferred to the surrounding structure of the test section. For the purpose of assessing its impact, vibration measurements with two PCB Piezotronics 352A24 accelerometers on a camera box of the stereo tracking system were conducted during the test series with single cylindrical bodies. These sensors feature a resonance frequency of 30 kHz and a linearity accuracy less than 1 %, while the sampling rate was set to 100 kHz. Figure 3.4 depicts their results of a free-flight test with and without flow measured by the accelerometer on the backside of a camera box. In the time domain, the impacts through the releases and landings of the model drops are visible in figure 3.4a. It is notable that the measured accelerations with flow are slightly higher than the signal during reference test with off-state WT and than the accuracy of the sensors. Therefore, the vibrations due to the operation of the H2K are weak, which is not surprising since a low reservoir pressure has been chosen. Based on the acceleration signal between the release and landing of the first model, a Fourier transform is carried out by the use of Welch's method [116] with several overlapping segments and Hann windows, which allows for less variance in the power spectrum. In figure 3.4b, both power spectra show a good alignment with just small deviations. However, a significant peak is identified at around 40 Hz, which only appears during on-state WT. This peak is also observed in the grey-value distributions of the point markers in the left and right camera's image series. In addition, the time series of the reference points' positions (see figure 3.5), that are placed on the ground plate of the test section, were evaluated. Their power spectra also show this dominant frequency. All of these points experience a synchronous motion, which leads to the conclusion that the stereo camera system is effected by a noticeable flow-induced vibration during the operation of the H2K. Furthermore, a local frequency peak is visible in the signal of the accelerometer with and without flow at around 100 Hz, which is produced by the cooling fans of the high-speed cameras running at a constant rotational speed. High-frequency components are not depicted in figure 3.4b and are neglected, because they cause a marginal position displacement less than or equal to 1 nm. The 6DoF motion data are also influenced by low-frequency vibration at 40 Hz, which is why a suitable post-processing for smoothing needs to be applied with the aim to damp out the unwanted signal component.

The Root-Mean-Square Deviation (RMSD) of the unsmoothed flight trajectory and attitude data were calculated based on model drops of a cylinder within the core flow and without flow in order to determine the vibrational effect on the measurement uncertainty, whereby quadratic

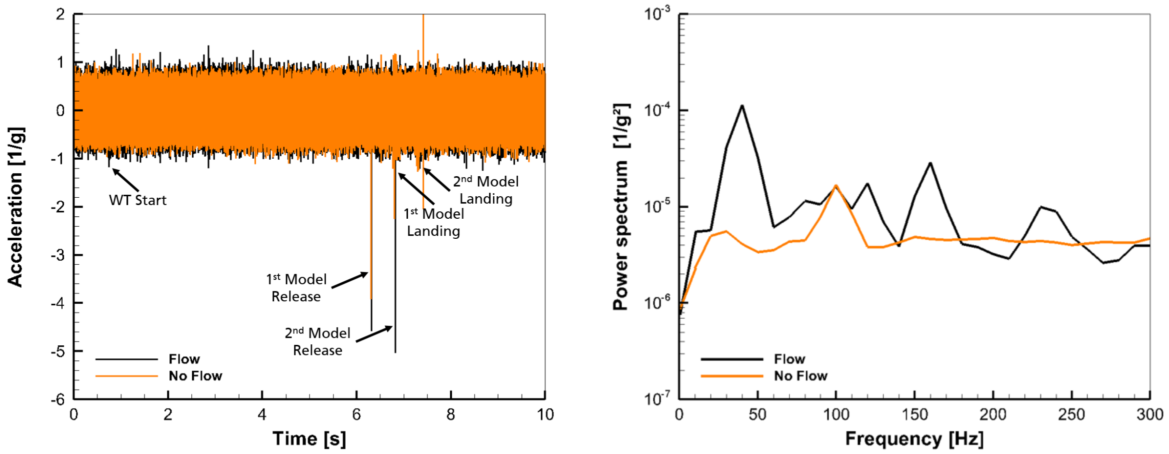

(a) Time domain **(b)** Frequency domain

Figure 3.4: Acceleration data of vibration measurement with accelerometer on the back of a camera box

and linear functions were fitted on the measurement data. If the test section is under ambient condition, the RMSD in x, y and z are $4\,\mathrm{\mu m}$, $8\,\mathrm{\mu m}$ and $9\,\mathrm{\mu m}$, respectively. This matches well with the scale deviation of the stereo tracking calibration. As soon as the flow is initiated, these deviations in position double on average as given in table 3.2. By contrast, the impact on the orientation angles due to flow-induced vibration is weaker with relative increases in the deviations of up to $25\,\%$ for φ and ϑ. These uncertainty values are representative for all performed tests.

Light Refraction

Steep density gradients appear in high-speed flow fields of blunt bodies due to flow phenomena such as shock waves, expansion fans or boundary layers. These density gradients cause deflections of light rays by refraction, which is also the effect that is used for flow visualization by means of schlieren photography. The refraction index n is defined as how quick light travels through a medium, whereby changes of this index are a measure of the changes in the angular deflection of a light ray as described by Snell's law. Equation (3.8) gives a relation between the

Table 3.2: Standard deviations of motion data from stereo tracking

	No flow	Flow
x [mm]	±0.004	±0.014
y [mm]	±0.008	±0.014
z [mm]	±0.009	±0.017
φ [°]	±0.025	±0.027
ϑ [°]	±0.012	±0.015
ψ [°]	±0.009	±0.020

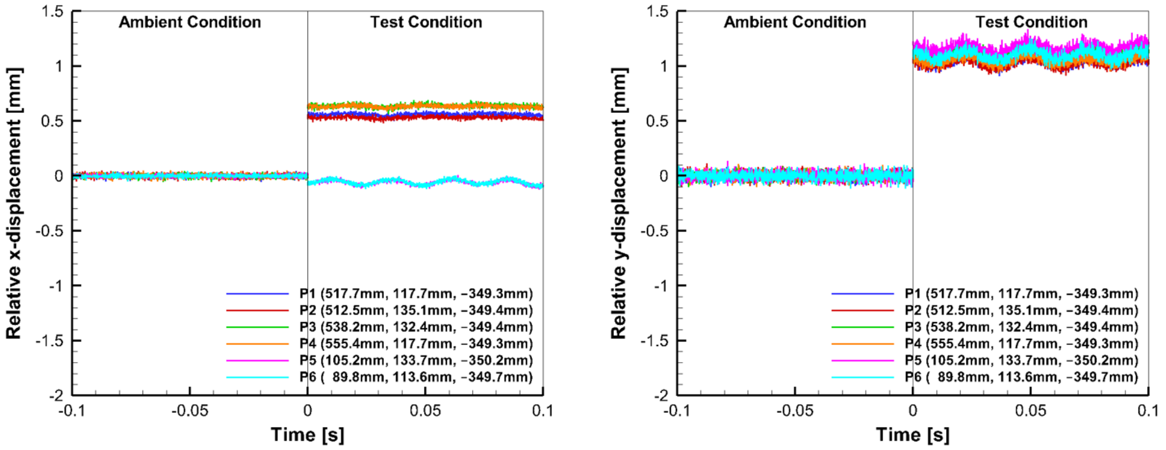

(a) X-coordinate **(b)** Y-coordinate

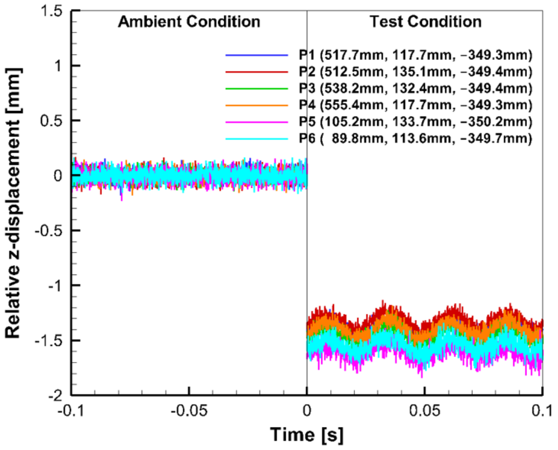

(c) Z-coordinate

Figure 3.5: Comparison of relative displacement in x, y and z between ambient and test condition of different reference points located on test section's ground plate

density and the refraction index that is valid for a compressible medium with transitions in the same fluid, where N_0 is the Avogadro number, P is the polarizability and $\mathcal{M}$ is the molar mass [8].

$$\frac{n^2 - 1}{(n^2 + 2)\,\rho} = \frac{4\pi}{3}\left(\frac{N_0 P}{\mathcal{M}}\right) \tag{3.8}$$

It follows that the refraction index alters with changes in density and polarizability. Light refraction due to aerodynamic and aerothermal effects can bias the displacement measurement of DIC measurement techniques by means of distortions in the raw images, which was observed in several studies [11, 38, 82, 105].

In the present work, the calibration of the stereo tracking system was conducted under ambient conditions, which is why optical distortion through density gradients of the flow field are not considered. Figure 3.5 shows a comparison of the relative displacement before (ambient condition) and during (test condition) the WT tests of reference points attached to the rigid plate of the test section in such a way that the stereo camera system is viewing through the free jet (see figure 2.5b). A single cylinder passes through the free jet during the test, which implies unsteady flow densities due to a changing flow field around the body. The comparison of displacement data can be used to investigate the impact of the flow field on the displacement measurement. As a result, all reference points experience constant shifts over time in x-, y- and z-coordinate up to $1.6\,\mathrm{mm}$ compared to the measurement without flow. It is notable that these shifts are not the same for all points indicating the presence of light refraction due to the flow field depending on its position, whereas the changes in the flow field caused by the test object does not seem to have a significant effect on the temporal changes in the displacement. The maximum changes in the mean distance between two reference points are roughly $\Delta x = 0.7\,\mathrm{mm}$, $\Delta y = 0.2\,\mathrm{mm}$ and $\Delta z = 0.3\,\mathrm{mm}$, whereby the range of values in x is considerably higher than in y and z. This means that the maximum changes due to light refraction are approximately three orders of magnitude lower than the overall displacements of the free-flying bodies in streamwise and vertical direction and are not relevant for the calculation of the motion derivatives. A general correlation of all components over the entire measurement volume can not be made due to the lack of spatially distributed reference points, which is why this finding is just a qualitative evidence for light refraction. Furthermore, no significant changes over time beyond the vibrational noise are observed in the present displacement data, which allows to conclude that the effect of light refraction on the relative displacement during the test can be neglected.

3.4.2 Overall Uncertainties

Just as two types of force and moment determination are employed, two different ways of uncertainty analysis are conducted in the present work to obtain the overall uncertainty of the aerodynamic coefficients. Monte Carlo simulations are performed for the stereophotogrammetry approach and the principle of Gaussian error-propagation is applied for the balance analysis approach. In the course of this, the former works with standard deviations, whereas the latter uses uncertainties. On this account, a 2-σ neighborhood is assumed for the uncertainty with $95\,\%$ confidence level, which enables a conversion between both quantities.

The uncertainties of flow parameters like Ma_{∞}, p_0 and κ are the same for both approaches. As described in section 3.4.1, the overall uncertainty of the free-stream Mach number is 0.0162. The uncertainty of the reservoir pressure is determined by the total accuracy of absolute pressure transducer having a value of $4.2\,\mathrm{kPa}$ or $2.8\,\mathrm{kPa}$, respectively (see section 2.4.1). As dried air is not an ideal diatomic gas, the assumption of a constant ratio of specific heats depends on the temperature and pressure. Hence, the absolute uncertainty is estimated here at 0.003 for the present flow conditions by means of pressure- and temperature-dependent tables from Hilsenrath *et al.* [45]. The uncertainties of the model parameters such as d, l, m and I_{yy} depend on the individual test objects. The overall uncertainty of the model size results from the manufacturing tolerance (according to DIN 5401 G100 for spheres or the measured size deviations for the other geometries) and the maximum permissible errors of the digital caliper with a value of $0.02\,\mathrm{mm}$. In addition, the varnished models have a variation in coating thickness of $0.012\,\mathrm{mm}$ (see section 2.2). The model mass was measured exactly, which is why its overall

Table 3.3: Typical standard deviations as input for Monte Carlo simulations and Gaussian error propagation calculations

	Single sphere	Single cube	Single cylinder	Tandem sphere	Tandem cube	Balance sphere
m [g]	±0.022	±0.022	±0.022	±0.022	±0.022	N/A
I_{yy} [10^{-6} kg m^2]	±0.064	±0.259	±0.563	±0.064	±0.259	N/A
κ [−]	±0.0015	±0.0015	±0.0015	±0.0015	±0.0015	±0.0015
p_0 [kPa]	±2.10	±2.10	±1.40	±1.40	±1.40	±1.40
Ma_∞ [−]	±0.0081	±0.0081	±0.0081	±0.0081	±0.0081	±0.0081
d [mm]	±0.0117	N/A	±0.0276	±0.0117	±0.0276	±0.02
l [mm]	N/A	±0.0276	±0.0276	N/A	±0.0276	N/A

uncertainty consists of the scale repeatability with $0.02\,\mathrm{g}$ and non-linearity with $0.04\,\mathrm{g}$. Since the moment of inertia is calculated from the actual mass and dimensions, its overall uncertainty results from the uncertainties of d, l and m. Typical standard deviations of single-body and multi-body experiments with free-flying and balance-mounted models are listed in table 3.3.

Stereophotogrammetry Data

Since the aerodynamic coefficients are not directly measured and are calculated from other quantities, a complex post-processing system with non-linear operations including digital smoothing and differentiation is used for the stereophotogrammetry data (see section 3.2). Numerical simulations with Monte Carlo methods are particularly suitable for this purpose, because the partial derivatives of the outputs to the motion data (or sensitivity coefficients) cannot be estimated reliably by conventional uncertainty analysis methods, especially when considering digital signal processing. However, the great advantage of these computational methods is the ability to consider partially correlated measurement uncertainties of input variables and to use a precise uncertainty estimation for non-linear systems with data manipulation [83]. The systematic uncertainties due to the use of signal processing methods cannot be taken into account.

The conducted Monte Carlo simulation can be summarized in the following steps. First, a large number of random samples is generated form the probability distributions of the input variables based on their measured values and their standard deviations as given in table 3.3. Thereby, each measurement value of the motion's time series is superimposed by a random value with its standard deviation as given in table 3.2. For the present computation, $20\,000$ samples were drawn, which guarantees a residual of the output standard deviations that is significantly lower than $1\,\%$. Second, each sample performs the deterministic computation from displacement computation to coefficient calculation as in figure 3.1, using the same settings as in the usual post-processing (see section 3.2.4). The resulting datasets of velocities, accelerations and aerodynamic coefficients are collected. Third, the standard deviations for each value in the time series are calculated for each output variable based on the large number of datasets. A sensitivity analysis showed that the free-stream Mach number and ratio of specific heats are the dominant sources of uncertainty, with the aerodynamic coefficients being very sensitive to them. For exemplary tests with tandem bodies, the results of uncertainty estimation are depicted later in figures 5.12 and 5.23 for aerodynamic coefficients, while the overall uncertainties of the motion data and derivatives are too small to be shown in exemplary plots.

Force Moment-Type Balance Data

Unlike the previous measurement technique, the aerodynamic loads are measured directly by wind tunnel balances, which is why a Gaussian error propagation approach is applied for the present uncertainty estimation. This approach allows a simple analytical calculation that is well suited for linear or quasi-linear post-processing systems. In the present uncertainty analysis, the sensitivities of the particular coefficients to the error-prone input variables as well as the respective uncertainties (see standard deviations in table 3.3) are needed to calculate the overall uncertainties. In doing so, the analysis considers the free-stream Mach number of the core flow, the reservoir pressure, the ratio of specific heats, the model diameter, as well as the force or moment, whereby the latter is determined by the balance calibration (see section 3.3.1). During the calibration, the uncertainties of different single loads on all measured force or moment components are determined, whereby the load of the normal force component is the dominant uncertainty source, here. Thus, the measurement uncertainties of all components due to the interference of the normal loads are merely considered in the following analysis except for the side force, which is based on its own load. In order to assess the uncertainties of the force or moment components, an array of various calibration loads in the range of the design limits along with the corresponding deviations are used for the interpolation of their uncertainties based on the measurement value. The sensitivities are estimated with the help of partial derivatives based on the definitions of the force and moment coefficients in section 3.1. By the use of equations (3.9) to (3.13), the partial derivatives of C_F = C_A, C_Y and C_N are calculated with F = X, Y and Z.

$$\frac{\partial C_\mathrm{F}}{\partial F} = \frac{1}{\frac{\kappa}{2} p_\infty Ma_\infty^2 S_{ref}} = \frac{C_\mathrm{F}}{F} \tag{3.9}$$

$$\frac{\partial C_\mathrm{F}}{\partial \kappa} = C_\mathrm{F} \cdot \left(\frac{\kappa Ma_\infty^2}{2\left(\kappa - 1\right)\left(1 + \frac{\kappa - 1}{2} Ma_\infty^2\right)} - \frac{\ln\left(1 + \frac{\kappa-1}{2} Ma_\infty^2\right)}{\left(\kappa - 1\right)^2} - \frac{1}{\kappa} \right) \tag{3.10}$$

$$\frac{\partial C_\mathrm{F}}{\partial p_0} = \frac{-F}{\frac{\kappa}{2} p_\infty p_0 Ma_\infty^2 S_{ref}} = \frac{-C_\mathrm{F}}{p_0} \tag{3.11}$$

$$\frac{\partial C_\mathrm{F}}{\partial Ma_\infty} = C_\mathrm{F} \cdot \frac{2Ma_\infty^2 - 4}{\left(\kappa - 1\right) Ma_\infty^3 + 2Ma_\infty} \tag{3.12}$$

$$\frac{\partial C_\mathrm{F}}{\partial d} = \frac{-2F}{\frac{\kappa}{2} p_\infty Ma_\infty^2 \frac{\pi}{4} S_{ref} d} = \frac{-2C_\mathrm{F}}{d} \tag{3.13}$$

For the moment coefficients of $C_\mathrm{M} = C_\mathrm{l}$, C_m and C_n, the partial derivatives are given in equations (3.14) to (3.18) with $M = L$, M and N.

$$\frac{\partial C_\mathrm{M}}{\partial M} = \frac{1}{\frac{\kappa}{2} p_\infty Ma_\infty^2 l_{ref} S_{ref}} = \frac{C_\mathrm{M}}{M} \tag{3.14}$$

$$\frac{\partial C_\mathrm{M}}{\partial \kappa} = C_\mathrm{M} \cdot \left(\frac{\kappa Ma_\infty^2}{2\left(\kappa - 1\right)\left(1 + \frac{\kappa-1}{2} Ma_\infty^2\right)} - \frac{\ln\left(1 + \frac{\kappa-1}{2} Ma_\infty^2\right)}{\left(\kappa - 1\right)^2} - \frac{1}{\kappa} \right) \tag{3.15}$$

$$\frac{\partial C_\mathrm{M}}{\partial p_0} = \frac{-M}{\frac{\kappa}{2} p_\infty p_0 Ma_\infty^2 l_{ref} S_{ref}} = \frac{-C_\mathrm{M}}{p_0} \tag{3.16}$$

$$\frac{\partial C_\mathrm{M}}{\partial Ma_\infty} = C_\mathrm{M} \cdot \frac{2Ma_\infty^2 - 4}{\left(\kappa - 1\right) Ma_\infty^3 + 2Ma_\infty} \tag{3.17}$$

$$\frac{\partial C_\mathrm{M}}{\partial d} = \frac{-3F}{\frac{\kappa}{2} p_\infty Ma_\infty^2 \frac{\pi}{4} l_{ref} S_{ref} d} = \frac{-3C_\mathrm{F}}{d} \tag{3.18}$$

Since the pitching and yawing moment coefficients are converted by the use of normal and side forces, the sensitivities of the moment coefficients to the forces have also to be taken into account. Its partial derivative is stated in equation (3.19), whereby x_{ref} is the distance between the model's CoG and the model's center of base plane, which is the surface in contact with the balance's adapter.

$$\frac{\partial C_\mathrm{M}}{\partial F} = \frac{-x_{ref}}{\frac{\kappa}{2} p_\infty Ma_\infty^2 \frac{\pi}{4} l_{ref} S_{ref}} \tag{3.19}$$

The results of the uncertainty analysis can be seen in figure 5.5 for an exemplary test.

3.5 Analytical Prediction

For comparison purposes, analytically determined aerodynamic coefficients under hypersonic conditions are calculated by the use of the simple modification of the Newtonian flow theory as described by Lees [63]. This hypersonic approximation enables the prediction of pressure distributions on solid bodies as a function of the local deflection angle ν between the free-stream direction and the tangent to the surface. Equation (3.20) depicts the used formula, where $c_{\mathrm{p}max}$ is the maximum value of the pressure coefficient that appears at a stagnation point downstream to a normal shock.

$$c_{\mathrm{p}} = c_{\mathrm{p}max} \sin^2(\nu) \tag{3.20}$$

This local surface inclination method is applied to a three-dimensional body, whereby ν is determined by use of the free-stream velocity as a vector $\vec{v_\infty}$ and the unit normal vector $\vec{n}$ to a surface element as in equation (3.21) from [4].

$$\sin(\nu) = \frac{\vec{v_\infty}}{|\vec{v_\infty}|} \cdot \vec{n} \tag{3.21}$$

For the test articles used in this study, it is assumed that the surface pressure distribution of windward surface elements is estimated by the Newtonian squared sine term, while the leeside elements experience a zero pressure coefficient. The flight attitude here is limited on the pitch angle like the focus of the present work. Aerodynamic coefficients are calculated by integrating the pressure coefficients of all surface elements. Based on this, analytical solutions as a function of ϑ were derived in chapter A for spheres, cubes and cylinders in this work by integrating the pressure distribution over the surface of each individual body. The results are presented below.

Due to the point-symmetric characteristic of spheres, their aerodynamic behavior features merely constant drag coefficients without a dependency of the body orientation as given in equation (3.22) (see derivation in section A.1).

$$C_{\mathrm{D}} = \frac{c_{\mathrm{p}max}}{2} \tag{3.22}$$

By contrast, the cube's aerodynamics exhibit drag and lift coefficients depending on the pitch angle as shown in equations (3.23) and (3.24) (see derivation in section A.2), whereas the pitching moment is constant zero owing to the symmetry of the surface pressure distribution with respect to the xy-, xz- and yz-plane.

$$C_\mathrm{D} = c_{\mathrm{p}max} \left(\left|\sin^3(\vartheta)\right| + \left|\cos^3(\vartheta)\right| \right) \tag{3.23}$$

$$C_\mathrm{L} = \frac{1}{2} c_{\mathrm{p}max} \sin(2\vartheta) \left(\left|\sin(\vartheta)\right| - \left|\cos(\vartheta)\right| \right) \tag{3.24}$$

In the same way, non-zero aerodynamic coefficients of cylinders are just available for drag and lift forces as can be seen in equations (3.25) and (3.26) (see derivation in section A.3), whereby a further influence factor here is the aspect ratio (l/d).

$$C_\mathrm{D} = c_{\mathrm{p}max} \left(\frac{8}{3\pi} \frac{l}{d} \left|\sin^3(\vartheta)\right| + \left|\cos^3(\vartheta)\right| \right) \tag{3.25}$$

$$C_\mathrm{L} = \frac{1}{2} c_{\mathrm{p}max} \sin(2\vartheta) \left(\frac{8}{3\pi} \frac{l}{d} \left|\sin(\vartheta)\right| - \left|\cos(\vartheta)\right| \right) \tag{3.26}$$

4 Experiments on Aerodynamics of Single Bodies

Results of several measurement series with slightly different settings are presented hereinafter to enhance understanding about the complex aerodynamic behavior of various blunt bodies in hypersonic flow fields. This chapter mainly focuses on how the body shape and inclination impacts the flow structures influencing the single-body aerodynamic forces and moments. For this purpose, the coefficients for the drag force (C_D), the lift force (C_L) and the pitching moment (C_M) relating to the pitch angle (ϑ) are investigated, whereas spanwise, roll and yaw displacements are intended to be avoided during the free-flight tests. Therefore, experimental data of spheres, cubes and cylinders are presented, addressing their flow characteristics, the reconstruction of their motions during free-flight as well as the analysis of their motion derivatives. Subsequently, the results are compared with each other with respect to the impact on the aerodynamic and stability behavior.

All measurements were conducted in H2K by use of the Mach-7 nozzle and usually the same nominal baseline test conditions of $p_0 = 520\,\mathrm{kPa}$ and $T_0 = 600\,\mathrm{K}$ (see table 2.2). Schlieren videography, stereophotogrammetry and facility instrumentation were always applied here. Please refer to chapter 2 for detailed information.

4.1 Results of Spheres

Stainless steel sphere models with a nominal diameter of $50\,\mathrm{mm}$ (see table 2.2) were employed for the present tests, whereby the full-free-flight setup with mechanical dropping system (see section 2.3) was implemented to facilitate three model drops per run.

4.1.1 Flow Topology

An exemplary sequence of schlieren images is shown in figure 4.1, which is consistent with the flow topology of blunt bodies as in the established literature [48] and described in section 1.3. The characteristic detached bow shocks of blunt bodies with round shape are apparent here. It is notable that phenomena with high density gradients like the bow shock are visible in the schlieren images, whereas low-density-gradient flow features like the wake region, compression waves and the compression shock (compare with figure 1.2) are not identifiable. The reason for this is that the sensitivity of the z-type schlieren system is too low for the prevailing free-stream density. In figure 4.1, the flow topology does not appear to change over time. Thus, it can be expected that the aerodynamics of the sphere are steady-state during the free-flight in the H2K's core flow.

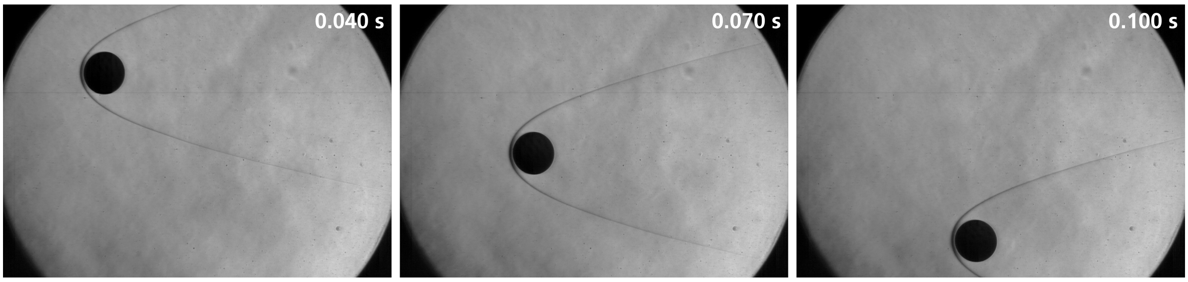

Figure 4.1: A schlieren image sequence showing the motion behavior of a sphere in free-flight

4.1.2 Model Motion

In order to assess the aerodynamic behavior of a body, the model motions of multiple WT tests are reconstructed by stereo tracking, whereby each three components of position and orientation angle are determined. Figure 4.2 shows an example for the measured displacement of a sphere configuration, whereby figure 4.2a depicts the translational displacement in streamwise (x), spanwise (y) and vertical (z) direction as well as figure 4.2b shows the angular displacement for roll (φ), pitch (ϑ) and yaw (ψ). It is expected that the motion is two-dimensional without any rotation due to the point symmetry of the model. This assumption can be confirmed with a view to the displacement data (shown in figure 4.2), whereby the roll, pitch, yaw and spanwise motion components are almost zero in contrast to the streamwise and vertical components over the entire free-flight time. In doing so, the changes in streamwise position ($\varDelta x = 198.5\,\mathrm{mm}$) and vertical position ($\varDelta z = -352.7\,\mathrm{mm}$) are about three orders of magnitude greater than the changes in spanwise position ($\varDelta y = 0.8\,\mathrm{mm}$), while the changes in roll angle ($\varDelta\varphi = 0.7°$), pitch angle ($\varDelta\vartheta = -1.0°$) and yaw angle ($\varDelta\psi = 0.6°$) are less than or equal to $1°$. These small variations in the orientation angles that exceed their measurement uncertainties can be attributed to minor disturbances during the release of the models from the dropping system in the form of friction between the model and mechanical components, which were also observed in the tests without flow. Nevertheless, all angular components as well as the spanwise position can be neglected due to the small magnitude of the changes and the motion can be assumed to be 2DoF.

Figure 4.3 provides two-dimensional flight trajectories of tests with single spheres displayed in the xz-plane referring to the center of the nozzle exit plane. In addition, the experimental data of the flow characterization (see section 2.1.2) are shown in the background, whereby the homogenous core flow is represented by the white area. From this gray contour layer, it is apparent that the majority of measurement data are within the homogenous region. All runs were carried out under the same nominal test conditions, but the model drops were performed at different times after start of WT due to multiple free-flights per run. However, one test (see cyan line in figure 4.3) was carried out at a different initial streamwise and vertical position to show that the vertical velocity of the sphere in the core flow does not affect the drag coefficient. The actual dynamic pressure shows a good repeatability with a relative difference of $\pm 1.6\,\%$. The results of the trajectory reconstruction indicate a significant streamwise acceleration of the spheres that cause an average streamwise displacement in core flow of $155.9\,\mathrm{mm}$. The trajectories of the spheres released from the same drop position clearly overlap despite the slight variation of the dynamic pressure. Thus, a good repeatability of free-flight tests despite slight

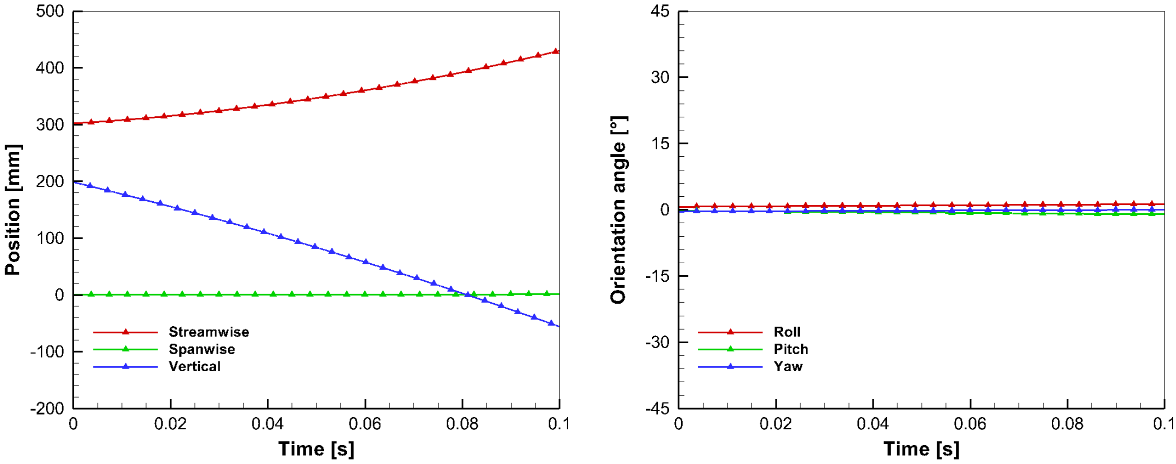

(a) Positions in x, y & z **(b)** Orientation angles in φ, ϑ & ψ

Figure 4.2: Evolution of sphere's 6DoF motion displacement in core flow referred to the FoR in figure 2.8

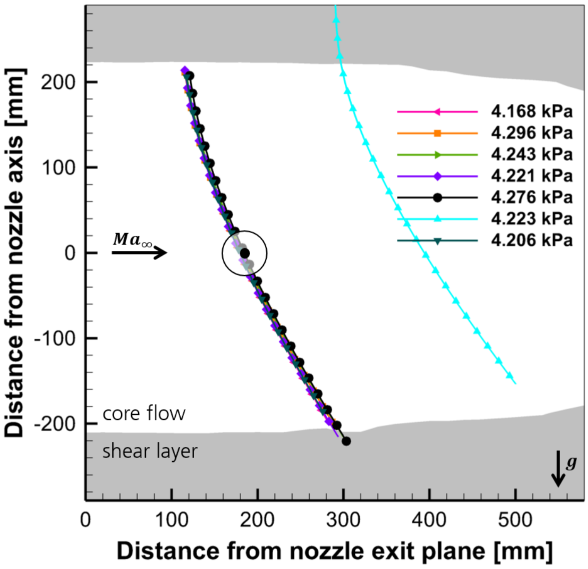

Figure 4.3: Sphere's flight trajectories of runs with the same nominal flow conditions relating to the flow regions of H2K's Mach-7 nozzle based on figure 2.2; black solid circle indicates position of the sphere at a certain moment

variations in the test conditions from run to run is demonstrated, having a relative difference in x of up to $\pm 2.1\,\%$.

Six-Degrees-of-Freedom velocities and accelerations of the same exemplary run (as of figure 4.2) are depicted in figure 4.4. As previously reported on the neglect of four motion components, the derivatives of roll, pitch, yaw and spanwise motion also confirm the previous observations, as these quantities are roughly zero over time. In terms of the angular acceleration in figure 4.4d, these quantities slightly vary around zero, whereby the fluctuations seem to be

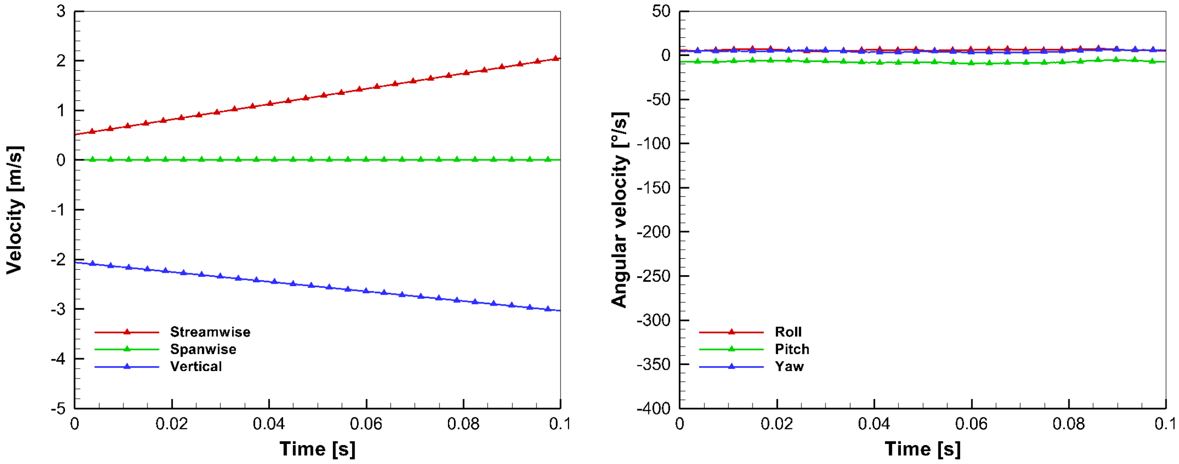

(a) Velocities in x, y & z

(b) Angular velocities in φ, ϑ & ψ

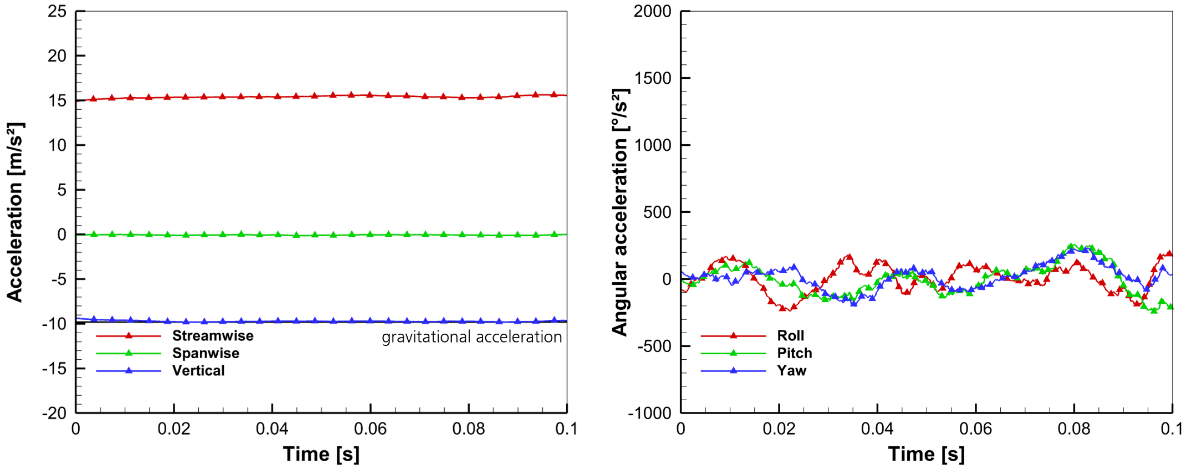

(c) Accelerations in x, y & z

(d) Angular accelerations in φ, ϑ & ψ

Figure 4.4: Evolution of sphere's 6DoF translational and angular motion derivatives in core flow

noise. Due to the higher sensitivity of the flow inhomogeneities on the angular derivatives, the roll, pitch and yaw accelerations are more strongly affected by the noise. By contrast, the translational accelerations exhibit a steadiness over the entire residence time in core flow as shown in figure 4.4c. From this chart, it can be seen that the measured vertical acceleration corresponds to gravitational acceleration within the uncertainties, which reveals the absence of lift forces as expected. Hence, the analysis of sphere's motion is focused just on the streamwise component in the following.

4.1.3 Aerodynamic Forces

The drag of spheres is obviously independent of the inclination relatively to the flow, because the geometry is rotationally symmetric regarding any axis through the CoG. By means of multiple free-flight tests in H2K, its drag coefficient was determined, which is depicted in figure 4.5 as a

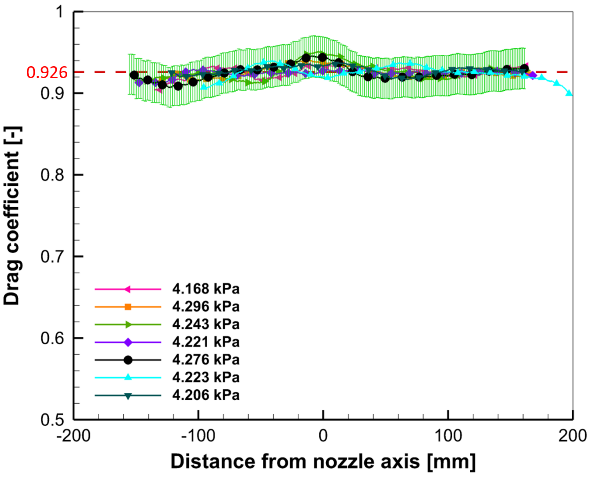

Figure 4.5: Sphere's drag coefficient in H2K's core flow including overall uncertainties for a representative test

function of the vertical position in the core flow. From this chart, it can be seen that a good repeatability is ensured and no significant deviations in the region of the core flow are apparent, except in the immediate vicinity of the nozzle axis. Here, the drag coefficient based on constant reference values for the flow is marginally higher due to slight local increases of ram pressure in the center of free jet. As illustrated by the error bars in figure 4.5, the overall measurement uncertainty for a representative test on the basis of Monte Carlo simulations is ± 0.024 (see section 3.4.2). Based on the averaged values of each dataset, the mean drag coefficient is 0.926. By use of the iterative MCMC method with normally distributed priors as described in section 3.2.5, this quantity is optimized on the basis of seven datasets with more than 1000 measurement values. Interestingly, the optimized outcome of $C_\mathrm{D} = 0.926$ is identical to the mean value having an overall uncertainty of ± 0.009 (as described in figure 3.2). Compared to the data from literature or analytical predictions, the present sphere drag coefficient exhibits a very good agreement with a deviation of $-0.4\,\%$ to Hoerner's value [48] as well as of $1.5\,\%$ to the approximation by modified Newtonian flow theory that are within the measurement uncertainty. It is somewhat surprising that such accurate value for the sphere's drag coefficient results from this simple analytical method. Such an accurate result for the sphere's drag coefficient using this simple analytical method demonstrates its suitability for simple geometries with a detached bow shock.

4.2 Results of Cubes

For the test series with cubes, the models made of structural steel have a nominal edge length of $50\,\mathrm{mm}$ (see table 2.2). The applied full-free-flight setup (see section 2.3) with an electromagnet device enables a single drop. The varied parameter in this test series is the initial pitch angle with values of $\vartheta_0 = \{-30°, -20°, 0°, 20°, 45°\}$.

4.2.1 Flow Topology

The parameter being varied in this present experimental study was the initial pitch angle ϑ_0, whereby $\vartheta_0 = 0°$ means that a plane of the cube is orthogonal to the inflow. This configuration is called plane-exposed as described in section 2.5.1. The flow field of a plane-exposed cube is shown in figure 4.6, where figure 4.6a presents a comparison of the experimental with computational schlieren representation based on numerical results and figure 4.6b depicts the experimental schlieren photograph with a schematic description of the aerodynamic phenomena. The numerical results originate from three-dimensional viscous laminar simulations with TAU from [39] and represent the absolute density gradient at the central plane. In figure 4.6, the hypersonic flow is compressed in front of the cube developing a bow shock. In the region of the stagnation streamline, this shock is normal. The stagnation streamline experiences the maximal deceleration. Moreover, the bow shock becomes more oblique downstream with lessening strength ending in an infinitely weak Mach wave, as can be seen in the schlieren photograph. In comparison to the bow shock shape of a sphere as depicted in figure 4.1, the shock in front of the cube is more planar due to the strong deceleration of the flow over a wide frontal area. Between the bow shock and the face area, a thin broad subsonic region enables a strong outward deflection of the flow, which corresponds to the numerical results by [39] as shown in figure B.1a. The sonic line in figure 4.6b encloses this area (see also streamlines in figure B.1a). Afterwards, the flow is deflected in the opposite direction and accelerated by an expansion fan originating from the edge (see figure 4.6a). At this point, the flow is not able to follow the contour resulting in very small separation bubble similar to the separation with reattachment downstream of a backward-facing step as in Halupovich *et al.* [40]. Yet, the separation bubble is difficult to identify in the schlieren representations due to its small size. A weak reattachment shock, which is visible in both representations of figure 4.6a, realigns the streamlines to the contour. However, since the flow upstream the separation is supersonic, it is expected that a separation shock occurs here to deflect the flow. This separation shock appears to merge with the reattachment shock on the schlieren images due to the very short length of the separation bubble, which is why only one shock can be seen in figure 4.6a. Further downstream, a second expansion fan at the trailing edge (see figure 4.6a) causes an inward flow towards the region behind the cube leading to an acceleration and separation of the flow. The resulting wake region with recirculating flow narrows with larger distance to the rear. At its shear layer, compression waves appear due to its concave shape resulting in an oblique shock at their intersection.

For an edge-exposed cube, figure 4.7 presents the flow field as a comparison of the experimental and numerical results in figure 4.7a as well as a description of the flow topology in figure 4.7b. This flow field shows nearly the same aerodynamic phenomena as for the plane-exposed configuration with exception of some characteristics on the forebody. On the leading edge, the bow shock is detached with a small non-zero shock stand-off distance, because the $45°$ inclination angle of upper and bottom side is higher than the maximal flow deflection angle for the present Mach number at which an oblique shock can form (see θ-β-M diagram in [5]). Downstream, there is a narrow elongated subsonic region that extends over the entire surface of the two leading planes. The size of the subsonic region can be derived from the Mach number distribution in figure B.1b based on TAU simulations by [39]. Further downstream of the stagnation point, the shock wave appears oblique until it interacts with the expansion fans

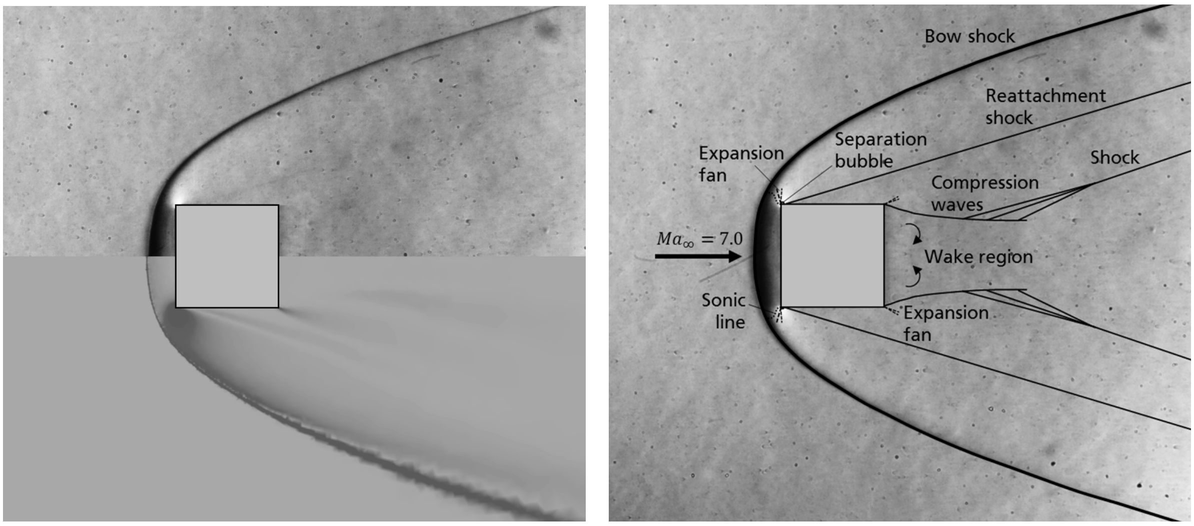

(a) Experimental versus numerical results **(b)** Experimental result

Figure 4.6: Qualitative flow field of one cube's base is exposed to the flow; numerical outcome taken from [39]

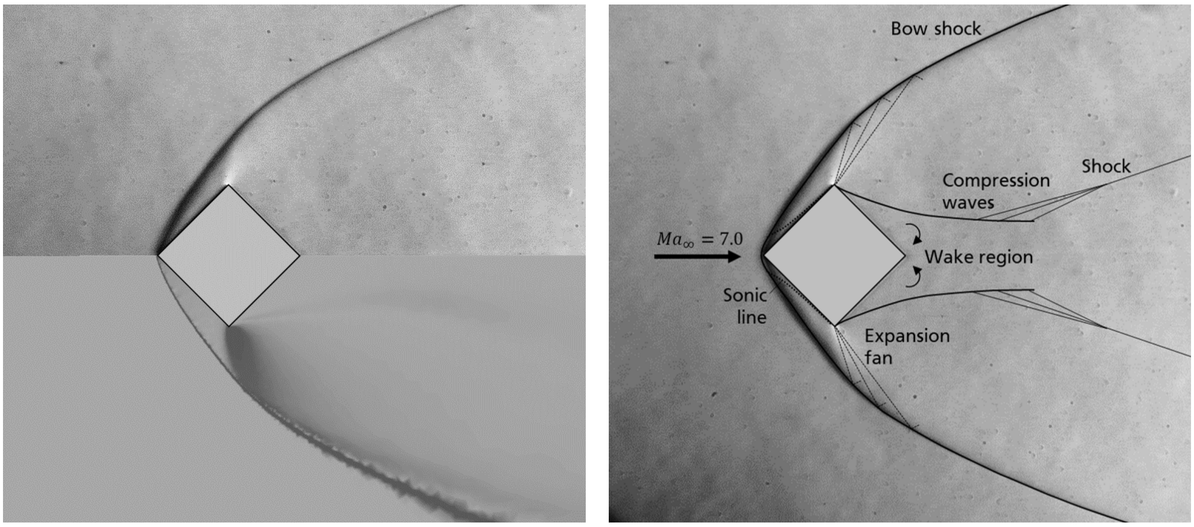

(a) Experimental versus numerical results **(b)** Experimental result

Figure 4.7: Qualitative flow field of one cube's edge is exposed to the flow; numerical outcome taken from [39]

from the top and bottom edge resulting in a bending of the shock over the length of interaction. The reflecting expansion waves are not visible on the schlieren image as they are to weak. Moreover, no separation bubbles with subsequent reattachment shocks arise. In comparison to the plane-exposed cube, this orientation exhibits higher bow shock radii further downstream.

Figure 4.8 illustrates sequences of schlieren images from several model drops with different initial pitch angle. These configurations were chosen to cover a broad range of pitch angles during free-flight as well as to avoid complications of additionally induced roll or yaw rotations. The duration between the first and last image of each series is $3/50\,\mathrm{s}$, while the test article is passing the core flow. The runs of figure 4.8 show a counterclockwise body rotation initiated by traversing the shear layer. While entering the upper shear layer, the test object experiences a negative pitching moment because of increasing stagnation pressure resulting in an asymmetric surface pressure distribution with a higher ram pressure on the lower body part (compare with $p_r/p_{r,t}$ in figure 2.2). This is quite different for $\vartheta_0 = -30°$ and $\vartheta_0 = -20°$ (shown in figures 4.8a and 4.8b) as the pitch seems to be constant because of an additional oppositely turning moment provoked by the angular position with respect to the flow direction. Thus, the rotation of cubes in the present measurements is determined by two effects: shear-layer-initiated as well as body-orientation-initiated aerodynamic moments. Moreover, no obvious rolling or yawing motions appear in these schlieren images.

In figure 4.8, the flow structures exhibit always detached bow shocks whose shape depends on the flow angle relatively to the cube. This happens, because the required flow deflection angle, to follow the contour, of one or both front planes is larger than the maximum possible value for $Ma_\infty = 7.0$. For more plane-exposed models, a bended shock appears with a great shock stand-off distance like in figure 4.8d. By turning the leading edge more into the flow, this stand-off distance decreases and the shock becomes oblique at some point (visualized in figures 4.8b and 4.8e). Furthermore, low-density regions occur at the body edges due to expansion coming from the deflection and consequently an acceleration of the flow. These expansion fans interact with the bow shock resulting in a curvature of the shock wave. Closely downstream of the leading edge, a second weak oblique shock becomes visible in some configurations (e.g. figures 4.8c and 4.8d). This reattachment shock is merging downstream with the bow shock.

4.2.2 Model Motion

The reconstruction of the rigid body motion by stereo tracking allows for determining the three-dimensional single components of position and orientation angle. As an example, figure 4.9 shows the angular (roll, pitch and yaw) and translational (streamwise, spanwise and vertical) displacements of a rotating cube configuration with an initial pitch angle of $20°$. Because of the mirror-symmetrical shape of this model, the motion behavior is as expected two-dimensional. As there is neither initial roll nor initial yaw angle, the body experiences merely a streamwise ($\Delta x = 167\,\mathrm{mm}$) and a vertical ($\Delta z = -369\,\mathrm{mm}$) movement as well as a pitch rotation ($\Delta\vartheta = 35°$). However, the spanwise ($\Delta y = -2\,\mathrm{mm}$), roll ($\Delta\varphi = 2°$) and yaw ($\Delta\psi = -2°$) motion components are almost constant and close to zero. Here, the change in pitch angle is 23 times and 17 times higher than the total roll and yaw displacement respectively (see figure 4.9). Therefore, the subsequent analysis treats the motion as 3DoF and neglects the out-of-plane motion (roll, yaw and spanwise displacement).

All two-dimensional CoG trajectories in x- and z-direction relatively to the center of the nozzle exit plane are plotted in figure 4.10 showing the distinct flow regions of the free jet at $Ma_\infty = 7.0$ as a gray contour layer, as well. As expected, the cube experiences a streamwise acceleration. The most visible feature of figure 4.10 is that the flight trajectories are close together, whereby the streamwise displacement in the core flow ranges between $167\,\mathrm{mm}$ (green line) and $203\,\mathrm{mm}$ (pink line). These results are somewhat unexpected, as the configurations with the largest frontal area have the lowest streamwise displacement. However, these extreme values do not permit a proper qualitative comparison with respect to the drag because the residence time in

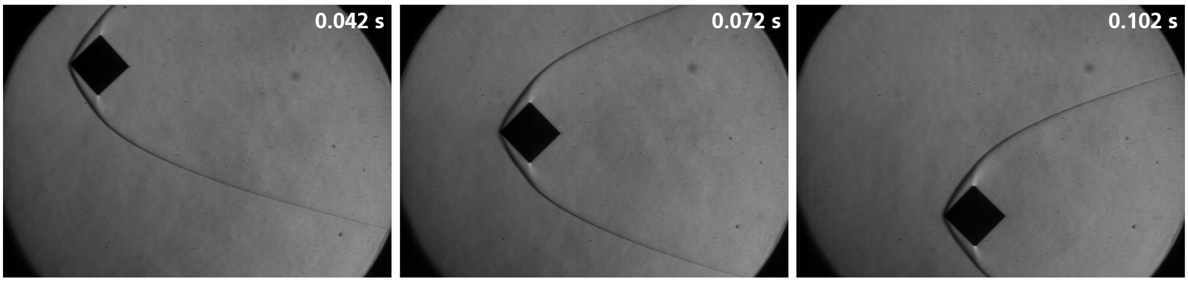

(a) $\vartheta_0 = -30°$

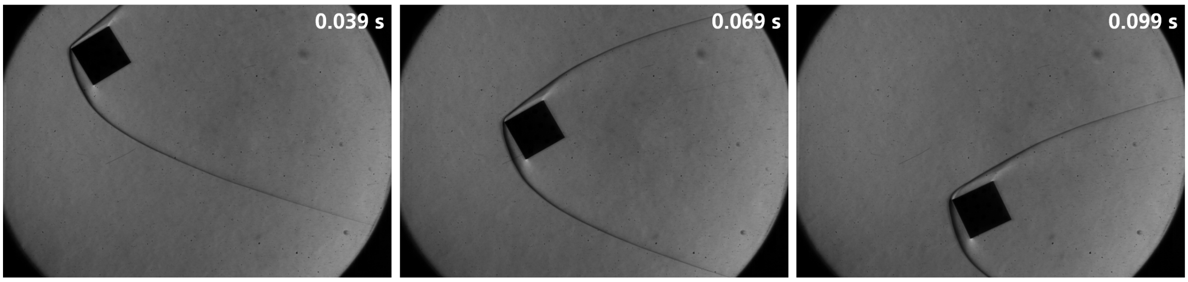

(b) $\vartheta_0 = -20°$

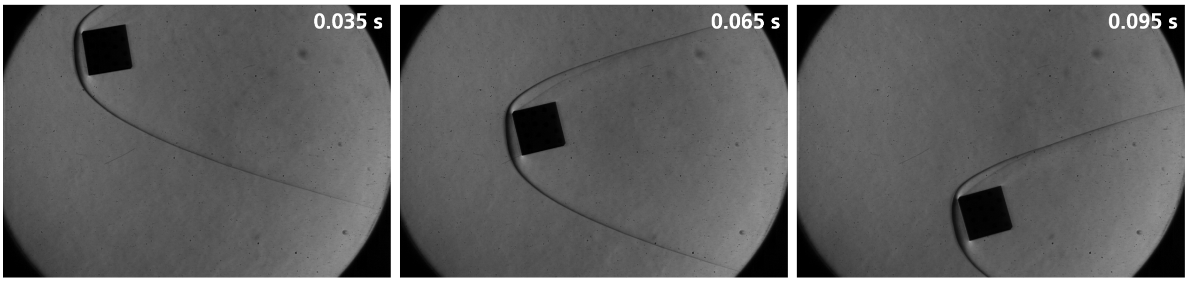

(c) $\vartheta_0 = 0°$

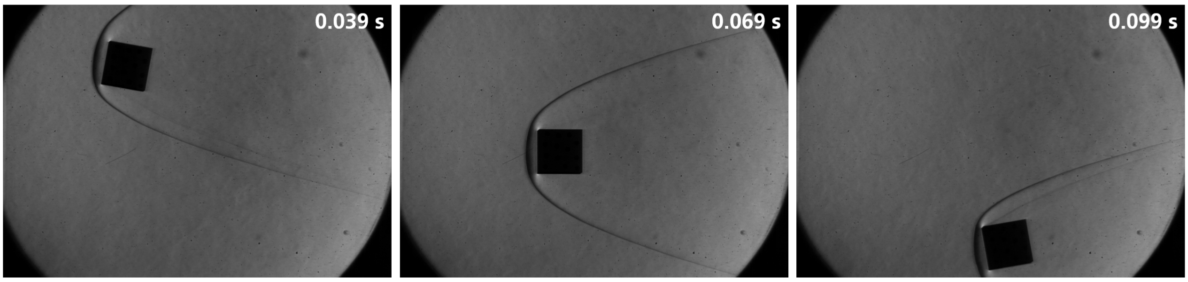

(d) $\vartheta_0 = 20°$

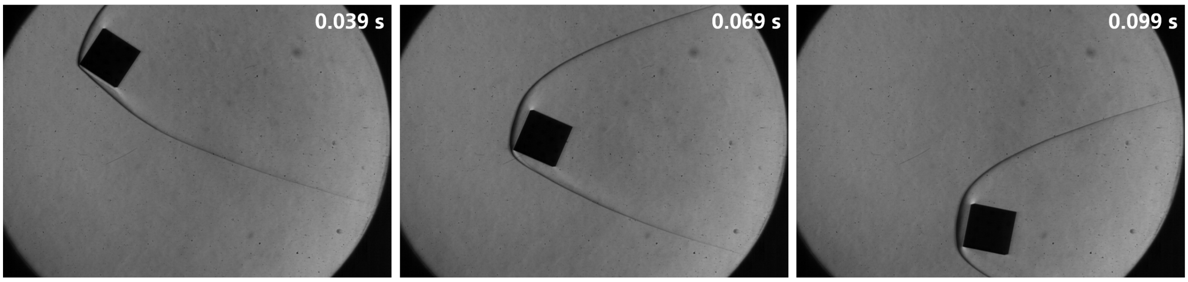

(e) $\vartheta_0 = 45°$

Figure 4.8: Selection of schlieren image sequences showing the motion behavior of a cube in free-flight with different initial pitch angle

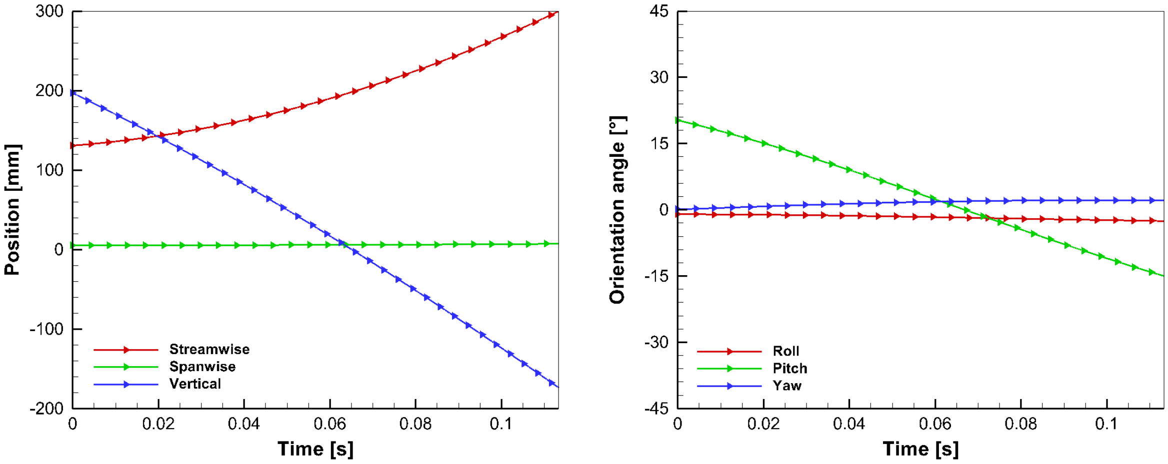

(a) Positions in x, y & z **(b)** Orientation angles in φ, ϑ & ψ

Figure 4.9: Evolution of cube's 6DoF motion displacement in core flow with $\vartheta_0 = 20°$

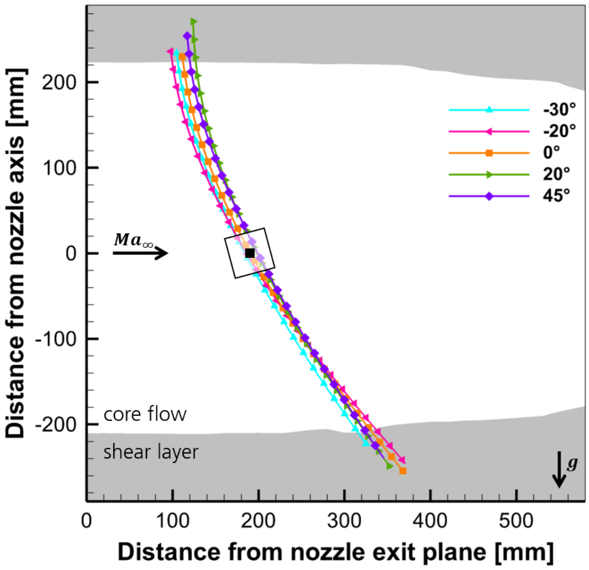

Figure 4.10: Cube's flight trajectories of runs with different initial pitch angle relating to the flow regions of H2K's Mach-7 nozzle based on figure 2.2; black solid square indicates position of the cube at a certain moment

the jet core of all runs are different varying between 113 ms (green line) and 126 ms (pink line). It is therefore necessary to analyze the single components of the motion derivatives in relation to the flight attitude, which will be discussed later.

The absence of roll, yaw and spanwise motions also appears in the derivatives of figure 4.11 as they are roughly zero over time. But it is notable that the yaw velocity in figure 4.11b is about 30 °/s at the beginning, though it tends to zero afterwards. A reasonable explanation for this initial velocity may be the inhomogeneity of the jet shear layer. Although the performance was not perfect, this discrepancy is considered as insignificant due small absolute changes in angle

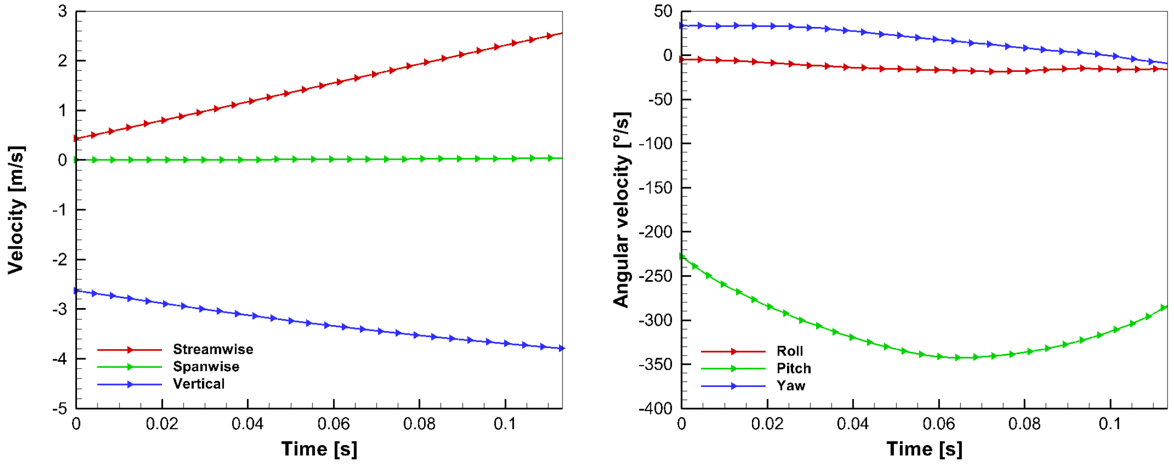

(a) Velocities in x, y & z **(b)** Angular velocities in φ, ϑ & ψ

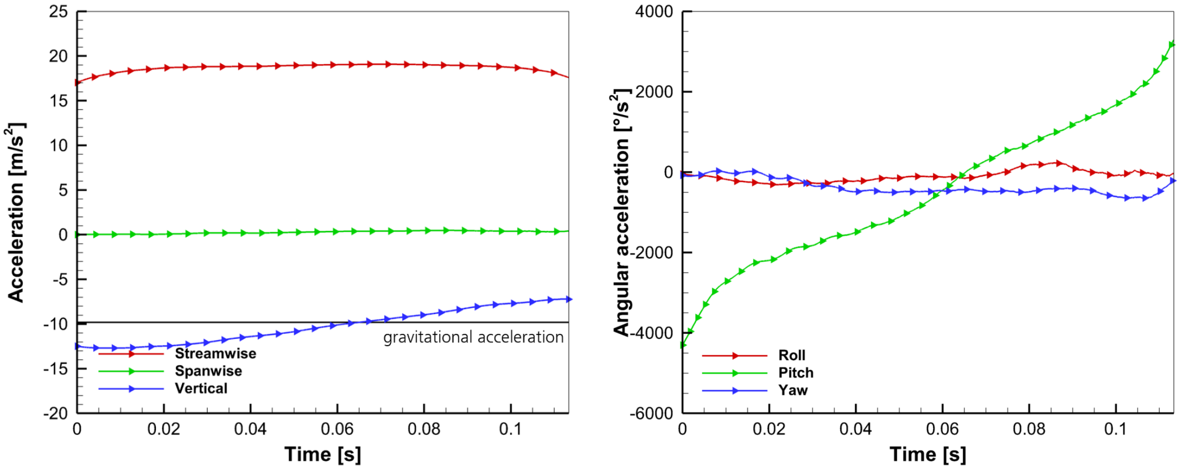

(c) Accelerations in x, y & z **(d)** Angular accelerations in φ, ϑ & ψ

Figure 4.11: Evolution of cube's 6DoF translational and angular motion derivatives in core flow with $\vartheta_0 = 20°$

of $2°$ as previously mentioned. The other motion components (streamwise, vertical and pitch) experience high accelerations up to $19\,\mathrm{m/s^2}$ for translation (see figure 4.11c) and $4300\,°/\mathrm{s}^2$ for rotation (see figure 4.11d). Moreover, a significant difference between the measured vertical and theoretical gravitational acceleration is visible in figure 4.11c, which suggests the occurrence of lift forces. Overall, these results verify the assumption that the subsequent analysis of forces and moments can be restricted to streamwise, vertical and pitch motion.

4.2.3 Aerodynamic Forces & Moments

In this section, the resulting motion derivatives are described. Figure 4.12 shows the force coefficients in streamwise (drag) and vertical (lift) direction as well as the moment coefficient around the spanwise axis (pitching). According to the results of the Monte Carlo simulation as in section 3.4.2, the estimated average uncertainties with respect to the maximum values

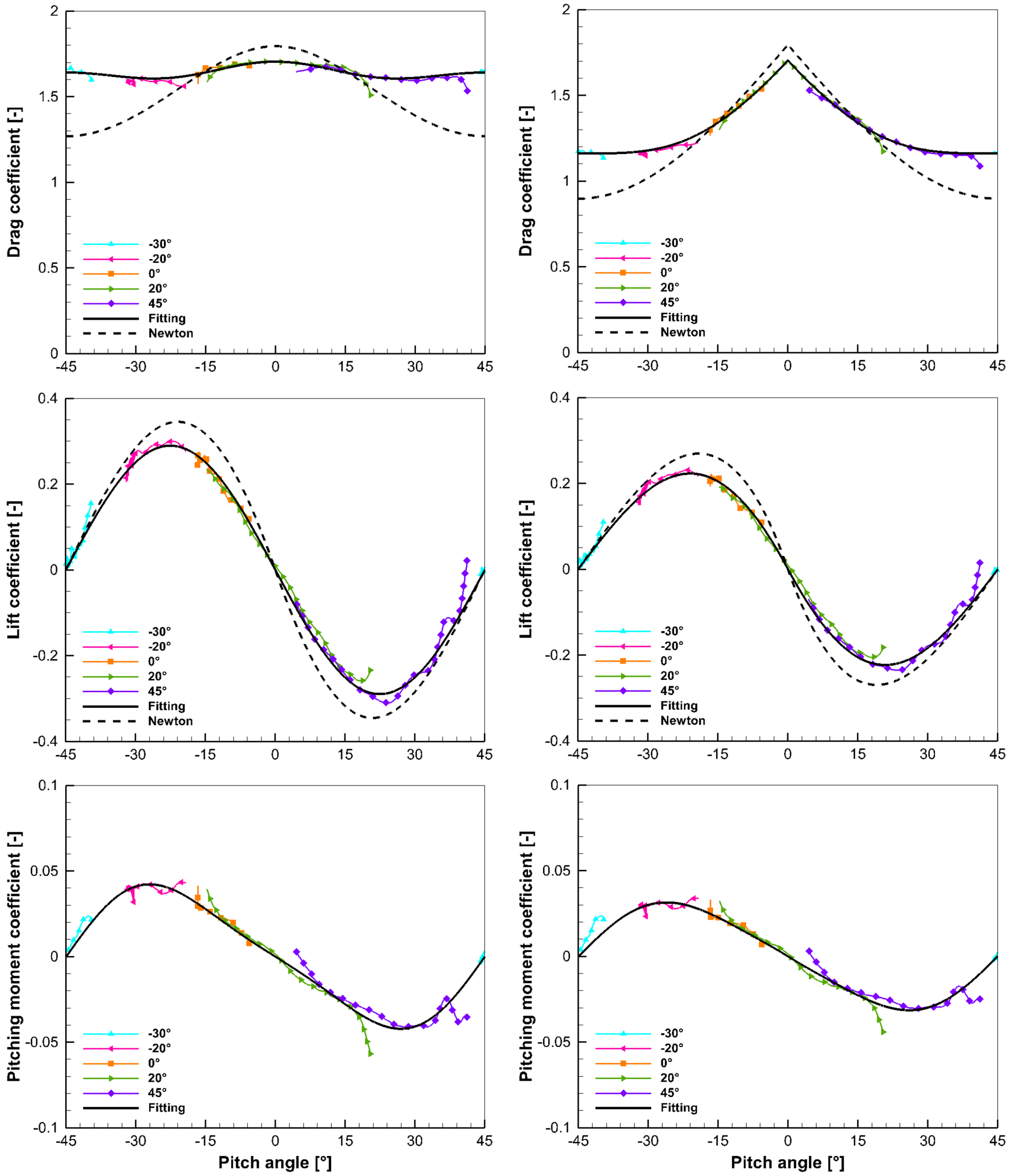

(a) Square base reference area ($S_{ref} = l^2$) **(b)** Projected reference area ($S_{ref} = f\left(l,\vartheta\right)$)

Figure 4.12: Influence of the pitch angle on cube's aerodynamic coefficients based on experimental data with different initial orientations

are $3\,\%$ for C_D, $8\,\%$ for C_L and $1\,\%$ for C_M. The aerodynamic coefficients are calculated by applying equations (3.1) and (3.2) with differently defined reference areas: a constant square base (figure 4.12a) and a pitch-angle-dependent projected frontal area (see figure 4.12b). The latter is determined by the use of equation (4.1).

$$S_{ref} = l^2 \left(\left|\sin\left(\vartheta\right)\right| + \left|\cos\left(\vartheta\right)\right|\right) \tag{4.1}$$

Additionally, trigonometric functions are fitted on these post-processed data by the method of least absolute residuals, as this is less sensitive to the presence of outliers than the more commonly used method of least squares regression. The reason for this choice of method is to weaken the effect of the measurement deviations at the dataset boundaries on the peak values of the fitting curves. For comparison, analytical curves based on equations (3.23) and (3.24) are added to the plots, which are determined by the modified Newtonian law as in [63].

The cube's symmetry allows to extend the results of pitch angles between $-45°$ and $45°$ on its aerodynamic characteristics at all inclinations, whereby an entire period of $90°$ is considered by amalgamating the measurement data of all cube configurations. As assumed by Hansche and Rinehart [41], the drag coefficient depends on the cube's flight attitude. This relationship is demonstrated in the plots of the aerodynamic coefficients versus the pitch angle (see figure 4.12), whose data are unprecedented and offer the first insights of their kind. The experimental drag coefficient based on a constant reference area has its global maximum of $C_{\mathrm{D}} = 1.71$ at $\vartheta = 0°$ and its local maxima at $45°$ and $-45°$ (see figure 4.12a). Compared to the already mentioned drag coefficient of $C_{\mathrm{D}} = 1.66$ from Hoerner [48], the mean value of the present study with $C_{\mathrm{D}} = 1.64$ corresponds quite well with a derivation of $-1.2\,\%$. Unlike a constant value, the drag is obviously a periodic function of the pitch angle. Moreover, lift forces and pitching moments arise just for non-zero angles as well as these quantities correlate periodically with the pitch angle. Their coefficients range roughly between -0.31 and 0.30 for C_{L} as well as between -0.06 and 0.04 for C_{M}, having continuous curve progressions with minima and maxima. Both therefore have characteristics of negative sine functions.

By means of Fourier series, trigonometric functions with a period of $90°$ are fitted on the indirectly measured aerodynamic coefficients as described in section 3.2.5. This implies that the angular frequency of each Fourier term is an integer multiple of 4. However, the high-order terms are neglected due to extremely low Fourier coefficients. The resulting regression functions are given in equations (4.2) to (4.4).

$$C_{\mathrm{D}} = 1.641 + 0.032 \cdot \cos\left(4\vartheta\right) + 0.031 \cdot \cos\left(8\vartheta\right) \tag{4.2}$$

$$C_{\mathrm{L}} = -0.290 \cdot \sin\left(4\vartheta\right) \tag{4.3}$$

$$C_{\mathrm{M}} = -0.040 \cdot \sin\left(4\vartheta\right) + 0.008 \cdot \sin\left(8\vartheta\right) \tag{4.4}$$

For the drag coefficient, the cosine function in equation (4.2) is an approximation of the measurement values with a standard deviation of 0.016. On the basis of a constant reference area in figure 4.12a, the drag coefficient has a maximum of 1.704 for a plane-exposed configuration and a minimum of 1.606 at a pitch angle of $\vartheta = \pm 26°$. It follows that the face-on cube (with $S_{ref} = l^2$) by Hoerner [48] is underestimated with a deviation of $2.7\,\%$. Contrary to expectations, a second local maximum with $C_\mathrm{D} = 1.637$ appears for an edge-exposed configuration. Several factors could explain this outcome. First, the detachment condition of the shock wave is fulfilled here for both the upper and bottom side. Furthermore, the edge-exposed cube has the largest frontal area of all pitch configurations. By contrast, the modified Newtonian analysis depicts only the global maximum. However, the deviation between the analytical and experimental drag coefficient is significant with a maximum absolute deviation of -0.368 for $\vartheta = \pm 45°$. There are several possible explanations for this discrepancy. First, the modified Newtonian flow theory is based on the assumption of a normal shock for the maximum pressure as described in section 3.5, which makes it particularly well suited for detached bow shocks. In contrast, the edge-exposed configuration exhibits a less detached bow shock (see figure 4.7). Second, the Newtonian flow theory assumes that the normal component of the flow's momentum is transferred to the force acting on the surface, while the tangential component is neglected. For the edge-exposed cube, the bow shock causes a strong deflection of the flow upstream of the body (see streamlines in figure B.1b) in contrast to the plane-exposed configuration with a more detached and less oblique bow shock ahead of the body (see streamlines in figure B.1a). As a result, the flow angle of the freestream and that within the stagnation region exhibit significant differences for edge-exposed cubes.

Turning now to the approximation of the lift coefficient. Only the amplitude of the trigonometric function is considered in the regression analysis of equation (4.3), while the phase angle and constant of the sine function are zero. This is reasonable due to the previously shown tendencies of the measurement values and the fact that no lift is to be expected for mirror-symmetrical flight attitudes such as $\vartheta = 0°$ and $\vartheta = \pm 45°$. Here, the approximation of the lift coefficient has a standard deviation of 0.014 and extreme values at ± 0.290, which is reached at the angle bisector ($\vartheta = \pm 22.5°$) of the mirror-symmetrical orientations. This extreme value is $17.0\,\%$ of the maximum drag coefficient. Hence, the lift component should also be taken into account for the motion modeling of rotating cubes as it cannot be neglected. The modified Newtonian flow theory partly shows a significant deviation from the experimental results for the lift coefficient. The maximum absolute deviation is 0.057 for $\vartheta = \pm 21°$.

Equation (4.4) describes the relationship of the pitch angle and its moment coefficient. The standard deviation of fitting function is 0.004. It is noticeable that the pitch angle with the maximum moment occurs at $\vartheta = \pm 27°$ and not at the angle bisector as with the C_L-function. In order to understand its causes, the distributions of surface pressure and skin friction have to be considered, but these are not available for the present study.

Slight deviations between the experimental results and their fitted curves can be seen in figure 4.12, which are mainly due to marginal roll and yaw angles as mentioned in section 4.2.2, as well as errors that become visible after post-processing. Especially, the boundaries of each dataset show higher discrepancies. The reason for this is that the tracked object is located at the edges of the field of view. Thus, fewer marker points are detected for an accurate geometry fitting as well as the position determination of these point centers has a higher measurement uncertainty. In addition, the aforementioned causes of discrepancies are exacerbated by a lower luminous intensity for the stereo camera system at the borders. As a consequence, the error-prone displacement computation leads to deviations in the reconstruction of the model motion.

It was shown previously in this study that the pitch angle has a weak effect on the drag coefficient with regard to a constant square base reference area. By referring to a pitch-angle-dependent parameter, figure 4.12b takes the aerodynamically effective frontal area into account. In doing so, the effect of attitude on the drag is clearly visible. The maximum remains the same for a plane-exposed cube (as the reference area is the same) while the minimum of $C_\mathrm{D} = 1.160$ for an edge-exposed body is $29.1\,\%$ below the value related to the square base area (as the reference area is increased by $41.4\,\%$). Additionally, the above value of an edge-exposed cube is $1.4\,\%$ lower than Hoerner's drag coefficient with $C_\mathrm{D} = 1.177$ related to the same projected frontal area of $S_{ref} = \sqrt{2}l^2$ [48]. In general, considering the frontal area affects an absolute decline in the aerodynamic coefficients, while the zero and extreme values occur at the same angles, except for the minimum of the drag coefficient. Expressed in relative figures, the maximum lift force and pitching moment coefficients are $23.5\,\%$ and $25.6\,\%$ below the values with constant reference area respectively. The approximation functions of the aerodynamic coefficients referred to a projected frontal area are determined by using equations (4.2) to (4.4) and dividing each of them by the trigonometric terms of equation (4.1), where the square base reference area with l^2 cancels out.

To summarize the relationships between aerodynamic coefficients and pitch angle, figure 4.13 depicts their functions from the curve fitting for a single period as well as the position of the stable trim point. Here, the equilibrium of moments ($C_\mathrm{M} = 0$) is ensured for two orientations: plane-exposed with $\vartheta = 0°$ and edge-exposed with $\vartheta = \pm 45°$. Looking at the profile of the pitching moment coefficient, the conditions for a stable trimmed flight are fulfilled, if an opposite moment is the response to an angle surge ($\partial C_\mathrm{M}/\partial\vartheta < 0$) in addition to the equilibrium of moments. As a result, the trim point is stable when one plane of the cube is exposed to the flow and unstable when one edge is exposed to the flow.

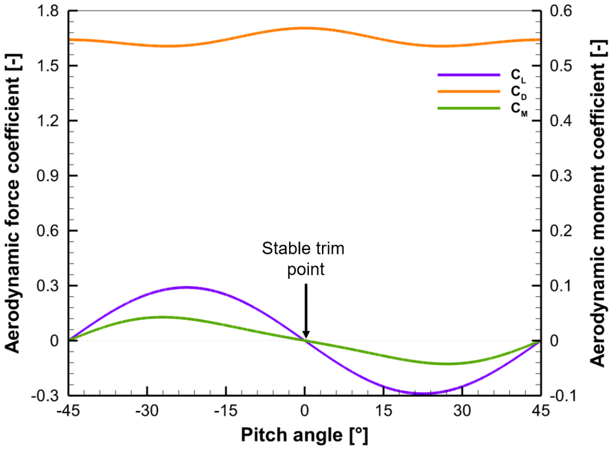

Figure 4.13: Static stability of cubes depending on pitch angle

4.3 Results of Cylinders

For the experiments in this section, cylindrical bodies with nominal values of $d = 50\,\mathrm{mm}$ and $l = 100\,\mathrm{mm}$ (see table 2.2) were employed. The full-free-flight setup (see section 2.3) here was adapted to two model drops by use of several electromagnets. Unlike the other test series, the reservoir pressure was set to $480\,\mathrm{kPa}$, as explained in section 2.1.1. It is not expected that the lower reservoir pressure and thus the lower free-stream Reynolds number have an influence on the aerodynamic coefficients and the flow topology. This can be justified with the Mach number independence principle for viscous flows and adiabatic walls according to Kliche *et al.* [53], since a variation of the free-stream Reynolds number has no significant influence on the aerodynamic coefficients. The initial pitch angle was specified as values of $\vartheta_0 = \{-10°, 0°, 5°, 10°, 30°, 50°, 70°, 90°\}$ in this study.

4.3.1 Flow Topology

The primarily examined parameter in this section is the pitch angle ϑ. A value of $\vartheta = 0°$ here means that the flat base of cylinder is orthogonal to the inflow as described in section 2.5.1. A visualization of the density gradients in x-direction of this base-exposed attitude under the equal flow conditions is depicted in figure 4.14a presenting the flow structures around the body. The upper part of figure 4.14a shows the integrated density gradient through the fluid domain in the schlieren image from free-flight tests, whereas the lower part depicts the computational image of the gradient merely on the central plane coming from viscous turbulent DES simulations by US3D assuming a reservoir pressure of $520\,\mathrm{kPa}$ [101]. This is intended just as a qualitative comparison of the flow fields, whereby both feature a detached bow shock, an expansion fan on leading edge and a high-density flow region in front of the cylinder. In addition, an expansion fan on the trailing edge followed by flow separation as well as shocks at the body's lateral surface downstream the leading edge and also at the shear layer of the wake region are just visible in the computational image, which are not visible on the schlieren image due to the low sensitivity of the schlieren system on free-stream density. In doing so, the schlieren setup was optimized for the visualization of the bow shock. Overall, the flow fields of experimental and computational image show a very good agreement, whereby the bow shock shape and stand-off distance seem to be identical.

A sketch of the supersonic flow phenomena with the corresponding schlieren photograph in the background is shown in figure 4.14b. The uniform incoming hypersonic flow first experiences a sudden deceleration by a bow shock in front of the cylinder. At a sufficient stand-off distance ahead of the stagnation point, this shock is normal and extends around the cylinder as a bended oblique shock reducing to a Mach wave further downstream, as can be seen in the schlieren photograph. On the streamline upstream of the stagnation point, the flow deceleration is maximal leading to a subsonic flow (see figure B.2a). The entire narrow region between the bow shock and the flat frontal area is subsonic (as indicated by dark gray in the experimental schlieren image), which facilitates a strong outward flow deflection. In this region, the flow begins to accelerate becoming supersonic at the sonic line. With proceeding acceleration, an expansion fan, coming from cylinder's leading edge (see figure 4.14b), causes a deflection of the flow. The flow is incapable to follow the contour at this point, which is why the boundary layer

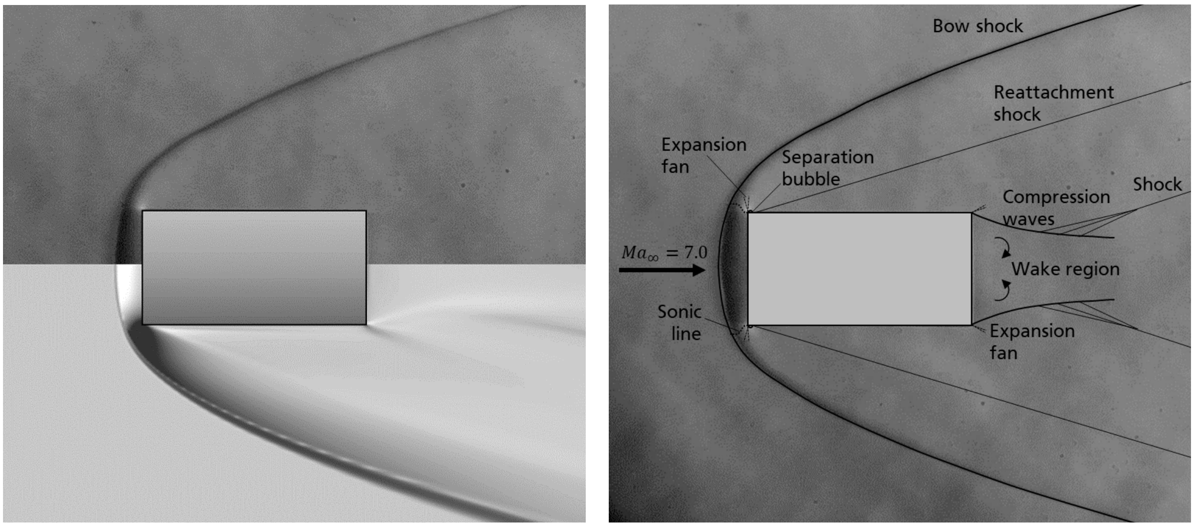

(a) Experimental versus numerical results

(b) Experimental result

Figure 4.14: Qualitative flow field of one cylinder's base is exposed to the flow; numerical outcome taken from [101]

separates and reattaches immediately afterwards to form a tiny separation bubble. This flow phenomenon is visible neither in the numerical nor in the experimental schlieren representation and is deduced from the presence of the visible upstream shock in figure 4.14a. The type of separation is called shoulder separation as described by Kaufman II *et al.* [50], which is caused by an adverse pressure gradient immediately downstream the leading edge resulting from recompressions of the flow. Such a separation on the cylinder's lateral surface was also observed by Matthews and Eaves Jr. [74]. Downstream of the reattachment, the flow turns back to a direction approximately parallel to the body contour by an oblique reattachment shock as shown in the numerical schlieren representation. In addition, a separation shock occurs upstream of the separation bubble as shown in [74], yet it merges with the reattachment shock, so that only a single shock can be seen on the schlieren representation. At the trailing edge, the flow accelerates and deflects inwards by a second expansion fan (see figure 4.14b) causing an extended region of separated flow. Subsequently, a wake region with recirculating flow arises, which becomes narrower with larger distance to the base. At the shear layer of the cylinder's wake, compression waves emerge due to its concave shape forming an oblique shock at their intersection.

The motion behavior of several drops with different initial pitch angle are qualitatively depicted in figure 4.15, whereby the duration between the first and last image of each sequence is $3/50\,\mathrm{s}$. The cylinders here experience streamwise, vertical and pitching displacements. Regarding the pitching, the bodies rotate counterclockwise except for $\vartheta_0 = 0^\circ$ and $\vartheta_0 = 10^\circ$ (shown in figures 4.15b and 4.15c). The reason for this counterclockwise rotation is a negative pitching moment caused by the top jet's shear layer as described in section 2.3 and also shown for cubes (see section 4.2.1). For $\vartheta_0 = 0^\circ$ and $\vartheta_0 = 10^\circ$, the flight attitude does not change significantly, because it seems that a moment, effected by cylinder's flow field at the current flight attitude, counteracts the rotational motion caused by the free jet's shear layer. It may be that asymmetrical pressure loads occur on the surface of the cylinder at small positive pitch angle, causing a positive pitching moment. The effect of pitch angle on aerodynamic moments is discussed in detail in section 4.3.3. All of the flow structures in figure 4.15 contain detached bow shocks, whereas the shock shape and stand-off distance depend on the flow angle relatively to the body. At the leading edges, expansion fans rise that encounter with the bow shock resulting in an aerodynamic interaction associated with a bending of the shock wave over the length of the interaction (see for example figure 4.15d).

4.3.2 Model Motion

By the use of the stereo tracking system, the motion of the rigid body is reconstructed. Figure 4.16 presents an example for the smoothed measurement data of a cylinder configuration with an initial pitch angle of $90°$ on the streamwise, spanwise and vertical displacement in figure 4.16a and the roll, pitch and yaw displacement in figure 4.16b. Due to the rotational symmetry of the model as well as the alignment of cylinder's axis and nozzle's axis, a two-dimensional motion is expected. From the displacement data in figure 4.16, it is apparent that the roll, yaw and spanwise motion components are almost zero over the whole free-flight time as opposed to the streamwise, vertical and pitch motion components. Changes in streamwise position ($\mathit{\Delta} x = 161.3\,\mathrm{mm}$), vertical position ($\mathit{\Delta} z = -339.3\,\mathrm{mm}$) and pitch angle ($\mathit{\Delta}\vartheta = -30.6°$) are at the same time about two orders of magnitude greater than the changes in spanwise position ($\mathit{\Delta} y = 3.0\,\mathrm{mm}$), roll angle ($\mathit{\Delta}\varphi = -0.6°$) and yaw angle ($\mathit{\Delta}\psi = -0.2°$). As a consequence, the out-of-plane motion with roll, yaw and spanwise displacements is neglected in the following analysis.

Figure 4.17 illustrates the two-dimensional trajectories of all runs in the xz-plane with respect to the center of the nozzle exit plane showing also the flow regions of the free jet from experimental flow characterizations as a gray contour layer. The white area represents the core flow with a homogenous ram pressure distribution. It is apparent that the flight trajectories do not overlap. Unlike the applied free-flight technique for experiments with cubes, two release mechanism at two different positions were employed for tests with inclined cylinders, whereby the initial positions in x- and z-direction vary due to the model alignment. Broadly speaking, a significant streamwise acceleration of all free-flight tests is visible in figure 4.17 as well as the majority of measured data points are within the homogenous flow.

The corresponding velocities and accelerations to figure 4.16 are detailed in figure 4.18. As indicated previously, the derivatives of roll, yaw and spanwise motion can be neglected, because these quantities are approximately zero during the free-flight in core flow. As a result, only the streamwise, vertical and pitching components are considered for the experimental results presented hereinafter and the motion analysis is 3DoF. The velocities of the streamwise, vertical and pitch motion components in figures 4.18a and 4.18b clearly differ from zero at $t = 0\,\mathrm{s}$, when the entire body is within core flow. These deviations from zero demonstrate the impact of the free jet's shear layer on the body motion causing a strong pitch rotation as well as a significant streamwise acceleration. Interestingly, the x-acceleration here reaches higher values than the gravitational acceleration up to $15\,\mathrm{m/s^2}$ (see figure 4.18c), while the absolute z-acceleration is lower than the gravitational acceleration indicating the presence of a positive lift force. It is notable that the pitch acceleration in figure 4.18d is negative at the beginning ($t = 0\,\mathrm{s}$) and turns to positive values shortly after. The reason for this change of sign seems to be that the first

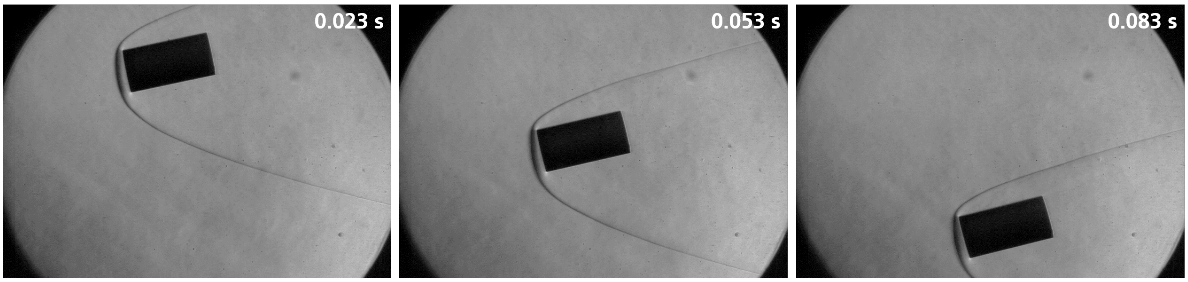

(a) $\vartheta_0 = -10°$

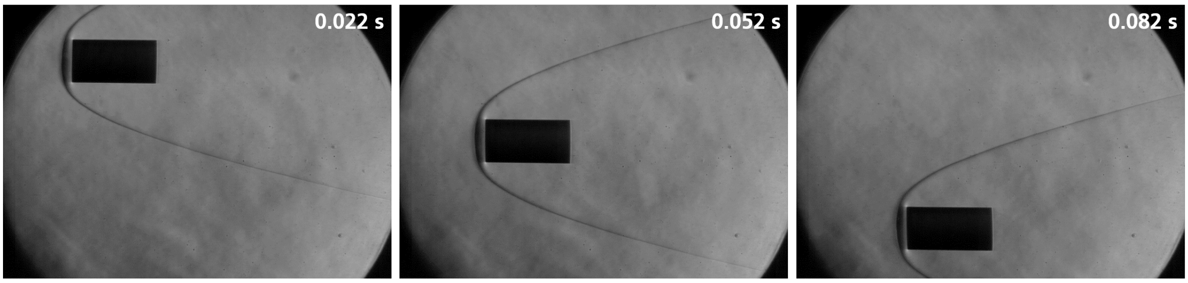

(b) $\vartheta_0 = 0°$

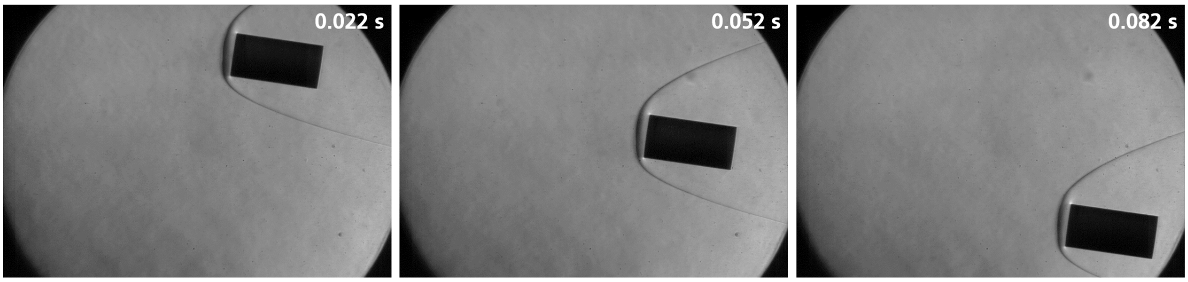

(c) $\vartheta_0 = 10°$

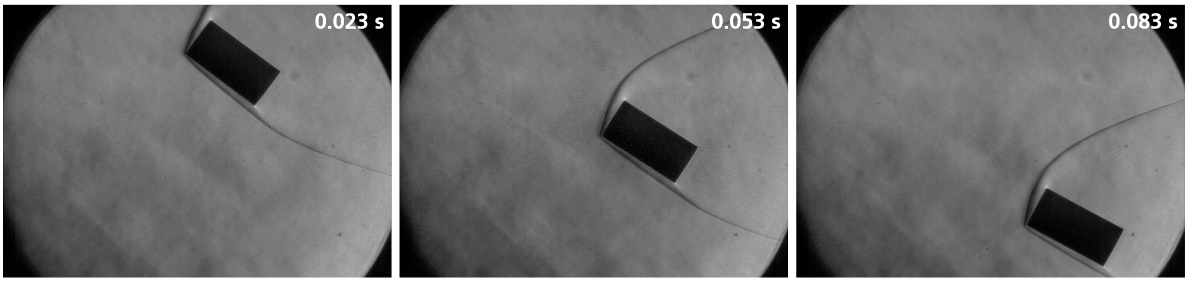

(d) $\vartheta_0 = 50°$

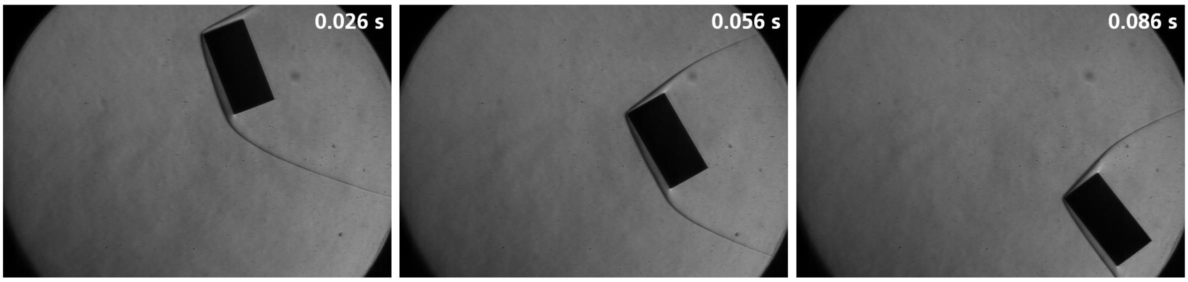

(e) $\vartheta_0 = 90°$

Figure 4.15: Selection of schlieren image sequences showing the motion behavior of a cylinder in free-flight with different initial pitch angle

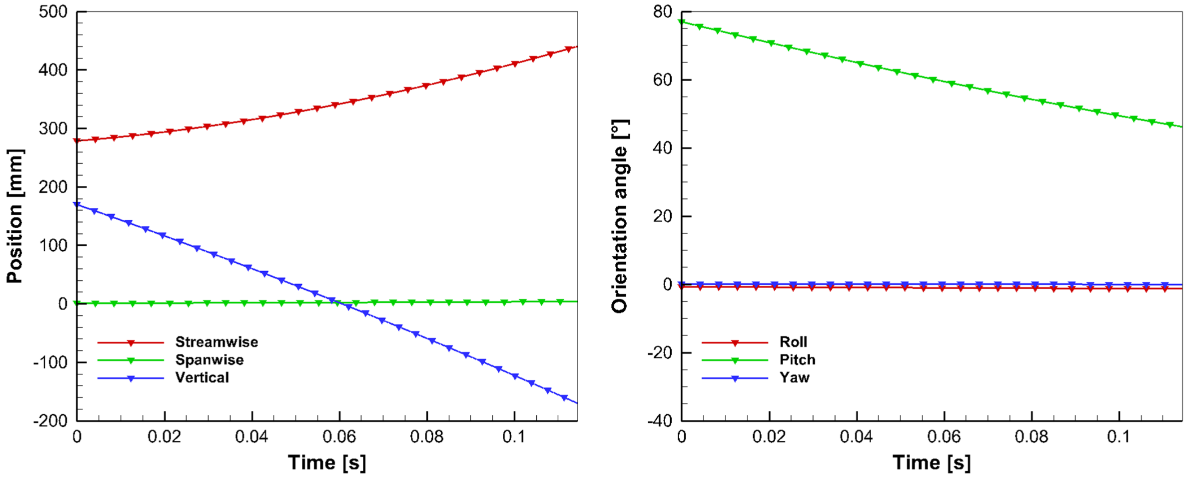

(a) Positions in x, y & z **(b)** Orientation angles in φ, ϑ & ψ

Figure 4.16: Evolution of cylinder's 6DoF motion displacement in core flow with $\vartheta_0 = 90°$

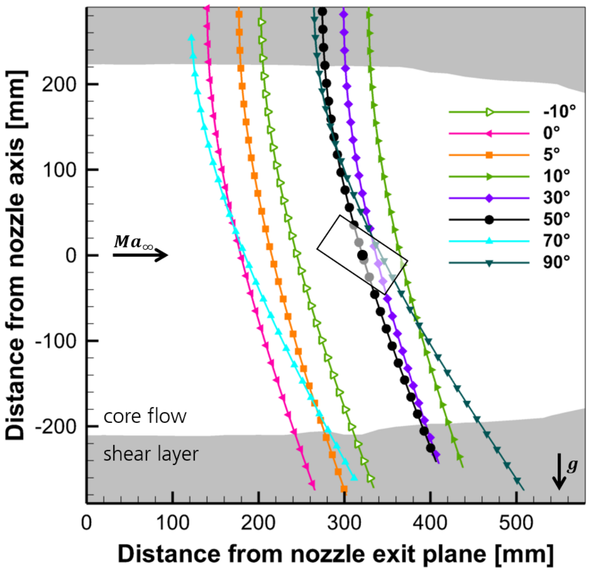

Figure 4.17: Cylinder's flight trajectories of runs with different initial pitch angle relating to the flow regions of H2K's Mach-7 nozzle based on figure 2.2; black solid circle indicates position of the cylinder at a certain moment

values are affected by adjacent data points during the filtering, for which the body experience a negative pitch acceleration due to the jet shear layer. For the determination of accelerations (second-order derivatives), the data is filtered three times by use of 100 adjacent data points before and after each value for all filtering steps. Thus, the first and also the last values in figure 4.18d are influenced by measurement points captured within the jet shear layer, which explains the strong deviations at the edges of the plot and can also be observed for the pitching moment coefficients. In contrast to the angular derivatives, the translational acceleration of cylinders in cross flow seems to be less sensitive to inhomogenous distributions of the ram

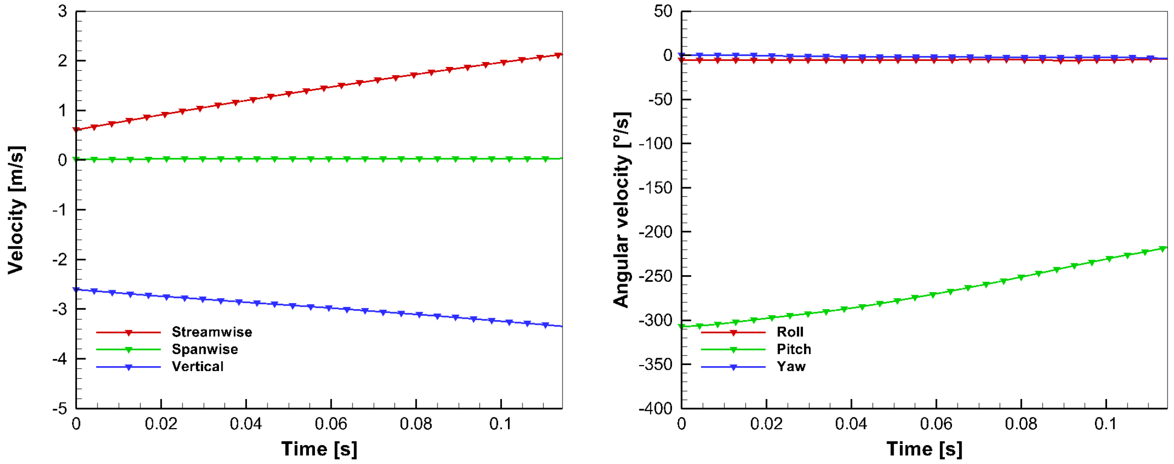

(a) Velocities in x, y & z **(b)** Angular velocities in φ, ϑ & ψ

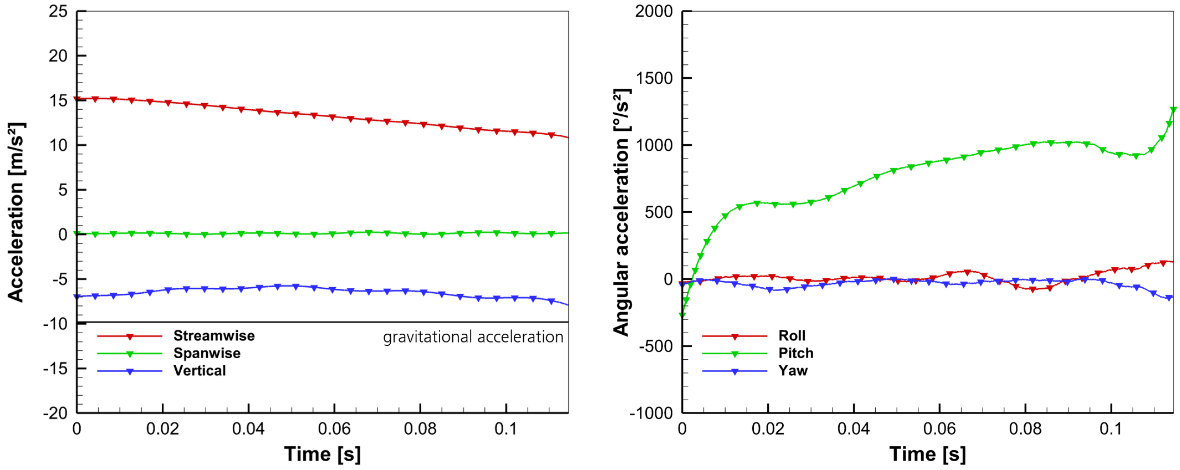

(c) Accelerations in x, y & z **(d)** Angular accelerations in φ, ϑ & ψ

Figure 4.18: Evolution of cylinder's 6DoF translational and angular motion derivatives in core flow with $\vartheta_0 = 90^\circ$

pressure than the pitch acceleration. Inside the core flow, the pitch acceleration in figure 4.18d has significant positive values, which cause a counter-rotation referred to the motion of the model within the top shear layer.

4.3.3 Aerodynamic Forces & Moments

The resulting aerodynamic coefficients, which are determined from the motion derivatives in streamwise (drag force) and vertical (lift force) direction as well as around the spanwise axis (pitching moment), are presented in figure 4.19 as a function of the pitch angle. This figure reports derived measurement data just in a positive range of pitch angle, where open symbols indicate mirrored values. In doing so, the absolute pitch angles are applied for this representation as well as the lift force and pitching moment coefficients experience a change of sign for the mirrored values. The average estimates of the overall uncertainties related to their peak values, as described in section 3.4.2, are $2\,\%$ for C_{D}, $4\,\%$ for C_{L} and $3\,\%$ for C_{M}. In addition to the experimental data of several runs with different initial pitch angles, trigonometric fitting and hypersonic approximation curves are shown in the diagrams, as well. Aerodynamic coefficients based on two different reference areas are presented in the line charts. On the one hand, a constant circular base area (figure 4.19a) and on the other hand, a pitch-angle-dependent projected frontal area (figure 4.19b) are shown here. The second reference quantity is calculated by means of equation (4.5).

$$S_{ref} = ld\left|\sin\left(\vartheta\right)\right| + \frac{\pi}{4}d^2\left|\cos\left(\vartheta\right)\right| \tag{4.5}$$

Due to the mirror symmetry of cylinders, the correlations between aerodynamic coefficients and pitch angle have a period of 180°. Thus, the results of pitch angles in the range from 0° to 180° can be extrapolated on its full-range aerodynamic characteristics. Trigonometric functions by means of Fourier series with a period of 180° are used to fit the curve to the experimental data. This means that the angular frequency of each Fourier term is an integer multiple of 2. For high-order terms, the Fourier coefficients are very small, with the exception of the pitching moment coefficient, which is why these terms are neglected for drag and lift coefficients. The resulting functions of drag force, lift force and pitching moment coefficient are given in equations (4.6) to (4.8) being subject to the pitch angle.

$$C_{\mathrm{D}} = 2.273 - 0.062 \cdot \sin\left(4\vartheta\right) - 0.667 \cdot \cos\left(2\vartheta\right) + 0.141 \cdot \cos\left(4\vartheta\right) \tag{4.6}$$

$$C_{\mathrm{L}} = 0.416 \cdot \sin\left(2\vartheta\right) - 0.424 \cdot \sin\left(4\vartheta\right) \tag{4.7}$$

$$\begin{split} C_{\mathrm{M}} = 0.034 \cdot \sin\left(2\vartheta\right) - 0.030 \cdot \sin\left(4\vartheta\right) + 0.003 \cdot \sin\left(6\vartheta\right) + 0.017 \cdot \sin\left(8\vartheta\right) \\ +0.012 \cdot \sin\left(10\vartheta\right) - 0.006 \cdot \sin\left(12\vartheta\right) \end{split} \tag{4.8}$$

In general, the aerodynamic coefficients in figure 4.19 reveal a significant dependence on the body orientation, which confirms previous findings of cubes as in section 4.2.3. From the data in figure 4.19a, it is apparent that the drag coefficient of cylinders based on a circular reference area exhibits a much greater influence of the inclination angle than that of cubes, as shown previously. Increasing the pitch angle of the cylindrical body causes firstly a slight decrease in the drag coefficient until 13°, before it increases significantly and peaks at around 90°. At a pitch angle of 0°, the drag coefficient is 1.747, which differs by $5.9\,\%$ from the value of $C_{\mathrm{D}} = 1.65$ determined by Hoerner [48]. This underestimation of the base-exposed cylinder's drag can be explained by the neglect of three-dimensional flow field phenomena and thus by the aerodynamic influence of the body ends. As opposed to this, the experimental drag coefficient at a pitch angle of 90° is identical to Hoerner's value of $C_{\mathrm{D}} = 3.08$ referred to

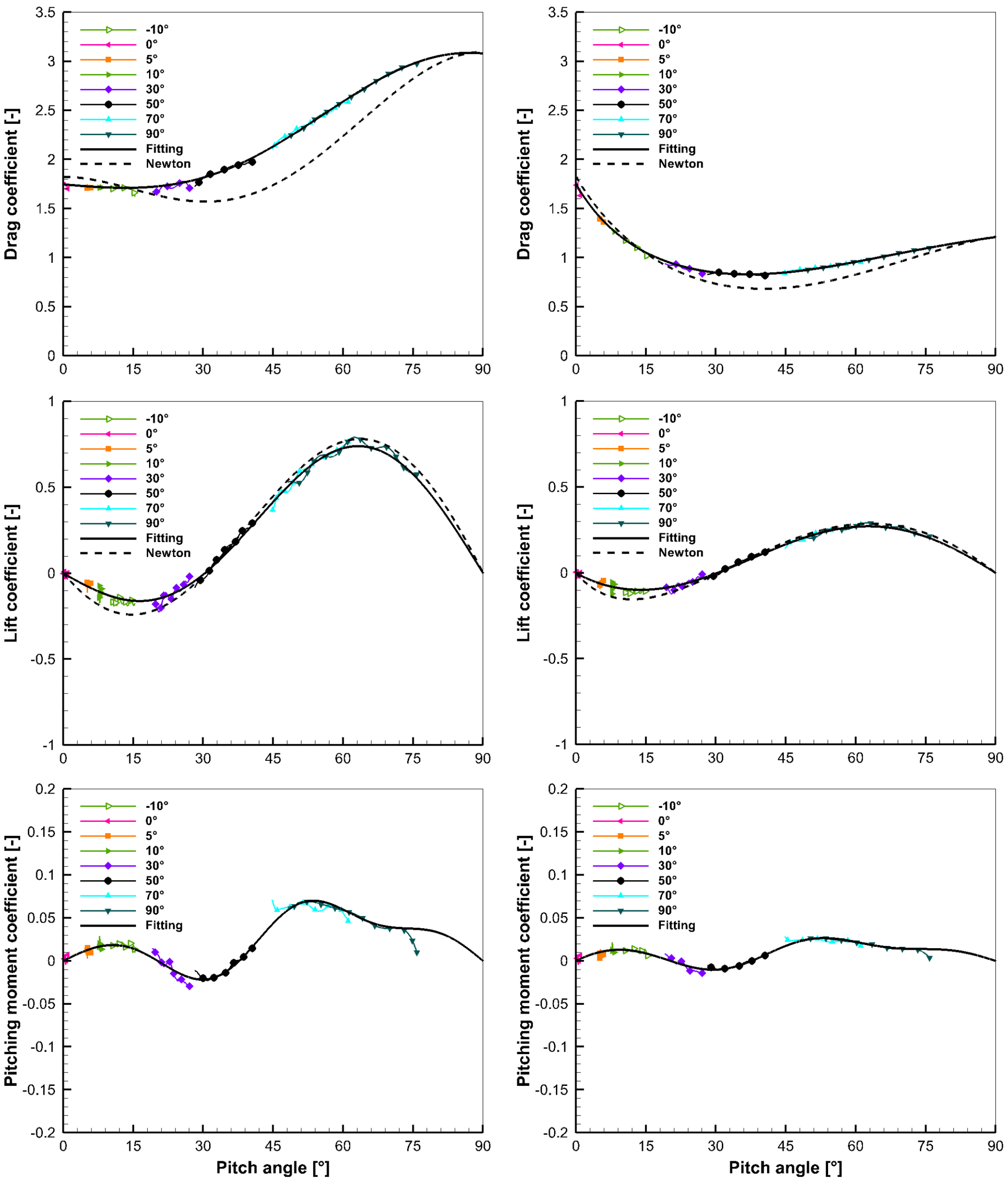

(a) Circular base reference area ($S_{ref} = \pi/4d^2$) **(b)** Projected reference area ($S_{ref} = f(d,l,\vartheta)$)

Figure 4.19: Influence of the pitch angle on cylinder's aerodynamic coefficients based on experimental data at different initial pitch angle determined with different reference areas

the base area, whereas it is overestimated by Penland [89] with $C_\mathrm{D} = 3.16$ showing a relative deviation of $2.5\,\%$. In comparison to the experimental outcome, the drag coefficient determined by the modified Newtonian flow theory decreases more strongly with increasing pitch angle and reaches its minimum at a higher pitch angle of $31°$, before it also begins to increase up to

$90°$. Moreover, the base-exposed drag coefficient is overestimated with a relative deviation of $4.4\,\%$ compared to the experimental value, while the side-exposed drag coefficient is almost identical with a relative deviation of $0.5\,\%$. In general, the hypersonic approximation shows a fairly good agreement with the experimental results.

Asymmetric flow fields in consequence of the body inclination cause the development of lift forces and pitching moments, whose function graphs behave sinusoidally. In figure 4.19a, the lift coefficient's maximum of 0.740 appears at a pitch angle of $63°$ and its minimum of -0.161 occurs at $16°$. The observed maximum can be attributed to the body orientation, where the space diagonal of the cylinder is orthogonal to the free-stream direction and thus the projected area is close to highest value. Referring to the circular base area, the maximum lift coefficient is $24.0\,\%$ of the maximum drag coefficient. The modified Newtonian flow theory reveals a good agreement with the experimental results of the lift coefficient, whereby the maximum absolute deviation is 0.086 at $\vartheta = 12°$. The graph of pitching moment coefficient has three zero-crossings within the half period at $0°$, $20°$ and $38°$, while its maximum occurs at a pitch angle of $54°$. Surprisingly, positive pitching moment coefficients occur at small positive pitch angles (as illustrated in figure 4.20), although negative values are expected due to a shift of the stagnation point in counterclockwise direction. However, the surface pressures near the leading edge are much higher on the bottom lateral surface than on the upper one. The reason for this is that the pressure on the bottom side increases due to a higher recompression of the flow in combination with a disappearance of the separation on the leading edge, while it decreases on the upper side due to a growth of the separation bubble with increasing pitch angle. As a result, the lateral surface's Center of Pressure (CoP) lies ahead of the CoG closer to the leading edge. This aerodynamic moment acts in opposite direction of rotation to the moment of the stagnation region, whereby the lever arm of the lateral surface's CoP is longer than that of the stagnation point. By rising the pitch angle of the cylinder, the CoP shifts backwards causing a decrease of its lever arm's length and aerodynamic moment, whereas both increase for the stagnation point. At a pitch angle of $20°$, the moment proportions are in equilibrium ($C_\mathrm{M} = 0$), which is not expected for an asymmetric flow field. This contradictory finding can be explained by the fact that the aerodynamic moment proportion of the base behave contrary to the one of the lateral surface leading to zero-crossings for inclined configurations. Analytical outcomes of C_M are not presented in figure 4.19, because the pitching moment is constant zero owing to the symmetry of the surface pressure distribution with respect to the xy-, xz- and yz-plane. These results offer vital evidence for the occurrence of significant lift forces and pitching moments of inclined cylinders in hypersonic flow fields, which are relevant that the effects on rigid body motion should be considered. In addition, there is also a high probability that the zero-crossings depend on cylinder's aspect ratio (l/d), since the pressure distribution on the lateral surface is inhomogeneous and its influence on the aerodynamic loads depends on its proportional surface area compared to the base area.

In this analysis, it has already been shown that an increasing pitch angle toward $90°$ results in an increase in the drag coefficient if a constant reference area is used for normalization. However, the frontal area also increases, which has a major influence on the rise of the drag coefficient. By referring to an inclination-dependent reference area as in figure 4.19b, the drag coefficient decreases between a pitch angle of $0°$ and $37°$ before it begins to increase with lower gradients and reaches a local maximum of 1.210 at $90°$. This drag coefficient based on the projected reference area is just $39.3\,\%$ of the value with constant base reference area, which

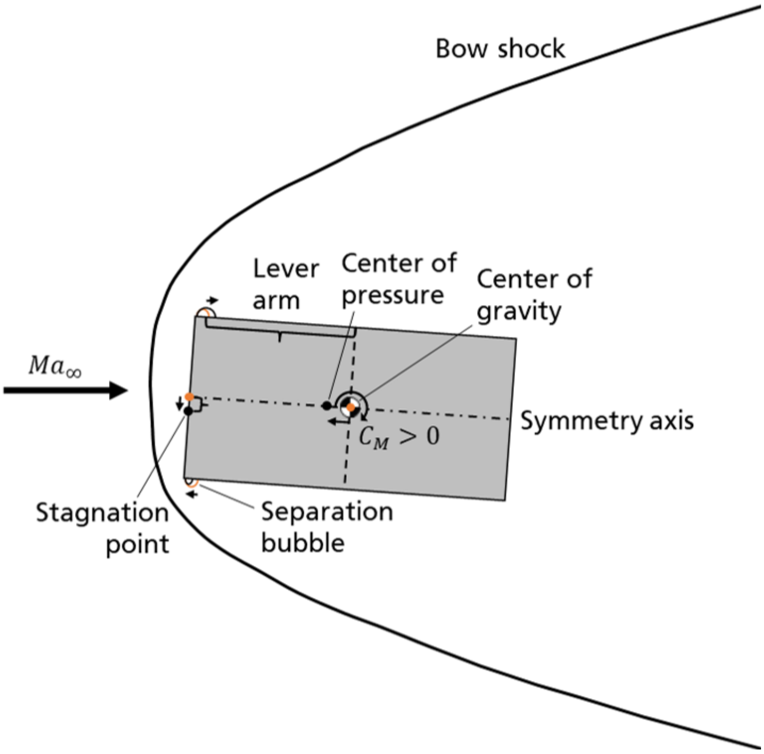

Figure 4.20: Schematic of changes in flow and moment characteristics for a cylinder at a small positive pitch angle (black lines) relative to a zero angle (orange lines)

is why the greater proportion of drag is attributed to the increase in frontal area. The global maximum occurs at a pitch angle of $0°$ and is significantly higher than the local maximum at about $90°$ with a relative difference of $44.4\,\%$. The minimum is reached with a value of 0.831 at an inclination, where the stagnation point is close to the cylinder's leading edge. In general, the aerodynamic coefficients are lower for the projected reference area, as it increases for a pitch-angle-dependent frontal area compared to the base area.

In addition to experimental and analytical results, figure 4.21 depicts the numerically determined aerodynamic coefficients from [101] using NASA's inviscid flow solver Cart3D [2, 3] and compressible Navier-Stokes solver US3D [77] for comparison purposes. It is notable that both numerical solutions show a very good agreement for the force coefficients with a relative deviation in drag coefficient of $1.1\,\%$ for the base-exposed cylinder and $0.3\,\%$ for the side-exposed cylinder, although the Cart3D solver neglects viscous effects in contrast to US3D. This is consistent with the well-established theory such as in [48] that the viscous effects of blunt bodies in hypersonic flows are subordinate to the compressibility effects for the aerodynamic forces. In general, all three aerodynamic coefficients of both numerical solutions match well with the experimental ones. Yet, the numerical results of the drag coefficient are lower than the experimental ones over the entire range of pitch angle up to $90°$, where they are almost equal. Thereby, the deviations based on the US3D data are -0.064 at a pitch angle of $0°$ and 0.012 at $90°$, with the former being slightly outside and the latter within the overall uncertainty. It is not surprising here that the numerical and experimental drag coefficients feature a very small deviation, because both flow fields perfectly match each other with identical shape and

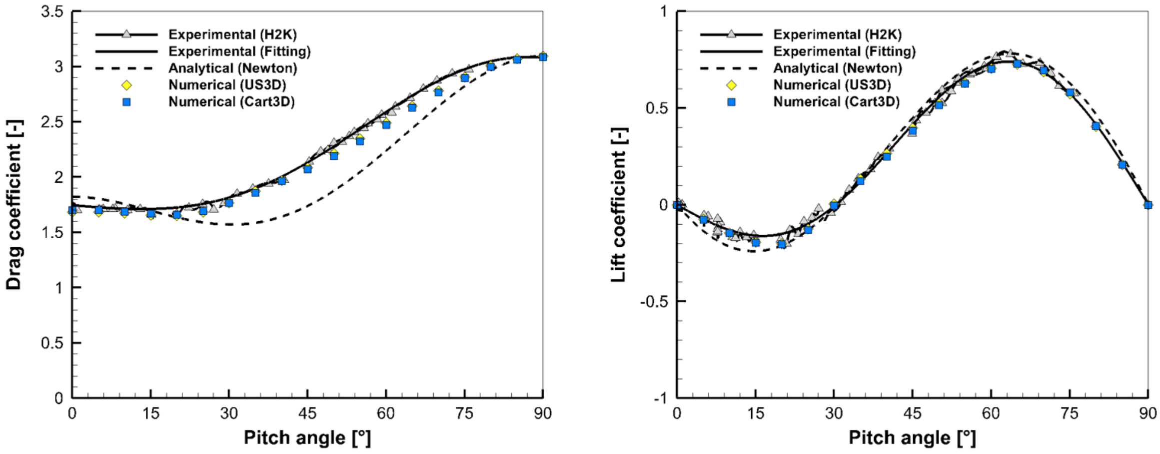

(a) Drag force **(b)** Lift force

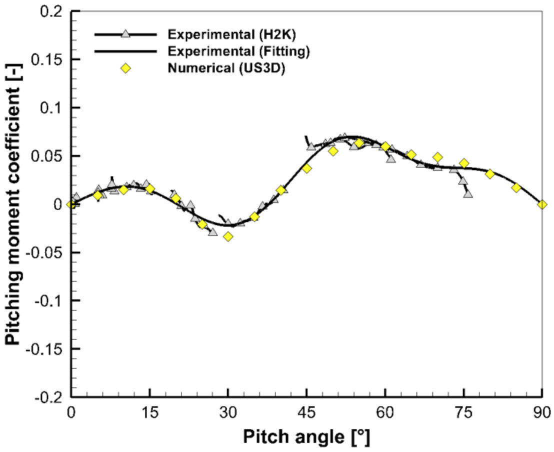

(c) Pitching moment

Figure 4.21: Comparison of different methods to determine the cylinder's aerodynamic coefficients as a function of pitch angle; numerical data taken from [101]

the same stand-off distance of the bow shock at a zero pitch angle (see figure 4.14a). As for the lift force coefficient, the results of experiments and corresponding numerical simulations show a very good agreement with zero-crossings at the same pitch angle, whereby the maximal relative deviation with respect to the maximum lift coefficient is very small with $1.3\,\%$. By contrast, the agreement between experimental and numerical pitching moment coefficients is good for most parts, but the maximal relative deviation with respect to the peak value is higher with a value of $16.7\,\%$ being however outside the uncertainty of $3\,\%$ as aforementioned.

Figure 4.22 summarizes all curves of the curve-fitted aerodynamic coefficients depending on the pitch angle for an entire period of $180°$. Furthermore, it depicts the positions of the stable trim points with regard to pitching motions. As requirements for statically stable trim points, the conditions of moment equilibrium with $C_\mathrm{M} = 0$ and negative stability derivative with $\partial C_\mathrm{M}/\partial\vartheta < 0$ need to be fulfilled. There are three stable trimmed flight attitudes at about $20°$, $90°$ and $160°$, where both conditions are satisfied, and three unstable ones at about $0°$ (or $180°$), $38°$ and $142°$, where only the first condition is met. Unexpectedly, the base-exposed

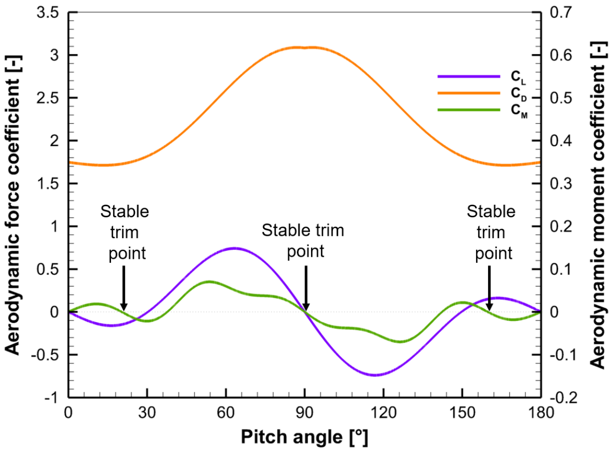

Figure 4.22: Static stability of cylinders depending on pitch angle

orientation does not fulfill both stability conditions and is therefore an unstable trimmed attitude, whereas a flight configuration at a pitch angle of 20° is a stable trimmed attitude despite an asymmetric flow field. Hence, the static stability of a cylinder reveals no dependency on the symmetry of flow topology. In the neighborhood of 90°, the highest negative stability derivative is achieved with an extreme value of $-0.260\,\frac{1}{\mathrm{rad}}$. In addition to the maximum stability at 90°, the pitch angle tends towards this attitude due to the opposite direction of its moment over a wide range from 38° to 142° unlike the asymmetric stable trim points, which is why a side-exposed configuration is a more likely final flight attitude for randomly tumbling cylinders. Both results of CFD simulations and wind tunnel tests confirm these findings.

4.4 Discussions on Body Shape & Inclination

Broadly speaking, the previous results have shown that the body shape and inclination heavily influence the gasdynamic flow topology and hence the aerodynamic forces and moments. In the following sections, the results of the different geometries are compared and discussed with regard to the flow field, the aerodynamic coefficients and the static stability.

4.4.1 Effect on Flow Field

As already mentioned in the literature review, the flow field of blunt bodies is complex with a typically bended detached bow shock. This accords with the present observations, which also showed that the bow shock's shape and stand-off distance are almost identical for cubes and cylinders in plane-exposed orientation (see figures 4.23b and 4.23c) but differ from spheres (see figure 4.23a). In the course of this, the shock radius, the stand-off distance and the subsonic stagnation region of plane-exposed configurations are greater than those of spheres, which have a more bended shock shape at their forebodies. A possible explanation for this might be that the required flow deflection angles are higher in a larger part of the stagnation region for blunter bodies. As a result, the local deflection angles of the surface exceed the maximal

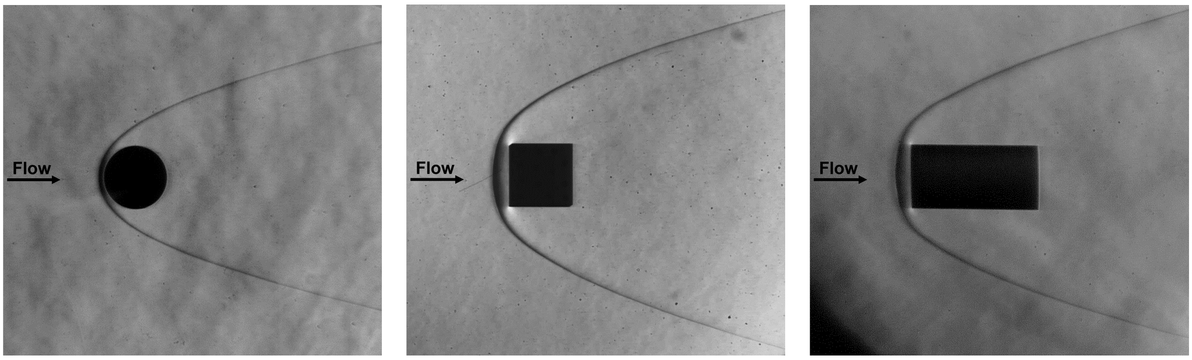

(a) Sphere **(b)** Cube at $\vartheta = 0°$ **(c)** Cylinder at $\vartheta = 0°$

Figure 4.23: Schlieren image of various bodies with same width at $Ma_\infty = 7.0$

deflection angle of the flow, so that a strong bow shock with a high shock angle decelerates the flow to subsonic over a wider region to enable the flow deflection. In doing so, greater bluntness has the same effect as a reduction in the free-stream Mach number for spheres with regard to the shape of the upstream flow phenomena. Moreover, unexpected flow phenomena such as separation with reattachment of the boundary layer at the leading edge downstream the expansion fan were observed for cubes and cylinders at small pitch angle, whereas the flow around spheres in the region of the narrowing body fully separates. This difference can be explained by a higher adverse pressure gradient at the afterbody of spheres due to a more converging geometry. However, the flow around the non-spherical objects also experiences a full separation at the afterbody, but this has its origin at the trailing edges. The reason for this boundary layer separation is that the flow can not follow the contour of the body, because the required angle to deflect the flow at the edges is higher than the maximum possible value for the Mach number. This leads to a drop in pressure downstream of the separation point due to the expansion fan in contrast to spheres, where a rise in pressure occurs across the separation shock.

In the current study, it was found that the flow fields become asymmetric and the aerodynamic phenomena become more complex (see for example figure 4.15d) as soon as the non-spherical bodies are inclined. All of these flow structures contain detached bow shocks, whereas the shock shape and stand-off distance depend on the flow angle relatively to the body. It was found that the more a body edge protrudes into the flow, the more the shock stand-off distance is reduced and the shock curvature is greater in the surrounding of the edge. At the leading edges, expansion fans rise that encounter with the bow shock resulting in an aerodynamic interaction associated with a bending of the shock wave over the length of the interaction. Downstream of the expansion fans (as shown in figures 4.6b and 4.14b), a separation bubble develops. This separation region grows with increasing pitch angle on the upper side while it disappears on the bottom side, as illustrated in figure 4.20. However, the boundary layer reattaches to the lateral surface and then separates again at the trailing edges, forming a wake region. For the cylinder, the separation bubble merges at a pitch angle of about $60°$ with the wake region and the flow no longer reattaches to the upper lateral surface (see figure B.3e). At around $75°$, the flow reattaches to the bottom base surface (see figure B.3f), while a small separation bubble appears and the wake region originates from the downstream edges again. It is interesting to see from the sequences of schlieren images in figures 4.8 and 4.15 that the position of the expansion fans changes depending on the orientation, which is an indicator for the shift of the separation points. From the numerical schlieren representations in figure B.3, a downstream shift of the separation points to the next body edge opposite to the direction of rotation is apparent by increasing the pitch angle. In doing so, the rising local deflection angle exceeds the maximum turn angle at some point so that it meets the condition for flow separation.

4.4.2 Effect on Aerodynamic Coefficients

It was shown previously that the drag coefficient of non-spherical objects is a function of the pitch angle and that this body inclination causes lift forces and pitching moments. Figure 4.24 depicts a comparison of different body shapes with regard to the aerodynamic force and moment coefficients over the pitch angle, whereby these coefficients are referred to the inclination-dependent projected frontal area. At a pitch angle of $0°$, the drag coefficients of cylinders and cubes are quite similar just like the shape and stand-off distance of the bow shock in the two-dimensional representation of the flow field as discussed in section 4.4.1. This finding leads to the conclusion that viscous effects are subordinate in terms of aerodynamic forces, while compressibility effects are dominant in the hypersonic flow regime. Surprisingly, the drag coefficient of cylinders falls below the constant value of spheres in the range of $21.8°$ to $56.4°$, whereby the minimum of 0.831 is reached at a pitch angle of $37.0°$. Here, the stagnation streamline impinges the surface near the cylinder's leading edge. This finding suggests that the part of the body which protrudes into the flow primarily determines the magnitude of the drag coefficient. From the plots of the drag coefficient, this relationship can be observed, whereby the flat-faced configuration (e.g. a cube at $\vartheta = 0.0°$ with $C_\mathrm{D} = 1.704$ or a cylinder at $\vartheta = 0.0°$ with $C_\mathrm{D} = 1.747$) exhibits a higher effective drag coefficient than the round-curved configuration (e.g. a cylinder at $\vartheta = 90.0°$ with $C_\mathrm{D} = 1.210$ or a sphere with $C_\mathrm{D} = 0.926$) and a much higher effective drag coefficient than the edge-on configuration (e.g. a cylinder at $\vartheta = 37.0°$ with $C_\mathrm{D} = 0.831$). Thereby, a lower drag coefficient correlates with a lower SSD of the bow shock (see figures 4.8 and 4.15), whereas the pitching moment coefficient depends on the position of the flow separation and reattachment.

Another difference is that no lift arises for spheres, whereas the lift coefficients of cylinders and cubes exhibit similar sinusoidal characteristics. It is apparent that the periodic here depends on the symmetry of geometry. In figure 4.24a, both function graphs of the non-spherical bodies have three zero-crossings, whereby just the second one varies from each other, with $30.3°$ for the cylinder ($l/d = 2$) and $45.0°$ for the cube ($l/d = 1$). It is therefore likely that the position of this zero-crossing tends to correlate with the aspect ratio of the body. Furthermore, the experimental data of this work show that the cylinder's maximum lift coefficient is $15.6\,\%$ of its maximum drag coefficient, while the cube's maximum lift coefficient is $13.1\,\%$ of its maximum drag coefficient. This finding underlines once again the dominance of drag over lift for blunt bodies, as is common knowledge in the scientific community.

On the question of pitching moment coefficients, this study found that their curves differ greatly for spheres, cubes and cylinders. These function graphs in figure 4.24b show different numbers of zeros, which represent the trimmed flight conditions. In doing so, the number of zero-crossings in an angular range of $90°$ is four for the cylinder, three for the cube and an infinite number for the sphere. It is also notable that the pitching moment coefficient is characterized

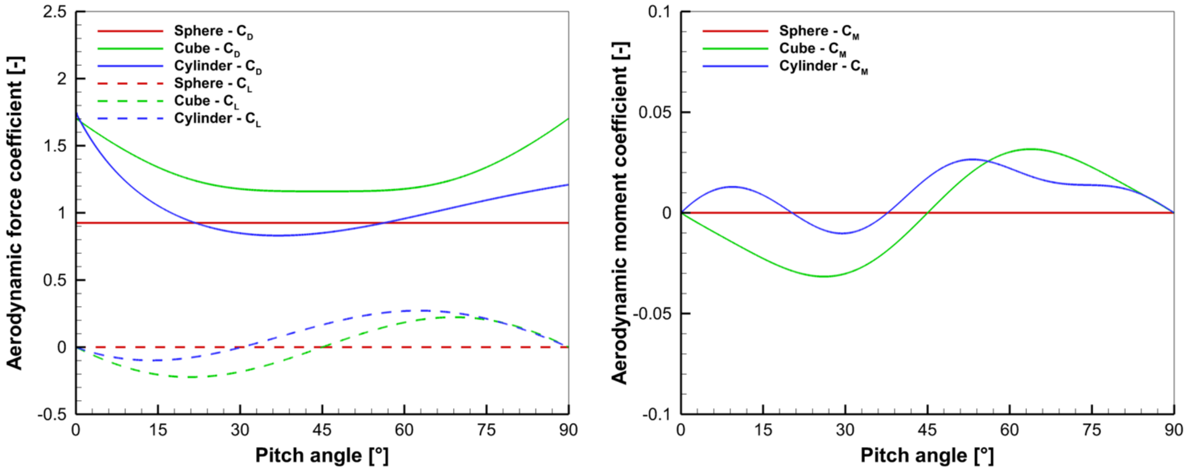

(a) Drag and lift force coefficients **(b)** Pitching moment coefficients

Figure 4.24: Comparison of aerodynamic force and moment coefficients from different bodies based on projected reference area as a function of the pitch angle

by unforeseeable points of extrema as well as an unexpected aerodynamic behavior depending on the pitch angle, specifically for the cylinder. This intriguing result is likely to be related to the separation and reattachment points of the flow depending on the pitch angle, as described in section 4.4.1. Accordingly, it could be indicated that the rotational behavior due to aerodynamic loads is highly sensitive to certain flow features like separation regions. Another finding that stands out from the shown results is that there is an interaction between the angular position of the body and its aerodynamic moment, which was found for the non-spherical objects. This can be attributed to the fact that the aerodynamic moment is dependent of the body orientation as a result of the rotation, while the change in orientation is caused by the aerodynamic moment traced back to the equations of motion (and thus the Newton's second law).

In general, an interaction between the aerodynamic loads and the flight quantities was observed for cubes and cylinders. Thereby, it was found that the lift force, drag force and pitching moment during the performed free-flight tests are permanently changing due to their effect on flight path angle, attitude and velocity, which again have an impact on the aerodynamic coefficients. If a stable trimmed flight attitude is reached, the lift is zero as well as the flight attitude remains constant, with the exception of the cylinder at trimmed pitch angles of $20°$ and $160°$. However, these flight attitudes are rather unlikely as described in section 4.3.3.

4.4.3 Effect on Static Stability Behavior

For a statically stable trim point, two requirements must be met as previously mentioned. A trimmed flight attitude is present as soon as the moments are in equilibrium with $C_\mathrm{M} = 0$, and this is statically stable if a negative stability derivative with $\partial C_\mathrm{M}/\partial\vartheta < 0$ also applies. As shown in figure 4.24b, it is apparent for the different bodies that the cylinder has two stable ($\vartheta = 20.3°$ and $\vartheta = 90.0°$) and two unstable ($\vartheta = 0.0°$ and $\vartheta = 37.7°$) flight attitudes, while the cube has two stable ($\vartheta = 0.0°$ and $\vartheta = 90.0°$) and one unstable ($\vartheta = 45.0°$) flight attitudes.

By contrast, all trim points of the sphere are neutral. What stands out here is that these three bodies in a hypersonic flow regime experience different static stability behavior at a trimmed pitch angle of $0.0°$, whereby the cube behaves stable, the sphere is neutral and the cylinder behaves unstable. Here again, it is expected that the static stability behavior depends on the aspect ratio.

The measure of a flying object's stability depends on the magnitude of the stability derivative. The highest negative stability derivative is achieved at $\vartheta = 90.0°$ for the cylinder with an extreme value of $-0.260\,\frac{1}{\mathrm{rad}}$ and at $\vartheta = 90.0°$ for the cube with an extreme value of $-0.097\,\frac{1}{\mathrm{rad}}$, which corresponds to the range of the highest drag coefficient and thus the highest pressure loads. This means that if an edge of the body moves upstream from a trimmed configuration due to an initiated rotation, the stagnation point shifts towards this upstream edge. As a consequence, the body part that protrudes more into the flow experiences higher surface pressures, which causes a reverse pitching moment and thus an opposite rotation. It is apparent from the data in section 3.5 of [101] that an applied axially symmetric cavity causes a reversal of the static stability behavior at a zero pitch angle with considerable magnitude unlike the body without cavity. Thereby, the stability derivative of the modified cylinder geometry at a pitch angle of $0°$ with $\partial C_{\mathrm{M}}/\partial\vartheta = -1.172\,\frac{1}{\mathrm{rad}}$ is roughly 5 times greater than of the cylinder's peak stability derivative at $90°$. This significant change in stability can be attributed to a shock-shock interaction in the cavity, which leads to an increase in surface pressure. Taken together, these results highlight the strong influence of body geometry on static stability behavior. In addition, the results also indicate that after a period of object rotation, the present blunt bodies are very likely to assume a stable flight attitude with a symmetrical orientation referred to the inflow. As a result, the aerodynamic loads are constant and there are no lift forces that cause lateral movements.

5 Experiments on Aerodynamic Interactions of Multiple Bodies

In the following part of the thesis, the configuration is extended by a second test object with the aim to study the aerodynamic interaction of two blunt bodies in hypersonic flow regime. One purpose of this chapter is to explore the relationship between the relative positioning of the objects and the aerodynamic behavior in terms of flow topology, aerodynamic coefficients and motion characteristics. Test series with two different approaches were performed therefore. On the one hand, a semi-free-flight setup with two equal spheres was applied that enables the study of the stationary trailing object in a wide continuous range of relative vertical positions, whereby the effects of the Reynolds number and the model size are assessed, as well. On the other hand, the use of the setup with two free-flying models allows the investigation of dynamic motions and provides new insights into the impact of the body shape and orientation in the case of a non-spherical geometry. Just as the analysis in chapter 4, this research also focuses on a 3DoF motion consisting of the streamwise, vertical and pitching components.

In the subsequent analysis, non-dimensional quantities for position and velocity data are depicted. The data are presented in the form of normalized separation distances, defined as:

$$\Delta\widehat{x} = (x_2 - x_1)/r \tag{5.1}$$

$$\Delta\widehat{z} = (z_2 - z_1)/r \tag{5.2}$$

where the radius of the sphere r is $0.025\,\mathrm{m}$. A value of $\Delta\widehat{x} = 2.0$ corresponds to the body contact of two axially aligned spheres (see definition in figure 2.8).

As in [58], the normalized time $\widehat{t}$, the separation velocities in streamwise direction ($\widehat{v}_x$) as well as in vertical direction ($\widehat{v}_z$) are defined as follows:

$$\widehat{t} = \sqrt{\rho_\infty/\rho_m}\, t v_\infty/r \tag{5.3}$$

$$\Delta\widehat{v}_x = \sqrt{\rho_m/\rho_\infty}(v_{x2} - v_{x1})/v_\infty \tag{5.4}$$

$$\Delta\widehat{v}_z = \sqrt{\rho_m/\rho_\infty}(v_{z2} - v_{z1})/v_\infty \tag{5.5}$$

whereby a negative vertical separation velocity indicates a repulsive tendency to the motion in lateral direction, since the respective separation distances are negative because the trailing objects enter the flow first. For the final lateral velocity $\widehat{v}_T$, reversed signs of the primary and secondary body's velocities are used for the present arrangements in order to indicate repulsive separation behavior by positive signs, defined as:

$$\widehat{v}_T = \sqrt{\rho_m/\rho_\infty}(v_{z1} - v_{z2})_{max}/v_\infty \tag{5.6}$$

The experimental results presented hereafter were obtained during tests in H2K at a Mach number of 7.0 and a baseline reservoir condition of $p_0 = 520\,\mathrm{kPa}$ and $T_0 = 600\,\mathrm{K}$ (see table 2.2). The same schlieren videography and facility instrumentation were applied for both setups, while two different techniques were used for the force and moment measurement. A detailed description of the experimental setup is given in chapter 2.

5.1 Results of Free-Flying & Balance-Mounted Spheres

The section below describes the results of the test series with the semi-free-flight setup as outlined in section 2.5.3. Pairs of smooth spheres with equal diameters were used for all performed tests, which have various nominal diameters of $50\,\mathrm{mm}$, $70\,\mathrm{mm}$ and $100\,\mathrm{mm}$ as characterized in table 2.4. In this experimental study, the focus is on the trailing sphere, that is equipped with a six-component balance (see section 2.4.4) to gauge the impact of the aerodynamic interactions on the drag force. A variation of the free-stream Reynolds number is realized by varying the diameter of the spheres while the unit Reynolds number is the same. In contrast, a variation of the model size is carried out by also varying the diameter of the spheres while the free-stream Reynolds number is the same. For all performed tests, the reservoir pressure is $p_0 = 520\,\mathrm{kPa}$, while the reservoir temperature is altered for varying the unit Reynolds number. The test matrix of this test series is given in table 5.1.

Table 5.1: Test matrix of balance measurements

Primary body	Secondary body	d [mm]	T_0 [K]	$Re_{\mathrm{u}\infty}\left[\frac{10^6}{\mathrm{m}}\right]$	Re_∞ [10^6]
Sphere	Sphere	50	600	2.1	0.11
Sphere	Sphere	50	478	3.0	0.15
Sphere	Sphere	70	600	2.1	0.15
Sphere	Sphere	100	600	2.1	0.21
Sphere	Sphere	100	763	1.5	0.15

5.1.1 Flow Topology

A continuous variation of the relative vertical position is achieved through a free-flying sphere that moves down due to gravity in front of a fixed-position sphere. Figure 5.1 shows a sequence of schlieren images from flow experiments of spheres with a diameter of $100\,\mathrm{mm}$ in which the leading body traverses the H2K's free jet while the trailing body remains at the centerline of the core flow. The time between the first and the last image is $97/150\,\mathrm{s}$. During the free flight, the leading sphere experiences more vertical than streamwise displacement being dominated by the gravitational acceleration. The schlieren images show the characteristic detached round bow shock in front of the blunt bodies. In the course of the sequence, the flow field of the trailing sphere changes from single-body topology (figure 5.1a), to the first aerodynamic interaction of both bow shocks (figure 5.1b), strong shock-shock interaction in the stagnation region (figure 5.1c), aerodynamic shielding in the primary wake (figure 5.1d), again strong SSI (figure 5.1e), and finally the end of interaction (figure 5.1f). Different types of SSI are visible in the schlieren images, which cause a change of the secondary bow shock in terms of shape, radius and stand-off distance. Especially, it is apparent that the secondary bow shock disappears when both bodies are axially aligned as in figure 5.1c.

While the front sphere moves past the aft one, all six Edney's types of SSI (see figure 1.4) between both bow shocks occur twice ahead of the trailing body, once when interacting with the lower part of the primary bow shock and then with its upper part. Figure 5.2 depicts sketches of these interaction patterns illustrating the description of the supersonic flow structures and the corresponding schlieren image in the background. Thereby, the lower oblique part of the primary bow shock represents the impingement shock. It is apparent that the type of SSI depends on the angular region of the forebody (as shown by Edney [24]), where the impingement shock interacts with the bow shock of the trailing sphere. The different interaction patterns affect the flow topology and in consequence the surface pressure as well as heat flux distribution on the trailing object [24]. Three of these patterns, namely types I, II and V (see figures 5.2a, 5.2b and 5.2e), cause a shock impingement on the model surface resulting in the well-known flow phenomenon of Shock-Wave/Boundary-Layer Interaction (SWBLI) as described in [119]. The Edney type III interaction provokes an attachment of the shear layer originating from the intersection point of impingement and bow shock (see figure 5.2c). An impingement of expansion waves, coming from the intersection point, can be seen for the type VI (see figure 5.2f), which leads to an interaction between the expansion fan and the boundary layer. However, the most relevant pattern is the Edney type IV interaction (see figure 5.2d), which is characteristic for SWS. The oblique impingement shock intersects near the normal part of the bow shock causing a supersonic jet that impinges the object in the vicinity of the stagnation point. This flow phenomenon is described in detail in section 5.2.1.

In addition, aerodynamic interactions of the primary bow shock with the secondary wake region were observed during the free-flight tests. Figure 5.3 presents the schlieren images of the trailing sphere in varying distances to the leading one within the context of WSI. In figure 5.3a, both the top of the trailing object and the bottom of the leading object share the same vertical position. In figure 5.3b, the trailing body begins to enter the primary wake region. In figure 5.3c, the shear layer of the primary wake impinges the secondary stagnation point. Finally, both spheres are axially aligned with the inflow in figure 5.3d. It has to be noted here that the flow features behind the primary body become difficult or impossible to see, because the density gradients

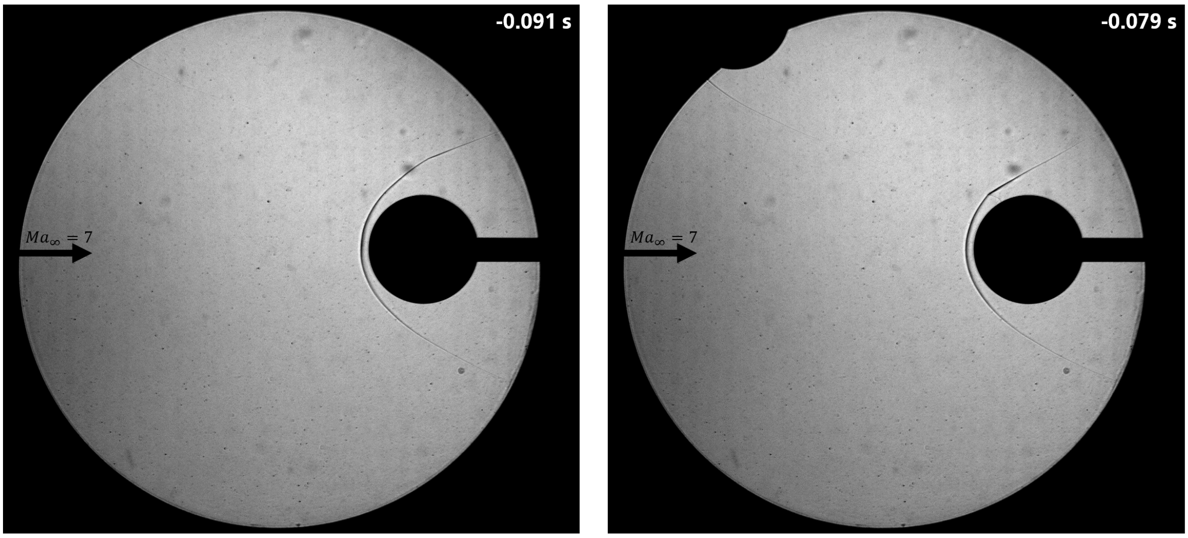

(a) No interaction **(b)** First interaction

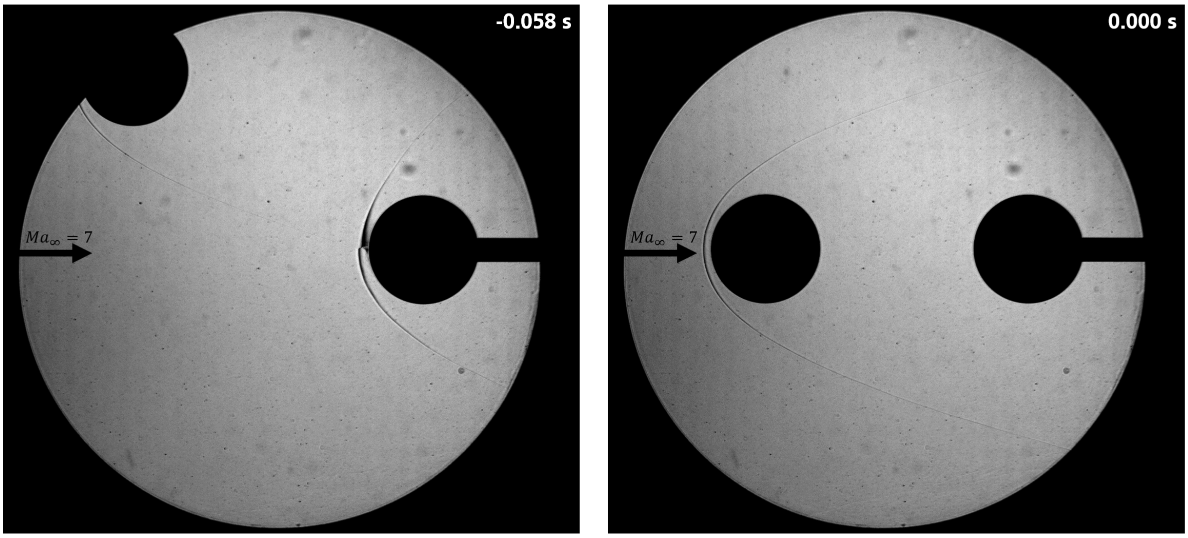

(c) First SSI in stagnation region **(d)** Aerodynamic shielding

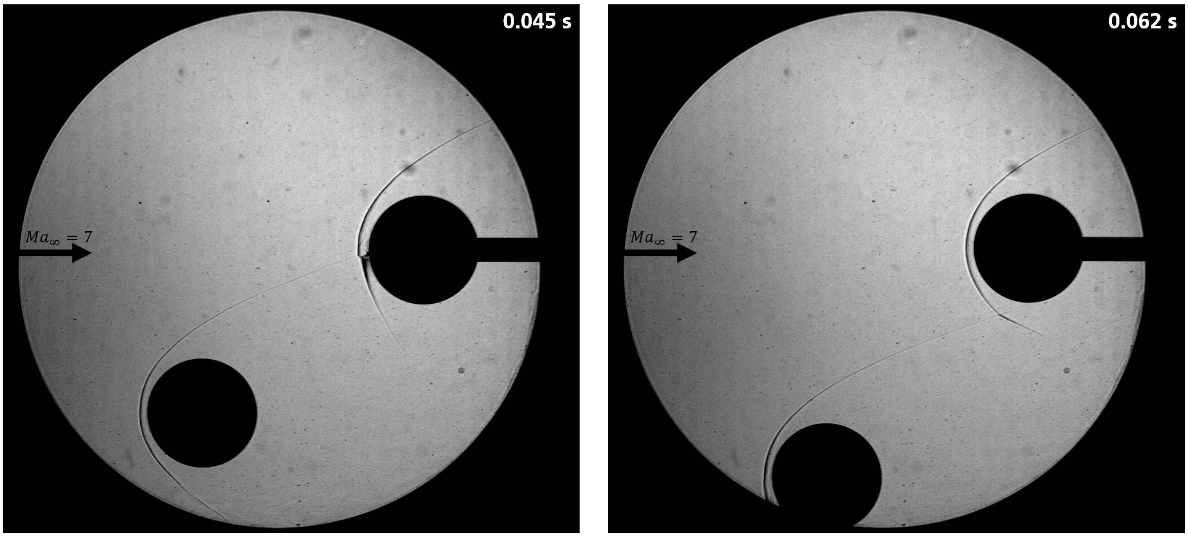

(e) Second SSI in stagnation region **(f)** Last interaction

Figure 5.1: A schlieren image sequence showing the motion behavior of aerodynamic interactions between a free-flying and a balance-mounted sphere

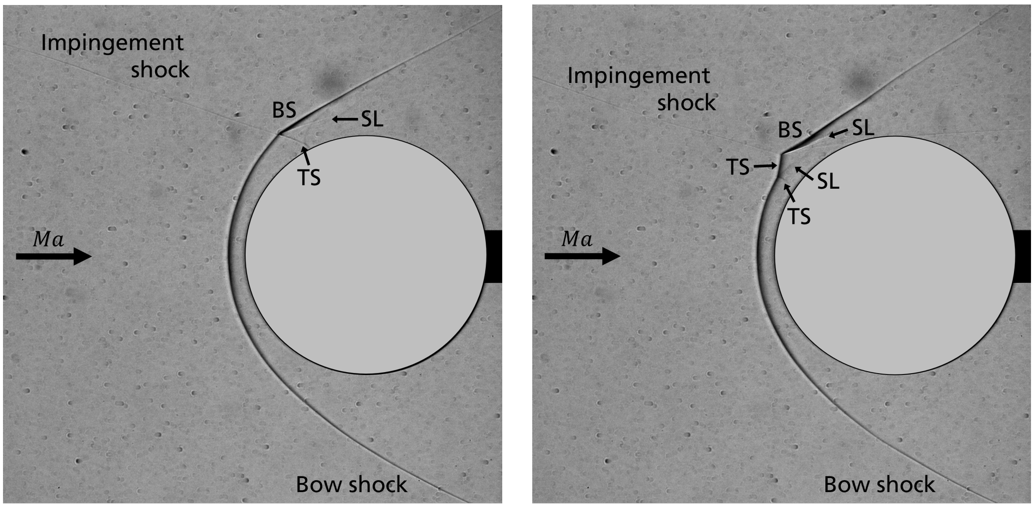

(a) Type I **(b)** Type II

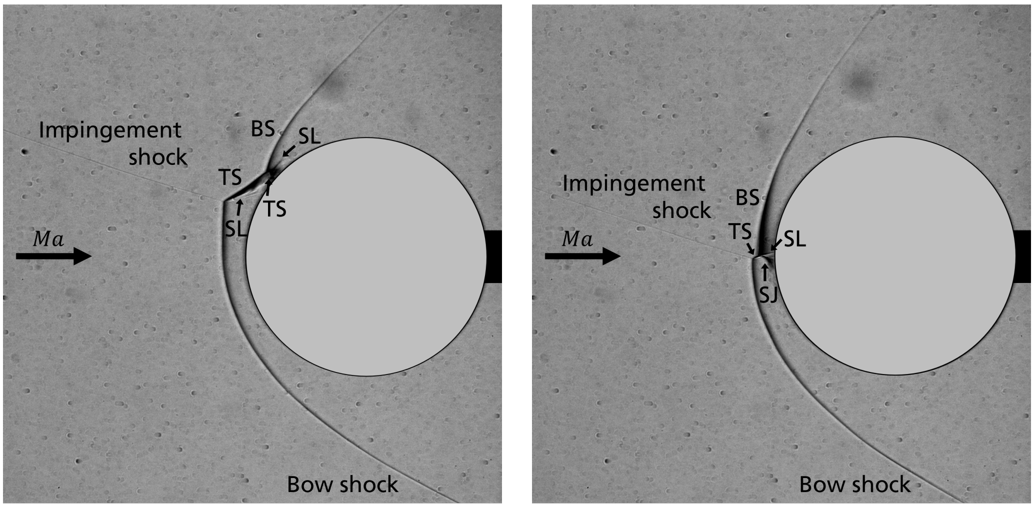

(c) Type III **(d)** Type IV

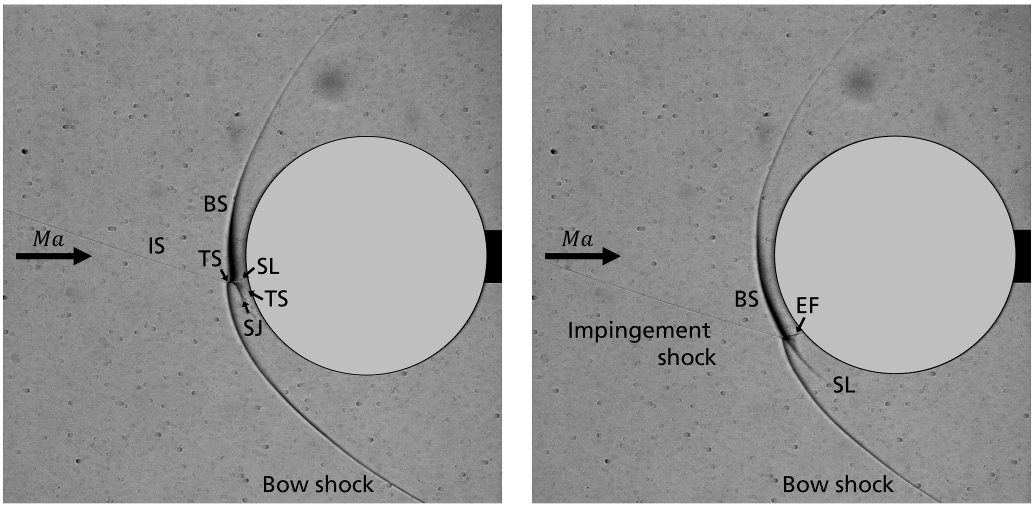

(e) Type V **(f)** Type VI

Figure 5.2: Edney's six types of SSI in qualitative flow field of sphere-sphere interactions including description of flow structures with Impingement Shock (IS), Bow Shock (BS), Transmitted Shock (TS), Shear Layer (SL), Supersonic Jet (SJ) and Expansion Fan (EF); leading sphere is outside the image at the top left

are too weak for the sensitivity of the present schlieren setup. While the trailing sphere gets further into the wake region of the leading one, the schlieren images show that the shape of the secondary bow shock alters significantly exhibiting a partial or full extinction of this shock wave. From figures 5.3a to 5.3c, the region of extinction gradually increases until the secondary bow shock completely disappears in figure 5.3d. A possible explanation for this might be that the subsonic part of the wake region extends to the trailing body, whereby a flow defection upstream the secondary stagnation region is enabled without the presence of a shock wave. This extension of the wake region can also be seen in the numerical schlieren representation of Patel and Navarro-Martinez [88]. In addition, a further interesting phenomenon can be seen in figures 5.3a to 5.3c as SSI is visible here, whereby the primary compression shock seems to aerodynamically interact with the secondary bow shock in such a way that the different Edney's types of shock-shock interaction appear in a weaker characteristic than with two bow shocks. This is visible in figure 5.3c and described schematically in figure 5.4, in which the impingement as a result of SSI occurs in the stagnation point of the aft object. In doing so, the Shock-Shock Interaction of the primary compression shock and the secondary bow shock represents an Edney type IV as shown in figure 5.2d. However, the upper part of the secondary bow shock interacts with the shear layer of the primary wake region, causing only a small part to be visible before it disappears.

5.1.2 Aerodynamic Forces & Moments

For the baseline configuration with a nominal diameter of $100\,\mathrm{mm}$, the force and moment coefficients are presented over time in figure 5.5 including the error bars of the overall uncertainties as described in section 3.4.2. The origin here is the time of axially aligned models. This configuration of the largest size is the best choice to present, because the sting-to-model-diameter ratio of 0.22 is favorable to minimize the sting effect on the aerodynamic forces as proposed by Gawehn *et al.* [33] as well as to enable a better utilization of the balance's calibrated measurement range leading to lower relative uncertainties. What stands out in these line charts is that strong fluctuations arise especially for the normal force (C_N), side force (C_Y) and yaw moment (C_n) components in the balance reference frame, whereas the measurement signals of the axial force (C_A), roll moment (C_l) and pitch moment (C_m) are largely unaffected by this. A possible explanation for this might be an oscillation of the sting-balance system, which was also observed in the schlieren images with the same frequency and phase. During the experiments, it was observed that the frequency of the oscillation changes with the mass of the sphere. Two flow phenomena seem to be responsible for this: On the one hand, the recirculation region of the wake on the back side provokes an unsteady interaction with the sting-balance system and on the other hand, the aerodynamic interactions with the leading body on the front side cause a changing asymmetric surface pressure distribution. As a result, the disturbance is much higher than the useful signals of these components that their data are not meaningful. Moreover, the roll moment coefficient exhibits a much higher uncertainty range than its fluctuations over time, while the pitch moment coefficient merely shows a weak effect of the aerodynamic interactions. However, the axial force coefficient features significant changes over time correlating to the different relative positions as well as a very good signal-to-noise ratio. In doing so, the axial force coefficient in figure 5.5a depicts the course of the different interaction phases as previously described in section 5.1.1, whereby the trailing sphere is initially isolated, then experiences SSI

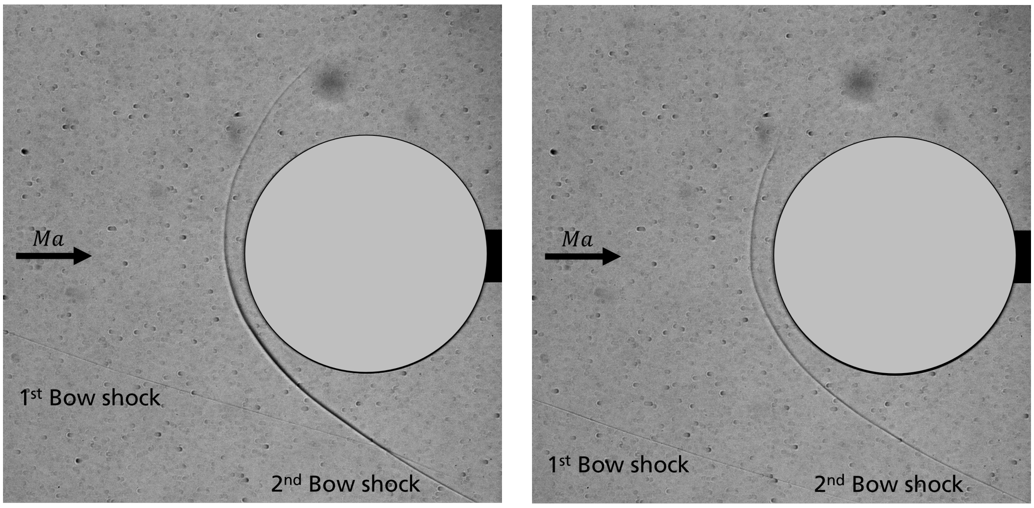

(a) Position 1 **(b)** Position 2

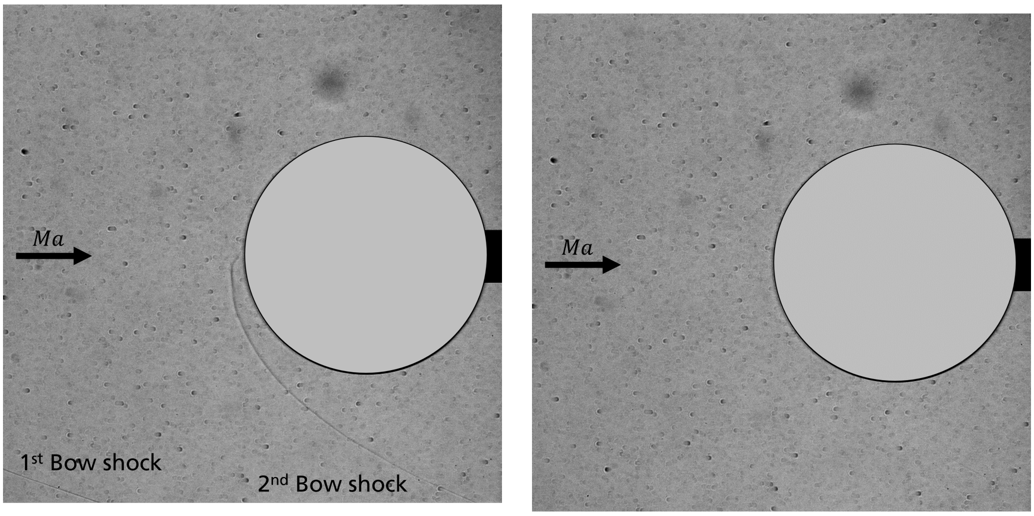

(c) Position 3 **(d)** Position 4

Figure 5.3: Different positions of WSI in qualitative flow field of sphere-sphere interactions including description of flow structures; leading sphere is outside the image at the top left or left

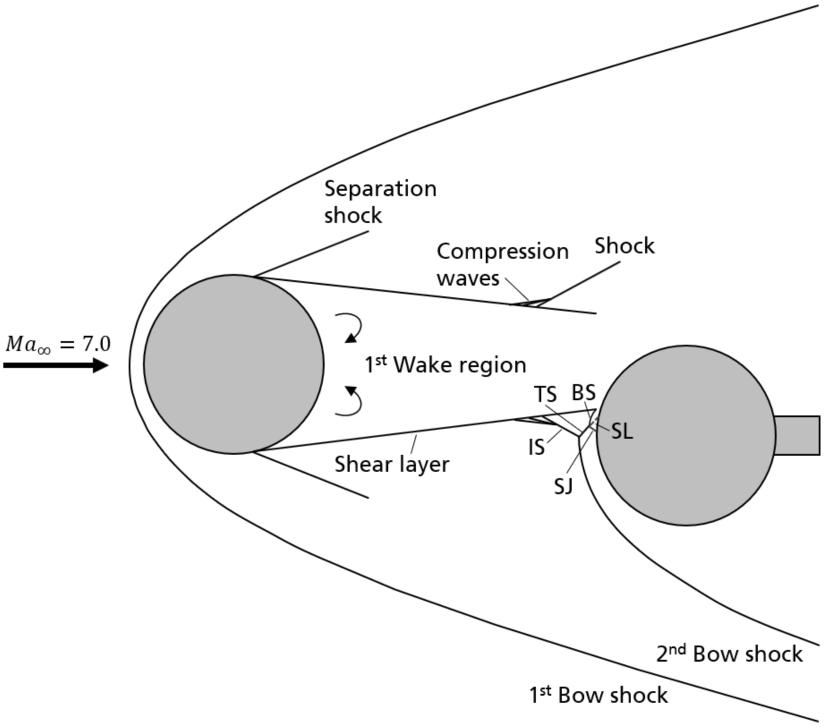

Figure 5.4: Schematic of qualitative flow field of a secondary sphere partially located in the near-wake of a primary sphere including flow features as Bow Shock (BS), Impingement Shock (IS), Transmitted Shock (TS), Supersonic Jet (SJ) and Shear Layer (SL)

followed by WSI, then SSI again, and finally an end of aerodynamic interactions. It is notable that further intense fluctuations are visible this time also in C_{A}, starting at a time of $t = 0.09\,\mathrm{s}$, although interaction phenomena do not occur anymore. The reason for this is the landing impact of the free-flying body on the bottom of the test section. All together, the following analysis is just focused on the axial force component.

5.1.3 Phenomena of Aerodynamic Interactions

Since the continuous vertical displacement of the free-flying sphere in front of the fixed one covers a full range of lateral positions, various flow phenomena were found that feature different motion behavior resulting from the affected aerodynamic loads. Figure 5.6a presents the trailing drag coefficient over the normalized vertical separation distance in the range from isolated to axial-aligned bodies, which is compared with a simplified numerical solution of the superposition method by Marwege *et al.* [72] based on an aerodynamic database of a single sphere at different free-stream Mach numbers. From this chart, it can be seen that the drag coefficient of the trailing object highly depends on the relative vertical distance between both bodies and thus on the type of interaction. Broadly speaking, the trailing drag coefficient increases compared to the single-body value for cases of SSI, whereas it decreases for arrangements with WSI. As expected, the maximum values arise with a peak of $C_{\mathrm{D2}} = 1.266$ for Edney type IV interactions with supersonic jet impingement, as it impinges almost vertically on the leading edge of the surface. This peak value exhibits an extremely good agreement with

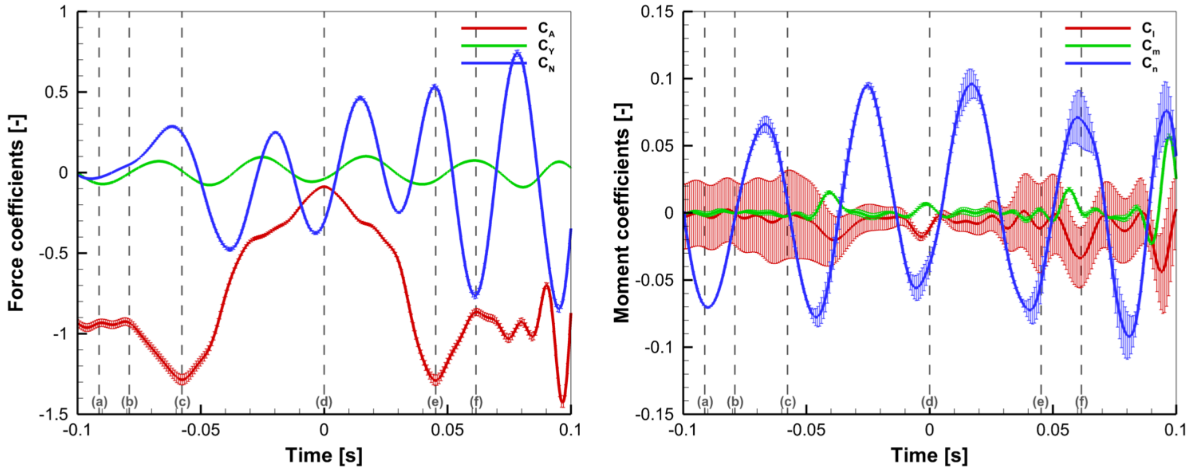

(a) Force coefficients **(b)** Moment coefficients

Figure 5.5: Exemplary evolution of force and moment coefficients including overall uncertainties of the balance-mounted trailing sphere with $d = 100\,\mathrm{mm}$; markers with letters indicate different phases according to figure 5.1

the superposition method, whereby the relative difference is just $0.16\,\%$. For the other Edney's types of SSI, it can be stated that the types I, II and VI have a low impact on the drag force, while the influence of the types III and V is moderate. This can be explained by the fact that the further the interaction is from the normal part of the bow shock, the weaker it is due to the decreasing shock wave strength.

Returning to the impact of WSI, it can be seen from figure 5.6a that the drag coefficient experiences a notable decline as the vertical distance between the sphere centers is reduced. This relationship is reasonable, because the total pressure also continuously decreases towards the wake's centerline according to the results of Erengil *et al.* [26]. Hence, the tailing body undergoes lower dynamic pressures. In doing so, a minimal value of $C_{\mathrm{D2}} = 0.078$ occurs for axially aligned spheres, which is $91.6\,\%$ lower than the single-body coefficient. The most interesting aspect of the experimental data in this line chart is the curve shape of the drag coefficient over the vertical separation distance after SSI with $\Delta\hat{z} > -0.6$ (referred to the shock radius), whereby the absolute gradient exhibits a continuous decrease firstly until it reaches an inflection point at $\Delta\hat{z} = -0.21$ and subsequently an increase. This agrees with the point where the curve significantly diverges from the prediction of the superposition method. The unexpected characteristic of the curve shape, especially the inflection point, can be explained by the flow topology, whereby SSI of the compression shock at the wake and the bow shock was found in figures 5.3a to 5.3c. This aerodynamic interaction is weaker than of two bow shocks, but it seems to cause a significant local increase of the pressure on the trailing body's surface. As a consequence, the drag force tendentiously rises, but yet the effect of lowering total pressures through the flow field behind the body is stronger. Another possible explanation, which applies in particular to small vertical distances, is that the subsonic region expands when a second sphere is present as described in section 5.1.1. In conclusion, the overall drag coefficient obviously decreases during WSI. However, it can be assumed that the maximum contribution to the drag due to this weaker SSI occurs once the aerodynamic interaction of the compression and bow shock impacts in the proximity of the secondary stagnation point (see figure 5.3c). The reason for this is that the primary compression shock has an almost identical shock angle at the present streamwise position than the secondary bow shock, whereby the peak arises at the same impingement point as the types of SSI in figure 5.2d. Thus, the inflection point is the state, when the maximum drag arise, that is contributed to the weaker SSI. Before, the lowering total pressures in the wake region provokes a decrease of the drag coefficient, whereas the weaker interaction of the compression and bow shock causes an increase. Afterwards, both effects lead to a decline of C_{D2}. This outcome is contrary to that of Erengil *et al.* [26], who explained the presence of the local peak in the stagnation pressure with the shear layer of the wake. Yet, the present study suggests that the SSI of the leading sphere's compression shock and the trailing sphere's bow shock is indeed the reason.

By comparing the experimental and simplified numerical results in figure 5.6a, it is apparent that high differences up to $67.2\,\%$ occurs as soon as a major part of the trailing body is inside the wake region of the leading object. Thereby, the drag coefficient for small vertical distances is highly overestimated by superposition as well as analytical methods like blast-wave analogy leading to overestimated decelerations during atmospheric entry. This discrepancy can be explained in part by the subsonic part of the wake, which is not considered in current analytical models, but in superposition method. However, the impact of the secondary sphere on the primary flow field in terms of an expanded subsonic region cannot be taken into account for this simplified numerical approach. It follows that experimental studies feature a big advantage for investigating WSI configurations.

On the question of the run-to-run repeatability, several tests with the same nominal test condition and models were carried out, which show minor variations in the actual free-stream dynamic pressure having a relative difference between maximum and mean value of $1.0\,\%$. The evolutions of the trailing drag coefficient with $d = 100\,\mathrm{mm}$ are provided in figure 5.6b. A very good repeatability of the curves can be seen here.

5.1.4 Effect of Reynolds Number & Size

A variation of the free-stream Reynolds number and model size was carried out in the test series with balance measurement, whereby both parameters were varied by means of the sphere diameter with a fixed reservoir condition for the former and an adjustable reservoir temperature for the latter. Furthermore, the models were initially positioned in such a way that a specified arrangement of $\Delta\widehat{x} = 4$ and $\Delta\widehat{z} = 3$ is established during the free flight of the leading object allowing a direct comparison. This is possible, because the shock angle and impingement point relative to the primary bow shock are the same by varying the sphere diameter. The drag coefficient of the trailing sphere over time is shown for different free-stream Reynolds numbers in figure 5.7a and for different diameters with $Re_{\infty} = 0.15 \cdot 10^{6}$ in figure 5.7b. In both line charts, it is apparent that the time difference between the two maxima decreases by reducing the diameter of the models. The reason for this is that the vertical distance between the extreme cases decreases due to the declining primary shock radius and sphere diameter while the velocity of fall remains nearly the same through the absence of lift forces. Moreover, closer inspections of the drag coefficient before aerodynamic interactions shows stronger fluctuations

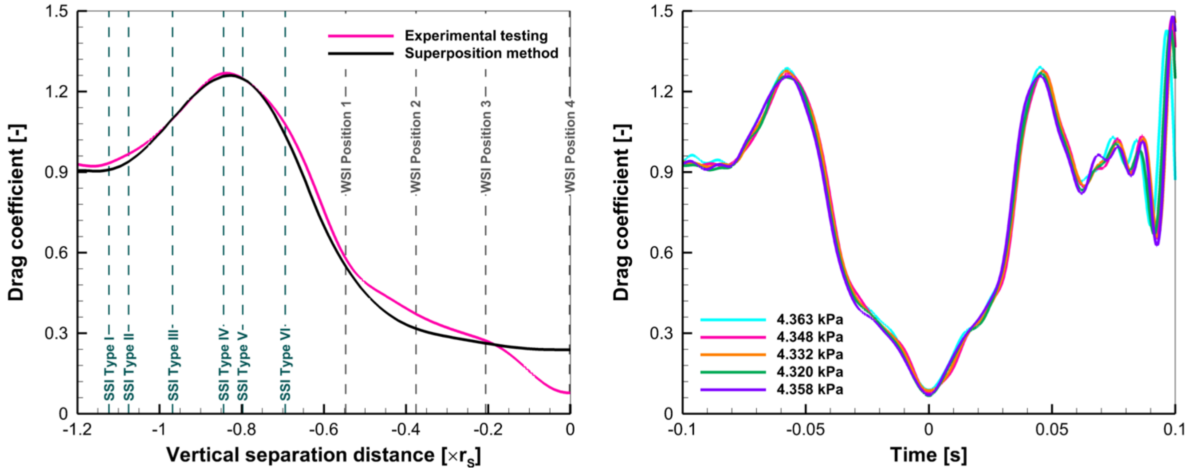

(a) Experimental and superposition data

(b) Repeatability

Figure 5.6: Comparison of trailing sphere's drag coefficients with $d = 100\,\mathrm{mm}$ between experimental and superposition data, as well as different tests with slightly different free-stream dynamic pressures

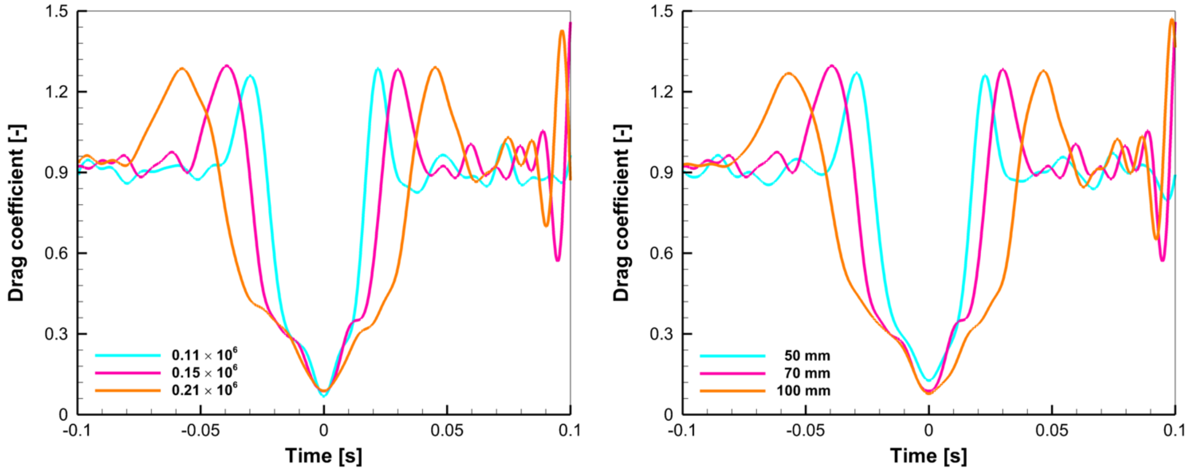

(a) Variation of diameter with same Re_u

(b) Variation of diameter with different Re_u

Figure 5.7: Influence of free-stream Reynolds number with $d = 100\,\mathrm{mm}$ and diameter with $Re_\infty = 0.15 \cdot 10^6$ on trailing sphere's drag coefficient

in the signal by decreasing the sphere diameter, which supports evidence for the explanation in section 5.1.2 concerning the choice of the baseline configuration.

Looking at the second maxima in figure 5.7 with the same normalized distance between the spheres, it can be seen that neither the Reynolds number nor the diameter have an effect on the drag coefficient during SSI. The same is true for the case of WSI. Although clear deviations between the different configurations are apparent in the minima of C_D, they are within the overall uncertainties. In this regard, the curves of the lowest sphere diameter show the outliers (see blue line in figures 5.7a and 5.7b), which is due to higher uncertainties of the drag coefficient as aforementioned. Thus, neither an effect of the free-stream Reynolds number nor of the model size could be demonstrated here. These findings are not surprising, because the influence of viscous effects on aerodynamic loads is negligible for blunt bodies in hypersonic turbulent flows.

5.2 Results of Two Free-Flying Blunt Bodies in Shock-Shock Interaction

Experimental results of out-of-line formations with spheres and cubes are presented in the following (see test matrix in table 5.2), which give an insight into the influence of body shape and inclination on stable shock-wave surfing in the presence of SSI. For a first impression, figure 5.8 depicts flight trajectories of various trailing bodies downstream a leading sphere in the xz-plane with an initial vertical distance of $\Delta\hat{z}_0 = 4.0$ overlaying the distinct flow regions of the free jet based on the experimental flow characterizations (see figure 2.2) as a gray contour layer. At the first glance, all trajectories show a complete agreement for the leading spheres and an intersection in the beginning with subsequent divergence in the middle and lower region of the core flow for the trailing bodies. There are clear differences between the two geometries of the secondary object, whereby the cubes undergo a significant higher streamwise displacement than the spheres.

This section begins by presenting the flow topology in combination with the corresponding measurement results of motion data and aerodynamic coefficients for an exemplary test case. Following this, the separation behavior between the leading and trailing body is examined. The

Table 5.2: Test matrix of SSI configurations

Primary body	Secondary body	ϑ_{01} [°]	ϑ_{02} [°]	$\Delta\hat{x}_0$ [$-$]	$\Delta\hat{z}_0$ [$-$]
Sphere	Sphere	N/A	N/A	4.8	0.0
Sphere	Sphere	N/A	N/A	4.8	2.4
Sphere	Sphere	N/A	N/A	4.8	3.2
Sphere	Sphere	N/A	N/A	4.8	4.0
Sphere	Sphere	N/A	N/A	4.8	5.0
Sphere	Sphere	N/A	N/A	7.2	3.2
Sphere	Sphere	N/A	N/A	7.2	4.0
Sphere	Cube	N/A	-30	4.8	4.0
Sphere	Cube	N/A	-30	7.2	4.0
Sphere	Cube	N/A	-20	4.8	4.0
Sphere	Cube	N/A	-20	7.2	4.0
Sphere	Cube	N/A	$+0$	4.8	4.0
Sphere	Cube	N/A	$+0$	7.2	4.0
Sphere	Cube	N/A	$+45$	4.8	4.0
Sphere	Cube	N/A	$+45$	7.2	4.0
Cube	Cube	$+20$	$+0$	4.8	4.0

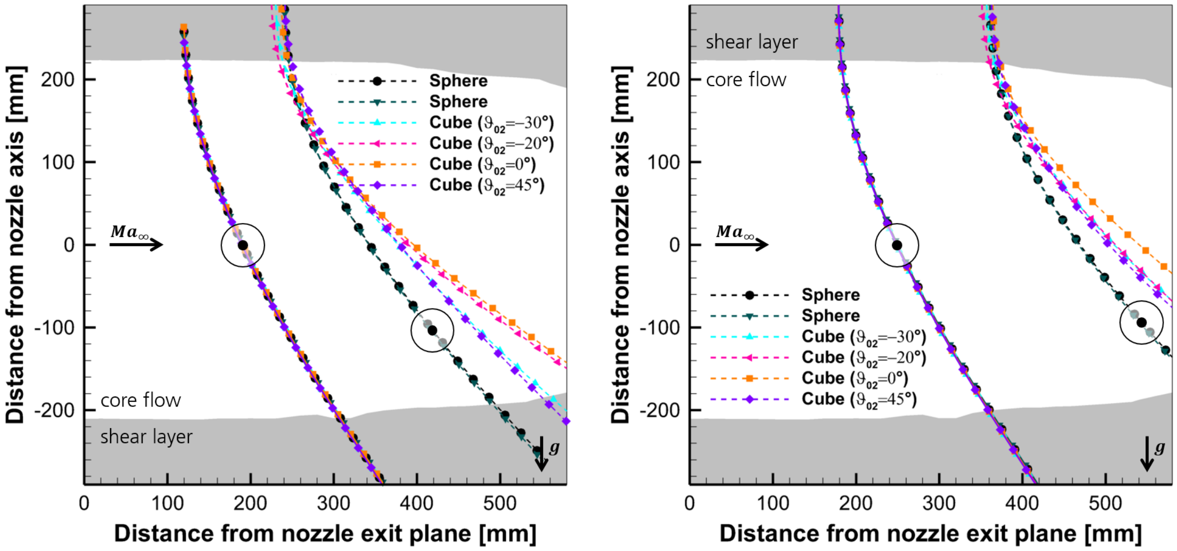

(a) $\Delta\hat{x}_0 = 4.8$ **(b)** $\Delta\hat{x}_0 = 7.2$

Figure 5.8: Flight trajectories of leading spheres (solid lines) and trailing bodies (dashed lines) for various configurations at $\Delta\hat{z}_0 = 4.0$ including flow areas of H2K's Mach-7 nozzle based on figure 2.2; black solid circles indicate position of both spheres at a certain moment

next subsection looks at the effect of body shape and inclination. Finally, the system dynamics of SSI are discussed.

5.2.1 Flow Topology

The two parameters varied in the experiments with two spheres were the initial distance between the model centers in streamwise and vertical direction, while the initial pitch angle is also taken into account for cubes. Figure 5.9 provides sequences of schlieren image with Sphere-Sphere (S-S) in figure 5.9a, Sphere-Cube (S-C) in figure 5.9b and Cube-Cube (C-C) in figure 5.9c configurations with almost the same initial positioning. For each image sequence, the time between the first and last recording is $4/75\,\mathrm{s}$. A pitch rotation of the cubes in the counter-clockwise direction due to the impact of the free jet's top shear layer can be seen in the images. From the schlieren images, it is apparent that cubes experience more streamwise displacement than spheres, regardless of whether these are leading or trailing objects, as expected. As a result, the trailing cubes are outside the viewing area of the schlieren image in the third snapshot of the sequence (see figures 5.9b and 5.9c) unlike the spheres (see figure 5.9a). In the flow fields of both bodies, detached bow shocks are visible, which undergo different Edney's types of SSI depending of the relative position. For example, figure 5.9a shows the Edney type IV interaction, figure 5.9b depicts the types III and IV, and figure 5.9c shows the types V and VI. Interestingly, two more shock-shock interactions can be seen just for the cube-cube configuration in figure 5.9c. Additionally, it can be seen that the bow shock of the trailing object becomes weaker until it disappears in the region of the primary wake region (see e.g. second image of figure 5.9c).

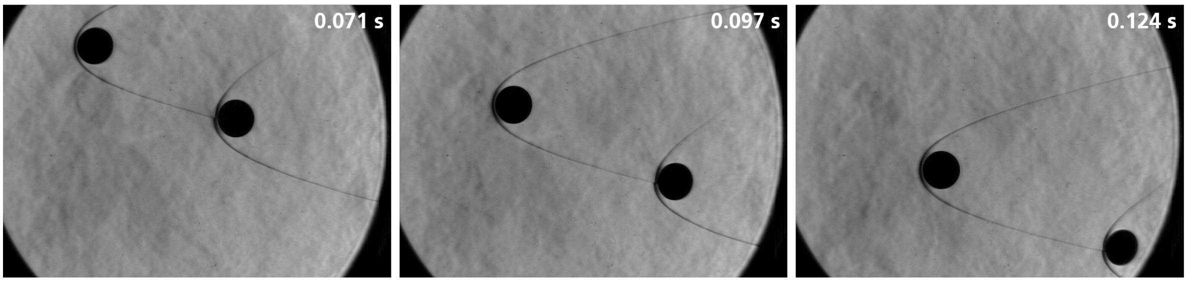

(a) Sphere-Sphere (S-S) configuration

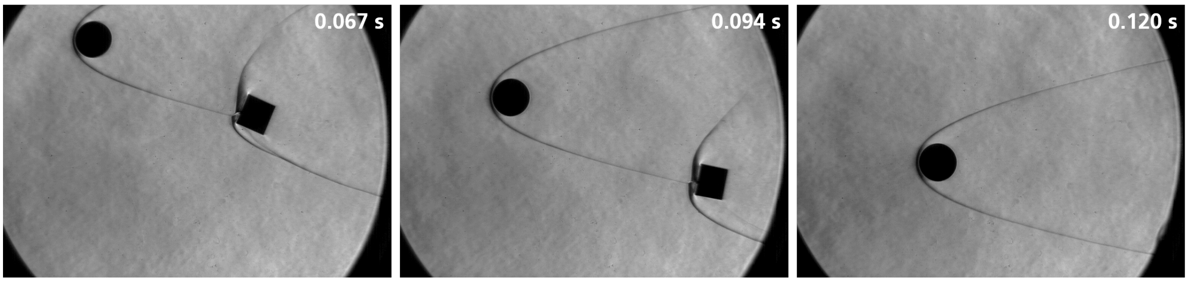

(b) Sphere-Cube (S-C) configuration with $\vartheta_{02} = -30°$

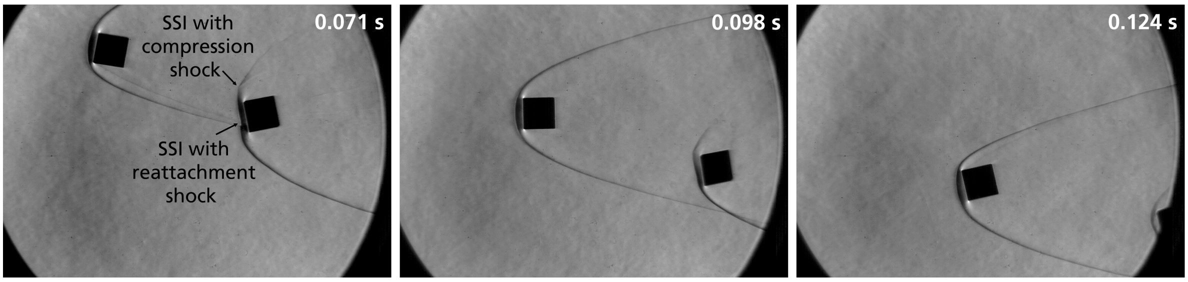

(c) Cube-Cube (C-C) configuration with $\vartheta_{01} = 20°$ and $\vartheta_{02} = 0°$

Figure 5.9: Selection of schlieren image sequences showing the motion behavior in free-flight for different tandem body pairs at $\Delta\widehat{x}_0 = 4.8$ and $\Delta\widehat{z}_0 = 4.0$

For a typical SSI configuration with two spheres, a sketch of the supersonic flow phenomena with the corresponding schlieren image in the background is presented in figure 5.10a, where the normalized separation distance is 4.8 in x-direction and 4.0 in z-direction. In doing so, the entire flow field of the leading object is identical to that of a single sphere as in [112], which indicates that the trailing body has no influence on the upstream flow field of the leading body. By contrast, the flow around the trailing sphere changes due to aerodynamic interactions as shown before. The shock-shock interaction of both bow shocks in the present case can be classified as type IV according to Edney [23]. As illustrated in the subfigure of figure 5.10a, the first bow shock impinges the second one in such a way that a supersonic jet as an extension of the impingement shock emerges at the intersection of the transmitted shock and inner bow shock. This supersonic jet flows toward the model surface and divides the subsonic region in front of the trailing body into two parts. Furthermore, the SSD of the second bow shock that is enclosed by the bow shock of the leading sphere is lower than in the free-stream. This observation is somewhat counter-intuitive, because a higher distance could be anticipated due to lower inflow Mach numbers in the region within the first bow shock compared to the free-stream Mach number. The wake region of the trailing spheres becomes asymmetric due to the inhomogeneous inflow. It is also apparent from figure 5.10a that the intensity of the second

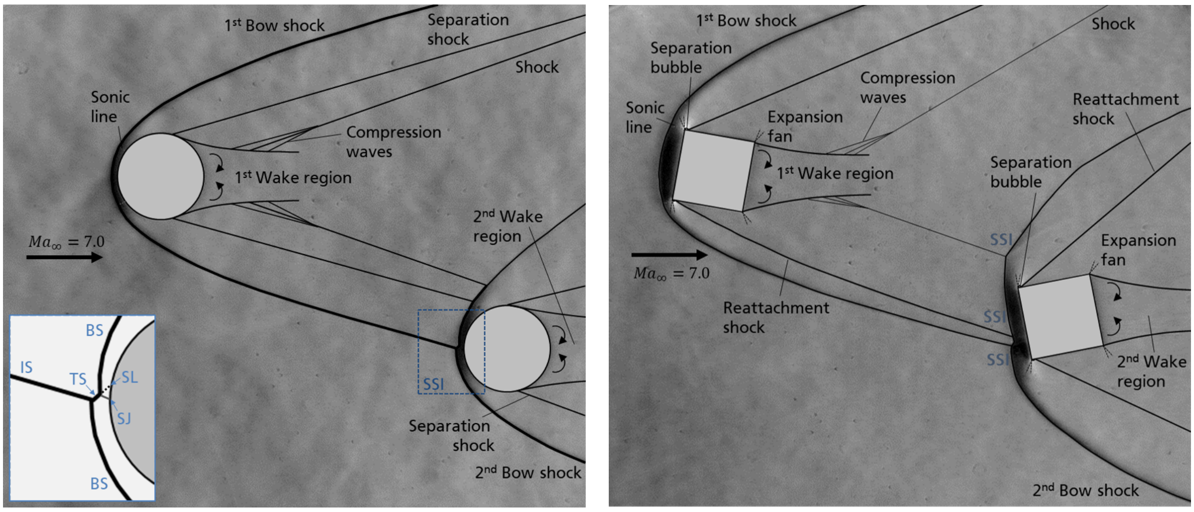

(a) S-S configuration **(b)** C-C configuration

Figure 5.10: Qualitative flow field of a secondary object located on the shock wave behind a primary object for a sphere-sphere configuration at $\Delta\hat{x} = 8.2$ and $\Delta\hat{z} = 4.0$ and a cube-cube configuration at $\Delta\hat{x} = 5.5$ and $\Delta\hat{z} = 2.3$ including schematic description of flow structures with Bow Shock (BS), Impingement Shock (IS), Transmitted Shock (TS), Supersonic Jet (SJ) and Shear Layer (SL)

bow shock decreases inside the region enclosed by the shock as a result of the lower Mach numbers in the wake.

Figure 5.10b shows the flow topology of two cubes with a normalized separation distance of 5.5 in x-direction and 2.3 in z-direction. As already mentioned, three simultaneous Shock-Shock Interactions are apparent in the schlieren image. In addition to the interaction of the two bow shocks, the reattachment shock as well as the shock from the compression waves of the primary body interact with the secondary bow shock in each case, that result in visible deformations of the bow shock. In contrast, no deformation of the secondary bow shock caused by the separation or compression shock can be seen in the schlieren images of figure 5.10a in the case of the two spheres. It is difficult to explain this result, but it might be related to the shape of the bodies and hence their three-dimensional flow topologies. In doing so, the shock waves of a sphere exhibit a stronger curvature in the transverse direction than a cube in its center region. Consequently, the S-S configuration exhibits point-wise interactions of the shock waves, while the C-C configuration shows line-wise interactions. For the cube-cube configuration, the SSI of the secondary bow shock with the primary bow shock, reattachment shock and compression shock causes greater deformation of the secondary bow shock within the shock region of the leading body than for a single interaction. In doing so, the Shock-Shock Interactions of the secondary bow shock with the reattachment shock and with the bow shock appear to approach the secondary bow shock closer to the front surface of the trailing cube due to their close proximity, which is why the SSD is reduced.

5.2.2 Model Motion

A single example for the displacement and velocity data of a front and aft sphere with an initial offset in z-direction is depicted in figure 5.11 that consist of the three-dimensional motion data with respect to their translation and their rotation. It is apparent that the trailing object enters the H2K's core flow some milliseconds before the leading one in all of the investigated tests. As a consequence, the shock-shock interaction on the trailing body is not fully established until the leading body has passed the shear layer and is fully in the core flow. To assess the alignment accuracy, the relative distances between both bodies in y-direction are examined, which exhibit a maximum deviation of $1.8\,\mathrm{mm}$. However, the maximum deviation in y-direction is $2.8\,\mathrm{mm}$ for the worse case of a leading sphere and a trailing cube, whereby the effect of the misalignment on the measurement uncertainty in the drag coefficient is less than $0.3\,\%$ referred to the single-body value. Thus, it can be assumed that both objects are approximately in the same xz-plane during free flight. In doing so, the roll, pitch, yaw and spanwise motion components of two interacting spheres are almost zero over the entire free-flight time unlike the streamwise and vertical motion components. For example, the changes of the trailing body in streamwise position ($\Delta x_2 = 219.0\,\mathrm{mm}$) and vertical position ($\Delta z_2 = -364.2\,\mathrm{mm}$) are about three orders of magnitude higher than the changes in spanwise position ($\Delta y_2 = 0.3\,\mathrm{mm}$) as shown in figures 5.11a and 5.11b, while the absolute changes in roll angle ($\Delta\varphi_2 = 0.3°$), pitch angle ($\Delta\vartheta_2 = -1.4°$) and yaw angle ($\Delta\psi_2 = 2.0°$) are less than or equal to $2°$. Thus, the analysis can be reduced to a two-dimensional motion. Concerning the tests with cubes, a significant change in the pitch angle was identified, while the maximal absolute changes in roll and yaw angle are slightly higher with $3°$ than of spheres. Consequently, the subsequent analysis in this work treats the motion as 3DoF (streamwise, vertical and pitch displacement) and neglects the out-of-plane motion (roll, yaw and spanwise displacement). In addition, the orientation angles for configurations with only spheres are neglected, as the maximum absolute changes in roll, pitch and yaw angle are low and they have no effect on drag and lift.

As shown in figures 5.11c and 5.11d, the absolute values of translational and angular velocities increase over time except for the spanwise component. Contrary to the assumption, the angular velocities of out-of-plane motion components show small deviations from zero, which indicates the high sensitivity of SSI on the motion derivatives due to very small deviations in alignment.

5.2.3 Aerodynamic Forces

As a result of the post-processing described in section 3.2, the aerodynamic coefficients are determined based on the previously shown motion data. Drag and lift force coefficients of a leading and trailing sphere in an out-of-line formation (see figure 5.9a) are plotted against the normalized time in figure 5.12. The pitching moment coefficients of both models are approximately zero and are therefore not depicted. In addition, error bars representing estimated overall uncertainties are shown as outlined in section 3.4.2, whereby the relative average uncertainties are $3\,\%$ for C_D and $7\,\%$ for C_L based to their peak values. Small deviations from the constant drag coefficient can be seen at the edges of leading body's graph, which are a minor effect of the free jet's shear layer. As expected, the drag coefficient of the leading sphere matches on average with the single-body value of $C_\mathrm{D} = 0.926$ (see section 4.1.3), whilst the lift

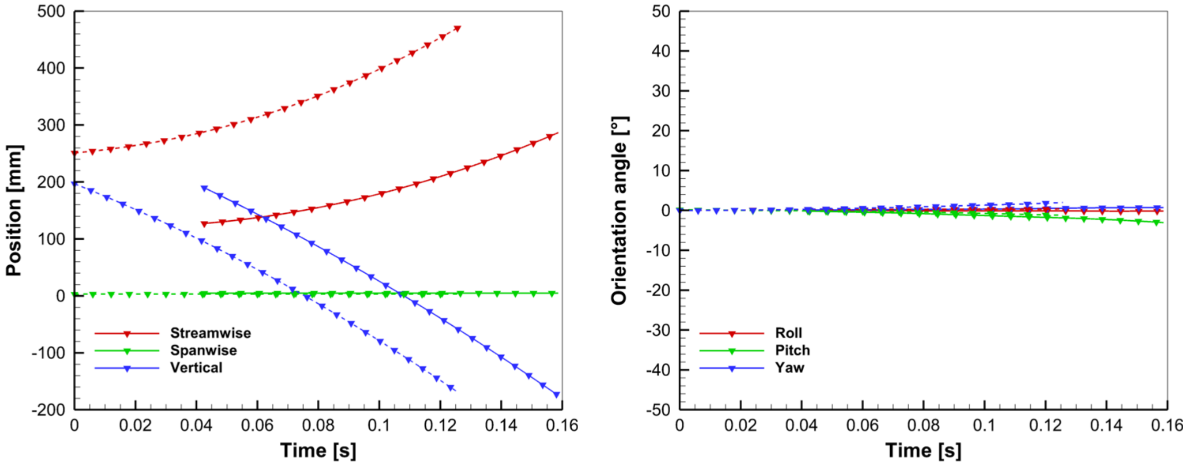

(a) Positions in x, y & z **(b)** Orientation angles in φ, ϑ & ψ

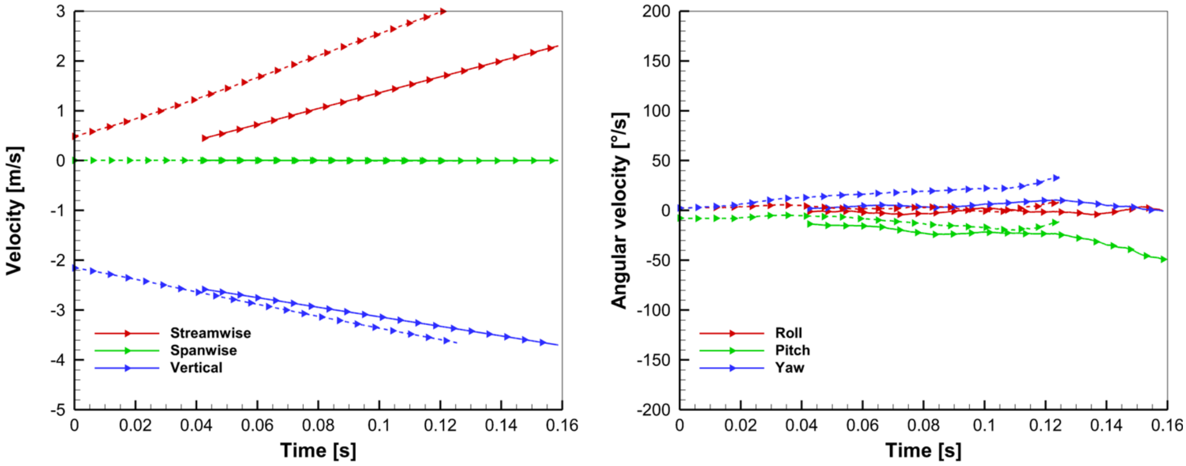

(c) Velocities in x, y & z **(d)** Angular velocities in φ, ϑ & ψ

Figure 5.11: Evolution of 6DoF translational and angular motion data in core flow of a leading (solid lines) and trailing sphere (dashed lines) with $\mathit{\Delta}\widehat{x}_0 = 4.8$ and $\mathit{\Delta}\widehat{z}_0 = 4.0$

coefficient is nearly zero. It is notable that the drag coefficient of the secondary body increases steadily from 0.92 to 1.22 in the beginning because of the aforementioned weaker aerodynamic interaction, as long as the leading object is located in the free jet's shear layer in contrast to the trailing object. Subsequently, the trailing drag coefficient yet reaches a roughly constant value as soon as both objects are inside the core flow of the free jet having a maximum value of $C_{\mathrm{D2}} = 1.28$. These results are in line with those of previous studies [e.g. 61]. Regarding the trailing lift force, it can be seen in figure 5.12 that a reduction of its coefficient over time emerges first due to the appearing interaction, followed by a rise due to the entrainment tending to zero (see the motion of both spheres in figure 5.9a).

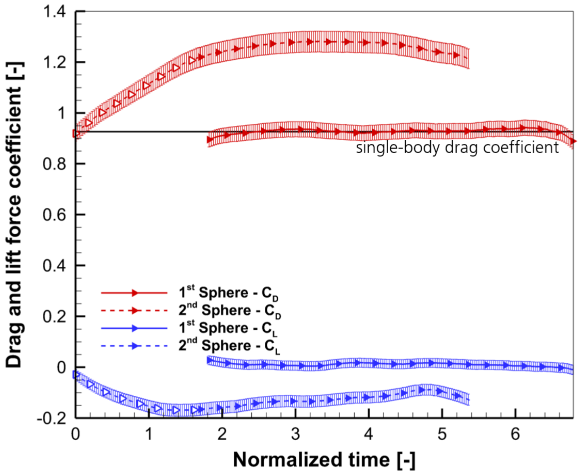

Figure 5.12: Exemplary evolution of drag (red) and lift force coefficients (blue) in core flow including overall uncertainties of a primary (solid lines) and a secondary sphere (dashed lines) with $\Delta\widehat{x}_0 = 4.8$ and $\Delta\widehat{z}_0 = 4.0$; open symbols indicate a leading body in top shear layer

5.2.4 Separation Behavior

Prior studies have noted the importance of the relative positioning on the separation behavior of multiple bodies. Figure 5.13 shows the flight trajectories of the trailing spheres plotted as $\Delta\widehat{z}$ (see equation (5.1)) against $\Delta\widehat{x}$ (see equation (5.2)) for different initial spacings. Please note that the two spheres relatively move away from each other in x-direction and slightly towards each other in z-direction before entering the core flow because of the shear-layer-influenced aerodynamic loads. What stands out in the chart of relative trajectories is that the streamwise separation distance rises in all out-of-line cases. This is due to an increase in the pressure on the windward surface of the secondary body resulting from the impinging flow feature of the flow structure behind two interacting bow shocks. This flow feature depends on the Edney's type of SSI and can be a supersonic jet or a transmitted shock. The variation of the initial vertical component reveals that the greater the lateral distance of the secondary sphere to the primary sphere in combination with a higher axial distance, the greater the increase in the streamwise separation distance over approximately the same period of time. In consequence, the trailing bodies tend to move into different flow regions of the leading objects after aerodynamic interaction. For $\Delta\widehat{z}_0 = 2.4$ and $\Delta\widehat{z}_0 = 3.2$, the trailing sphere moves away from the leading sphere in streamwise direction and then tends to move towards it. In doing so, the trailing sphere reaches the near-wake more quickly in the test cases with $\Delta\widehat{z}_0 = 2.4$ (see purple line) than with $\Delta\widehat{z}_0 = 3.2$ (see black line). Increasing the initial vertical separation distance to $\Delta\widehat{z}_0 = 4.0$ results in shock-wave surfing, whereby the secondary sphere ends in the far-wake for $\Delta\widehat{x}_0 = 7.2$ (see cyan and blue-gray dashed lines) afterwards or continues to interact with the shock for $\Delta\widehat{x}_0 = 4.8$ (see cyan and blue-gray solid lines). The necessary condition according to Marwege *et al.* [72] for shock-wave surfing is fulfilled for the tests with $\Delta\widehat{x}_0 = 4.8$ and $\Delta\widehat{z}_0 = 4.0$ (as presented in section 5.2.3), but this only applies to the last third of the data. Previous studies such as [91] have identified the near-wake, the far-wake and the shock region as final zones, which is consistent with the present results.

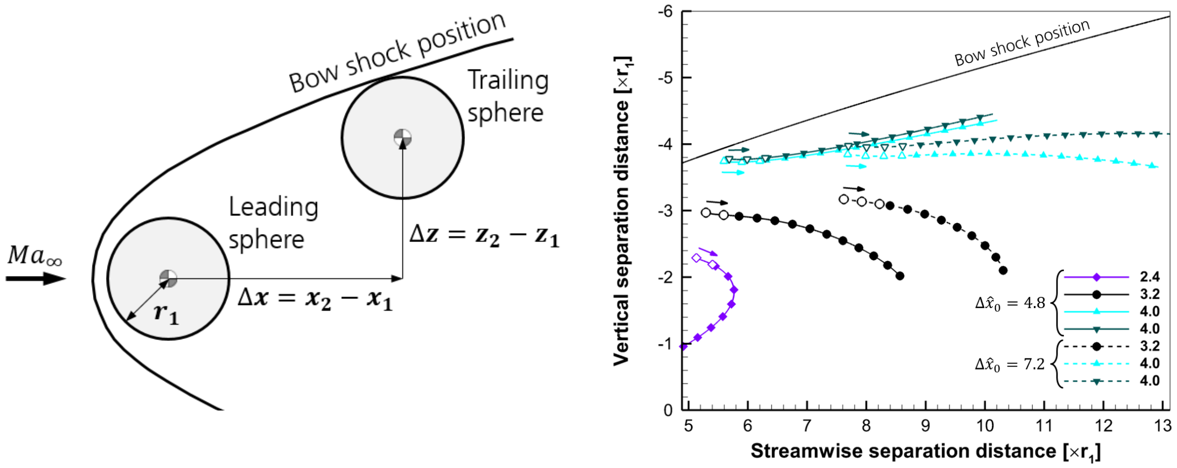

(a) Definition of separation distances

(b) Flight trajectories

Figure 5.13: Normalized flight trajectories of trailing spheres related to leading spheres in core flow (closed symbols) and bottom shear layer (open symbols) for different initial vertical positions at $\Delta\hat{x}_0 = 4.8$ (solid lines) and $\Delta\hat{x}_0 = 7.2$ (dashed lines); reversed vertical chart axis

Figure 5.14 shows the drag and lift coefficients of the trailing sphere for multiple tests with different initial streamwise and vertical distances. In doing so, the data are plotted against the normalized vertical separation distance based on the calculated shock radius. The results show a strong impact of the vertical separation distance on both force coefficients, whereas the moment coefficients are not shown as they were found to be negligibly small with $|C_{\mathrm{M2}}| < 0.005$. The drag coefficient continuously increases from $C_{\mathrm{D2}} = 0.07$ for axially aligned bodies to 1.29 during the shock-wave surfing, which is $39.3\,\%$ more than the single-body value without aerodynamic interactions. As regards the lift coefficient, this quantity is positive (attractive force) with a peak of $C_{\mathrm{L2}} = 0.24$ until the zero-crossing at $\Delta\hat{z} = -0.80$ (referred to the shock radius) and turns to negative coefficients (repulsive force) afterwards. The comparison of the absolute difference between single-body and peak value of the drag and lift coefficients shows that neither a general dominance of the streamwise nor the lateral separation is apparent for two identical spheres. The most striking result to emerge from the coefficient data is that the curves at the same vertical separation distances (compare black solid and dashed line with circles in figure 5.14) are in very good agreement, although the streamwise separation distance differs on average by approximately two times the radius (see black lines in figure 5.13). It follows that the drag and lift coefficients are less sensitive to the separation distance in the streamwise than in the vertical direction. This is reasonable, because the shock angle β of the primary bow shock changes less further downstream for tandem configurations in contrast to proximal bodies. For SSI cases that have the same distance of the secondary body to the primary bow shock, the shock angle mainly influences the aerodynamic force coefficients. As a result, it can be assumed that the sensitivity decreases with increasing streamwise separation distance, since the shock angle converges.

To validate the aerodynamic coefficients determined with the stereo tracking method, experimental force-balance measurements as in section 5.1.2 are also presented in figure 5.14a. In comparison, the drag coefficients of both measurement methods are in very good agreement,

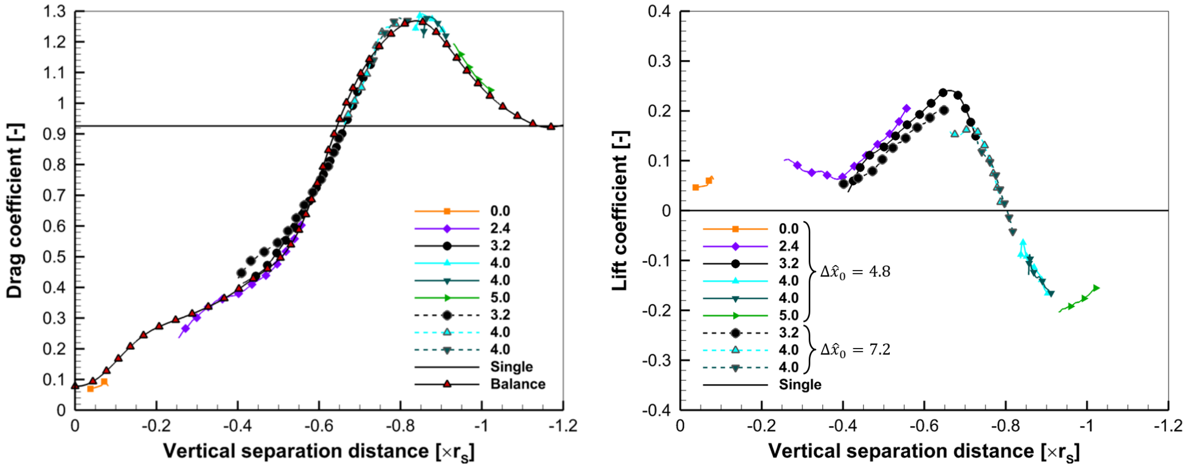

(a) Drag force **(b)** Lift force

Figure 5.14: Influence of vertical separation distance on trailing sphere's force coefficients based on force-balance and stereo tracking measurements at $\Delta\hat{x}_0 = 4.8$ (solid lines) and $\Delta\hat{x}_0 = 7.2$ (dashed lines); vertical separation distance is normalized with shock radius

although their streamwise distances from each other differ by up to 7 times the sphere radius as well as the wake of the secondary sphere is disturbed by the balance.

5.2.5 Effect of Body Shape & Inclination

To understand the effect of body shape and inclination on the separation behavior, the trailing sphere is replaced by a cube with nearly equal mass and a variation of its initial pitch angle is carried out. In figure 5.15, relative flight trajectories in the xz-plane and their corresponding pitch angles are illustrated for different initial inclinations of sphere-cube pairings with $\Delta\hat{x}_0 = 4.8$. What stands out in figure 5.15 is that the separation distance and pitch angle highly depend on the shape and initial orientation for the same nominal initial positions. Concerning the translational component in figure 5.15a, the trailing cube experiences an immediate entrainment within the primary bow shock for $\vartheta_{02} = -20°$ and $\vartheta_{02} = 0°$, a slow expulsion from the primary bow shock for $\vartheta_{02} = 45°$ as well as an extended shock-wave surfing for $\vartheta_{02} = -30°$. For the latter, the necessary condition for stable shock-wave surfing ($\tan\beta = \frac{\Delta a_z}{\Delta a_x}$) is satisfied. After aerodynamic interactions, these objects tend to end in the far-wake, the aerodynamically independent region and the shock region, respectively. The results also show a correlation between the final vertical separation distance and the absolute initial pitch angle starting from the orientation of plane-exposed to edge-exposed, which is also consistent with the results of tests at $\Delta\hat{x}_0 = 7.2$. This relationship may be explained by the fact that the induced lift force due to the body inclination is positive (attractive) for pitch angles larger than $-45°$ and negative (repulsive) for pitch angles smaller than $-45°$ (compare with figure 4.12). In the case of shock-wave surfing, a trailing cube roughly traces the same trajectory referred to the leading sphere just like a trailing sphere (compare cyan solid line in figure 5.15a with cyan solid line in figure 5.13). Thereby, the cube undergoes an increased streamwise separation in nearly the same time. Concerning the angular component in figure 5.15b, the secondary body's pitch

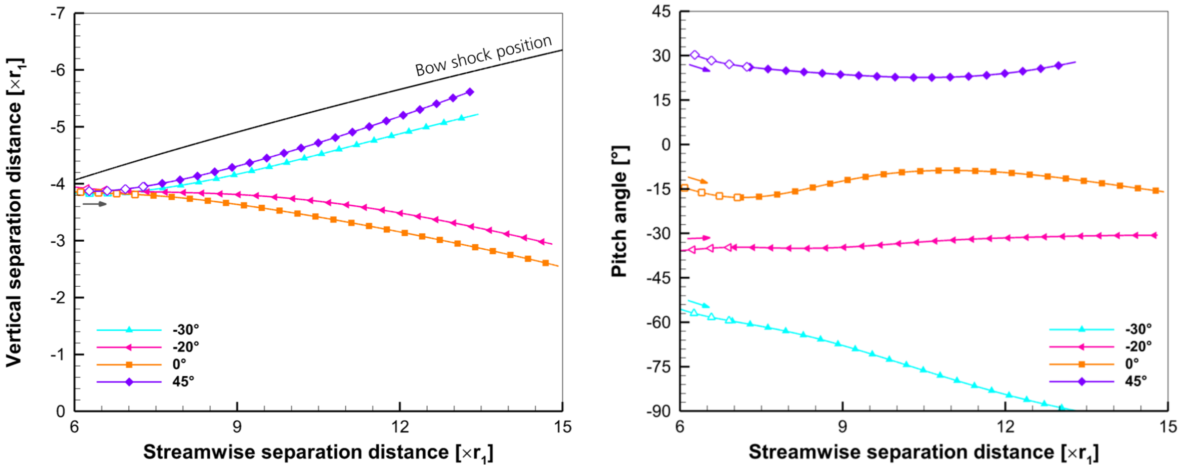

(a) Flight trajectories **(b)** Pitch angles

Figure 5.15: Normalized flight trajectories and pitch angles of trailing cubes related to leading spheres in top shear layer (open symbols) and core flow (closed symbols) for different initial pitch angles at $\Delta\widehat{x}_0 = 4.8$ and $\Delta\widehat{z}_0 = 4.0$; reversed vertical chart axis for flight trajectories

angle experiences an oscillation for $\vartheta_{02} = 0°$, a slight uniform increase for $\vartheta_{02} = -20°$, a rapid decrease for $\vartheta_{02} = -30°$ as well as a reversal of the rotational direction for $\vartheta_{02} = 45°$. As a result, the pitch motion is affected by the pitching moment induced by the orientation of the body as well as by the SSI between both objects as previously shown for the lateral separation. This finding is reasonable, since Edney's type III and IV interactions can produce very high local pressures on the surface [23] and it is well known that the aerodynamic moments are very sensitive to the exact pressure distribution. Consequently, the position of the impingement point strongly influences the magnitude and sign of the superimposed pitching moment and also the lift force. Hence, the aerodynamic load through the body inclination can cause an amplification or attenuation of the pitch and vertical displacement, which explains the different types of motion.

The results for the normalized vertical separation velocity are shown together with the pitch angles of the trailing bodies in figure 5.16. It should be noted that negative values represent repulsive motion tendencies regarding the vertical component, since the measured vertical separation distances are negative as the aft object enters the flow first. First of all, it can be seen that the velocity curves tend to values close to 0.3 at $\widehat{t} = 0$, which is the result of the positive lift force due to the shear layer as aforementioned. Just as already shown for the separation distance and the pitch angle, a major difference between various initial inclinations was found for the vertical separation velocity in terms of the observed motion behavior. On the one hand, the curves of the trailing cubes with $\vartheta_{02} = -30°$ and $\vartheta_{02} = 45°$ increase more steeply and reach higher extreme values than those of sphere-sphere arrangements that feature shock-wave surfing. The extrema in figure 5.16a are higher compared to those of other studies with side-by-side test cases like by Li *et al.* [66] or Park *et al.* [85]. On the other hand, the vertical separation velocity for sphere-cube configurations with $\vartheta_{02} = -20°$ and $\vartheta_{02} = 0°$ turns into increasing attractive values as soon as the trailing cube is fully entrained within the region bounded by the primary

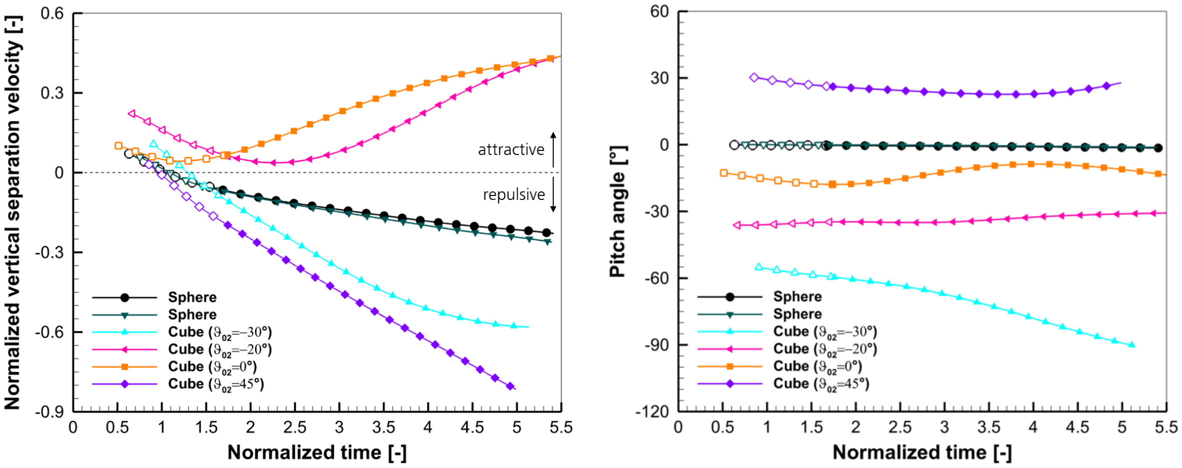

(a) Normalized vertical separation velocities **(b)** Pitch angles

Figure 5.16: Evolution of trailing body's normalized vertical separation velocity with view to a leading sphere and pitch angle in top shear layer (open symbols) and core flow (closed symbols) for different configurations at $\Delta\widehat{x}_0 = 4.8$ and $\Delta\widehat{z}_0 = 4.0$

bow shock. The strong impact of the initial pitch angle is related to the induced lift force due to the body inclination.

The final lateral velocity here is defined as the peak value of the repulsive vertical separation velocity attained in the H2K's core flow. Table 5.3 reports the normalized final lateral velocity $\widehat{v}_T$ and the Passey's constant C based on equation (1.2) for different configurations of the trailing body. Comparing the present results with those from Laurence *et al.* [61] at $\widehat{v}_T = 0.24$, the final lateral velocity is almost the same in the case of two equal spheres and the constant is in the range identified by Passey and Melosh [87]. For trailing cubes, it is remarkable to see that the non-dimensional parameters in table 5.3 are higher than for spherical bodies and depend on the initial pitch angle, while the normalized final lateral velocity of cubes is two to three times larger than that of spheres. However, this result differs from Park *et al.* [85], who found significantly lower values with $C = 0.094$ (without rotation) for side-by-side configurations representative of the position after an actual fragmentation event.

Closer inspections of the force coefficients should aid to find the cause of the cube's higher

Table 5.3: Experimental normalized final lateral velocities $\widehat{v}_T$ and Passey's constants C for various shapes and initial pitch angles ϑ_{02}

Shape	ϑ_{02} [°]	$\widehat{v}_T$ [−]	C [−]
Sphere	N/A	+0.246	0.040
Cube	−30	+0.581	0.183
Cube	−20	−0.037	N/A
Cube	+0	−0.042	N/A
Cube	+45	+0.815	0.360

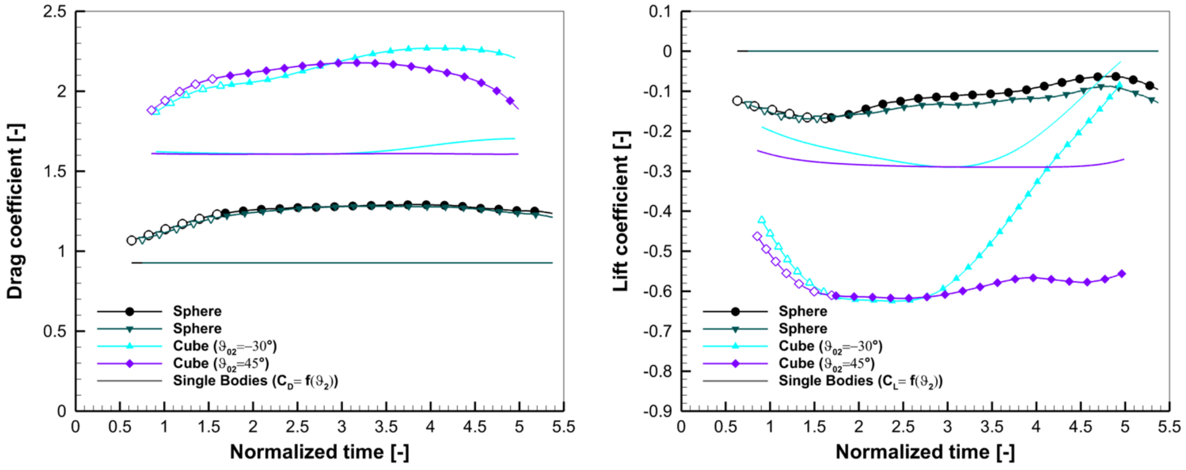

(a) Drag forces **(b)** Lift forces

Figure 5.17: Comparison of trailing object's force coefficients in terms of leading spheres in top shear layer (open symbols) and core flow (closed symbols) with $\Delta\widehat{x}_0 = 4.8$ and $\Delta\widehat{z}_0 = 4.0$ and single-body values (no symbols) based on equations (4.2) and (4.3) with measured pitch angle

separation velocities. For this reason, the drag and lift coefficients over the normalized time of tests with occurring shock-wave surfing are compared in figure 5.17 with single-body values calculated with the correlations of equations (4.2) and (4.3) using the secondary body's pitch angle measured in this work. It is apparent from this figure that the extreme values of the force coefficients are in general higher in terms of shock-shock interaction. Interestingly, the relative increases of the drag coefficient in figure 5.17a with respect to the single-body value tend to $40\,\%$ regardless of the trailing object's shape. However, the maximum value of the cubes is nearly twice as much as that of the spheres resulting in a faster streamwise separation. Regarding the lift coefficient in figure 5.17b, it is noticeable that this quantity approximately doubles for cubes in comparison to the single-body value at the same pitch angle. By comparing the lift coefficients of both body shapes, the extreme value of the trailing cubes is even three times as large as that of the spheres. It can therefore be concluded that the lateral separation is determined by the shock-shock interaction as well as the induced lift force due to the body inclination of non-spherical bodies. This study confirms the initial finding of two superimposed effects by Park *et al.* [85]. As a result, the discrepancy between real-world observations and previous laboratory studies with only spherical bodies can be explained by the current finding to some extent.

In conclusion, the body orientation of a rotating non-spherical secondary object in the present study causes an increase in the final lateral velocity and streamwise displacement in the case of shock-wave surfing, which is consistent with [66]. This is expected, since the lift force due to the inclination is zero for cubes in statically stable trim flight attitudes, whereas a rotating body can effect a strong attractive lift force depending on its orientation.

5.2.6 System Dynamics

In order to analyze the stability behavior of tandem bodies in SSI configurations, an appropriate frame of reference based on the position of primary bow shock was applied as per equations (5.7) and (5.8), which are similar to that of Laurence and Deiterding [58]. Here, $\widehat{r}_S$ represents the shock radius, which is normalized by the sphere radius and varies as a function of $\Delta\widehat{x}$. This is also true for the shock angle, as the bow shock has a curvature. Thus, the normalized vertical shock distance $\widehat{\eta}$ is the distance in z-direction between the center of the secondary model and the position of primary bow shock as a multiple of the sphere radius. The shock angle is time-dependent, because the trailing body changes its relative streamwise distance to the leading body over time. However, the maximal differences in the shock angle from start to end of free-flight are less than $3°$ in the present tests, which results in a maximum change in the vertical shock velocity $\widehat{v}_\eta$ of $6.8\,\%$ relative to the maximum change in the vertical shock velocity that neglects the dependence of shock angle and streamwise separation distance. As a consequence, the influence of the aerodynamic forces on shock-wave surfing is significantly higher here than of the shock curvature, which is why the effect of the shock angle on the stability enhancement is neglected in the following. Hence, the system of differential equations related to the relative translational motion between two spheres can be simplified to a two-dimensional approach to enable a phase-plane analysis. Please note here that the phase space of the sphere-cube cases has a higher dimension due to the influence of the pitch angle on the aerodynamic coefficients, which is why a two-dimensional projection is used for the graphical representation to enable a direct comparison with the sphere-sphere pairs.

$$\widehat{\eta} = \Delta\widehat{z} - \widehat{r}_S \tag{5.7}$$

$$\widehat{v}_\eta = \Delta\widehat{v}_z - \tan\left(\beta\right)\Delta\widehat{v}_x \tag{5.8}$$

Figure 5.18 presents multiple phase paths of the trailing object's motion for spheres and cubes in different initial configurations. Stationary points lie at $\widehat{v}_\eta = 0$ enabling shock-wave surfing, whereas positive values indicate an instantaneous tendency towards expulsion of the trailing body from the region bounded by the primary bow shock while negative values suggest a tendency towards entrainment. With regard to the stability of shock-wave surfing, the phase path moves around the stationary point for a stable state, whereas the phase path approaches the stationary point along one direction and moves away from it along the other direction for an unstable state.

For trailing spheres at different initial vertical separation distances as shown in figure 5.18a, it can be seen that the trajectories approach an equilibrium solution in the vicinity of $\widehat{\eta} = -0.9$, whereby the vertical shock velocity increases in absolute terms as the trajectories move away from the stationary point. Thus, this is a saddle point indicating the state of unstable shock-wave surfing. Interestingly, this relative vertical position of the saddle point matches to that of the sphere-wedge case in [58] with a wedge angle of $10°$. This similarity can be explained by the fact that the primary bow shock of the sphere is approximately equivalent to an oblique

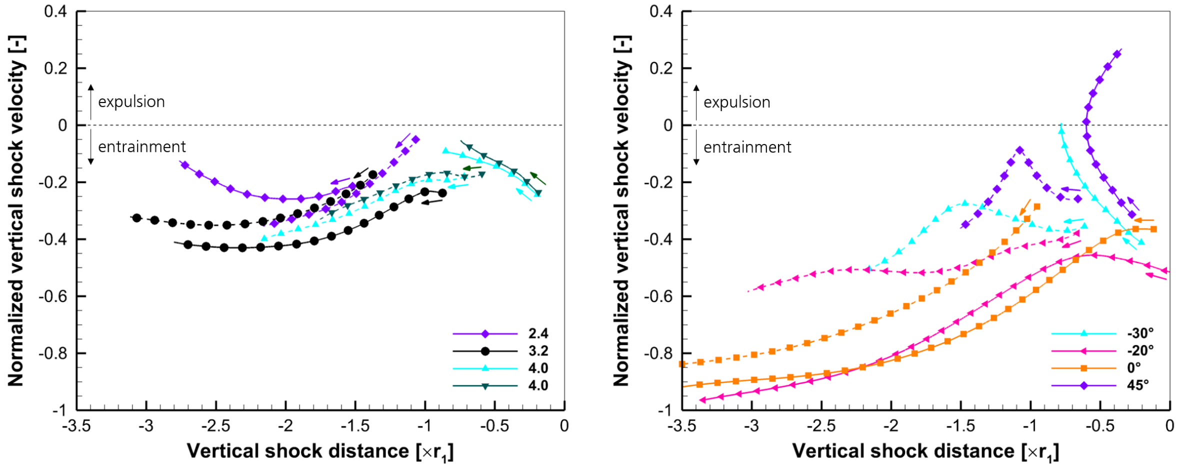

(a) Sphere at various $\Delta\widehat{z}_0$ **(b)** Cube at various ϑ_{02}

Figure 5.18: Phase diagrams of the trailing body's motion behavior related to the leading sphere for different configurations at $\Delta\widehat{x}_0 = 4.8$ (solid lines) and $\Delta\widehat{x}_0 = 7.2$ (dashed lines)

shock far downstream, which has roughly the same shock angle as that of the wedge. Thus, the positions of stationary points significantly depend on the shock angle. Moreover, it seems that the purple solid line in figure 5.18a is a part of a cycle limit suggesting a stable stationary point roughly around $\widehat{\eta} = -2$.

For trailing cubes at different initial pitch angles as shown in figure 5.18b, there is a clear indication that a stable stationary point is located at low vertical shock distances close to zero due to the appearance of bounding orbits. In doing so, the trailing cube with an initial setting of $\vartheta_{02} = -30°$ (see cyan solid line in figure 5.18b) has a stable orbit in the phase plane for which the body follows the bow shock downstream without oscillations in the translational components as can be seen in figure 5.15a. From the present phase portrait, it is apparent once again that the initial pitch angle of the trailing cube at the same initial positioning is crucial for the separation behavior, since the phase paths tend to completely different directions. For example, both test cases at $\vartheta_{02} = -30°$ and $\vartheta_{02} = 45°$ with $\Delta\widehat{x}_0 = 7.2$ indicate a saddle point at negative vertical shock distances, whereby the stationary point of the former seems to be further away from zero than of the latter.

By comparing the phase paths of the two body shapes, it can be seen that the cubes (see figure 5.18b) experience in general higher absolute vertical shock velocities unlike spheres (see figure 5.18a). The most interesting aspect of this comparison is that the trailing cube with $\vartheta_{02} = -30°$ (see cyan solid line in figure 5.18b) experience stable shock-wave surfing in contrast to the sphere (see blue-gray solid line in figure 5.18a) with an unstable behavior, even though the initial points of the sphere trajectory are within the stable region of the cube's phase path. This result suggests that non-spherical trailing bodies may have a larger region of stability that depends on their orientation. These findings might be explained by fact that the motion of trailing cubes is a result of both the body-inclination and the shock-shock interaction, which leads to mutual amplifications or attenuations of motion characteristics.

5.3 Results of Two Free-Flying Blunt Bodies in Wake-Shock Interaction

The following subsections will discuss the impact of aerodynamic drafting during WSI of two axially aligned objects for several different test cases with $\varDelta\widehat{z}_0 = 0.0$ (see test matrix in table 5.4). Flight trajectories of various trailing objects downstream a leading sphere in the xz-plane are shown in figure 5.19, whereby the distinct flow regions of the free jet are visible as a gray contour layer in the background. It can be seen that all trajectories of both objects with $\varDelta\widehat{x}_0 = 4.8$ exhibit a complete agreement regardless the shape and orientation of the trailing body until a sudden change of direction occurs in the center region of the core flow (see figure 5.19a). After the short impact, the flight trajectories of both objects show a much higher variation than before as discussed below. For the trailing bodies with an initial streamwise distance of $\varDelta\widehat{x}_0 = 7.2$, the trajectories of the cubes differ greatly from each other after entering the core flow (see figure 5.19b), in contrast to the configurations with a smaller initial distance.

This section firstly presents results concerning the flow structure, the motion behavior and aerodynamic coefficients of the front and aft object by way of example. The analysis of aerodynamic drafting will follow this part. Subsequently, the effect of body shape and inclination as well as the difference in the collision behavior are discussed, followed by the system dynamics of WSI.

5.3.1 Flow Topology

In order to assess the impact of aerodynamic drafting, the key parameter in this subsection is the streamwise positioning with axial alignment of both bodies. Such a configuration is shown in figure 5.20a as a visualization of a stationary flow field with a schematic description of aerodynamic phenomena. The flow structures for the front half of the leading sphere are identical to the single-sphere topology as in [112] and figure 5.20b until the point of boundary layer separation. Interestingly, the resulting wake region is bigger and narrows less downstream than of a single body. The reason for this is that the subsonic parts of the first wake region and

Table 5.4: Test matrix of WSI configurations

Primary body	Secondary body	ϑ_{01} [°]	ϑ_{02} [°]	$\varDelta\widehat{x}_0$ [−]
Sphere	Sphere	N/A	N/A	4.8
Sphere	Sphere	N/A	N/A	7.2
Sphere	Sphere	N/A	N/A	10.0
Sphere	Cube	N/A	+0	4.8
Sphere	Cube	N/A	+45	4.8
Sphere	Cube	N/A	+45	7.2
Cube	Cube	+45	+0	4.8
Cube	Cube	+45	+0	7.2

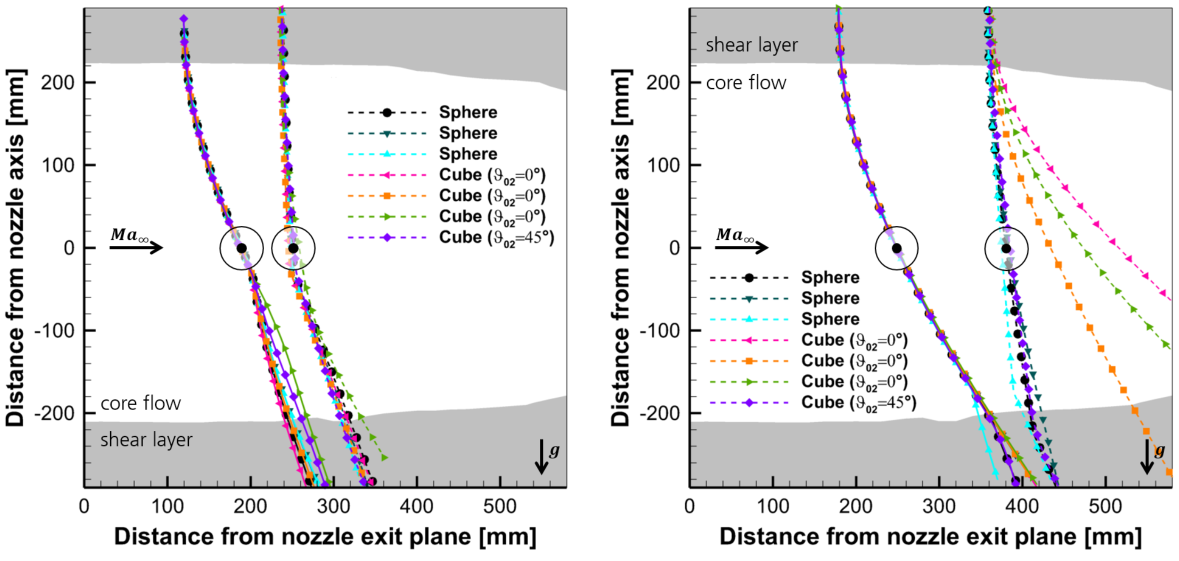

(a) $\Delta\widehat{x}_0 = 4.8$ **(b)** $\Delta\widehat{x}_0 = 7.2$

Figure 5.19: Flight trajectories of leading spheres (solid lines) and trailing bodies (dashed lines) for various configurations including flow areas of H2K's Mach-7 nozzle based on figure 2.2; black solid circles indicate position of both spheres at a certain moment

the second stagnation region merge into one another, so that the deflection of the flow occurs further upstream. Outside the first wake region, the flow field is supersonic and undergoes compression in front of the lateral areas of the trailing sphere by a usual bow shock that enables an outward flow deflection. However, this second bow shock is weaker in terms of the density gradient than the first one, since the Mach number of the inflow near the wake is lower than that of the free-stream flow due to its decrease over the bow shock of the primary object. As can be seen from the schlieren representation, the bow shock of the trailing sphere originates from the end of the wake region's shear layer. Just like the single-body topology, the flow accelerates around the sides of the secondary sphere until the boundary layer separates, producing a typical wake flow.

Figure 5.21 displays three sequences of schlieren images with different combinations of spheres and cubes, whereby the time span between the first and last image of each sequence is $1/15\,\mathrm{s}$. Each image depicts a different snapshot, with the first column showing the approach, the second column capturing the moment before the collision, and the third column showing the moment after. The exception to this is the pair of cubes (see figure 5.21c), which experience the first contact shortly before the second snapshot followed by a motion as coupled bodies. What is noticeable in the rotation of the bodies until the collision is that the cubes are pitching in the counter-clockwise direction, which is attributed to a negative pitching moment resulting from an uneven surface pressure distribution as the object passes through the top shear layer of the free jet as outlined in section 2.3. Regarding the flow structures, the characteristically detached bow shock of blunt bodies is apparent in figure 5.21, whereby the shock shape for cubes depends on their orientation angle relative to the inflow (see section 4.2.1). Furthermore, weak bow shocks ahead the trailing bodies as well as expansion fans and reattachment shocks on cube's leading edges can be seen in the schlieren images.

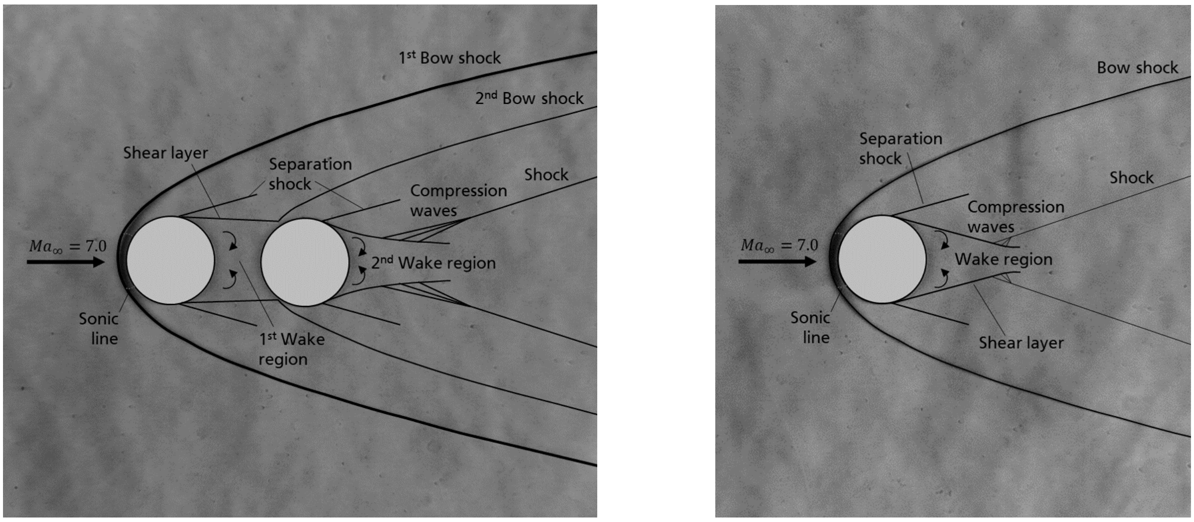

(a) Tandem spheres **(b)** Single sphere

Figure 5.20: Qualitative flow field of a secondary sphere located in the near-wake of a primary sphere at $\Delta\hat{x} = 3.0$ compared to a single sphere

5.3.2 Model Motion

With the help of the stereo tracking measurement system, the three-dimensional motion components of the front and aft body can be determined in a stationary coordinate system. An example for the measured displacement and its first derivative is provided in figure 5.22, whereby the translational (streamwise, spanwise and vertical) and angular (roll, pitch and yaw) components of the leading and trailing sphere are presented over time. It is apparent from these charts that these objects collide with each other $76\,\mathrm{ms}$ after the complete entering of the secondary model into the core flow. Until this moment, the results indicate a very good axial alignment during free flight with a maximum deviation in the separation distance of $0.5\,\mathrm{mm}$ in spanwise direction and of $1.8\,\mathrm{mm}$ in vertical direction. However, the maximum deviation is $2.1\,\mathrm{mm}$ in the y-direction and $2.0\,\mathrm{mm}$ in the x-direction for the worse case of a leading sphere and a trailing cube. For the investigated tandem configurations, a two-dimensional motion is anticipated due to the mirror symmetry of the models, alongside the alignment of the nozzle's axis and two axes of both bodies within the same plane. This assumption can be verified by examining the effect of the misalignment using the deviations mentioned above, which results in a measurement uncertainty in the drag coefficient of less than $0.3\,\%$ relative to the single-body value. In addition, the changes in the displacement data (shown in figures 5.22a and 5.22b) of the trailing body from entry into the core flow to the impact are considered. On this matter, the changes in streamwise position ($\Delta x_2 = 9.6\,\mathrm{mm}$) and vertical position ($\Delta z_2 = -371.8\,\mathrm{mm}$) are about two to four orders of magnitude greater than its changes in spanwise position ($\Delta y_2 = 0.1\,\mathrm{mm}$), while its absolute changes in roll angle ($\Delta\varphi_2 = -0.1°$), pitch angle ($\Delta\vartheta_2 = -0.9°$) and yaw angle ($\Delta\psi_2 = -0.2°$) are less than $1°$. By contrast, a significant pitch rotation with a maximum change in pitch angle of $\Delta\vartheta_2 = -9.7°$ was observed for the trailing cube in a representative sphere-cube test due to the asymmetric flow field being discussed further below. Hence, the roll, yaw and spanwise displacements are neglected and the motion analysis is treated as 3DoF in the following. For trailing spheres, the maximum absolute changes in roll, pitch and yaw

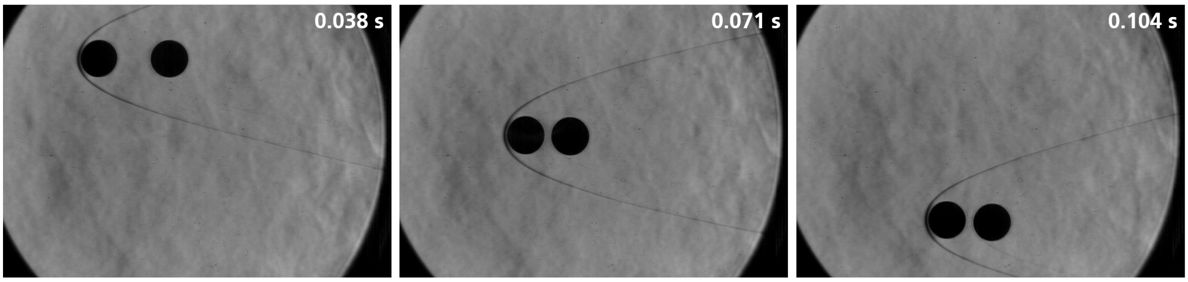

(a) Sphere-Sphere (S-S) configuration

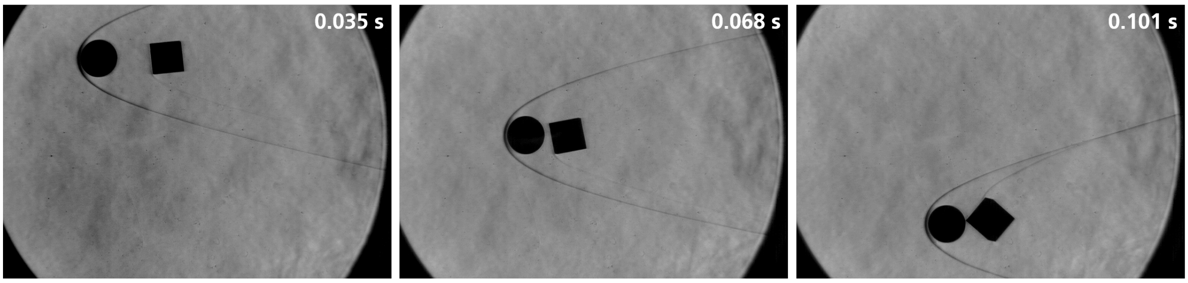

(b) Sphere-Cube (S-C) configuration with $\vartheta_{02} = 0^\circ$

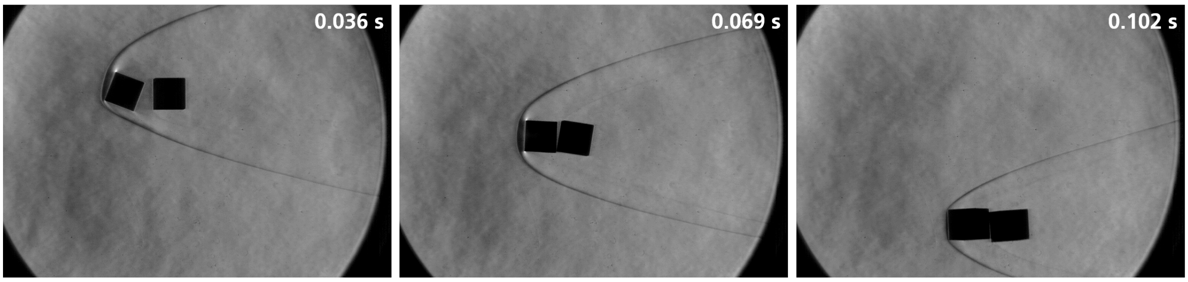

(c) Cube-Cube (C-C) configuration with $\vartheta_{01} = 45^\circ$ and $\vartheta_{02} = 0^\circ$

Figure 5.21: Selection of schlieren image sequences showing the motion behavior in free-flight for different axial-aligned body pairs at $\mathit{\Delta}\widehat{x}_0 = 4.8$

angle are low and they have no effect on the aerodynamics, which is why all orientation angles are neglected for these test cases.

As can be seen from figures 5.22c and 5.22d, a collision causes sudden changes in the translational and angular velocities, particularly in pitch, yaw and streamwise direction. Small misalignments in combination with the impact lead to strong changes in all orientation angles, which are more pronounced for trailing cubes than for spheres. For this reason, the aerodynamic forces below are usually only shown for displacement data prior to a collision.

5.3.3 Aerodynamic Forces

The resulting aerodynamic coefficients of an S-S configuration derived from the motion derivatives in streamwise (drag force) and vertical (lift force) direction are presented over the normalized time in figure 5.23, which also includes the error bars of the uncertainty estimation as described in section 3.4.2. The reported force coefficients have a relative average uncertainty of $2\,\%$ for C_D and $7\,\%$ for C_L based on their maximum values. It can be seen that the drag

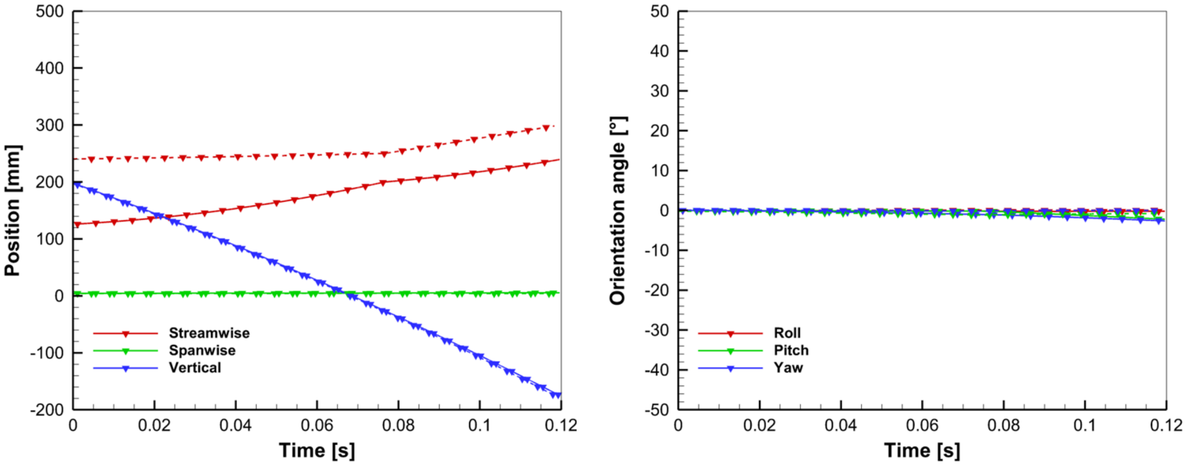

(a) Positions in x, y & z **(b)** Orientation angles in φ, ϑ & ψ

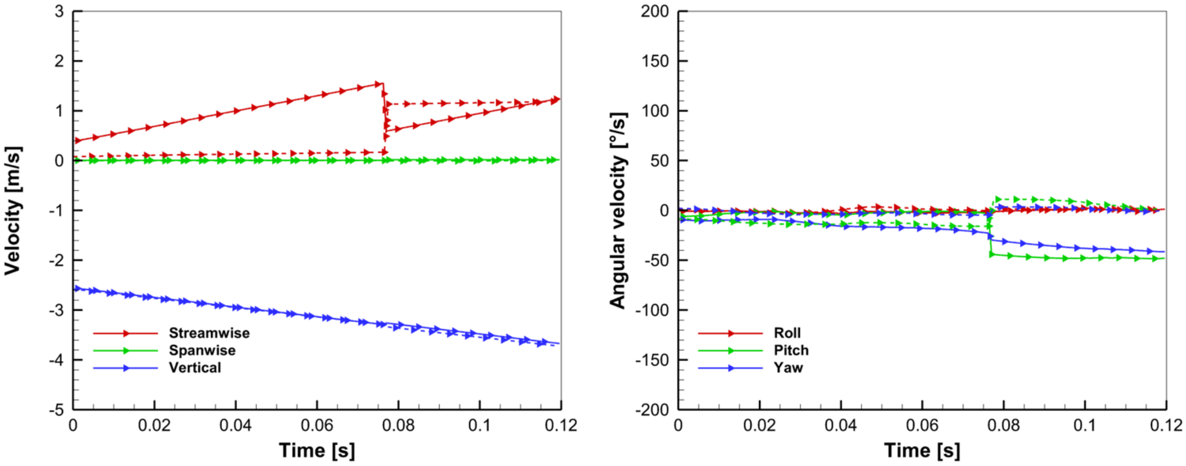

(c) Velocities in x, y & z **(d)** Angular velocities in φ, ϑ & ψ

Figure 5.22: Evolution of 6DoF translational and angular motion data in core flow of a leading (solid lines) and trailing sphere (dashed lines) with $\Delta\widehat{x}_0 = 4.8$

coefficient of the trailing sphere is $93.0\,\%$ lower than that of the leading one with an average of $C_{\mathrm{D}2} = 0.06$. The lift coefficients of both objects are close to zero, whereby the mean values for the entire time window in figure 5.23 are roughly 0.01 for $C_{\mathrm{L}1}$ and 0.03 for $C_{\mathrm{L}2}$. Interestingly, this positive lift force of the secondary body is opposite to the negative vertical separation distance, since the vertical position of the aft body is slightly smaller than of the front one (see figure 5.21a). This result suggests that the primary wake region has a stabilizing effect on the trailing object. In addition, the discontinuity seen in each aerodynamic coefficient in figure 5.23 is a shortcoming in the data reduction due to the collision of the models.

5.3.4 Aerodynamic Drafting

The term 'aerodynamic drafting' refers to a situation in which an axial alignment of objects reduces the drag of the downstream object, and compressibility effects such as WSI dominate for

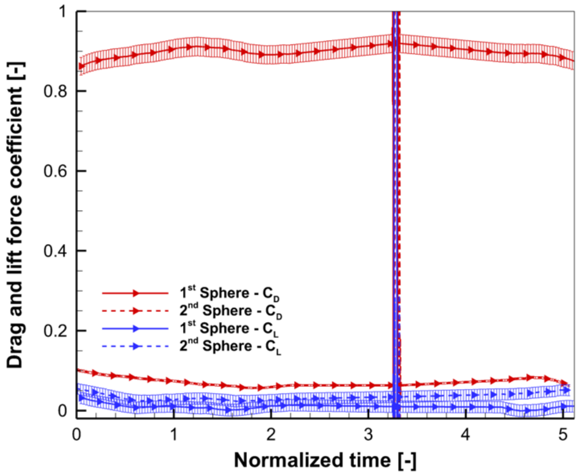

Figure 5.23: Exemplary evolution of drag (red) and lift force coefficients (blue) in core flow including overall uncertainties of a primary (solid lines) and a secondary sphere (dashed lines) with $\varDelta\widehat{x}_0 = 4.8$

supersonic flows. The reduction of the drag coefficient was previously demonstrated for a single test case in figure 5.23. This result is somewhat unexpected, since the effect of aerodynamic drafting is significantly lower in the hypersonic regime than in the subsonic one. Hoerner [48] showed that the relative difference in drag coefficient between trailing and leading body is $134\,\%$ for two equal cylinders in subsonic cross flow with the same Reynolds number and the same relative distance as in the present study, which is significantly higher than for the two equal spheres at $Ma_\infty = 7.0$ in figure 5.23. The difference in the drag coefficient of the trailing body can be explained by the fact that wake-shock interaction leads to higher pressure loads on the windward surface and hence higher drag forces for hypersonic flow fields in contrast to subsonic ones. In addition, the wake region appears to be smaller for hypersonic flows.

Figure 5.24 depicts the primary and secondary drag coefficients of several tests with different initial streamwise positions as a function of the streamwise separation distance. Please note that the first and the last values of each dataset are partially influenced in the process of filtering by measurement points captured within the shear layer leading to slightly higher deviations at the edges of the graphs. From the chart, it can be seen that by far the trailing drag coefficient is strongly dependent on the streamwise separation distance. Its minimum with a median value of $C_{\mathrm{D2}} = 0.05$ arises shortly before the contact of both spheres at $\varDelta\widehat{x} = 2.0$. By increasing the streamwise separation distance, the drag coefficient of the trailing sphere rises linearly until a transition point with a sharp increase and then remains nearly constant at approximately 0.20 within the observed range. Wakes of blunt bodies in hypersonic flows can have large lengths as in [112]. Nevertheless, the present result is somewhat surprising, because the high impact of drafting still maintains for a large range of separation distances. Even up to a separation distance of $\varDelta\widehat{x} = 10.0$, the reduction is at least $75\,\%$ of the single-body drag, although the mixing with the surrounding flow occurs at such distances (see the shadowgraph of a sphere at $Ma_\infty = 4.01$ in [112]). It is apparent from figure 5.24 that the transition point is in the vicinity of $\varDelta\widehat{x} = 6.5$, but the exact distance cannot be determined due to significant deviations between different runs at this point. This transition could be attributed to the flow field of arrangements

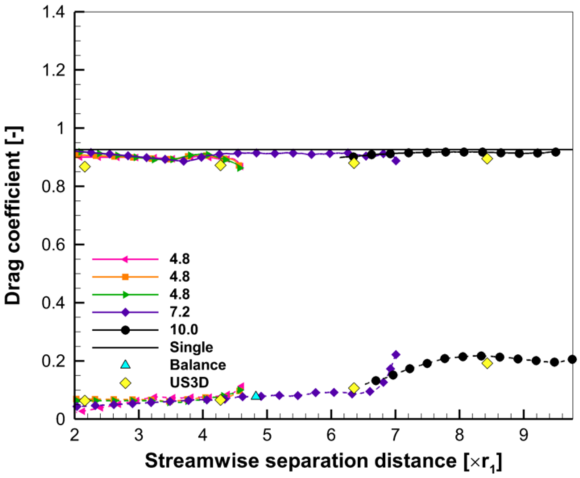

Figure 5.24: Influence of streamwise separation distance on drag coefficient concerning leading (solid lines) and trailing sphere (dashed lines) for different initial streamwise positions; numerical data taken from [113]

where the trailing body is affected by the compression waves and the shock originating from the primary wake region.

Turning now to the drag of the leading object, a weak upstream effect of WSI can be seen in figure 5.24, whereby its drag coefficient is on average $1.7\,\%$ lower than the value of a single sphere with an overall uncertainty of $1.0\,\%$ (see section 4.1.3). This finding is consistent with that of a previous study by Erengil *et al.* [26] with hemispherical bodies. It can be seen that this difference decreases with higher separation distance in x-direction, whereby a minimum is apparent at $\Delta\hat{x} = 3.7$. The observed reduction of drag coefficient can be attributed to the subsonic wake region between both bodies as depicted in section 5.3.1. In contrast to supersonic flows, the subsonic wake flow causes a pressure rise in upstream direction due to the stagnation in front of the trailing object. As a result, the pressure on the leeward surface of the leading sphere increases, which results in a reduction of the overall drag force.

To demonstrate the accuracy of the present experimental results with stereo tracking, they are compared with the data of force-balance measurements with a free-falling and a fix-mounted sphere as described in section 5.1. The secondary drag coefficient for the same nominal distance of $\Delta\hat{x} = 4.8$ exhibits a very good agreement between both the stereo tracking system and the force moment-type balance (see cyan triangle in figure 5.24) having a relative difference of $0.4\,\%$. In addition, the corresponding outcome of previous numerical simulations by using the viscous solver are provided in figure 5.24 according to Venkatapathy *et al.* [113]. Although the data show a good agreement in general, the drag coefficients of the leading sphere are slightly underestimated by the numerical simulations compared to the experiments.

Figure 5.25 presents relative flight trajectories in the xz-plane of in-line S-S configurations with different initial streamwise distances. What stands out first is the occurrence of a relative vertical displacement in the beginning of all shown test cases. The reason why these slight separations have emerged is that the free-flying objects experience a positive lift induced by the jet shear layer as already mentioned. In doing so, the trailing body is affected by a lower force due to the

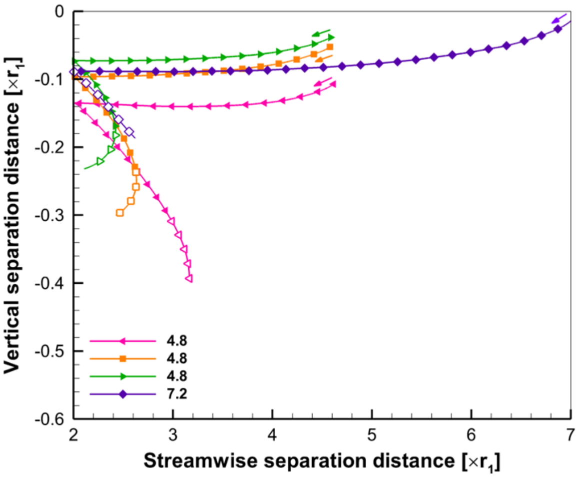

Figure 5.25: Normalized flight trajectories of trailing related to leading spheres in core flow (closed symbols) and bottom shear layer (open symbols) for two different initial streamwise positions

shielding by the leading one in the contrast to SSI configurations (see section 5.2.4). However, it can also be seen that this separation approach quickly ends and the vertical separation distance stays constant until the collision. Thereupon, both spheres separate in streamwise as well as in vertical direction. The most important aspect of figure 5.25 is that in-line arrangements are mainly driven by a strong attraction of both bodies in streamwise direction, which results in the trailing objects remaining in the near-wake of their leading objects. However, the present experiments show that the trailing bodies undergo a slight lateral separation after collision, whereby they tend to be attracted again in the flow direction and to slow down the separation in the vertical direction. Due to the two occurring effects of aerodynamic drafting and collision, it is not possible to state with absolute certainty whether the trailing body of sphere-sphere configurations is expelled from the near-wake after the collision or remains in it as a final zone location according to Register *et al.* [91].

On the question of run-to-run repeatability, figure 5.25 provides trajectories of three tests with the same initial position. It is notable that a small discrepancy between these trajectories is apparent with a maximum deviation of $7.2\,\%$ related to the sphere radius. This discrepancy could be attributed to a repeat inaccuracy in the detachment of one model from the electromagnets mainly due to slight local variations in the coating thickness of the models, which could result in a temporal offset of a few milliseconds between two detachments. Interestingly, these minor deviations in the vertical separation distance provoke significant differences in the motion after the collision indicating a high influence of the impact point on the subsequent flight path.

5.3.5 Effect of Body Shape & Inclination

A comparison of the trailing object's outcomes with different body shapes, initial orientation angles and initial streamwise positions is depicted in figure 5.26 as a function of the streamwise separation distance to the leading sphere. Figures 5.26a and 5.26b show the drag coefficients

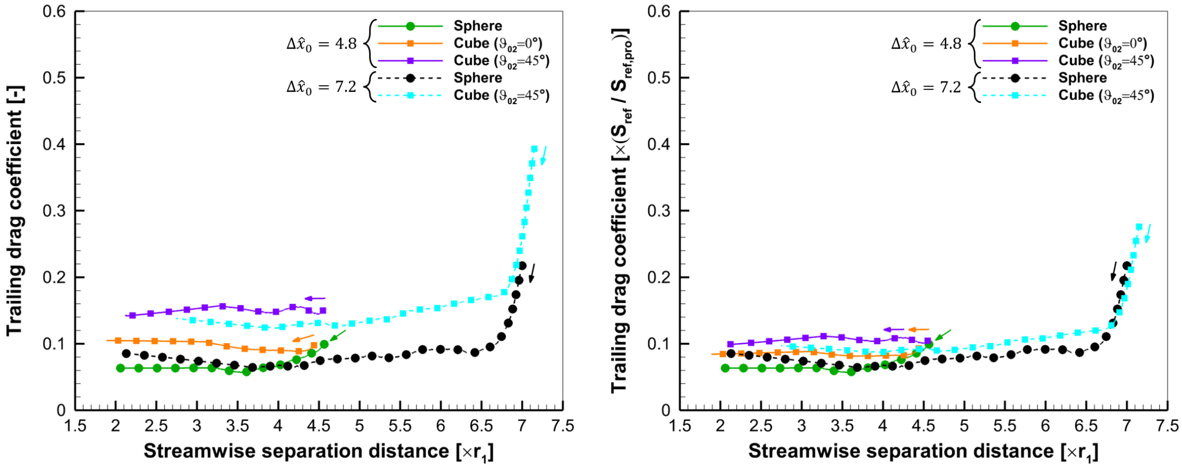

(a) C_{D2} based on base reference area **(b)** C_{D2} based on projected reference area

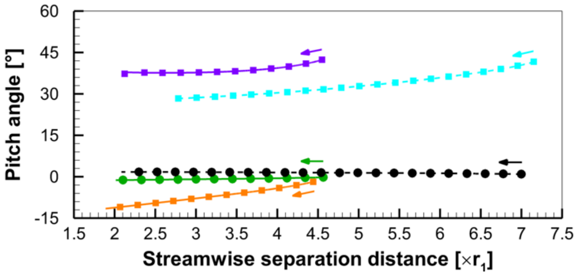

(c) Pitch angles

Figure 5.26: Trailing drag coefficient and pitch angle as a function of the normalized streamwise separation distance for different configurations

based on a reference area with a constant base area S_{ref} and a pitch-angle-dependent projected frontal area $S_{ref,pro}$, respectively. The pitch angle is provided in figure 5.26c. From this figure, it can be seen that trailing cubes have a higher pitch velocity due to the shear layer (as outlined in section 5.3.1) compared to spheres. In figure 5.26a, it is apparent that the drag coefficients of cubes are higher than of spheres and become even higher as the pitch angle changes from plane-exposed ($\vartheta = 0°$) to more edge-exposed ($\vartheta = \pm 45°$) orientations. However, the differences in the trailing drag coefficient between the present configurations are reduced when the projected reference area is used (see in figure 5.26b). Interestingly, this finding is contrary to the outcome of single cubes as in section 4.2.3, which depicts a strong influence of the pitch angle on the drag coefficient based on the projected reference area as well as a decrease in drag for configurations with more slender ends in the stagnation region as the edge-exposed cube. As a result, the main driver for the observed deviations in figure 5.26a for S-C configurations is the effective aerodynamic front face, while a slight influence of the geometry was found for the secondary drag coefficient by comparing spherical and cubical bodies. Interestingly, the relative difference between the drag coefficient of the trailing and the single body ranges from 90 to $95\,\%$, regardless of the body shape. Moreover, no significant influence on the transition point's position was identified between both geometries.

In these experiments, much higher absolute relative velocities were found in streamwise direction

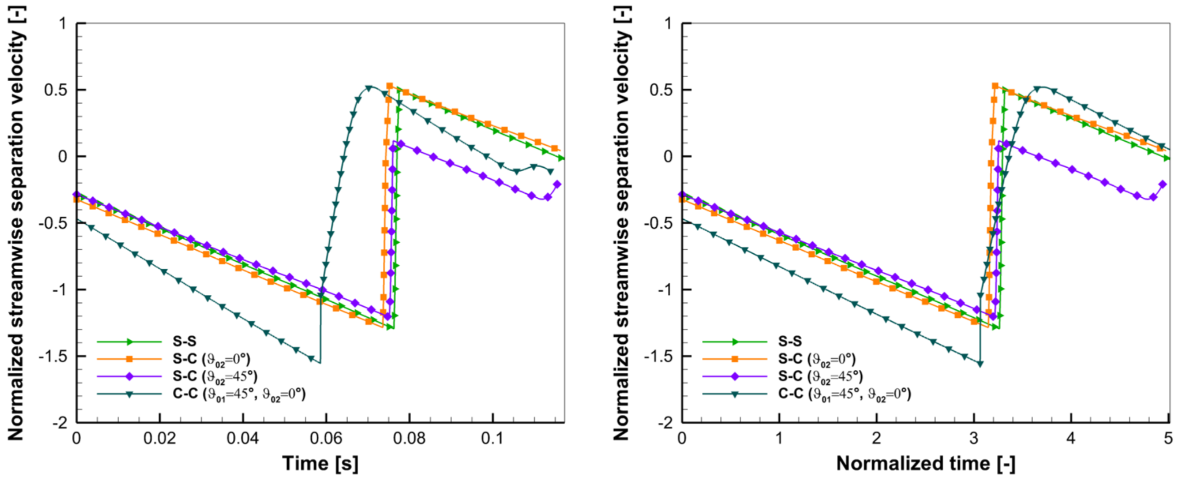

(a) Physical time **(b)** Normalized time

Figure 5.27: Evolution of normalized streamwise separation velocity for different configurations at $\varDelta\widehat{x}_0 = 4.8$

than in lateral direction as a result of the aforementioned aerodynamic drafting. Figure 5.27 provides the normalized streamwise separation velocity over time for different configurations. The results depict a roughly linear characteristic having their absolute extremum at $\varDelta\widehat{v}_x = -1.56$ for cubes, which is nearly twice as high as the maximum of the vertical component in SSI configurations (see figure 5.16a). In figure 5.27, there is no evidence that either trailing body shape or orientation have a significant influence on the global extremum of the streamwise separation velocity. By contrast, the geometry of the leading object has a strong effect on the extremum of the streamwise separation velocity and the time of collision (see figure 5.27a), while a good agreement of the latter for different body shapes can be seen by using the normalized time (see figure 5.27b) indicating the suitability of equation (5.3) as a scaling law. A much higher extreme value and a steeper slope of the streamwise separation velocity in case of a leading cube compared to a sphere can be seen in figure 5.27, whose extrema differ by $20.0\,\%$ based on the median value of the three tests with primary sphere. This finding is not surprising, because the ballistic coefficient of the cube is lower than of the sphere causing a larger acceleration in x-direction and hence a higher relative magnitude of the velocity.

5.3.6 Effect of Collision

It is also of interest to discuss how the collision impacts the subsequent motion behavior as well as the final zone location of the secondary object, which has not been investigated before. Figure 5.28 shows the relative flight trajectories of the trailing body for different combinations of shape and orientation with the same initial distance of $\varDelta\widehat{x}_0 = 4.8$. In addition to the significant influence of the vertical separation distance mentioned earlier, it is apparent from this line chart that the motion behavior after impact also seems to depend strongly on the shape and orientation of both bodies. For example, a sphere (see green line in figure 5.28) moves in the opposite direction after a collision in contrast to a cube (see orange line in figure 5.28) in the case where they collide with a leading sphere at almost the same vertical separation distance. This finding

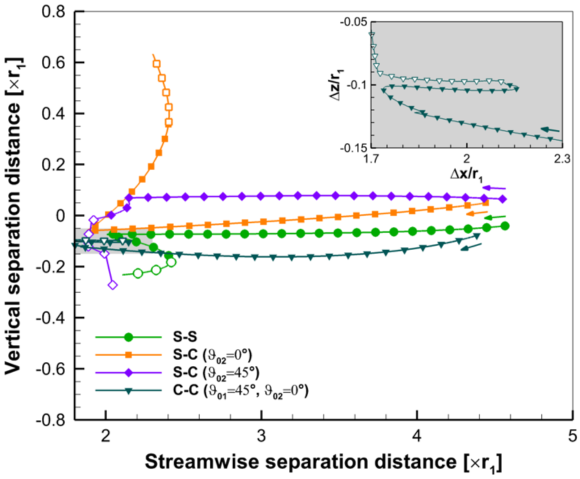

Figure 5.28: Normalized flight trajectories of trailing related to leading bodies in core flow (closed symbols) and bottom shear layer (open symbols) for different configurations at $\varDelta\widehat{x}_0 = 4.8$ including an enlarged view of a single configuration in the top right corner

can be explained by comparing the second schlieren image of figures 5.21a and 5.21b, where the sphere impacts the front body on the lower surface while the cube has the impact point on the upper surface. Surprisingly, although the final streamwise separation velocities of both trailing objects are roughly the same (see figure 5.27), the cube experiences a much stronger separation in lateral direction after the collision than the sphere. An interesting implication of this finding is that if the aft object continues to separate in lateral direction, it will be impinged by the primary bow shock. As a result, the trailing object ends in another final zone. This seems to be more likely for non-spherical bodies. Furthermore, multiple collisions can be seen in the enlarged view of figure 5.28 for trailing cubes, which shows a coupling of both bodies with increasingly weaker impacts. In extreme case, both objects are coupled immediately without strong impacts (see blue-gray line in figure 5.28), which was also observed for this C-C configuration in figure 5.21c.

A detailed analysis of the trailing object's total kinetic energy E over time could help in understanding the characteristics of colliding bodies as shown in figure 5.29 for the previously compared S-S and S-C test cases. Here, the total kinetic energy of a rigid body in free flight consists of the three components due to its translation (E_x, E_y and E_z) plus the three components due to its rotation (E_φ, E_ϑ and E_ψ). These individual kinetic energy components are calculated on the basis of their absolute velocities. First of all, the major portion in all in-line tests is the kinetic energy in z-direction, which is not surprising because of the gravitational acceleration. Yet, the collision mainly causes a sudden increase of the kinetic energy in x-direction, whereas the other components are little or not affected as can be seen in figure 5.29. This is reasonable, because the normal to the surface of the primary and secondary bodies' impact points are roughly parallel to the streamwise direction, which enables a momentum transfer from the leading to the trailing body in the same direction. It is apparent from this stacked area chart that the trailing cube in figure 5.29b experiences a reduction of vertical kinetic energy through the collision unlike the sphere in figure 5.29a, because the normal to the surface at the cube's impact point exhibit a significant component in z-direction resulting in an increase of the

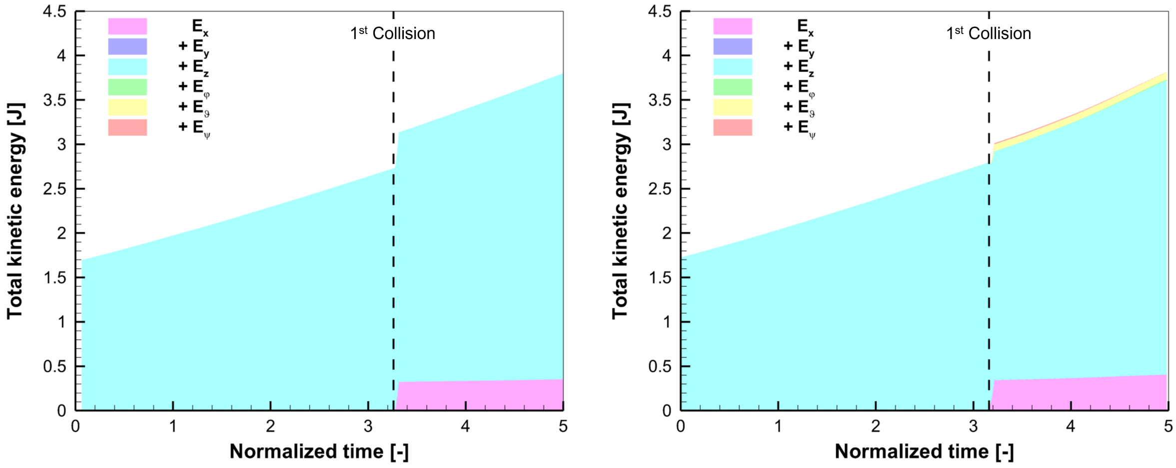

(a) S-S configuration **(b)** S-C configuration with $\vartheta_{02} = 0°$

Figure 5.29: Evolution of trailing body's total kinetic energy divided into its angular and translational components: sphere-sphere configuration compared to sphere-cube configuration at $\vartheta_{02} = 0°$

leading sphere's vertical kinetic energy. Interestingly, this collision leads also to a transfer of momentum into angular kinetic energy, especially for pitching. This matches with the observed strong rotation of the cube after the impact. Since the vertical kinetic energy of the trailing cube decreases in contrast to the constant of this quantity for the sphere, it is possible to explain the differences in the direction of motion after collision as previously mentioned.

Taken together, these results suggest that the surface curvature at both impact points depending on the geometry as well as the distribution of primary and secondary total kinetic energy by components before the impact are the main drivers for the motion behavior in terms of an elastic collision.

5.3.7 System Dynamics

A phase-plane analysis was carried out to assess the stability behavior of the objects in the proximity of the primary wake region until the collision. Only the vertical motion component is considered, because no significant dependence of the streamwise distance on the lift force was found for in-line configurations. Thus, the system of differential equations is as follows:

$$\frac{d(\Delta\widehat{z})}{d\widehat{t}} = \Delta\widehat{v}_z \tag{5.9}$$

$$\frac{d(\Delta\widehat{v}_z)}{d\widehat{t}} = f C_\mathrm{L}(\Delta\widehat{z}) \tag{5.10}$$

where the shape factor f is $3/8$ for spheres and $1/4$ for cubes. This results from the derivation of the lift coefficients in equation (5.10) using the definition of the mass and the reference area for the respective bodies. It should be noted that the speed of the free-flying object is negligible compared to the free-stream velocity. Several phase paths of the trailing body's motion are presented in figure 5.30 for different combinations of primary and secondary model. From this phase portrait, it is apparent that all system trajectories are neutrally stable for a variety of initial conditions in terms of axial distance, shape and orientation, indicating an attraction of the trailing object towards the primary wake region. A stationary point exists when the separation distance and velocity in z-direction are both zero. The state of the stationary point can also be assessed by determining the eigenvalues of the Jacobian matrix of equations (5.9) and (5.10). As a linearized solution, the following eigenvalues are obtained:

$$\lambda = \pm\sqrt{f\frac{dC_\mathrm{L}}{d(\Delta\hat{z})}} \tag{5.11}$$

At the stationary point, the gradient of lift coefficient is negative for both positive and negative vertical separation distances (see figure 5.14b). Thus, the eigenvalues are imaginary and hence the stationary point is a center. Consequently, the primary wake region is a statically stable trimmed position for trailing blunt objects with regard to the vertical direction, which is true for the present configurations regardless of the shape of the leading and trailing body. This finding provides the explanation for why the near-wake and far-wake are steady-state final zone locations without consideration of collisions as found by Register *et al.* [91]. Several factors from the flow field could elucidate this static stability. First, a decreasing total pressure behind the leading object from the bow shock to the center of the wake has the effect of a sink. Second, the high momentum of the wake's shear layer, as shown by Erengil *et al.* [26], acts like a barrier hampering the escape of the trailing object from the wake region. However, it can be assumed that the lift coefficient of trailing cubes in asymmetric flight attitudes is non-zero unlike spheres, because their lift coefficient also depends of the pitch angle. This implies that the stationary point is slightly shifted away from axial alignment in vertical direction, so that the pitching moment becomes zero.

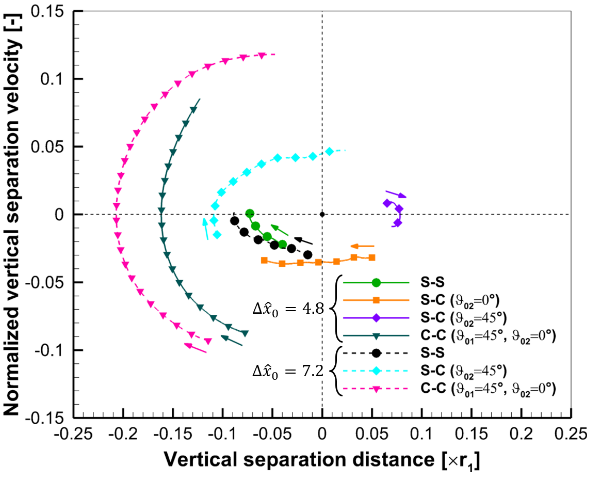

Figure 5.30: Phase diagram of the trailing body's motion behavior related to the leading object for different configurations at $\Delta\widehat{x}_0 = 4.8$ (solid lines) and $\Delta\widehat{x}_0 = 7.2$ (dashed lines)

6 Conclusion

The threat posed by asteroids and space debris is of increasing relevance for the protection of the population and for the safe and sustainable use of space. Understanding the phenomena that occur during the atmospheric entry of objects from outer space is crucial for the reliable prediction of flight trajectories and the impact footprint influenced by the final mass and velocity of surviving fragments (as outlined in chapter 1). The recent push towards stricter requirements such as shorter residence time after end-of-life and lower on-ground casualty risk of space debris as part of ESA's new Space Debris Mitigation Guidelines [28] is leading to higher demand for space technology to mitigate and avoid space debris. Re-entry analysis tools and their aerodynamic modeling are also becoming more important in order to make the prediction of impact footprints and thus the casualty risk assessment more accurate.

According to a study by Passey and Melosh [87], several different effects are responsible for the scattering of multiple fragments after atmospheric breakup, with the gravity, the lift force of the single fragment and the aerodynamic interaction of several bow shocks being the dominant causes. Aerodynamic lift forces arise for the single fragment due to their non-spherical body shape, which can lead to a lateral separation depending on the direction of lift. Shock-Shock Interactions affect locally higher surface pressures on downstream fragments, which can result in a separation of the objects with large lateral velocities. In contrast to the two previously mentioned effects, Wake-Shock Interactions do not cause any scattering, but the downstream fragments in the wake region of another experience aerodynamic drafting resulting in a reduced drag. Due to their position in the wake, aerodynamic shielding by the upstream object may cause a much reduced material recession of the downstream fragments because of lower thermal loads as shown by Patel and Navarro-Martinez [88]. In addition, the streamwise velocities of upstream and downstream objects can be higher through momentum transfers as a result of collisions. Both effects together provoke a higher momentum of grouped fragments compared to isolated ones, which in fact increase the impact velocities and thus the crater depth. This is why the consideration of Wake-Shock Interaction is important for the impact footprint. In conclusion, the aerodynamic behavior of single and multiple objects during atmospheric entry influences the motion and thus the impact characteristics. The experimental database and modeling capabilities for these aerodynamic effects are limited, especially for the influence of body shape and orientation that play an important role for the flow topology and thus for the stagnation, separation and reattachment points.

6.1 Summary of Single-Body Aerodynamics

Several series of free-flight tests were performed with simple blunt bodies such as spheres, cubes and cylinders in the hypersonic flow regime. In addition to the body shape, the angle of attack was varied in chapter 4 to show the impact on flow field and aerodynamic loads. A high-speed non-intrusive stereo tracking measurement system captured the model motions during free-flight, and high-speed schlieren videography provided documentation of the flow topology (as described in chapter 2). Based on the measured 6DoF motion data, aerodynamic coefficients were determined in an extensive post-processing (see figure 3.1) including regression and uncertainty analysis. To enhance the data quality, mathematical optimization was applied to the results of the single-sphere tests using MCMC simulations in a multiple-sampling approach (as described insection 3.2.5).

The results of these experiments have provided the evidence that the aerodynamic coefficients depend on the geometry and the flight attitude of the object (as shown in figure 4.24), which heavily influences the flow field around the body. From the schlieren images in figure 4.23, it is apparent that the greater the bluntness of the body, the greater the shock radius, the shock stand-off distance and the size of the subsonic stagnation region (as discussed in section 4.4.1). As a result of the regression analysis, a relationship between aerodynamic coefficients and the pitch angle was established by fitting trigonometric functions to the measurement data. Resulting drag, lift and pitching moment coefficients are listed as single values and relationships in table 6.1. In comparison to the present experimental results, it was shown that literature values given by [48] usually underestimate the aerodynamic drag coefficients, whereas analytically values determined by modified Newtonian flow theory mostly overestimate the effect of the flight attitude on aerodynamic coefficients (as discussed in sections 4.2.3 and 4.3.3). Especially, the sphere drag coefficient determined by modified Newtonian theory has a very good agreement with the experimental data (as discussed in section 4.1.3). The effect of the flight attitude is most obvious for cylinders, where the drag coefficient based on a constant base reference area almost doubles as the pitch angle increases from $0°$ to $90°$ (as shown in figure 4.19). However, the sharp increase in C_D with increasing pitch angle is primarily an effect of the rising effective aerodynamic frontal area. When looking at the drag coefficient based on the pitch-angle-dependent frontal reference area, it can be seen that its curve deviates significantly compared to a constant reference area, so that by contrast the maximum value occurs for a cylinder in axial flow ($\vartheta = 0°$). In general, the experiments have shown that the influence of the flight attitude on the aerodynamic forces and moments consists of two main causes with opposing effects, namely the change in the surface pressure distribution on the one hand and the change in the effective aerodynamic frontal area on the other (as discussed in section 4.4.2). Concerning the pressure loads, the part of the body that protrudes into the flow tends to determine the magnitude of the drag coefficient, with the flat-faced configuration (e.g. a cube at $\vartheta = 0°$ or a cylinder at $\vartheta = 0°$) having a higher effective drag coefficient than the round-curved configuration (e.g. a cylinder at $\vartheta = 90°$ or a sphere) and a much higher effective drag coefficient than the edge-on configuration (e.g. a cylinder at $\vartheta = 37°$). In addition, the tests with different bodies have demonstrated that their shape and dimension have a great influence on the static stability behavior (as discussed in section 4.4.3), whereby cubes are statically stable, spheres are statically neutral and right circular cylinders are statically unstable at a pitch angle of $0°$.

Table 6.1: Overview of results from single-body experiments

Geometry	Configuration	Result
Sphere	Variable AoA	$C_\mathrm{D} = 0.926 \pm 0.009$
Cube	Face-on	$C_\mathrm{D} = 1.704 \pm 0.045$
Cube	Edge-on	$C_\mathrm{D} = 1.640 \pm 0.043$
Cube	Variable AoA	Equations (4.2) to (4.4)
Cylinder	End-on	$C_\mathrm{D} = 1.747 \pm 0.045$
Cylinder	Side-on	$C_\mathrm{D} = 3.081 \pm 0.079$
Cylinder	Variable AoA	Equations (4.6) to (4.8)

6.2 Summary of Multi-Body Aerodynamics

Experiments with an improved free-flight technique, that ensures the synchronized dropping of two objects at various initial conditions of pitch angle, relative streamwise and vertical distance, were carried out with tandem-body configurations in the hypersonic flow regime. The influence of the body shape and orientation on aerodynamic and stability behavior in the case of SSI and WSI were studied in chapter 5 for sphere-sphere, sphere-cube and cube-cube arrangements. Just like the single-body experiments, a stereo tracking measurement technique was applied to determine the 6DoF motion data and schlieren videography was used to visualize the flow topology (as described in chapter 2). Aerodynamic coefficients including estimated overall uncertainties were computed with the same smoothing and differentiation procedure as with the single bodies (as described in section 3.2). To consider the singularity in the event of a collision, the post-processing was modified to ensure separate treatment of the signals before and after the singularity. In addition, well-established force-balance measurements (as described in section 3.3) were conducted with a free-falling and a fix-mounted sphere in a wide continuous range of relative vertical positions in order to assess the effect of the Reynolds number. These directly measured force data were also used to validate the aerodynamic coefficients determined with the stereo tracking method for configurations of the same flow conditions and relative distance.

In section 5.1, it was shown in the test series with force-balance measurements that the flow topology and the drag coefficient of the trailing sphere changes significantly during SSI and WSI by varying the lateral distance (as shown in figure 5.6a). All six Edney's types of SSI between both bow shocks appear in figure 5.2 depending on the position of interaction relative to the stagnation point. In addition, a partial or full extinction of the secondary bow shock was observed in figure 5.3 when the trailing sphere enters the wake region of the leading object. The results of the trailing body's drag coefficient show a good agreement in the case of SSI. By contrast, they exhibit high discrepancies between the experiments and the simplified approximation methods in the case of WSI, especially for axially aligned bodies (as discussed in section 5.1.3). Two effects were identified during WSI, which have a partially opposing influence on the drag: a weak SSI of the compression shock from the primary wake's shear layer and the secondary bow shock as well as the lowering total pressure of the trailing body's inflow. Confirming the current state of knowledge for blunt bodies in hypersonic flows, no effect of the Reynolds number on the aerodynamic coefficients was determined for aerodynamically interacting bodies (as discussed in section 5.1.4).

For tandem configurations with SSI in section 5.2, experimental data were gained on the strong relationship between the lateral distance of two equal spheres and the aerodynamic force coefficients. Additional reference drag data of the force-balance measurement exhibit a very good agreement with the data by stereo tracking (as shown in figure 5.14). The results also show that the sensitivity of the relative distance on the drag and lift coefficients is higher in lateral than in streamwise direction (as discussed in section 5.2.4). Regarding the shape effect of the trailing body (as discussed in section 5.2.5), it has become apparent that cubes have significantly higher absolute drag and lift coefficients by a factor of 2 to 3 for tests with observed shock-wave surfing in contrast to spheres. As a result, the normalized final lateral velocities are mostly many times higher for cubical objects (as listed in table 5.3), which is due to the two effects of the shock-shock interaction and the inclination-induced lift force. An implication of this inclination effect is that an additional factor was found, which explains in part the discrepancy between real-world observations and previous scientific studies. One of the more significant findings to emerge from this work is that the initial pitch angle of the trailing cube highly influences its entire flight trajectory and pitch orientation resulting in completely different separation behaviors (as shown in figure 5.15). These experiments have confirmed the observation of Li *et al.* [66] and Lukashenko and Maksimov [71] that the region of stable shock-wave surfing can be increased by means of a rotating trailing cube in comparison to a spherical object at the same initial conditions (as discussed in section 5.2.6). The occurrence of this effect seems to depend on the initial flight attitude and direction of rotation. In the schlieren images of figure 5.21c, three simultaneous shock-shock interactions ahead the trailing object were observed for cube-cube arrangements, which indicates the possible growth of the aerodynamic force coefficients compared to a leading sphere.

In the free-flight tests with occurring WSI from section 5.3, an attraction in flow direction of two axially aligned blunt bodies was observed, a phenomenon which is called aerodynamic drafting (as discussed in section 5.3.4). The results of these tests show that the streamwise distance between two objects has an important impact on the flow field and drag coefficient (as shown in figure 5.24). Regardless of the shape and inclination of both objects, the secondary drag coefficient decreases by 90 to $95\,\%$ relative to its single-body value (as discussed in section 5.3.5). In terms of the absolute values, it was found that trailing cubes experience higher drag forces than spheres, whereby higher pitch angle causes an increase in drag due to larger frontal area. This research has also shown that the leading object undergoes a slight reduction of drag due to a large subsonic region between both aligned objects. The most obvious finding to emerge from this study is that the primary wake region has a stabilizing effect on the relative lateral position of the trailing object (as discussed in section 5.3.7). In this context, the stable trimmed position of the trailing object is in the vicinity of the primary wake's centerline. In contrast, collisions of both models with subsequent lateral separation of the trailing body were observed in some cases (as discussed in section 5.3.6), with the motion depending on the geometry and attitude.

6.3 Outlook

Given the variety of aspects regarding the supersonic aerodynamics of single and multiple bodies, it is crucial to have reliable modeling approaches on various levels of fidelity and to evaluate their suitability for different application of re-entry analysis. Progress in modeling is closely tied to suitable experiments, which are essential for validation and enhancing the fundamental understanding of underlying mechanisms. An extension of the existing data is necessary to further advance this field of research. This allows the aerodynamic models such as those for the re-entry analysis tools DRAMA [14] or ORSAT [22] to be further developed. Hence, it is proposed in future work to develop an appropriate aerodynamic model for re-entry analysis tools based on a complete database that covers the aerodynamic behavior of one- and two-body configurations with respect to different shapes, orientations and aspect ratios of the body, as well as different size ratios and relative distances of the two objects. Further test series with one and two bodies are planned for this purpose, which are part of the ongoing DLR research project TEMIS-DEBRIS on technologies for the mitigation of space debris.

Aerodynamic interaction of multiple blunt bodies with more than two objects that take into account the effect of their shapes and orientations is a particularly important subject for further study as it appears to be very challenging for analytical modeling. As previous and current studies have shown a large influence of both the number and geometry of fragments, the combined analysis aims to address the gap between real-world observations of asteroid impact and previous scientific studies in terms of the lateral separation. Regarding cases with SSI, the motion behavior of free-flying fragments needs to be analyzed in detail, since the lateral position of the downstream object relative to the impingement shock is very sensitive to the flight trajectory and therefore the final zone location. Furthermore, a key question arising from this work is how the aerothermodynamic behavior of the entering space object with regard to destructive processes such as ablation and fragmentation influences the number and nature of fragments. The results of this potential investigation should provide information about relevant configurations for further experimental and numerical setups. This research topic is also very important for human-generated objects, since the novel concept of Design for Demise (D4D) aims to reduce the on-ground casualty risk by completely disintegrating space debris upon re-entry into the atmosphere through disruptive spacecraft design.

Looking ahead, there are several avenues for enhancing the current data processing techniques that could significantly advance the efficiency and quality of future studies. Implementing MCMC simulations with variable time steps for complex models such as a rotating non-spherical body or two interacting blunt bodies could significantly improve the accuracy of the aerodynamic coefficients in post-processing. In addition, this approach enables an included uncertainty estimation based on the measurement uncertainties of the input variables. A quantitative analysis of the schlieren images by the use of computer vision techniques could provide information about the characteristics of the bow shocks, on the one hand, and an additional source of measurement signals to increase the accuracy of the motion data, on the other.

7 Bibliography

[1] Achner, M., “TMK Technische Notiz 04”, DLR, Köln, Tech. Rep. TMK-TN04, 2011.

[2] Aftosmis, M. J., M. J. Berger, and G. Adomavicius, “A parallel multilevel method for adaptively refined Cartesian grids with embedded boundaries”, in *38th Aerospace Sciences Meeting and Exhibit*, Reno: American Institute of Aeronautics and Astronautics (AIAA), 2000. DOI: 10.2514/6.2000-808.

[3] Aftosmis, M. J., M. J. Berger, and J. E. Melton, “Robust and efficient Cartesian mesh generation for component-based geometry”, *AIAA Journal*, vol. 36, no. 6, pp. 952–960, 1998. DOI: 10.2514/2.464.

[4] Anderson, J. D., *Hypersonic and high temperature gas dynamics*, 1. ed., Brown, A. T., L. Beamesderfer, and J. M. Morriss, Eds., McGraw-Hill series in aeronautical and aerospace engineering. New York: McGraw-Hill, 1989, ISBN: 0-07-001671-2.

[5] Anderson, J. D., *Fundamentals of aerodynamics*, 5. ed., Bearnesderfer, L. and E. Castellano, Eds., McGraw-Hill series in aeronautical and aerospace engineering. New York: McGraw-Hill, 2011, ISBN: 978-0-07-128908-5.

[6] Artemieva, N. A. and V. V. Shuvalov, “Interaction of shock waves during the passage of a disrupted meteoroid through the atmosphere”, *Shock Waves*, vol. 5, no. 6, pp. 359–367, 1996. DOI: 10.1007/BF02434011.

[7] Artemieva, N. A. and V. V. Shuvalov, “Motion of a fragmented meteoroid through the planetary atmosphere”, *Journal of Geophysical Research: Planets*, vol. 106, no. E2, pp. 3297–3309, 2001. DOI: 10.1029/2000JE001264.

[8] Atkins, P. W. and J. De Paula, *Atkins’ Physical chemistry*, 8 ed. Oxford: Oxford University Press, 2006, ISBN: 9780198700722.

[9] Bailey, A. B. and J. Hiatt, “Sphere drag coefficients for a broad range of Mach and Reynolds numbers”, *AIAA Journal*, vol. 10, no. 11, pp. 1436–1440, 1972, ISSN: 0001-1452. DOI: 10.2514/3.50387.

[10] Barri, N. G., “Meteoroid fragments dynamics: Collimation effect”, *Solar System Research*, vol. 44, no. 1, pp. 55–59, 2010, ISSN: 0038-0946. DOI: 10.1134/S0038094610010077.

[11] Berke, R. B. and J. Lambros, “Ultraviolet digital image correlation (UV-DIC) for high temperature applications”, *Review of Scientific Instruments*, vol. 85, no. 045121, pp. 1–10, 2014. DOI: 10.1063/1.4871991.

[12] Billig, F. S., “Shock-wave shapes around spherical-and cylindrical-nosed bodies”, *Journal of Spacecraft and Rockets*, vol. 4, no. 6, pp. 822–823, 1967. DOI: 10.2514/3.28969.

[13] Borovička, J., P. Spurný, P. Brown, P. Wiegert, P. Kalenda, D. Clark, and L. Shrbený, "The trajectory, structure and origin of the Chelyabinsk asteroidal impactor", *Nature*, vol. 503, no. 7475, pp. 235–237, 2013. DOI: 10.1038/nature12671.

[14] Braun, V., Q. Funke, S. Lemmens, and S. Sanvido, "DRAMA 3.0 - Upgrade of ESA's debris risk assessment and mitigation analysis tool suite", *Journal of Space Safety Engineering*, vol. 7, no. 3, pp. 206–212, 2020, ISSN: 2468-8967. DOI: 10.1016/j.jsse.2020.07.020.

[15] Brown, P. G., J. D. Assink, L. Astiz, *et al.*, "A 500-kiloton airburst over Chelyabinsk and an enhanced hazard from small impactors", *Nature*, vol. 503, no. 7475, pp. 238–241, 2013. DOI: doi:10.1038/nature12741.

[16] Butler, C. S., T. J. Whalen, C. E. Sousa, and S. J. Laurence, "Dynamics of a spherical body shedding from a hypersonic ramp. Part 2. Viscous flow", *Journal of Fluid Mechanics*, vol. 906, no. A29, pp. 1–32, 2020. DOI: 10.1017/jfm.2020.757.

[17] Cardona, V., R. Joussot, and V. Lago, "Shock/shock interferences in a supersonic rarefied flow: Experimental investigation", *Experiments in Fluids*, vol. 62, no. 6, 2021. DOI: 10.1007/s00348-021-03225-4.

[18] Cardona, V. and V. Lago, "Aerodynamic forces of interacting spheres representative of space debris re-entry: Experiments in a supersonic rarefied wind-tunnel", *Acta Astronautica*, vol. 191, pp. 148–159, 2022. DOI: 10.1016/j.actaastro.2021.10.036.

[19] Charters, A. C. and R. N. Thomas, "The aerodynamic performance of small spheres from subsonic to high supersonic velocities", *Journal of the Aeronautical Sciences*, vol. 12, no. 4, pp. 468–476, 1945. DOI: 10.2514/8.11287.

[20] Clark, A. B. J. and F. T. Harris, "Free-flight air-drag measurement techniques", *Journal of the Aeronautical Sciences*, vol. 19, no. 6, pp. 385–390, 1952. DOI: 10.2514/8.2303.

[21] Daub, D., "Experimental investigation of supersonic fluid-structure interaction for future space transportation systems", DLR-FB 2023-09, PhD thesis, DLR/RWTH Aachen University, Cologne/Aachen, 2023. DOI: 10.57676/cbaa-ce26.

[22] Dobarco-Otero, J., R. N. Smith, K. J. Bledsoe, R. M. DeLaune, W. C. Rochelle, and N. L. Johnson, "The Object Reentry Survival Analysis Tool (ORSAT) - Version 6.0 and its application to spacecraft entry", in *56th International Astronautical Congress*, American Institute of Aeronautics and Astronautics (AIAA), 2005. DOI: 10.2514/6.IAC-05-B6.3.06.

[23] Edney, B. E., "Anomalous heat transfer and pressure distributions on blunt bodies at hypersonic speeds in the presence of an impinging shock", The Aeronautical Research Institute of Sweden, Stockholm, Tech. Rep. FFA Report 115, 1968. URL: https://www.osti.gov/servlets/purl/4480948.

[24] Edney, B. E., "Effects of shock impingement on the heat transfer around blunt bodies", *AIAA Journal*, vol. 6, no. 1, pp. 15–21, 1968, ISSN: 0001-1452. DOI: 10.2514/3.4435.

[25] Engeln-Müllges, G. and F. Uhlig, *Numerical algorithms with C*, 1. ed. Berlin: Springer, 2014, 624 pp., ISBN: 978-3-642-64682-9.

[26] Erengil, M. E., W. G. Reinecke, D. S. Dolling, and J. A. Pike, “The aerodynamics of tandem bodies at Mach 5 - Part I: Preliminary experimental results”, in *33rd Aerospace Sciences Meeting and Exhibit*, Reno: American Institute of Aeronautics and Astronautics (AIAA), 1995. DOI: 10.2514/6.1995-319.

[27] ESA Space Debris Office, “ESA’s annual space environment report”, European Space Agency, Darmstadt, Tech. Rep. GEN-DB-LOG-00288-OPS-SD, 2023. URL: https://www.esa.int/Space_Safety/ESA_s_Space_Environment_Report_2023.

[28] ESA Space Mitigation Working Group, “ESA space debris mitigation requirements”, European Space Agency, Darmstadt, Tech. Rep. ESSB-ST-U-007, 2023. URL: https://sdup.esoc.esa.int/documents/download/ESSB-ST-U-007_Issue_1_30October2023.pdf.

[29] European Space Agency, *Tiangong 1: Chinesische Raumstation im Sinkflug*, 2018. URL: https://www.esa.int/ger/ESA_in_your_country/Germany/Tiangong_1_Chinesische_Raumstation_im_Sinkflug.

[30] European Space Agency, *ESA’s fragmentation database*, 2021. URL: https://fragmentation.esoc.esa.int.

[31] Ganzer, U., *Gasdynamik*, 1. ed. Berlin: Springer, 1988, ISBN: 978-3-642-48345-5.

[32] Garcia, D., J.-J. Orteu, and M. Devy, “Accurate calibration of a stereovision sensor: Comparison of different approaches”, in *5th Workshop on Vision, Modeling and Visualization*, Saarbrücken, 2000, pp. 25–32. URL: https://dblp.uni-trier.de/db/conf/vmv/vmv2000.html#GarciaOD00.

[33] Gawehn, T., T. Schleutker, and A. Gülhan, “Capsule aerodynamics and shock-wave boundary layer interaction (SBLI) in supersonic and transonic flow”, *Experiments in Fluids*, vol. 63, no. 3, 2022. DOI: 10.1007/s00348-022-03392-y.

[34] Gelman, A. and D. B. Rubin, “Inference from iterative simulation using multiple sequences”, *Statistical Science*, vol. 7, no. 4, 1992, ISSN: 0883-4237. DOI: 10.1214/ss/1177011136.

[35] Gerasimov, S. I., V. I. Erofeev, V. A. Kikeev, R. V. Gerasimova, I. I. Kanygin, and A. P. Fomkin, “Visualization of supersonic flow around a cube”, *Scientific Visualization*, vol. 7, no. 3, pp. 44–52, 2015, ISSN: 2079-3537. URL: http://sv-journal.org/2015-3/06.php?lang=en.

[36] GOM, “Digital image correlation and strain computation basics”, GOM-Gesellschaft für Optische Messtechnik mbH, Tech. Rep., 2018. URL: https://www.gom.com/en/topics/digital-image-correlation.

[37] Gowen, F. E. and E. W. Perkins, “Drag of circular cylinders for a wide range of Reynolds numbers and Mach numbers”, Ames Aeronautical Laboratory, Moffett Field, California, Tech. Rep., 1953. URL: https://ntrs.nasa.gov/api/citations/19930087134/downloads/19930087134.pdf.

[38] Gramola, M., P. J. K. Bruce, and M. Santer, “Photogrammetry for accurate model deformation measurement in a supersonic wind tunnel”, *Experiments in Fluids*, vol. 60, no. 8, 2018. DOI: 10.1007/s00348-018-2652-7.

[39] Gülhan, A., S. Willems, and T. Schleutker, “Multibody aerothermodynamics of space debris fragments”, in *VKI Lecture Series: Activity on Space Debris Re-Entry and Mitigation*, STO-AVT-262, Von Karman Institute for Fluid Dynamics (VKI), Brussels, 2016.

[40] Halupovich, Y., B. Natan, and J. Rom, “Numerical solution of the turbulent supersonic flow over a backward facing step”, *Fluid Dynamics Research*, vol. 24, no. 5, pp. 251–273, 1999, ISSN: 0169-5983. DOI: 10.1016/S0169-5983(98)00025-2.

[41] Hansche, G. E. and J. S. Rinehart, “Air drag on cubes at Mach numbers 0.5 to 3.5”, *Journal of the Aeronautical Sciences*, vol. 19, no. 2, pp. 83–84, 1952. DOI: 10.2514/8.2166.

[42] Hayes, W. D. and R. F. Probstein, “Viscous hypersonic similitude”, *Journal of the Aerospace Sciences*, vol. 26, no. 12, pp. 815–824, 1959. DOI: 10.2514/8.8327.

[43] Henderson, C. B., “Drag coefficients of spheres in continuum and rarefied flows”, *AIAA Journal*, vol. 14, no. 6, pp. 707–708, 1976. DOI: 10.2514/3.61409.

[44] Hills, J. G. and M. P. Goda, “The fragmentation of small asteroids in the atmosphere”, *The Astronomical Journal*, vol. 105, no. 3, pp. 1114–1144, 1993. DOI: 10.1086/116499.

[45] Hilsenrath, J., C. W. Beckett, W. S. Benedict, L. Fano, H. J. Hoge, J. F. Masi, R. L. Nuttall, Y. S. Touloukian, and H. W. Woolley, *Tables of thermal properties of gases comprising tables of thermodynamic and transport properties of air, argon, carbon dioxide, carbon monoxide hydrogen, nitrogen, oxygen, and steam*. Washington, 1955, vol. 564. DOI: 10.6028/nbs.circ.564.

[46] Hirschel, E. H., *Basics of aerothermodynamics*, 1. ed. Berlin: Springer, 2006, ISBN: 978-3-540-26519-1.

[47] Hodges, A. J., “The drag coefficient of very high velocity spheres”, *Journal of the Aeronautical Sciences*, vol. 24, no. 10, pp. 755–758, 1957. DOI: 10.2514/8.3958.

[48] Hoerner, S. F., *Fluid-dynamic drag: Practical information on aerodynamic drag and hydrodynamic resistance*, 2. ed. Bakersfield: Hoerner Fluid Dynamics, 1965, ISBN: 978-9991194448.

[49] Hoffman, M. D. and A. Gelman, “The No-U-Turn Sampler: Adaptively setting path lengths in Hamiltonian Monte Carlo”, *Journal of Machine Learning Research*, vol. 15, no. 47, pp. 1593–1623, 2014. URL: https://jmlr.org/papers/volume15/hoffman14a/hoffman14a.pdf.

[50] Kaufman II, L. G., L. Meckler, and S. A. Hartofilis, “An investigation of flow separation and aerodynamic controls at hypersonic speeds”, *Journal of Aircraft*, vol. 3, no. 6, pp. 555–561, 1966. DOI: 10.2514/3.43776.

[51] Kenkmann, T., N. A. Artemieva, K. Wünnemann, M. H. Poelchau, D. Elbeshausen, and H. Núñez del Prado, “The Carancas meteorite impact crater, Peru: Geologic surveying and modeling of crater formation and atmospheric passage”, *Meteoritics & Planetary Science*, vol. 44, no. 7, pp. 985–1000, 2009. DOI: 10.1111/j.1945-5100.2009.tb00783.x.

[52] Kessler, D. J. and B. G. Cour-Palais, “Collision frequency of artificial satellites: The creation of a debris belt”, *Journal of Geophysical Research: Space Physics*, vol. 83, no. A6, pp. 2637–2646, 1978. DOI: 10.1029/JA083iA06p02637.

[53] Kliche, D., C. Mundt, and E. H. Hirschel, “The hypersonic Mach number independence principle in the case of viscous flow”, *Shock Waves*, vol. 21, no. 4, pp. 307–314, 2011. DOI: 10.1007/s00193-011-0318-y.

[54] Klinkrad, H., “Space Debris: Models and risk analysis”, in 1 ed. Berlin: Springer, 2006, ch. Re-entry prediction and on-ground risk estimation, pp. 241–287, ISBN: 978-3-540-37674-3. DOI: 10.1007/3-540-37674-7.

[55] Kovács, D. G., G. Grossir, G. Dimitriadis, and O. Chazot, “Space debris interaction across a two-dimensional oblique shock wave”, *Experiments in Fluids*, vol. 64, no. 8, 2023. DOI: 10.1007/s00348-023-03686-9.

[56] Kroll, N., S. Langer, and A. Schwöppe, “The DLR flow solver TAU - Status and recent algorithmic developments”, in *52nd Aerospace Sciences Meeting*, National Harbor: American Institute of Aeronautics and Astronautics (AIAA), 2014. DOI: 10.2514/6.2014-0080.

[57] Laurence, S. J., “Proximal bodies in hypersonic flow”, PhD thesis, California Institute of Technology, Pasadena, 2006. URL: https://ui.adsabs.harvard.edu/abs/2006PhDT.......187L/abstract.

[58] Laurence, S. J. and R. Deiterding, “Shock-wave surfing”, *Journal of Fluid Mechanics*, vol. 676, pp. 396–431, 2011. DOI: 10.1017/jfm.2011.57.

[59] Laurence, S. J., R. Deiterding, and G. Hornung, “Proximal bodies in hypersonic flow”, *Journal of Fluid Mechanics*, vol. 590, pp. 209–237, 2007. DOI: 10.1017/s0022112007007987.

[60] Laurence, S. J., R. Deiterding, and H. G. Hornung, “Tandem spheres in hypersonic flow”, in *Shock Waves*, Hannemann, K. and F. Seiler, Eds., vol. 1, Berlin: Springer, 2009, pp. 713–718. DOI: 10.1007/978-3-540-85168-4_115.

[61] Laurence, S. J., N. J. Parziale, and R. Deiterding, “Dynamical separation of spherical bodies in supersonic flow”, *Journal of Fluid Mechanics*, vol. 713, pp. 159–182, 2012. DOI: 10.1017/jfm.2012.453.

[62] Lee, S., H. Song, and G. Park, “Freefalling heated sphere in a shock tunnel”, *AIAA Journal*, vol. 55, no. 11, pp. 3995–3998, 2017. DOI: 10.2514/1.J055967.

[63] Lees, L., “Hypersonic flow”, *Journal of Spacecraft and Rockets*, vol. 40, no. 5, pp. 700–735, 2003. DOI: 10.2514/2.6897.

[64] Leiser, D., S. Löhle, F. Zander, D. R. Buttsworth, R. Choudhury, and S. Fasoulas, “Analysis of reentry and break-up forces from impulse facility experiments and numerical rebuilding”, *Journal of Spacecraft and Rockets*, vol. 59, no. 4, pp. 1276–1288, 2022. DOI: 10.2514/1.A35204.

[65] Lemieux, P., “The instability of shear layers produced by curved shocks”, PhD thesis, California Institute of Technology, Pasadena, 1999. URL: https://ui.adsabs.harvard.edu/abs/1999PhDT.......168L/abstract.

[66] Li, T., J. Sui, S. Gong, and C. Wu, "Dynamical separation of rigid bodies in supersonic flow", *Science China Technological Sciences*, vol. 58, no. 12, pp. 2110–2121, 2015. DOI: 10.1007/s11431-015-5966-1.

[67] Li, T., J. Sui, and C. Wu, "Numerical investigation of dynamical behavior of tethered rigid spheres in supersonic flow", *Applied Mathematics and Mechanics*, vol. 37, no. 6, pp. 749–760, 2016. DOI: 10.1007/s10483-016-2090-6.

[68] Lieberman, C., K. Willcox, and O. Ghattas, "Parameter and state model reduction for large-scale statistical inverse problems", *Journal on Scientific Computing*, vol. 32, no. 5, pp. 2523–2542, 2010. DOI: 10.1137/090775622.

[69] Lips, T. and B. Fritsche, "A comparison of commonly used re-entry analysis tools", *Acta Astronautica*, vol. 57, no. 2-8, pp. 312–323, 2005. DOI: 10.1016/j.actaastro.2005.03.010.

[70] Loth, E., "Compressibility and rarefaction effects on drag of a spherical particle", *AIAA Journal*, vol. 46, no. 9, pp. 2219–2228, 2008. DOI: 10.2514/1.28943.

[71] Lukashenko, V. T. and F. A. Maksimov, "On the separation of two meteoroid fragments of different shapes", *Journal of Physics: Conference Series*, vol. 1479, 2020. DOI: 10.1088/1742-6596/1479/1/012132.

[72] Marwege, A., S. Willems, A. Gülhan, M. J. Aftosmis, and E. C. Stern, "Superposition method for force estimations on bodies in supersonic and hypersonic flows", *Journal of Spacecraft and Rockets*, vol. 55, no. 5, pp. 1166–1180, 2018. DOI: 10.2514/1.A34128.

[73] Maslach, G. J. and S. A. Schaaf, "Cylinder drag in the transition from continuum to free molecule flow", *Physics of Fluids*, vol. 6, no. 3, pp. 315–321, 1963, ISSN: 0031-9171. DOI: 10.1063/1.1706736.

[74] Matthews, R. K. and R. H. Eaves Jr., "Comparison of theoretical and experimental pressure and heat transfer distributions on three blunt nosed cylinders in hypersonic flow", Arnold Engineering Development Center, Arnold Air Force Station, Tennessee, Tech. Rep. AEDCTR-67-148, 1967. URL: https://apps.dtic.mil/sti/pdfs/AD0819547.pdf.

[75] McCormick, N. and J. Lord, "Digital image correlation", *Materials Today*, vol. 13, no. 12, pp. 52–54, 2010, ISSN: 1369-7021. DOI: 10.1016/S1369-7021(10)70235-2.

[76] Niezgodka, F.-J., "Der Hyperschallwindkanal H2K des DLR in Köln-Porz (Stand 2000)", DLR, Köln, Tech. Rep., 2001. URL: https://elib.dlr.de/13874.

[77] Nompelis, I., T. Drayna, and G. Candler, "A parallel unstructured implicit solver for hypersonic reacting flow simulation", in *17th AIAA Computational Fluid Dynamics Conference*, Toronto: American Institute of Aeronautics and Astronautics (AIAA), 2005. DOI: 10.2514/6.2005-4867.

[78] Oliver, T. A. and R. D. Moser, "Accounting for uncertainty in the analysis of overlap layer mean velocity models", *Physics of Fluids*, vol. 24, no. 075108, 2012. DOI: 10.1063/1.4733455.

[79] Orfanidis, S. J., *Introduction to signal processing*, 1. ed. New Brunswick: Prentice Hall, 2010, ISBN: 0-13-209172-0.

[80] Oswatitsch, K., "Similarity laws for hypersonic flow", in *Contributions to the development of gasdynamics*, Schneider, W. and M. Platzer, Eds., 1. ed, Braunschweig: Vieweg, 1980, pp. 76–88, ISBN: 978-3-322-91082-0. DOI: 10.1007/978-3-322-91082-0_8.

[81] Ozawa, H., K. Kitamura, K. Hanai, K. Mori, and Y. Nakamura, "Unsteady aerodynamic interaction between two bodies at hypersonic speed", *Transactions of the Japan Society for Aeronautical and Space Sciences*, vol. 53, no. 180, pp. 114–121, 2010, ISSN: 0549-3811. DOI: 10.2322/tjsass.53.114.

[82] Pan, B., D. Wu, and L. Yu, "Optimization of a three-dimensional digital image correlation system for deformation measurements in extreme environments", *Applied Optics*, vol. 51, no. 19, pp. 4409–4419, 2012. DOI: 10.1364/AO.51.004409.

[83] Papadopoulos, C. E. and H. Yeung, "Uncertainty estimation and Monte Carlo simulation method", *Flow Measurement and Instrumentation*, vol. 12, no. 4, pp. 291–298, 2001. DOI: 10.1016/S0955-5986(01)00015-2.

[84] Park, C. and J. D. Brown, "Fragmentation and spreading of a meteor-like object", *The Astronomical Journal*, vol. 144, no. 6, 2012. DOI: 10.1088/0004-6256/144/6/184.

[85] Park, S.-H., J. Kim, I. Choi, and G. Park, "Experimental study of separation behavior of two bodies in hypersonic flow", *Acta Astronautica*, vol. 181, pp. 414–426, 2021. DOI: 10.1016/j.actaastro.2021.01.037.

[86] Park, S.-H. and G. Park, "Separation process of multi-spheres in hypersonic flow", *Advances in Space Research*, vol. 65, no. 1, pp. 392–406, 2020. DOI: 10.1016/j.asr.2019.10.009.

[87] Passey, Q. R. and H. J. Melosh, "Effects of atmospheric breakup on crater field formation", *Icarus*, vol. 42, no. 2, pp. 211–233, 1980. DOI: 10.1016/0019-1035(80)90072-X.

[88] Patel, M. and S. Navarro-Martinez, "Heat transfer to proximal cylinders in hypersonic flow", *Physics of Fluids*, vol. 35, no. 036125, 2023. DOI: 10.1063/5.0137905.

[89] Penland, J. A., "Aerodynamic characteristics of a circular cylinder at Mach number 6.86 and angles of attack up to $90°$", Langley Aeronautical Laboratory, Tech. Rep., 1954. URL: https://ntrs.nasa.gov/api/citations/19930093717/downloads/19930093717.pdf.

[90] Prévereaud, Y., "Contribution à la modélisation de la rentrée atmosphérique des débris spatiaux", PhD thesis, Institut Supérieur de l'Aéronautique et de l'Espace, Toulouse, 2014. URL: https://hal.science/tel-01171757/file/DMAE15028.1434445612.pdf.

[91] Register, P. J., M. J. Aftosmis, E. C. Stern, J. M. Brock, P. M. Seltner, S. Willems, A. Gülhan, and D. L. Mathias, "Interactions between asteroid fragments during atmospheric entry", *Icarus*, vol. 337, no. 113468, 2020. DOI: 10.1016/j.icarus.2019.113468.

[92] Rouse, H., *Elementary mechanics of fluids*, 1. ed. Dover Publications, 1946, ISBN: 0-486-63699-2.

[93] Rumpf, C. M., H. G. Lewis, and P. M. Atkinson, "Asteroid impact effects and their immediate hazards for human populations", *Geophysical Research Letters*, vol. 44, no. 8, pp. 3433–3440, 2017. DOI: 10.1002/2017GL073191.

[94] Savitzky, A. and M. J. E. Golay, "Smoothing and differentiation of data by simplified least squares procedures", *Analytical Chemistry*, vol. 36, no. 8, pp. 1627–1639, 1964. DOI: `10.1021/ac60214a047`. eprint: `http://dx.doi.org/10.1021/ac60214a047`.

[95] Schultz, P. H. and S. Sugita, "Penetration and escaping the atmosphere of Venus and Earth", in *25th Lunar and Planetary Science Conference*, Houston: Lunar and Planetary Institute (LPI), 1994, pp. 1215–1216.

[96] Seltner, P. M., S. Willems, and A. Gülhan, "Experiments on the aerodynamic interaction of multiple free-flying objects", Poster presented at *61st Course of Hypersonic Meteoroid Entry Physics (HyMEP)*, Erice, 2017.

[97] Seltner, P. M., S. Willems, and A. Gülhan, "Experimental determination of aerodynamic coefficients of simple-shaped bodies free-flying in hypersonic flow", in *First International Conference on High-Speed Vehicle Science Technology (HiSST)*, Moscow: Council of European Aerospace Societies (CEAS), 2018.

[98] Seltner, P. M., S. Willems, and A. Gülhan, "Aerodynamic coefficients of free-flying cubes in hypersonic flowfield", *Journal of Spacecraft and Rockets*, vol. 56, no. 6, pp. 1725–1734, 2019. DOI: `10.2514/1.a34345`.

[99] Seltner, P. M., S. Willems, and A. Gülhan, "Mehrkörperaerodynamik während der Fragmentation beim atmosphärischen Wiedereintritt", in *Sicherheitslagen und Sicherheitstechnologien - Beiträge der ersten Sommerakademie der zivilen Sicherheitsforschung 2018*, Zivile Sicherheit, Ellebrecht, S., N. Eschenbruch, and P. Zoche, Eds., 1. ed, vol. 19, Muenster: LIT Verlag, 2020, pp. 157–182, ISBN: 978-3643145475.

[100] Seltner, P. M., S. Willems, and A. Gülhan, "Aerodynamic interactions of blunt bodies free-flying in hypersonic flow", *Experiments in Fluids*, vol. 65, no. 80, 2024. DOI: `10.1007/s00348-024-03818-9`.

[101] Seltner, P. M., S. Willems, A. Gülhan, E. C. Stern, J. M. Brock, and M. J. Aftosmis, "Aerodynamics of inclined cylindrical bodies free-flying in a hypersonic flowfield", *Experiments in Fluids*, vol. 62, no. 9, 2021. DOI: `10.1007/s00348-021-03269-6`.

[102] Settles, G. S., *Schlieren and shadowgraph techniques*, 2. ed. Berlin: Springer, 2006, 400 pp., ISBN: 3-540-66155-7.

[103] Sousa, C. E., R. Deiterding, and S. J. Laurence, "Dynamics of a spherical body shedding from a hypersonic ramp. Part 1. Inviscid flow", *Journal of Fluid Mechanics*, vol. 906, no. A28, pp. 1–30, 2020. DOI: `10.1017/jfm.2020.756`.

[104] Spearman, M. L., "Aerodynamics of spheres for Mach numbers from 0.6 to 10.5 including some effects of test conditions", in *11th Aerodynamic Decelerator Systems Technology Conference*, American Institute of Aeronautics and Astronautics (AIAA), 1991. DOI: `10.2514/6.1991-894`.

[105] Spottswood, S. M., T. J. Beberniss, T. G. Eason, R. A. Perez, J. M. Donbar, D. A. Ehrhardt, and Z. B. Riley, "Exploring the response of a thin, flexible panel to shock-turbulent boundary-layer interactions", *Journal of Sound and Vibration*, vol. 443, pp. 74–89, 2019. DOI: `10.1016/j.jsv.2018.11.035`.

[106] Sutton, M. A., J. J. Orteu, and H. W. Schreier, *Image correlation for shape, motion and deformation measurements*, 1. ed. Springer, 2009, ISBN: 978-0-387-78747-3. DOI: `10.1007/978-0-387-78747-3`.

[107] Taguema, L., “Investigation of aerodynamic interactions between a free-flying and a balance-mounted object”, Master’s thesis, RWTH Aachen University, 2017. URL: https://elib.dlr.de/214125/.

[108] Takayama, K., H. Tanno, K. Itoh, and A. Abe, “Interactions of shock waves with a sphere and arrayed spheres”, in *Structures under shock and impact VIII*, Structures and Materials, Jones, N. and C. A. Brebbia, Eds., 1 ed., vol. 73, Southampton: WIT Press, 2004, pp. 95–107, ISBN: 978-1-85312-706-9. DOI: 10.2495/SU040101.

[109] Tanno, H., T. Komuro, K. Sato, and K. Itoh, “Wind tunnel test comparison between JAXA-HIEST and ONERA-S4MA with HYFLEX lifting-body”, in *7th European Conference for Aeronautics and Space Scienes (EUCASS)*, Milano, 2017. DOI: 10.13009/EUCASS2017-187.

[110] Tropea, C., A. L. Yarin, and J. F. Foss, *Springer handbook of experimental fluid mechanics*, 1. ed. Berlin: Springer, 2007, ISBN: 978-3-540-25141-5.

[111] UN Office for Outer Space Affairs, *Online index of objects launched into outer space*, 2023. URL: https://www.unoosa.org/oosa/osoindex/search-ng.jspx.

[112] Van Dyke, M. D., *An album of fluid motion*, 1. ed. Stanford: Parabolic Press, 1982, ISBN: 978-0915760022.

[113] Venkatapathy, E., A. Gülhan, M. J. Aftosmis, J. M. Brock, D. Mathias, D. Neeb, D. Rodriguez, P. M. Seltner, E. C. Stern, and S. Willems, “In pursuit of improving airbust and ground damage predictions: Recent advanced in multi-body aerodynamic testing and computational tools validation”, Poster presented at *Fifth Planetary Defense Conference (PDC)*, Tokio: International Academy of Astronautics (IAA), 2017.

[114] Vennard, J. F., *Elementary fluid mechanics*, 1. ed. New York: John Wiley & Sons, 1940.

[115] Vincenti, W. G. and C. H. Kruger, *Introduction to physical gas dynamics*, 2. ed. Huntington: Krieger, 1975, ISBN: 978-0882753096.

[116] Welch, P. D., “The use of fast Fourier transform for the estimation of power spectra: A method based on time averaging over short, modified periodograms”, *IEEE Transactions on Audio and Electroacoustic*, vol. 15, no. 2, pp. 70–73, 1967. DOI: 10.1007/978-3-322-89521-9_13.

[117] Whalen, T. J. and S. J. Laurence, “Experiments on the separation of sphere clusters in hypersonic flow”, *Experiments in Fluids*, vol. 62, no. 4, 2021. DOI: 10.1007/s00348-021-03157-z.

[118] Whalen, T. J., S. J. Laurence, and R. Deiterding, “A numerical investigation of clustered spheres separating in Mach 20 flow”, in *AIAA Aviation 2020 Forum*, Virtual Event, Online: American Institute of Aeronautics and Astronautics (AIAA), 2020. DOI: 10.2514/6.2020-2970.

[119] Willems, S., “Strömung-Struktur-Wechselwirkung in Überschallströmungen”, DLR-FB 2017-07, PhD thesis, DLR/RWTH Aachen University, Aachen/Cologne, 2017. URL: https://elib.dlr.de/116735/.

[120] Zhdan, I. A., V. P. Stulov, and P. V. Stulov, “Aerodynamic interaction of two bodies in a supersonic flow”, *Doklady Physics*, vol. 49, no. 5, pp. 315–317, 2004. DOI: 10.1134/1.1763624.

[121] Zhdan, I. A., V. P. Stulov, and P. V. Stulov, “3D configurations of broken body fragments in a supersonic flow”, *Doklady Physics*, vol. 50, no. 10, pp. 514–518, 2005. DOI: `10.1134/1.2123300`.

[122] Zhukov, B. G., R. O. Kurakin, S. I. Rozov, V. A. Sakharov, M. V. Beloborodii, E. M. Drobyshevski, and N. Y. Shibanova, “Synchronous EM launch of two bodies with double-barrel railgun and some peculiarities of their hypersonic flight in air”, in *Fourth International Workshop on Magnetoplasma Aerodynamics*, Moscow: International Liaison Groupon on MHD Energy Conversion, 2002.

[123] Zhukov, B. G., R. O. Kurakin, V. A. Sakharov, S. V. Bobashev, S. A. Ponyaev, B. I. Reznikov, and S. I. Rozov, “Synchronous acceleration of two millimeter-sized bodies up to hypersonic velocities in a multichannel railgun”, *Technical Physics Letters*, vol. 39, no. 12, pp. 1057–1059, 2013, ISSN: 1063-7850. DOI: `10.1134/S1063785013120146`.

A Derivation of Analytical Expressions

Analytical expressions for the aerodynamic coefficients can be derived from the modified Newtonian flow theory as in equation (3.20) by using the local surface inclination method for three-dimensional bodies as in equation (3.21). In this approach, the moment coefficients for the analyzed bodies are zero due to their symmetries, whereas the force coefficients can be determined using the following surface integral:

$$\vec{C_{\mathrm{F}}} = \frac{1}{S_{ref}} \iint_A \vec{n} \cdot c_{\mathrm{p}} \, dA \tag{A.1}$$

where dA is the differential surface element of the body. The derivations are shown below for spheres (see section A.1), cubes (see section A.2) and cylinders (see section A.3). It should be noted that the resulting approximations are valid for all pitch angles.

A.1 Spheres

Starting from the spherical coordinates for a spherical body with the polar angle θ and the azimuthal angle ϕ, the normal vector can be expressed as follows:

$$\vec{n} = \begin{pmatrix} \sin(\theta)\cos(\phi) \\ \sin(\theta)\sin(\phi) \\ \cos(\theta) \end{pmatrix} \tag{A.2}$$

Since spheres are point-symmetric, the angle of attack does not play a role for the forces in the aerodynamic FoR, which means that the unit vector of free-stream velocity can be simplified to:

$$\frac{\vec{v_\infty}}{|\vec{v_\infty}|} = \begin{pmatrix} 1 \\ 0 \\ 0 \end{pmatrix} \tag{A.3}$$

From the normal vector of spheres in equation (A.2) and the unit vector of the free-stream velocity in equation (A.3), the following local deflection angle results by using equation (3.21):

$$\nu = \arcsin\left(\sin\left(\theta\right)\cos\left(\phi\right)\right) \tag{A.4}$$

This local deflection angle from equation (A.4) is inserted into the modified Newtonian flow theory as in equation (3.20) and the following pressure coefficient is obtained:

$$c_{\mathrm{p}} = c_{\mathrm{p}max}\sin^2\left(\theta\right)\cos^2\left(\phi\right) \tag{A.5}$$

In order to determine the force coefficients, the differential element of the spherical surface is required, which is determined by the cross product of the tangent vectors in spherical coordinates, resulting in the following differential element for a sphere with radius r:

$$dA = r^2\sin\left(\theta\right)\,d\phi\,d\theta \tag{A.6}$$

As the lift force and the side force are zero, the force coefficients consist only of the drag coefficient. This is determined by inserting equations (A.2), (A.5) and (A.6) into the first component of equation (A.1). By taking into account that the ambient pressure applies to the afterbody and the pressure coefficient is therefore zero, the integral is calculated only over the surface area of the forebody as follows:

$$C_{\mathrm{D}} = \frac{1}{S_{ref}}\int_{-\frac{\pi}{2}}^{\frac{\pi}{2}}\int_{\frac{\pi}{2}}^{\frac{3}{2}\pi} r^2 c_{\mathrm{p}max}\sin^4\left(\theta\right)\cos^3\left(\phi\right)\,d\phi\,d\theta \tag{A.7}$$

By solving the integrals in equation (A.7), the drag coefficient of spheres is:

$$C_{\mathrm{D}} = \frac{c_{\mathrm{p}max}}{2} \tag{A.8}$$

A.2 Cubes

In contrast to the derivation for spheres, Cartesian coordinates are used for cubes, whereby the normal vector of their six square faces can be expressed as follows:

$$\vec{n} = \left\{\pm\begin{pmatrix}1\\0\\0\end{pmatrix},\pm\begin{pmatrix}0\\1\\0\end{pmatrix},\pm\begin{pmatrix}0\\0\\1\end{pmatrix}\right\} \tag{A.9}$$

Since a body-fixed FoR is employed, the variation of the body orientation is achieved by rotating the vector of the free-stream velocity. The unit vector of free-stream velocity for just pitch rotations is given by:

$$\frac{\vec{v_\infty}}{|\vec{v_\infty}|} = \begin{pmatrix} \cos(\vartheta) \\ 0 \\ \sin(\vartheta) \end{pmatrix} \tag{A.10}$$

As the free-stream velocity in the y-direction is zero, just the faces in the x- and z-directions are considered. Based on the normal vector of cubes as in equation (A.9) and the unit vector of the free-stream velocity as in equation (A.10), the local deflection angle is determined using equation (3.21) to obtain:

$$\nu = \begin{cases} \arcsin(\pm\cos(\vartheta)); & \text{for the surfaces parallel to the } yz\text{-plane} \\ \arcsin(\pm\sin(\vartheta)); & \text{for the surfaces parallel to the } xy\text{-plane} \end{cases} \tag{A.11}$$

Substituting the local deflection angle from equation (A.11) into the modified Newtonian flow theory from equation (3.20), the pressure coefficient is determined as follows:

$$c_\mathrm{p} = \begin{cases} c_{\mathrm{p}max}\cos^2(\vartheta); & \text{for the surfaces parallel to the } yz\text{-plane} \\ c_{\mathrm{p}max}\sin^2(\vartheta); & \text{for the surfaces parallel to the } xy\text{-plane} \end{cases} \tag{A.12}$$

The differential surface element of the cube for determining the force coefficients is defined as:

$$dA = \begin{cases} dy\,dz; & \text{for the surfaces parallel to the } yz\text{-plane} \\ dx\,dy; & \text{for the surfaces parallel to the } xy\text{-plane} \end{cases} \tag{A.13}$$

Using equation (A.1), the force coefficients are calculated in the body-fixed FoR, whereby the surface pressure distribution of the windward faces are estimated by means of equation (A.12) and the leeside faces experience a zero pressure coefficient. Substituting equations (A.9) and (A.13) into the equation, the surface integrals for the axial and normal force coefficients are obtained:

$$C_\mathrm{A} = \frac{1}{S_{ref}} \int_{-\frac{l}{2}}^{\frac{l}{2}} \int_{-\frac{l}{2}}^{\frac{l}{2}} c_{\mathrm{p}max}\cos^2(\vartheta)\; dy\,dz \tag{A.14}$$

$$C_{\mathrm{N}} = \frac{1}{S_{ref}} \int_{-\frac{l}{2}}^{\frac{l}{2}} \int_{-\frac{l}{2}}^{\frac{l}{2}} c_{\mathrm{p}max} \sin^2(\vartheta)\, dx\, dy \tag{A.15}$$

To determine the drag and lift coefficients, the force coefficients in the body-fixed FoR are transformed into the aerodynamic FoR:

$$C_{\mathrm{D}} = C_{\mathrm{A}} \left|\cos(\vartheta)\right| + C_{\mathrm{N}} \left|\sin(\vartheta)\right| \tag{A.16}$$

$$C_{\mathrm{L}} = -C_{\mathrm{A}} \operatorname{sgn}(\cos(\vartheta)) \sin(\vartheta) + C_{\mathrm{N}} \operatorname{sgn}(\sin(\vartheta)) \cos(\vartheta) \tag{A.17}$$

After substituting equations (A.14) and (A.15) into equations (A.16) and (A.17) and simplifying, the drag and lift coefficient of cubes are:

$$C_{\mathrm{D}} = c_{\mathrm{p}max} \left(\left|\sin^3(\vartheta)\right| + \left|\cos^3(\vartheta)\right| \right) \tag{A.18}$$

$$C_{\mathrm{L}} = \frac{1}{2} c_{\mathrm{p}max} \sin(2\vartheta) \left(\left|\sin(\vartheta)\right| - \left|\cos(\vartheta)\right|\right) \tag{A.19}$$

A.3 Cylinders

Since cylinders consist of bended and planar surface elements, Cartesian coordinates are used for the base surfaces and polar coordinates with the polar angle θ for the lateral surface. The resulting normal vector is given as:

$$\vec{n} = \begin{cases} \pm(1, 0, 0); & \text{for the base surfaces} \\ (0, \sin(\theta), \cos(\theta)); & \text{for the lateral surface} \end{cases} \tag{A.20}$$

As with the cube, the variation of the body orientation is achieved by the rotation of the free-stream velocity's vector, whereby for the present work only the pitch rotation is taken into account as given by:

$$\frac{\vec{v_\infty}}{|\vec{v_\infty}|} = \begin{pmatrix} \cos(\vartheta) \\ 0 \\ \sin(\vartheta) \end{pmatrix} \tag{A.21}$$

As a result of equation (A.21), the free-stream velocity in the y-direction can be neglected. Substituting the two equations for the normal vector from equation (A.20) and the unit vector of the free-stream velocity from equation (A.21) into equation (3.21) gives the local deflection angle:

$$\nu = \begin{cases} \arcsin(\pm\cos(\vartheta)); & \text{for the base surfaces} \\ \arcsin(\sin(\vartheta)\cos(\theta)); & \text{for the lateral surface} \end{cases} \tag{A.22}$$

By combining the equations for the local deflection angle from equation (A.11) and the modified Newtonian flow theory from equation (3.20), the pressure coefficient on the entire surface of the cylinders can be expressed as:

$$c_\mathrm{p} = \begin{cases} c_{\mathrm{p}max}\cos^2(\vartheta); & \text{for the base surfaces} \\ c_{\mathrm{p}max}\sin^2(\vartheta)\cos^2(\theta); & \text{for the lateral surface} \end{cases} \tag{A.23}$$

The differential surface element of the cylinder, that is used for determining the force coefficients, is defined as:

$$dA = \begin{cases} r\,d\theta\,dr; & \text{for the base surfaces} \\ r\,d\theta\,dx; & \text{for the lateral surface} \end{cases} \tag{A.24}$$

Next, the force coefficients are determined in the body-fixed FoR by substituting equations (A.20) and (A.24) into equation (A.1), using the circular base area as the reference area ($S_{ref} = \pi d^2/4$). In doing so, the solution of the side force coefficient's surface integral is zero and can therefore be neglected. Considering that the ambient pressure applies to the afterbody and thus the pressure coefficient is zero, the surface integral is evaluated solely over the surface area of the forebody, resulting in the bounds of integration in equations (A.25) and (A.26). The surface integral for the axial component is determined by the pressure distribution of the base surfaces, while for the normal component it results from the lateral surface's pressure distribution, as shown below:

$$C_\mathrm{A} = \frac{1}{S_{ref}} \int_0^r \int_0^{2\pi} r c_{\mathrm{p}max} \cos^2(\vartheta)\; d\theta\, dr \tag{A.25}$$

$$C_{\mathrm{N}} = \frac{1}{S_{ref}} \int_{-\frac{l}{2}}^{\frac{l}{2}} \int_{-\frac{\pi}{2}}^{\frac{\pi}{2}} r c_{\mathrm{p}max} \sin^2(\vartheta) \cos^3(\theta) \; d\theta \, dx \tag{A.26}$$

In the transformation to the aerodynamic FoR, the drag and lift coefficients are related to the axial and normal force coefficients by the following equations:

$$C_{\mathrm{D}} = C_{\mathrm{A}} \left|\cos(\vartheta)\right| + C_{\mathrm{N}} \left|\sin(\vartheta)\right| \tag{A.27}$$

$$C_{\mathrm{L}} = -C_{\mathrm{A}} \operatorname{sgn}(\cos(\vartheta)) \sin(\vartheta) + C_{\mathrm{N}} \operatorname{sgn}(\sin(\vartheta)) \cos(\vartheta) \tag{A.28}$$

After equations (A.25) and (A.26) have been inserted into equations (A.27) and (A.28), the integrals are solved and the solutions are simplified. The final result is the following equations, that describe the aerodynamic coefficients of cylinders with different aspect ratios (l/d).

$$C_{\mathrm{D}} = c_{\mathrm{p}max} \left(\frac{8}{3\pi} \frac{l}{d} \left|\sin^3(\vartheta)\right| + \left|\cos^3(\vartheta)\right| \right) \tag{A.29}$$

$$C_{\mathrm{L}} = \frac{1}{2} c_{\mathrm{p}max} \sin(2\vartheta) \left(\frac{8}{3\pi} \frac{l}{d} \left|\sin(\vartheta)\right| - \left|\cos(\vartheta)\right| \right) \tag{A.30}$$

B Numerical Results from CFD Simulations

In addition to the experimental study in this thesis, corresponding numerical analyses for single-body and multi-body configurations were performed by others. On the one hand, CFD simulations were performed internally with the flow solver TAU for single cubes [39] as well as single-body and two-body configurations with spheres [72]. On the other hand, external CFD simulations were carried out by NASA's Ames Research Center with the flow solvers Cart3D and US3D for configurations with single blunt bodies [101] and multiple spheres [91].

B.1 Single Cube

By using the DLR's flow solver TAU, three-dimensional viscous laminar simulations of a plane-exposed and edge-exposed cube were performed. TAU is a tool for the numerical solution of compressible flows with unstructured meshes [56]. The flow conditions as in table 2.2 were used for these simulations. To create the following figures, the flow field data from a previous study by [39] were used.

Figure B.1 shows the Mach number distribution with streamlines for a cube at $\vartheta = 0°$ in figure B.1a and $\vartheta = 45°$ in figure B.1b.

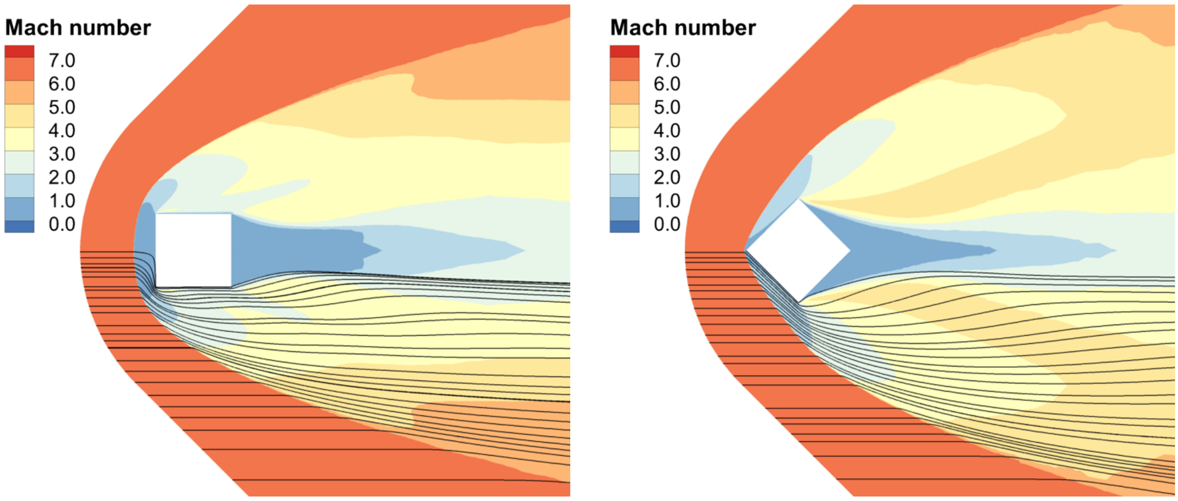

(a) $\vartheta = 0°$ **(b)** $\vartheta = 45°$

Figure B.1: Mach number distribution with streamlines of one cube's plane or edge is exposed to the flow based on [39]

B.2 Single Cylinder

Viscous turbulent DES simulations on a single cylinder with an aspect ratio of 2 at different pitch angle were carried out by using the compressible flow solver US3D. This tool is a Navier-Stokes solver for unstructured finite volumes [77], whose settings for the present configurations are described in [101]. Therefore, the flow conditions with a reservoir pressure of $520\,\mathrm{kPa}$ given in table 2.2 were applied. The following figures are taken from the numerical results of an earlier study [101].

Figure B.2 presents the flow field around a base-exposed cylinder with isothermal boundary condition of their walls. In figure B.2a, the Mach number distribution with streamlines is shown. In figure B.2b, the distributions of the flow temperature as well as the surface pressure are depicted. As soon as the cylinder is inclined, the flow field around the body becomes asymmetric as well as aerodynamic phenomena become more complex, which is illustrated in computational schlieren images in figure B.3. These schlieren representations depict the density gradient of the flow in x-direction merely at the central plane.

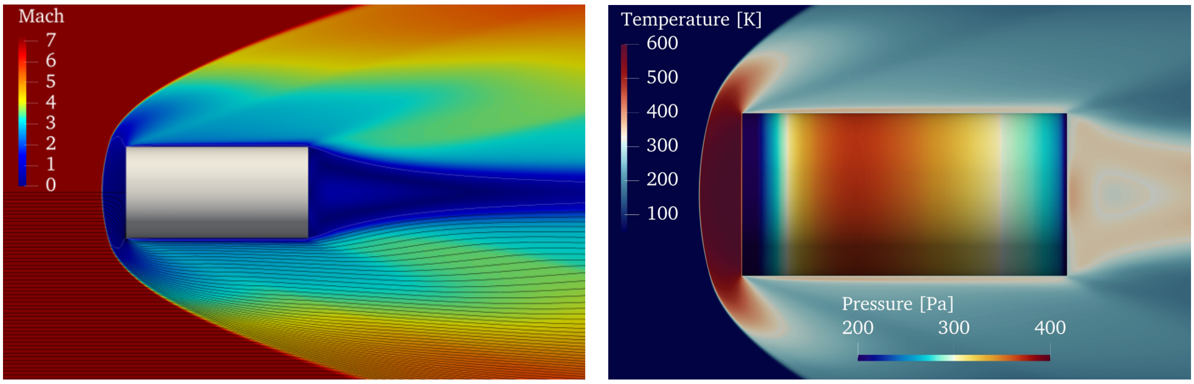

(a) Mach number and streamlines **(b)** Flow temperature and surface pressure

Figure B.2: Numerical flow field of one cylinder's base is exposed to the flow showing distributions of Mach number with streamlines and flow temperature with surface pressure [101]

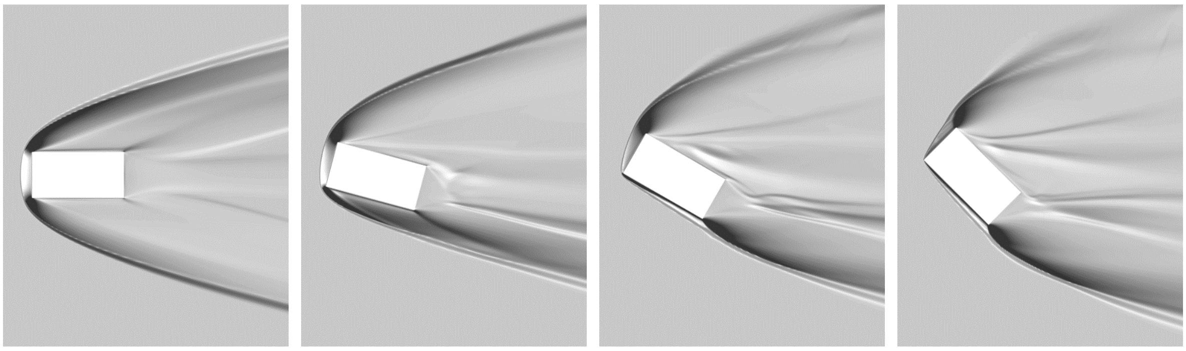

(a) $\vartheta = 0°$ **(b)** $\vartheta = 15°$ **(c)** $\vartheta = 30°$ **(d)** $\vartheta = 45°$

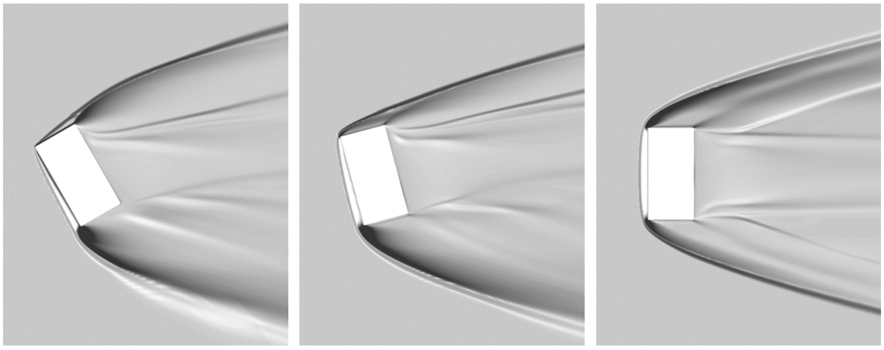

(e) $\vartheta = 60°$ **(f)** $\vartheta = 75°$ **(g)** $\vartheta = 90°$

Figure B.3: Computational schlieren images of a cylinder at different pitch angles [101]